



**HAL**  
open science

# Multiscale experimental and numerical study of the structure and the dynamics of water confined in clay minerals

Emmanuel Guillaud

► **To cite this version:**

Emmanuel Guillaud. Multiscale experimental and numerical study of the structure and the dynamics of water confined in clay minerals. Material chemistry. Université de Lyon; Friedrich-Alexander-Universität Erlangen-Nürnberg, 2017. English. NNT : 2017LYSE1123 . tel-01587720

**HAL Id: tel-01587720**

**<https://theses.hal.science/tel-01587720>**

Submitted on 14 Sep 2017

**HAL** is a multi-disciplinary open access archive for the deposit and dissemination of scientific research documents, whether they are published or not. The documents may come from teaching and research institutions in France or abroad, or from public or private research centers.

L'archive ouverte pluridisciplinaire **HAL**, est destinée au dépôt et à la diffusion de documents scientifiques de niveau recherche, publiés ou non, émanant des établissements d'enseignement et de recherche français ou étrangers, des laboratoires publics ou privés.



N° d'ordre NNT : 2017LYSE1123

**THÈSE DE DOCTORAT DE L'UNIVERSITÉ DE LYON**  
opérée au sein de  
**l'Université Claude Bernard Lyon 1**  
et de  
**l'Université Friedrich Alexander-Erlangen Nürnberg**

**École Doctorale ED34**  
**Matériaux**

**Spécialité de doctorat : Physique et science des matériaux**  
**Discipline : Physico-chimie**

**Soutenue publiquement le 10/07/2017, par :**  
**Emmanuel Bertrand Guillaud**

---

**Multiscale experimental and numerical study of the  
structure and the dynamics of water confined in clay  
minerals**

**(Étude multi-échelles expérimentale et numérique de la structure  
et de la dynamique de l'eau confinée dans les argiles)**

---

Devant le jury composé de :

Caupin Frédéric, Professeur, Université Claude Bernard Lyon 1	Président
Marry Virginie, Professeure, Université Pierre et Marie Curie Paris 6	Rapporteuse
Roy Pascale, Directrice de Recherche, Université Paris-Sud et Synchrotron Soleil	Rapporteuse
Götz-Neunhoeffler Friedlinda, Professeure, Universität Erlangen Nürnberg	Examinatrice
Valeriani Chantal, Assistant-Professeure, Universidad Complutense de Madrid	Examinatrice
De Ligny Dominique, Professeur, Universität Erlangen Nürnberg	Directeur de thèse, rapporteur
Joly Laurent, Maître de Conférences, Université Claude Bernard Lyon 1	Directeur de thèse
Merabia Samy, Chargé de Recherche, Université Claude Bernard Lyon 1	Co-directeur de thèse, invité
Panczer Gérard, Professeur, Université Claude Bernard Lyon 1	Co-directeur de thèse, invité

# UNIVERSITE CLAUDE BERNARD - LYON 1

## Président de l'Université

Président du Conseil Académique  
 Vice-président du Conseil d'Administration  
 Vice-président du Conseil Formation et Vie Universitaire  
 Vice-président de la Commission Recherche  
 Directrice Générale des Services

## M. le Professeur Frédéric FLEURY

M. le Professeur Hamda BEN HADID  
 M. le Professeur Didier REVEL  
 M. le Professeur Philippe CHEVALIER  
 M. Fabrice VALLÉE  
 Mme Dominique MARCHAND

## COMPOSANTES SANTE

Faculté de Médecine Lyon Est - Claude Bernard  
 Faculté de Médecine et de Maïeutique Lyon Sud - Charles Mérieux  
 Faculté d'Odontologie  
 Institut des Sciences Pharmaceutiques et Biologiques  
 Institut des Sciences et Techniques de la Réadaptation  
 Département de formation et Centre de Recherche en Biologie Humaine

Directeur : M. le Professeur G. RODE  
 Directeur : Mme la Professeure C. BURILLON  
 Directeur : M. le Professeur D. BOURGEOIS  
 Directeur : Mme la Professeure C. VINCIGUERRA  
 Directeur : M. X. PERROT  
 Directeur : Mme la Professeure A-M. SCHOTT

## COMPOSANTES ET DEPARTEMENTS DE SCIENCES ET TECHNOLOGIE

Faculté des Sciences et Technologies  
 Département Biologie  
 Département Chimie Biochimie  
 Département GEP  
 Département Informatique  
 Département Mathématiques  
 Département Mécanique  
 Département Physique  
 UFR Sciences et Techniques des Activités Physiques et Sportives  
 Observatoire des Sciences de l'Univers de Lyon  
 Polytech Lyon  
 Ecole Supérieure de Chimie Physique Electronique  
 Institut Universitaire de Technologie de Lyon 1  
 Ecole Supérieure du Professorat et de l'Education  
 Institut de Science Financière et d'Assurances

Directeur : M. F. DE MARCHI  
 Directeur : M. le Professeur F. THEVENARD  
 Directeur : Mme C. FELIX  
 Directeur : M. Hassan HAMMOURI  
 Directeur : M. le Professeur S. AKKOUCHE  
 Directeur : M. le Professeur G. TOMANOV  
 Directeur : M. le Professeur H. BEN HADID  
 Directeur : M. le Professeur J.C. PLENET  
 Directeur : M. Y. VANPOULLE  
 Directeur : M. B. GUIDERDONI  
 Directeur : M. le Professeur E. PERRIN  
 Directeur : M. G. PIGNAULT  
 Directeur : M. le Professeur C. VITON  
 Directeur : M. le Professeur A. MOUGNIOTTE  
 Directeur : M. N. LEBOISNE



Der Technischen Fakultät der  
**Universität Erlangen-Nürnberg**  
zur Erlangung des Grades

## DOKTOR-INGENIEUR

vorgelegt von  
**Herr. M.Sc. Emmanuel Bertrand Guillaud**

---

**Multiscale experimental and numerical study of the  
structure and the dynamics of water confined in clay  
minerals**

**(Multiskale experimentelle und numerische Untersuchung der  
Struktur und der Dynamik in Tonmineralien eingeschlossenen  
Wasser)**

---

Prüfungskollegium:

Prof. Caupin Frédéric, Université Claude Bernard Lyon 1

Vorsitzender

Prof. Marry Virginie, Université Pierre et Marie Curie Paris 6

Gutachterin

Dr. Habil. Roy Pascale, Université Paris-Sud und Synchrotron Soleil

Gutachterin

Prof. Götz-Neunhoffer Friedlinde, Universität Erlangen Nürnberg

Prüferin

Dr. Valeriani Chantal, Universidad Complutense de Madrid

Prüferin

Prof. De Ligny Dominique, Universität Erlangen Nürnberg

Betreuer, Gutachter

Dr. Habil. Joly Laurent, Université Claude Bernard Lyon 1

Betreuer

Dr. Habil. Merabia Samy, Université Claude Bernard Lyon 1

Co-Betreuer, Gast

Prof. Panczer Gérard, Université Claude Bernard Lyon 1

Co-Betreuer, Gast

## Fundings



Contrat doctoral du  
Ministère de l'Éducation Nationale,  
de l'Enseignement Supérieur et  
de la Recherche



Aides à la mobilité doctorale  
du Programme Avenir Lyon Saint Etienne  
année 2015



Université  
franco-allemande  
Deutsch-Französische  
Hochschule

Allocation de soutien aux  
cotutelles de thèse Franco-Allemandes  
années 2016-2017  
<http://www.dfh-ufa.org/>

## Technical support



Projets n° 20150736  
et 20160170



CEntre COmmun de  
Microscopie Optique



Projets n°t2015087230  
et t2016087230



Pôle Scientifique de  
Modélisation Numérique

# Acknowledgements

This dissertation constitutes the end of three years of work (ok... much more actually if one considers internships!) with wonderful people who I would like to warmly thank. Their presence in the following lines is at least as important as the six chapters of scientific content that come next! However, it is a difficult task to thank everybody. I hope I will not forget anybody. I sincerely apologize if some people are missing.

First, I would like to thank my supervisors. Of course, there is no PhD if there is no supervisor! So, I thank Dominique de Ligny for introducing this very interesting topic about water and clays, and Laurent Joly, Samy Merabia, Alain Mermet and Gérard Panczer for converting what was initially just an internship subject into a full research project. Especially, thank you Laurent and Samy for making me discover the world of simulations. Clearly, it was the dark side of science for me before.

Then, I would like to thank the members of my PhD defense evaluation committee, who kindly accepted to read and review the present dissertation, and gave me precious advices to improve it or to go further about some topics.

During the three last years, I had the opportunity to work in two labs, in two different countries, and I benefited from many large-scale facilities. I would like to thank the head of the Light and Matter Institute (ILM) and of the Institute for Glass and Ceramics (WW3), as well as the different organisms which supported the project financially and / or technically: the French Ministry for Education and Research, the PALSE (Programme Avenir Lyon Saint-Etienne) program, the DFH/UFA (Université Franco-Allemande), the TGCC (Très Gros Centre de Calculs), the PSMN (Pôle Scientifique de Modélisation Numérique) and the CeCoMO (Centre Commun de Microscopie Optique), and all people who helped to organize these fundings. Especially, I would like to warmly thank Amel Nemili, Céline Fiordalisi, Jean-Claude Plenet and Jean-Yves Buffière.

I learned a lot during those last three years, about a huge variety of subjects and technics thanks to fruitful discussions with many people who kindly accepted to give a little of their time to me. Especially, I would like to thank Bruno Issenmann for discussions about water, Pierre Mignon, Benjamin Rotenberg, Virginie Marry and Angelos Michaelides for discussions about classical and quantum simulations, Micheline Boudeulle for discussions about clays, François Gaillard for discussions about FTIR technics, Dominique Ectors, Friedlinde Götz-Neunhoeffler and Jürgen Neubauer for discussions about TD-NMR. This also includes people who helped me performing some measurements, especially Dominique Ectors for TD-MNR, Eva Springer for SEM, Alfons Stiegelschmitt and Hana Strelec for porosimetry, Sabine Fiedler for thermogravimetry, and also engineers and technicians from the electronic and mechanic workshops, Peter Reinhardt, Yann Guillin, Heiko Huber and Pierre Beneteau, without whom no experiment would be possible.

I also would like to thank the staff of the AILES beamline for fruitful scientific discussions and technical support during the two intense experimental journeys in Synchrotron SOLEIL, especially Pascale Roy, Jean-Blaise Brubach, Maxime Deutsch, Simona Dalla-Bernardina, Tania Tibiletti and Kelly Rader. I also thank Antoine Cornet for his night-time help during the second session of measurements.

I received also a lot of help, but also moral support, from my team mates and wonderful roommates: Rita Cicconi, Nastya and Sasha Veber, Heike Reinfelder, Nahum Travitzky, Tobias Fey, Martin Brehl, Monika Holzner, Michael Schneider, Michael Bergler, Sana Rachidi, Hatim Laadoua, André Posch, Julie Pradas and Alexis Gonez, Nadia Tiabi, Abderrazak Masmoudi, Franziska Eichhorn, Ruth Hammerbacher, Christoph Ebner, Simone Kellermann

and Markus Rachinger in WW3, and Dominique Vouagner, Valérie Martinez, Jacques Le Brusq, Christine Martinet, Bernard Champagnon, Jérémie Margueritat, Gianpietro Cagnoli, Olivier Pierre-Louis, Thierry Biben, David Rodney, Tristan Albaret, Dome Tanguy, Pierre-Antoine Geslin, Thomas Niehaus, Elodie Coillet, Antoine Cornet, Adrien Girard, Quentin Martinet, Simon Degioanni, Hamed Bouchouicha, Hanan Belradhia, Mounira Amraoui, Marie Adier, Stéphane Tromp, Li Fu, Ali Alkurdi, Maxence Fombonne, Amira Saoudi, Benjamin Wodey, ... (sorry for people I missed...), in Villeurbanne. Thank you also to other people in WW3: Jonas, Felix, Corinna, Azatuhi, Hannes, Martina, Philip, Bastian, Julia, Maja, Anh-Dai... I regret we did not have enough time to know each other better. I especially thank Stefan Wolf and Martin Brehl for their help for German translations. I will miss Glass group parties and excursions, as well as coffee breaks with some cakes of some piece of chocolate with the SOPRaNO group. Concerning this last point, I thank also all cake tasters: people of the SOPRaNO team, Aline, Emilie...

Then, I would like to thank all the "Fête de la Science" team: Cécile Le Luyer, Bernard Moine, Amina Bensalah-Ledoux, Helainne Girão, Justine Baronnier... I hope the adventure will continue during many years.

I must also thank my students and other teachers I have worked with. The few teaching hours I did during the last three years were a really rich experience. I hope I did not make anybody disgusted with physics!...

Finally, this PhD would not have been possible without the moral support of my friends and family. I warmly thank them.

And I must conclude by a special dedication to Marky, Dee-Dee, Joey and their coworkers for livening the second floor of the Lippmann building up.

# Contents

<b>Acknowledgements</b> .....	v
<b>Contents</b> .....	vii
<b>Résumé</b> .....	xi
<b>Zusammenfassung</b> .....	xv
<b>Introduction</b> .....	1
<b>Chapter 1. Liquid water from bulk to confined media</b> .....	5
1 Pure bulk water .....	5
1.1 Liquid water and its anomalies .....	5
1.2 The water “liquid phase” diagram .....	6
1.3 Viscoelasticity of water .....	8
2 Salt water .....	10
2.1 Solvation and structure .....	10
2.2 Colligative properties .....	11
2.3 Hydrodynamic transport .....	12
3 Confined water .....	14
3.1 Structure of confined water .....	14
3.2 Hydrodynamics in confined media: notions of nanofluidics .....	16
4 Water confined in clays .....	18
4.1 Clay structure .....	18
4.2 Swelling processes .....	20
4.3 Water structure and dynamics .....	21
5 Appendix: Table of effective ionic radii .....	24
<b>Chapter 2. Probing water from electrons to bulk: numerical and experimental methods</b> .....	25
1 Atoms and molecules .....	25
1.1 Atoms .....	25
1.2 Molecules .....	26
1.3 Beyond the molecule: molecular interactions .....	27
2 Infrared absorption spectroscopy .....	27
2.1 Theory (with applications to water) .....	27
2.2 Instrumentation .....	30
3 Classical and ab initio molecular dynamics .....	34
3.1 Molecular dynamics .....	34
3.2 Computing forces (I): density functional theory .....	39
3.3 Computing forces (II): point charge force fields .....	41
<b>Chapter 3. Viscoelastic properties of pure liquid water</b> .....	45
1 Long time dynamics of water: water as a viscous liquid .....	45
1.1 Computational details .....	46
1.2 Structural relaxation times .....	46
1.3 Shear viscosity .....	48
1.4 Stokes-Einstein relation .....	49
1.5 Summary .....	52
2 Links with the short time dynamics: from viscous liquid to elastic solid .....	52
2.1 Numerical methods .....	52

2.2	Slow dynamics vs elastic modulus . . . . .	53
2.3	Hall-Wolynes equation . . . . .	54
2.4	Summary . . . . .	55
3	Towards a consideration of quantum effects: ab initio approach . . . . .	55
3.1	Aim of the study and methods . . . . .	55
3.2	Pulay stress correction . . . . .	56
3.3	Structural and dynamical predictions . . . . .	57
4	Conclusion . . . . .	60
	<b>Chapter 4. Water hydrodynamics near a hydrophobic surface</b> . . . . .	67
1	Aim of the study . . . . .	67
2	Simulations details . . . . .	67
3	Temperature dependence of the friction coefficient and the slip length . . . . .	68
4	Origin of the friction temperature dependence . . . . .	71
4.1	Structure of the liquid near the interface . . . . .	71
4.2	Corrugation of the solid surface . . . . .	73
4.3	Liquid and interface relaxation . . . . .	73
5	Summary and conclusion . . . . .	75
	<b>Chapter 5. Influence of dissolved salts on the transport and structural properties of water</b> . . . . .	77
1	Molecular Dynamics in Electronic Continuum . . . . .	78
1.1	Principle . . . . .	78
1.2	Dielectric constant of TIP4P/2005f water . . . . .	78
1.3	Application, pros and cons of the method . . . . .	79
2	Force field optimization . . . . .	80
3	Molecular dynamics methods . . . . .	82
4	Application of the model . . . . .	82
4.1	Crystal structures . . . . .	82
4.2	Liquid structure . . . . .	82
4.3	Water self diffusion . . . . .	84
4.4	Shear viscosity . . . . .	85
4.5	Mid-infrared absorption spectrum . . . . .	87
5	Conclusion . . . . .	88
	<b>Chapter 6. Structure and dynamics of water confined in clay minerals</b> . . . . .	91
1	Evolution of the structure and connectivity of water adsorbed in clay minerals upon swelling . . . . .	91
1.1	Experimental methods . . . . .	92
1.2	Results . . . . .	93
1.3	Discussion . . . . .	98
1.4	Summary and conclusion . . . . .	102
2	Mono- and bi-layer configurations of interlayer water . . . . .	103
2.1	Numerical methods . . . . .	103
2.2	Identification of the stable mono- and bi-layer hydration configurations by molecular simulation . . . . .	104
2.3	Vibrational density of states of the mono- and bi-layer configurations . . . . .	105
3	Low temperature dynamics of confined water . . . . .	106
3.1	Water thermally induced migration and dynamics singularities . . . . .	106
3.2	Low temperature hydrodynamic properties of interlayer water . . . . .	110
4	Summary and conclusion . . . . .	111
5	Appendix: Temperature dependance of the far-infrared absorption spectrum for various hydration states . . . . .	113
	<b>Conclusion</b> . . . . .	115
	<b>Bibliography</b> . . . . .	119

# Table des matières

<b>Remerciements</b> .....	v
<b>Table des matières</b> .....	vii
<b>Résumé</b> .....	xi
<b>Zusammenfassung</b> .....	xv
<b>Introduction</b> .....	1
<b>Chapitre 1. L'eau liquide : de l'eau en volume aux milieux confinés</b> .....	5
1 L'eau pure en volume .....	5
1.1 L'eau liquide et ses anomalies .....	5
1.2 Le diagramme des "phases liquides" de l'eau .....	6
1.3 Viscoélasticité de l'eau .....	8
2 L'eau salée .....	10
2.1 Solvatation et structure .....	10
2.2 Propriétés colligatives .....	11
2.3 Transport hydrodynamique .....	12
3 L'eau confinée .....	14
3.1 Structure de l'eau confinée .....	14
3.2 Hydrodynamique en milieux confinés : éléments de nanofluidique ..	16
4 L'eau confinée dans les argiles .....	18
4.1 Structure des argiles .....	18
4.2 Mécanismes de gonflement .....	20
4.3 Structure et dynamique de l'eau .....	21
5 Annexe : Table des rayons ioniques effectifs .....	24
<b>Chapitre 2. Sonder l'eau de l'électron au liquide : méthodes numériques et expérimentales</b> .....	25
1 Atomes et molécules .....	25
1.1 Atomes .....	25
1.2 Molécules .....	26
1.3 Au-delà des molécules : interactions moléculaires .....	27
2 Spectroscopie d'absorption infrarouge .....	27
2.1 Théorie (avec des applications à l'eau) .....	27
2.2 Instrumentation .....	30
3 Dynamique moléculaire classique et ab initio .....	34
3.1 Dynamique moléculaire .....	34
3.2 Calcul des forces (I) : théorie de la fonctionnelle de la densité .....	39
3.3 Calcul des forces (II) : charges ponctuelles dans un champ de forces ..	41
<b>Chapitre 3. Propriétés viscoélastiques de l'eau liquide pure</b> .....	45
1 Dynamique de l'eau aux temps longs : l'eau vue comme un liquide visqueux .	45
1.1 Méthodes numériques .....	46
1.2 Temps de relaxation structuraux .....	46
1.3 Viscosité de cisaillement .....	48
1.4 Relation de Stokes-Einstein .....	49
1.5 Résumé .....	52
2 Liens avec la dynamique aux temps courts : du liquide visqueux au solide élas-	
tique .....	52

2.1	Méthodes numériques . . . . .	52
2.2	Dynamique aux temps longs vs module élastique . . . . .	53
2.3	Équation de Hall-Wolynes . . . . .	54
2.4	Résumé . . . . .	55
3	Vers une prise en compte des effets quantiques : approche ab initio . . . . .	55
3.1	Objectifs de l'étude et méthodes . . . . .	55
3.2	Correction de la contrainte de Pulay . . . . .	56
3.3	Prédictions structurales et dynamiques . . . . .	57
	Conclusion . . . . .	60
	<b>Chapitre 4. Propriétés hydrodynamiques de l'eau près d'une surface hydrophobe . . .</b>	<b>67</b>
1	Objectifs de l'étude . . . . .	67
2	Méthodes numériques . . . . .	67
3	Dépendance du coefficient de frottement et de la longueur de glissement à la température . . . . .	68
4	Origine de la dépendance du frottement à la température . . . . .	71
4.1	Structure du liquide près de l'interface . . . . .	71
4.2	Corrugation de la surface solide . . . . .	73
4.3	Relaxation du liquide et de l'interface . . . . .	73
5	Résumé et conclusion . . . . .	75
	<b>Chapitre 5. Influence de sels dissouts sur les propriétés structurales et de transport de l'eau . . . . .</b>	<b>77</b>
1	Dynamique moléculaire en continuum électronique . . . . .	78
1.1	Principe . . . . .	78
1.2	Constante diélectrique de l'eau TIP4P/2005f . . . . .	78
1.3	Application, avantages et inconvénients de la méthode . . . . .	79
2	Optimisation du champ de force . . . . .	80
3	Dynamique moléculaire : méthodes . . . . .	82
4	Application du modèle . . . . .	82
4.1	Structures cristallines . . . . .	82
4.2	Structure du liquide . . . . .	82
4.3	Auto-diffusion de l'eau . . . . .	84
4.4	Viscosité de cisaillement . . . . .	85
4.5	Spectre d'absorption dans l'infrarouge moyen . . . . .	87
5	Conclusion . . . . .	88
	<b>Chapitre 6. Structure et dynamique de l'eau confinée dans les minéraux argileux . . .</b>	<b>91</b>
1	Évolution de la structure et de la connectivité de l'eau adsorbée dans les minéraux argileux lors du gonflement . . . . .	91
1.1	Méthodes expérimentales . . . . .	92
1.2	Résultats . . . . .	93
1.3	Discussion . . . . .	98
1.4	Résumé et conclusion . . . . .	102
2	Configurations mono- et bi-couches de l'espace interfoliaire . . . . .	103
2.1	Méthodes numériques . . . . .	103
2.2	Identification des configurations d'hydratation stables mono- et bi-couches par simulation moléculaire . . . . .	104
2.3	Densité d'états vibrationnels des configurations mono- et bi-couches . . . . .	105
3	Dynamique à basse température de l'eau confinée . . . . .	106
3.1	Migration par activation thermique de l'eau et singularités dynamiques . . . . .	106
3.2	Propriétés hydrodynamiques de l'eau interfoliaire à basse température . . . . .	110
4	Résumé et conclusion . . . . .	111
	<b>Conclusion . . . . .</b>	<b>115</b>

# Résumé

Les argiles sont des matériaux complexes pouvant adsorber de l'eau. Ces matériaux jouent un rôle important dans des domaines aussi variés que l'habitat, la catalyse ou encore le stockage des déchets radioactifs. Pour autant, les propriétés de l'eau confinée dans les argiles restent à ce jour mal comprises. L'objectif de ce travail est d'essayer de comprendre l'évolution de la structure et de la dynamique de l'eau confinée à basse température, en mêlant simulations de dynamique moléculaire et spectrométrie infrarouge. En particulier, afin de valider les modèles utilisés pour l'étude numérique, nous étudions dans un premier temps chacun des éléments qui constituent l'argile, à savoir l'eau pure, l'eau près d'une interface solide et l'eau salée, puis dans le dernier chapitre, nous essayons d'assembler ces différents éléments pour comprendre la dynamique de l'eau dans l'argile.

## Chapitre 1. L'eau liquide : de l'eau en volume aux milieux confinés.

---

Ce chapitre introduit les principaux concepts qui interviennent dans l'étude et décrit l'état de l'eau. L'eau est le liquide le plus abondant sur Terre, et intervient dans de nombreux processus biologiques. Pour autant, sur le plan physico-chimique, c'est un liquide atypique, avec pas moins de 73 anomalies par rapport à un liquide simple. Un grand nombre de ces anomalies sont dues aux liaisons hydrogènes, interactions directionnelles d'intensité intermédiaire entre liaison covalente et interaction de Van der Waals, qui font de l'eau un liquide associé, avec un arrangement local tétraédrique des molécules.

Aux températures inférieures à sa température de cristallisation, il n'est pas rare de rencontrer l'eau à l'état surfondu, c'est-à-dire liquide métastable, voire même à l'état vitreux si le liquide est refroidi suffisamment vite, suggérant l'existence d'une transition vitreuse. Mais la question fait débat, car cette transition, si elle existe, se trouverait dans une zone du diagramme de phase inaccessible à l'expérience. Une façon de contourner le problème consiste à extrapoler aux basses températures les propriétés viscoélastiques de l'eau dans le domaine surfondu au travers de modèles visqueux ou élastiques, fondés respectivement sur la dynamique aux temps longs ou aux temps courts de l'eau.

Lorsqu'un sel est ajouté dans l'eau, il se dissout et les ions ainsi formés sont solvatés par des molécules d'eau, affectant ainsi l'organisation du liquide. En particulier, certains ions, dits kosmotropes, tendent à renforcer la structuration du liquide induite par les liaisons hydrogène, tandis que d'autres ions, dits chaotropes, affaiblissent cette structure. Il en résulte diverses conséquences sur la dynamique de l'eau, notamment les propriétés dites "colligatives" (abaissement du point de fusion, de la pression de vapeur saturante...), ou encore une augmentation ou une diminution du coefficient d'auto-diffusion de l'eau ou de sa viscosité.

Le confinement de l'eau par des parois solides peut également affecter la structure et la dynamique de l'eau, en modifiant notamment les températures de changement d'état. Dans un nano-canal, on peut également observer des phénomènes de glissement de l'eau au niveau des parois solides, augmentant ainsi la perméabilité hydrodynamique du canal.

Les argiles constituent un exemple de milieu où l'eau peut être trouvée à l'état confiné. Il s'agit de minéraux en feuillets, généralement chargés et liés par des cations dits interfoliaires, dont l'empilement irrégulier supporte une porosité multi-échelles. Sous atmosphère

humide, les argiles s'hydratent suivant un processus complexe contrôlé à la fois par la structure des feuillets et la nature des cations interfoliaires. L'eau ainsi confinée présente un comportement singulier vis-à-vis de la température, avec diverses transitions de phases à basse température encore mal appréhendées à ce jour. L'étude des propriétés structurales et dynamiques de l'eau dans différents environnements se rapprochant de plus en plus de celui des argiles fait l'objet des chapitres suivants.

## Chapitre 2. Sonder l'eau de l'électron au liquide : méthodes numériques et expérimentales.

---

Ce chapitre présente les méthodes numériques et expérimentales utilisées tout au long de cette thèse. La matière est constituée d'atomes, eux-mêmes formés de noyaux et d'électrons. Ces atomes interagissent et peuvent se lier via une réorganisation de leur nuage électronique pour former des matériaux et/ou des molécules dont l'énergie est quantifiée. On distingue des niveaux d'énergie électroniques, vibrationnels et rotationnels, tous caractéristiques des espèces en présence et de leur environnement.

La spectrométrie infrarouge est une méthode d'analyse des niveaux vibrationnels des édifices moléculaires. Elle s'appuie aujourd'hui sur des spectromètres à transformée de Fourier. Deux gammes spectrales sont utilisées : l'infrarouge moyen, domaine d'énergie correspondant aux transitions entre niveaux de vibrations intramoléculaires de l'eau, et l'infrarouge lointain, domaine des vibrations intermoléculaires. Deux techniques sont présentées, l'une permettant d'analyser la lumière absorbée en transmission, où l'échantillon est traversé par le faisceau, et l'autre, dite par réflexion totale atténuée, permettant d'analyser la lumière absorbée après réflexion du faisceau à la surface de l'échantillon. Ces deux méthodes offrent la possibilité de contrôler la température et l'humidité autour de l'échantillon.

La dynamique moléculaire permet également de sonder la matière à l'échelle atomique, mais numériquement. La méthode est fondée sur le calcul des trajectoires des atomes en utilisant les lois de la mécanique classique. Cela implique d'estimer les forces qui s'exercent entre les atomes, ce qui peut être réalisé directement à partir d'une évaluation de la distribution des électrons autour des atomes via la théorie de la fonctionnelle de la densité, ou bien de manière empirique à l'aide de "champs de force". On peut ensuite à partir des trajectoires atomiques calculer diverses observables structurales ou dynamiques.

## Chapitre 3. Propriétés viscoélastiques de l'eau liquide pure.

---

Dans ce chapitre, les deux approches introduites au premier chapitre (modèles visqueux et modèles élastiques) sont testées à travers des simulations de dynamique moléculaire classique pour évaluer les propriétés viscoélastiques de l'eau dans les domaines liquide stable et surfondu.

Nous commençons par utiliser le champ de force empirique TIP4P/2005f pour décrire l'eau. Nos calculs montrent que ce modèle est très précis pour reproduire les valeurs tabulées de viscosité et de coefficient d'auto-diffusion de l'eau sur toute la plage de température considérée. En extrapolant des calculs de viscosité et du temps de relaxation  $\alpha$  du liquide jusqu'à la température de transition vitreuse au moyen de modèles tels que les lois de Vogel-Tammann-Fulcher ou de Speedy-Angell, nous montrons notamment que, pour des conditions de simulation données, le choix de l'observable influe sur la prédiction de la température de transition vitreuse. En particulier, ces deux observables sont découplées à basse température. En outre, la loi de Stokes-Einstein, qui traduit le couplage entre auto-diffusion et viscosité ou temps de relaxation  $\alpha$ , est violée à partir de températures différentes pour ces deux quantités. Aux températures plus basses, viscosité et temps de relaxation  $\alpha$  sont bien décrits par les modèles dits "élastiques", qui relie la dynamique du

liquide aux temps longs, à ses propriétés élastiques aux temps courts, notamment à travers son module de cisaillement à haute fréquence.

La dynamique moléculaire classique, aussi précise soit-elle pour décrire l'eau, ne permet néanmoins pas d'évaluer le rôle des effets quantiques dans le comportement de l'eau. Dans un second temps, nous testons la théorie de la fonctionnelle de la densité (DFT) pour rendre compte de la structure de l'eau liquide et de ses propriétés de transport hydrodynamique, en évaluant pour cela différentes fonctionnelles. En menant les calculs dans l'ensemble isotherme-isobare, et en corrigeant la pression vis-à-vis de la contrainte de Pulay – erreur qui est intrinsèque à l'approche DFT – nous montrons que la fonctionnelle VdW-DF2 permet de rendre compte de manière presque quantitative de la structure et de la dynamique de l'eau pure à température ambiante, ouvrant ainsi la voie à des systèmes complexes pour lesquels la dynamique moléculaire classique est mise en défaut, notamment lorsque l'eau est en contact avec des corps chargés (ions ou surfaces).

## Chapitre 4. Propriétés hydrodynamiques de l'eau près d'une surface hydrophobe.

---

Nous analysons ensuite le comportement particulier de l'eau au voisinage d'une surface modèle hydrophobe. En particulier, nous nous intéressons, par dynamique moléculaire classique, au rôle de la température sur les propriétés de glissement de l'eau au voisinage de la surface. Deux méthodes sont mises en œuvre : la méthode de Green-Kubo, basée sur les fluctuations du système à l'équilibre, et une méthode de cisaillement stationnaire. Cette dernière prédit une forte augmentation de la longueur de glissement de l'eau sur la surface solide à basse température, ce qui, appliqué à un écoulement dans un canal nanofluidique, pourrait conduire à des effets de perméabilité géante. Néanmoins, les calculs de longueur de glissement obtenus via la méthode de Green-Kubo sont en désaccord avec ces prédictions.

En essayant d'analyser les différents paramètres influençant le glissement, nous montrons que l'augmentation de la longueur de glissement à basse température pourrait être liée à une transition d'un régime de frottement solide-liquide vers un régime de frottement solide-solide à basse température. En revanche, la raison pour laquelle les deux méthodes de calculs diffèrent reste un problème ouvert.

## Chapitre 5. Influence de sels dissouts sur les propriétés structurales et de transport de l'eau.

---

Un dénominateur commun à tous les modèles numériques empiriques de sels est qu'ils ne rendent pas compte de l'augmentation du coefficient d'auto-diffusion de l'eau lors de l'ajout d'un sel chaotrope en solution. Dans ce chapitre, en partant d'un modèle d'ion existant proposé par Mao et Pappu des sels à l'état cristallin, nous proposons d'optimiser les paramètres de Lennard-Jones du modèle pour reproduire les propriétés de diffusion du solvant en traitant la charge portée par les ions comme un paramètre ajustable. L'idée est de pallier la mauvaise restitution des propriétés diélectriques du solvant par le champ de force TIP4P/2005f. Les ions considérés sont les alcalins et les halogènes.

Nous évaluons ensuite la précision du nouveau modèle en comparant calculs et données tabulées pour la structure du cristal, la distribution de paires des atomes d'oxygène dans le liquide, l'évolution du coefficient d'auto-diffusion du solvant et de sa viscosité en fonction de la concentration en sel dissout, et l'évolution du spectre d'absorption infrarouge. Une étude expérimentale par spectrométrie infrarouge est également menée pour la comparer aux calculs. Notre modèle reproduit précisément les propriétés des sels formés de petits ions, mais échoue à modéliser l'effet des ions plus gros sur les propriétés de l'eau. Une ré-optimisation des paramètres du modèle en suivant un autre protocole, basé sur les pro-

priétés du liquide et non du solide comme c'est le cas ici, permettrait peut-être dans le futur d'obtenir de meilleurs résultats.

## Chapitre 6. Structure et dynamique de l'eau confinée dans les minéraux argileux.

---

En raison de leur caractère multi-échelles, les argiles sont délicates à étudier, autant sur le plan expérimental que sur le plan numérique. Dans ce chapitre, nous montrons tout d'abord que la spectrométrie infrarouge peut être utilisée pour caractériser à elle seule les différentes étapes d'hydratation et de déshydratation d'une argile. À cette occasion, nous proposons une attribution des bandes dans la gamme de connectivité du spectre, c'est-à-dire dans l'infrarouge lointain.

Pour autant, la seule étude infrarouge ne permet pas d'exploiter toutes les informations contenues dans le spectre. Aussi, pour aller plus loin, nous montrons que la dynamique moléculaire reproduit bien les propriétés vibrationnelles de l'eau pour une argile hydratée, et permet d'isoler la contribution de l'eau interfoliaire, pour une unique couche d'eau adsorbée, ou deux couches d'eau adsorbées.

Ensuite, en appliquant les attributions précédemment établies des bandes dans l'infrarouge lointain, nous analysons l'évolution du spectre de l'argile en fonction de la température. Nous montrons que cette évolution n'est pas linéaire et présente plusieurs singularités correspondant à un gel progressif de l'eau confinée dans chacun des pores. En outre, lorsque la température varie, nous observons une migration de l'eau adsorbée d'un pore à l'autre. Nous montrons également que l'eau ne cristallise pas.

Pour autant, pour l'eau, la spectrométrie infrarouge ne permet pas de distinguer la présence de liquide de celle de verre. Nous montrons alors que la dynamique moléculaire permet d'aller plus loin en sondant la dynamique de l'eau à travers sa viscosité. Elle permet par ailleurs d'étudier la perméabilité de l'argile dans le contexte du stockage des déchets nucléaires.

# Zusammenfassung

Tone sind komplexe Materialien, die Wasser adsorbieren können. Diese Materialien spielen eine wichtige Rolle in Bereichen wie der Umwelt, der Katalyse oder der Lagerung von radioaktiven Abfällen. Die Eigenschaft des Verbleibens des Wassers im Ton ist jedoch bis zum heutigen Tag nicht gut verstanden. Das Ziel dieser Arbeit ist die Entwicklung der Struktur und der Dynamik des eingeschlossenen Wassers bei niedrigen Temperaturen durch die Kombination von Molekulardynamik-Simulationen und Infrarot-Spektroskopie zu verstehen. Insbesondere um die Modelle für die numerische Untersuchung zu validieren untersuchen wir zunächst die einzelnen Wasserarten, die im Ton vorhanden sind machen, nämlich reines Wasser, Wasser in Oberflächennähe und das Salzwasser. Im letzten Kapitel versuchen wir diese Elemente zu kombinieren, um die Dynamik des Wassers im Ton zu beschreiben.

## Kapitel 1. Flüssiges Wasser: Vom Volumenwasser bis zum einschließenden Medium.

---

Dieses Kapitel stellt die wichtigsten Konzepte, die an der Studie beteiligt sind, dar und beschreibt den Stand der Technik. Wasser ist die am häufigsten vorkommende Flüssigkeit auf der Erde und ist an vielen biologischen Prozessen beteiligt. Aus physikalisch-chemischer Sicht ist es mit mehr als 73 Anomalien eine atypische Flüssigkeit. Eine große Anzahl dieser Anomalien sind durch Wasserstoffbrückenbindungen begründet. Aufgrund der Richtungsabhängigkeit und der Bindungsstärke, welche zwischen der kovalenten und der Van der Waals Bindungen liegt, ordnen sich die Wassermoleküle lokal tetraedrisch an.

Bei Temperaturen unterhalb der Kristallisationstemperatur ist es nicht ungewöhnlich, dass Wasser in den unterkühlten Zustand (metastabile Flüssigkeit) oder sogar in den glasigen Zustand (Vorhandensein eines Glasübergang), wenn die Flüssigkeit schnell genug abgekühlt wird, übergeht. Dieses Thema ist jedoch umstritten, weil dieser Übergang, wenn er denn vorhanden ist, in einem nicht experimentell beobachtbaren Bereich des Phasendiagramms. Eine Möglichkeit um dem Problem Abhilfe zu schaffen ist die Extrapolation der viskoelastischen Eigenschaften des Wassers im unterkühlten Bereich durch viskose oder elastische Modelle bei niedrigen Temperaturen, anhand von langen bzw. Relaxationszeiten.

Wenn Wasser ein Salz hinzugefügt wird, löst sich dieses auf und die Ionen werden von den Wassermolekülen solvatisiert, wodurch die Organisation der Flüssigkeit modifiziert wird. Einige Ionen, wie beispielsweise kosmotrope, induzieren eine stärkere Strukturierung durch Wasserstoffbindungen, während anderen Ionen, so genannte Chaotropen, die Strukturierung auflockern. Daraus resultieren verschiedene Konsequenzen für die Dynamik des Wassers, einschließlich der sogenannten „kolligativen“ Eigenschaften (Schmelzpunkt Depression, Dampfdruckabsenkung, ...), sowie Anstieg oder Rückgang des Selbstdiffusionskoeffizienten des Wassers oder der Viskosität.

Der Einschluss des Wassers durch undurchdringliche Wände, wechselnde Temperaturen und damit verbundene Zustandsänderungen können auch Auswirkungen auf die Struktur und Dynamik des Wassers haben. In einem Nano-Kanal kann man auch das Phänomen des Gleitens, das die hydrodynamische Durchlässigkeit des Kanals ändert, von Wasser auf Oberflächen beobachten.

Tone sind ein Beispiel für eine Umgebung an denen Wasser im eingeschlossenen Zustand gefunden werden kann. Der Ton ist ein Schichtmineral. Die Schichten sind negativ geladen und durch Zwischenschicht-Kationen miteinander verbunden, unregelmäßig gestapelt und mit einer multiskaligen Porosität durchzogen. In feuchter Atmosphäre hydratisieren die Tone nach einem komplexen Prozess, der durch die Struktur der Schichten und durch die Zwischenschicht-Kationen kontrolliert wird. Eingeschlossenes Wasser zeigt ein einzigartiges temperaturabhängiges Verhalten. Jedoch sind die Phasenübergänge bei niedrigen Temperaturen noch immer schlecht verstanden. Die Untersuchung der strukturellen- und dynamischen Eigenschaften des Wassers in verschiedenen Umgebungen, die sich mehr und mehr dem Ton annähert, werden in den folgenden Kapiteln untersucht.

## Kapitel 2. Vom atomaren Aufbau zur Flüssigkeit: numerische und experimentelle Methoden.

---

In diesem Kapitel werden experimentelle und numerische Methoden vorgestellt, die in dieser Arbeit verwendet werden. Materie besteht aus Atomen, die aus Kernen und Elektronen zusammengesetzt sind. Diese Elektronen interagieren und können sich durch eine Reorganisation ihrer elektronischen Wolke miteinander verbinden, um Materialien und / oder Moleküle zu bilden, deren Energie quantifiziert werden kann. Man unterscheidet Elektronische-, Vibrations- und Rotationsniveaus, die alle charakteristisch für ihre Verbindungen sind.

Infrarotspektroskopie (Fourier-Transformationsspektroskopie) ist ein Analyseverfahren der Schwingungsniveaus von molekularen Verbindungen. Es werden zwei Spektralbereiche verwendet: zum einen die mittlere Infrarotdomäne, die den Übergängen zwischen intramolekularen Schwingungsenergien entspricht und Ferninfrarot, was intermolekulare Vibrationen entspricht. Es existieren zwei verschiedene Messmethoden. Zum einen die Messung und Analyse des transmudierten Strahls. Zum anderen die Detektion und Auswertung des von der Probe reflektierten Strahls („Total Attenuated Reflection“) Beide Methoden ermöglichen es, die Temperatur und die Feuchtigkeit um die Probe zu kontrollieren.

Die Molekulardynamik kann numerisch auch im Atommaßstab angewendet werden. Diese Methode basiert auf der Berechnung von Atomtrajektorien nach den klassischen Mechanikgesetzen. Dies erfordert die Auswertung der interatomaren Kräfte, die direkt aus der Elektronenverteilung um die Atome resultieren. Mit Hilfe der Dichtefunktionstheorie oder mit emotionalen Kraftfeldern (empirischer Ansatz) können verschiedene strukturelle oder dynamische Observablen aus den atomaren Trajektorien berechnet werden.

## Kapitel 3. Viskoelastische Eigenschaften des reinen flüssigen Wassers.

---

In diesem Kapitel eingeführten Methoden (viskose Modelle und elastische Modelle) durch klassische molekulardynamische Simulationen getestet, um viskoelastische Eigenschaften von Wasser in stabilen und unterkühlten Bereichen zu bewerten.

Wir verwenden zuerst das TIP4P/2005f empirische Kraftfeld, um Wasser zu beschreiben. Unsere Berechnungen zeigen, dass dieses Modell sehr genau ist, um tabellierte Werte der Viskosität und des Selbstdiffusionskoeffizienten von Wasser über den gesamten Bereich der betrachteten Temperaturen zu reproduzieren. Durch die Extrapolation der berechneten Werte der Viskosität und der Alpha-Relaxationszeit der Flüssigkeit bis hin zur Glasübergangstemperatur mit Modellen wie dem Vogel-Tammann-Fulcher-Gesetz oder dem Speedy-Angell-Gesetz können wir zeigen, dass bei gegebenen Simulationsbedingungen die Wahl der Parameter einen Einfluss auf die Vorhersage der Glasübergangstemperatur hat. Insbesondere sind diese beiden Observablen bei niedrigen Temperaturen entkoppelt. Darüber hinaus wird das Stokes-Einstein-Gesetz, das die Kopplung zwischen dem Selbstdiffusionskoeffizienten und der Viskosität oder der Alpha-Relaxationszeit ausdrückt, bei verschiede-

nen Temperaturen für diese beiden Observablen verletzt. Bei niedrigeren Temperaturen werden die Viskosität und die Alpha-Relaxationszeit durch sogenannte „Elastik“-Modelle beschrieben, die die Langzeitdynamik der Flüssigkeit mit ihren kurzzeitigen elastischen Eigenschaften einschließlich ihres Hochfrequenz-Schermoduls verbinden.

Die klassische Molekulardynamik, ermöglicht es nicht, die Rolle der Quanteneffekte auf das Verhalten von Wasser zu bewerten. Als zweite Möglichkeit wurde die Dichtefunktions-theorie (DFT) getestet, ob die Struktur des flüssigen Wassers und seiner hydrodynamischen Eigenschaften mit verschiedenen Funktionalitäten zu verifizieren ist. Mit der Durchführung von Berechnungen im isothermisch-isobaren Ensemble und durch die Korrektur des Drucks in Bezug auf Pulay-Stress – ein Fehler, der dem DFT-Ansatz innewohnt – zeigen wir, dass das VdW-DF2-Funktional die Möglichkeit bietet die Struktur und die Dynamik von flüssigem Wasser bei Raumtemperatur nahezu quantitativ zu reproduzieren. Dadurch eröffnen sich Möglichkeiten zum Studium komplexer Systeme, für die die klassische Molekulardynamik fehlschlägt, beispielsweise, wenn Wasser mit geladenen Körpern (Ionen oder Oberflächen) in Berührung kommt.

## Kapitel 4. Hydrodynamische Eigenschaften von Wasser in der Nähe einer hydrophoben Oberfläche.

---

Wir analysieren das besondere Verhalten von Wasser in der Nähe einer modellhaften hydrophoben Oberfläche. Insbesondere unter Verwendung der klassischen Molekulardynamik betrachten wir die Rolle der Temperatur auf die gleitenden Eigenschaften von Wasser in Oberflächennähe. Es werden zwei Methoden verwendet: erstens die Green-Kubo-Methode, die auf den Fluktuationen des Systems im Gleichgewicht beruht, und zweitens eine stationäre Scherungsmethode. Letztere prognostiziert eine große Zunahme der Wasser-Schlupf-Länge auf der Oberfläche bei niedrigen Temperaturen, die, wenn sie auf eine Strömung innerhalb eines nanofluidischen Kanals angewendet werden, zu riesigen Permeabilitätseffekten führt. Allerdings stimmen die nach der Green-Kubo-Methode erhaltenen Schlupflängenberechnungen mit diesen Vorhersagen nicht überein.

Durch den Versuch, die verschiedenen Parameter zu analysieren, die den Schlupf beeinflussen, zeigen wir, dass die Zunahme der Schlupflänge bei niedrigen Temperaturen mit einem Übergang von einem Regime der Fest-Flüssig-Reibung zu einem Regime der Fest-Fest-Reibung zusammenhängen könnte. Allerdings ist der Grund, warum die beiden Methoden unterschiedliche Ergebnisse zeigen, immer noch eine offene Frage.

## Kapitel 5. Einfluss von gelösten Salzen auf die Struktur- und Transporteigenschaften von Wasser.

---

Ein gemeinsames Merkmal aller empirischen numerischen Salzmodelle ist, dass durch die Zugabe eines chaotropen Salzes keine Zunahme des Selbstdiffusionskoeffizienten von Wasser auftritt. Ausgehend von einem existierenden Ionenmodell, das von Mao und Pappu für kristalline Salze aufgestellt wurde, schlagen wir vor, die Lennard-Jones-Parameter des Modells zu optimieren, um die Diffusionseigenschaften von Wasser zu reproduzieren, indem die Ladung von Ionen als abstimmbarer Parameter behandelt wird. Die Idee besteht darin, die schlechte Restitution der dielektrischen Eigenschaften von Wasser durch das TIP4P/2005f Kraftfeld zu kompensieren. Die betrachteten Ionen sind Alkalien und Halogenide.

Wir bewerten dann die Genauigkeit unseres neuen Modells durch Vergleich der berechneten und tabellierten Daten der Kristallstruktur, der Paarverteilungsfunktion von Sauerstoffatomen innerhalb der Flüssigkeit, der Entwicklung des Selbstdiffusionskoeffizienten und der Viskosität von Wasser in Bezug auf die Salzkonzentration sowie die Entwicklung des Infrarotabsorptionsspektrums. Eine experimentelle Studie mit Infrarotabsorptionsspektroskopie wird ebenfalls durchgeführt, um Daten mit den Berechnungen zu vergleichen. Unser

Modell reproduziert genau die Eigenschaften von Salzen mit kleinen Ionen, jedoch nicht die Wirkung von größeren Ionen auf die modellierten Eigenschaften des Wassers. Eine weitere Optimierung der Parameter des Modells mittels eines alternativen Verfahrens, basierend auf flüssigen anstelle von festen Eigenschaften, könnte in Zukunft helfen bessere Ergebnisse zu erzielen.

## Kapitel 6. Struktur und Dynamik des eingeschlossenen Wassers in Tonmineralien.

---

Aufgrund ihrer multiskaligen Struktur sind Tone kompliziert zu studieren, sowohl aus experimenteller wie auch aus numerischer Sicht. In diesem Kapitel zeigen wir zunächst, dass die Infrarotabsorptionsspektroskopie verwendet werden kann, um die verschiedenen Hydratations- und Dehydratationsschritte von Tonen zu charakterisieren. Zudem vermuten wir die Absorptionsbanden des Konnektivitätsbereiches im Ferninfrarot.

Die Infrarotstudie allein ermöglicht jedoch nicht den Zugriff auf sämtliche Informationen. Aus diesem Grund zeigen wir, dass die Molekulardynamik die Vibrationseigenschaften von Wasser in hydratisierten Tonen genau wiedergibt und dass adsorbiertes Zwischenschichtwasser von einer bzw. zwei Schichten isoliert werden konnte. Durch die Anwendung der bisherigen Zuordnungen von fernen Infrarotbändern können wir die Entwicklung des Tonpektrums in Bezug auf die Temperatur analysieren. Wir zeigen, dass diese Evolution nicht-linear ist und mehrere Singularitäten aufweist, die einem progressiven Einfrieren von Wasser entspricht, das in jeder Pore eingeschlossen ist. Zudem beobachten wir mit der Variation der Temperatur eine Migration von Wasser von einer Pore zur anderen. Wir zeigen auch, dass das Wasser nicht kristallisiert.

Im Falle von Wasser ermöglicht die Infrarotabsorptionsspektroskopie jedoch nicht, zwischen Flüssigkeit und Glas zu unterscheiden. Wir zeigen, dass die molekulare Dynamik es ermöglicht weiter zu gehen, indem wir die Wasserdynamik durch ihre Viskosität untersuchen. Darüber hinaus ermöglicht diese die Permeabilität von Tonen im Kontext der nuklearen Abfallwirtschaft zu untersuchen.

# Introduction

From the dawn of humanity – and thus, far before knowing the structure of matter – humans took advantage from the impermeability of clay minerals to cook and store food using potteries, and to insulate housing with bricks. And by an amusing twist of fate, this material is used again nowadays in construction industry as an eco-friendly insulator. It is however a negligible part of the millions of tons of clay used each year in industry. Among its numerous uses, this material is considered for nuclear waste and carbon dioxide storage, acting as a barrier for the diffusion of pollutant [Delage et al., 2010]. It is also a major catalyst. It helps the polymerization of RNA and DNA, and hydrocarbons cracking. Actually, it might have played a role in the synthesis of the first DNA molecules, enabling the apparition of life on Earth. People also think that it takes part in the oil and natural gas formation, catalyzing the maturation of kerogen [Heller-Kallai et al., 1996, Mignon et al., 2009, Yu and Schmidt, 2011, Swadling et al., 2013]. Since clays largely constitutes soils at the surface of Earth, it also acts as a water reservoir that accumulate water during humid periods to reconstitute it during droughts. However, the same process also induces volume variations of soils that constitutes a major issue in civil engineering. Damages on housings and industrial plants costs billions of dollars each year [Rinnert, 2004, Carrier et al., 2013, Rotenberg, 2014].

The main difficulties in the study of this material come from its multiscale porous structure and from water itself. Clays are layered materials [Mott, 1988, Cases et al., 1992]. Due to substitution defects inside the layers, these layers have a negative charge, called interlayer charge, balanced by the adsorption of cations at the surface of the layers. Cations also bond layers together, forming aggregates called tactoids. The space between layers is called interlayer space and is of nanometric size, whereas the spaces between tactoids are called mesopores and their size ranges from hundreds of nanometers to a few microns. There are also other nanometric pores, called micropores, due to defects in the stacking of layers. Each pore can be hydrated, inducing the macroscopic swelling of the clay. However, due to the very different sizes of pores, and the presence or not of cations, the properties of adsorbed water highly depend on the nature of the pore where it is confined.

Water, taken out of the context of clays, is also a curiosity for scientists, with more than seventy three abnormal properties with respect to other liquids, including the well-known density maximum at 277 K [Chaplin, 2017, Gonzalez et al., 2016, Pallares et al., 2016]. Most of these anomalies originate from the existence of hydrogen bonds between water molecules. Due to them, water is an associated liquid. Decreasing the temperature, water can remain liquid below the crystallization temperature, and is said supercooled. When it is cooled fast enough, a glassy state can be obtained, suggesting the existence of a glass transition of water. However, the topic is debated, since this transition should occur in a domain of the phase diagram that cannot be accessed experimentally. The study of supercooled water is of particular interest to understand water anomalies since hydrogen bonds are stronger at low temperatures and thus anomalous properties are more visible.

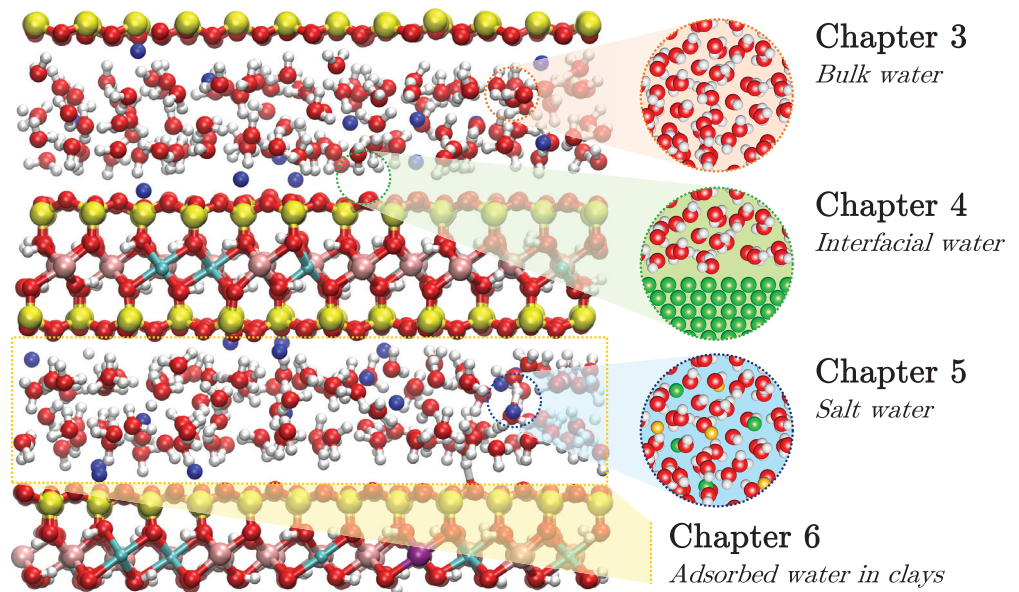
Previous studies on clay minerals also revealed various thermal singularities of water adsorbed in clays at low temperatures, that could be explained on the one hand by a partial crystallization of water molecules adsorbed at the surfaces of clay layers around 288 K [Maheshwari et al., 2013], and on the other hand by a glass transition of interlayer water around 193 K [Gailhanou, 2005], with water staying in a metastable state at higher temperatures.

**The aim of the present work is to provide an atomistic description of the structure and the dynamics of water confined in clays at room and low temperatures, and moreover to try to understand the thermal singularities previously mentioned.**

Various numerical and experimental methods will be coupled. At molecular scale, vibrational spectroscopy, such as infrared absorption spectroscopy, can probe inter- and intramolecular interactions. Especially, it can be used to analyze molecules connectivity with neighboring molecules and with the mineral. To this extent, we will focus on low energy vibrational signatures, in the far-infrared domain, which are associated to hydrogen bonds. Molecular simulations will be also used to probe the dynamics of adsorbed water, using both empirical molecular dynamics and ab initio molecular dynamics. These methods fit well to the scale of nano-channels, and thus are of particular interest to investigate the interactions between water and mineral layers. However, since clays are complex, modeling them is not a simple task. Consequently, a large part of the present work will be devoted to the analysis of the accuracy of molecular simulations to reproduce the properties of water in simpler systems that constitute the key elements of the interlayer space. It includes pure bulk water, interfacial water and salt water. This will help us to conclude about the benefits and drawbacks of molecular simulations to model clay.

Thus, the present dissertation is organized as follows. In the first chapter, we introduce the concepts that will be used in this manuscript, and review recent works about pure and adsorbed water. In the second chapter, we introduce the numerical and experimental methods used in the following chapters. Then, chapters three to five are dedicated to a numerical investigation of the three “building blocks” of clays previously mentioned and shown in Fig. 0.1: the third chapter is about pure bulk water, the fourth chapter is about water near a model solid surface, and the fifth chapter is about salt water. Finally, in the sixth chapter, we confront experiments and simulations about water confined in clays, trying to use one method to complete the weaknesses of the other, in order to describe the dynamics of clay upon swelling at room temperature and upon cooling.

**Figure 0.1** ► Organization of the present manuscript, dividing water confined in clays in various “building blocks”.



# Introduction

Dès l'aube de l'humanité – et donc bien avant de connaître la structure de la matière – les hommes ont su tirer profit des propriétés d'imperméabilité de l'argile pour cuisiner et stocker la nourriture à l'aide de poteries, ou encore isoler les habitations avec des briques. Et par une ironie du sort, ce matériau est à nouveau utilisé aujourd'hui dans l'industrie du bâtiment en tant qu'isolant écologique. Cela représente néanmoins qu'une part négligeable des millions de tonnes d'argile utilisées chaque année dans l'industrie. Parmi ces nombreuses applications, ce matériau est envisagé pour jouer le rôle de barrière à la diffusion des polluants pour le stockage des déchets nucléaires [Delage et al., 2010]. C'est également un catalyseur majeur. Il favorise la polymérisation de l'ARN et de l'ADN, ainsi que le craquage des hydrocarbures. D'ailleurs, il pourrait avoir joué un rôle dans la synthèse des premières molécules d'ADN, permettant ainsi l'apparition de la vie sur Terre. On pense aussi qu'il intervient dans la formation du pétrole et du gaz naturel, en catalysant le processus de maturation du kérogène [Heller-Kallai et al., 1996, Mignon et al., 2009, Yu and Schmidt, 2011, Swadling et al., 2013]. Par ailleurs, comme l'argile constitue une grande partie des sols à la surface de la Terre, elle constitue un réservoir qui accumule l'eau pendant les périodes humides et la restitue pendant les sécheresses. Cependant, ce même processus provoque des variations de volume du sol qui posent de nombreux problèmes dans le génie civil. Les dégâts sur les habitations et les sites industriels coûtent plusieurs milliards de dollars chaque année [Rinnert, 2004, Carrier et al., 2013, Rotenberg, 2014].

Les principales difficultés dans l'étude de ce matériau proviennent de sa structure poreuse multi-échelles et de l'eau elle-même. Les argiles sont des matériaux en feuillets [Mott, 1988, Cases et al., 1992]. En raison de la présence de défauts de substitution dans les feuillets, ces derniers portent une charge négative, appelée charge interfoliaire, contrebalancée par l'adsorption de cations à la surface des feuillets. Ces cations lient également les feuillets entre eux, formant ainsi des agrégats appelés tactoïdes. L'espace entre les feuillets s'appelle l'espace interfoliaire et est de taille nanométrique, tandis que les espaces entre les tactoïdes s'appellent les mésopores et leur taille varie d'une centaine de nanomètres à quelques micromètres. Il existe aussi d'autres pores de taille nanométrique, appelés micropores, dus à des défauts d'empilement des feuillets. Chaque pore peut être hydraté, provoquant un gonflement macroscopique de l'argile. Cependant, en raison des tailles très différentes des pores, et de la présence ou non de cations à l'intérieur, les propriétés de l'eau adsorbée dépendent fortement de la nature du pore où elle se trouve.

L'eau, sortie du contexte des argiles, constitue également une curiosité pour les scientifiques, avec pas moins de soixante-treize propriétés anormales au regard des autres liquides, dont l'existence du célèbre maximum de densité à 277 K [Chaplin, 2017, Gonzalez et al., 2016, Pallares et al., 2016]. La plupart de ces anomalies sont dues à l'existence de liaisons hydrogène entre les molécules d'eau. A cause d'elles, l'eau est un liquide associé. Lorsque l'on diminue la température, l'eau peut rester liquide au-dessous de la température de cristallisation, on dit alors qu'elle est surfondue. Par ailleurs, si le refroidissement est suffisamment rapide, on peut obtenir un état vitreux, ce qui suggère l'existence d'une transition vitreuse de l'eau. Cependant, la question fait débat, puisque cette transition, si elle existe, devrait se trouver dans une partie du diagramme de phases inaccessible à l'expérience. L'étude du liquide surfondu est d'un intérêt tout particulier pour comprendre les anomalies de l'eau, puisque les liaisons hydrogène sont plus fortes à basse température, et donc les anomalies sont plus marquées.

De précédents travaux sur les minéraux argileux ont mis en évidence plusieurs singularités

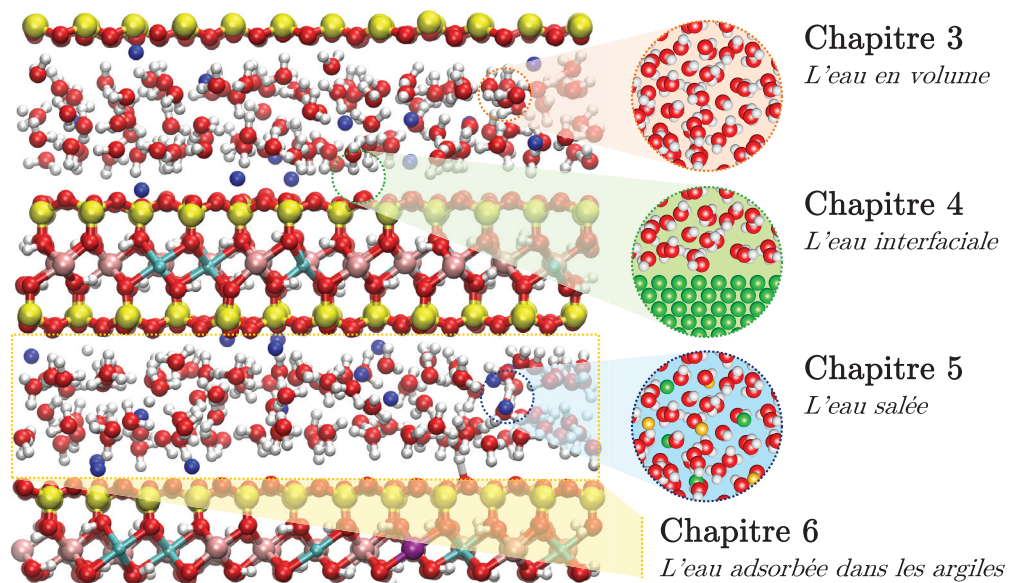
de l'eau adsorbée dans les argiles à basse température, qui pourraient s'expliquer d'une part par une cristallisation partielle des molécules d'eau adsorbées à la surface des feuillets autour de 288 K [Maheshwari et al., 2013], et d'autre part par une transition vitreuse de l'eau interfoliaire vers 193 K [Gailhanou, 2005], l'eau restant dans un état métastable aux températures supérieures.

**Le but de ce travail est de fournir une description atomistique de la structure et de la dynamique de l'eau confinée dans les argiles à température ambiante et à basse température, et plus particulièrement de comprendre les singularités thermiques susmentionnées.**

Diverses méthodes numériques et expérimentales seront couplées. À l'échelle moléculaire, les spectroscopies vibrationnelles, telles que la spectroscopie d'absorption infrarouge, permettent de sonder les interactions inter- et intra-moléculaires. En particulier, elles peuvent être utilisées pour analyser la connectivité des molécules avec les molécules environnantes et avec le minéral. Dans ce but, nous nous intéresserons aux signatures vibrationnelles de basse énergie, dans l'infrarouge lointain, qui sont associées aux liaisons hydrogène. Les simulations moléculaires seront également utilisées pour sonder la dynamique de l'eau adsorbée. Cependant, comme les argiles sont des milieux complexes, leur modélisation n'est pas une tâche facile. Par conséquent, une grande partie de ce travail sera consacrée à l'analyse de la précision des simulations moléculaires pour reproduire les propriétés de l'eau dans des systèmes plus simples qui constituent les éléments principaux de l'espace interfoliaire, à savoir l'eau pure, l'eau interfaciale et l'eau salée. Cela nous aidera à conclure quant aux avantages et inconvénients des simulations moléculaires pour modéliser l'argile.

Ainsi, cette thèse s'organise de la manière suivante. Dans le premier chapitre, nous introduisons les concepts qui seront utilisés tout au long du manuscrit, et passons en revue quelques travaux récents sur l'eau pure et l'eau adsorbée. Dans le deuxième chapitre, on introduit les méthodes numériques et expérimentales utilisées dans les chapitres suivants. Ensuite, les chapitres trois à cinq sont dédiés à l'étude numérique des « briques » constitutives de l'argile précédemment mentionnées et représentées sur la Fig. 0.1 : le troisième chapitre traite de l'eau pure, le quatrième chapitre de l'eau près d'une surface solide, et le cinquième chapitre de l'eau salée. Enfin, dans le sixième chapitre, nous confronterons expériences et calculs sur l'eau confinée dans les argiles, en essayant avec chacune des méthodes de combler les lacunes de l'autre, afin de décrire la dynamique des argiles lors du gonflement à température ambiante et à basse température.

**Figure 0.1** ►  
Organisation de ce manuscrit, en décomposant l'eau confinée dans les argiles en plusieurs « briques ».



# Chapter 1

## Liquid water from bulk to confined media

### Outline

1	Pure bulk water . . . . .	5
1.1	Liquid water and its anomalies . . . . .	5
1.2	The water “liquid phase” diagram . . . . .	6
1.3	Viscoelasticity of water . . . . .	8
2	Salt water . . . . .	10
2.1	Solvation and structure . . . . .	10
2.2	Colligative properties . . . . .	11
2.3	Hydrodynamic transport . . . . .	12
3	Confined water . . . . .	14
3.1	Structure of confined water . . . . .	14
3.2	Hydrodynamics in confined media: notions of nanofluidics . . . . .	16
4	Water confined in clays . . . . .	18
4.1	Clay structure . . . . .	18
4.2	Swelling processes . . . . .	20
4.3	Water structure and dynamics . . . . .	21
5	Appendix: Table of effective ionic radii . . . . .	24

## 1 Pure bulk water

### 1.1 Liquid water and its anomalies

Water is the most abundant chemical species on Earth, and is a key element of almost all biological processes, with both acid and basic properties. This molecule is made of one oxygen atom bound to two hydrogen atoms organized in a bent geometry (see Fig. 1.1). It stands in a **liquid state** at ambient conditions, but can also easily be found in a crystalized state in daily life (snow) or gaseous state (water vapor in the atmosphere) due to the proximity of the triple point with respect to ambient conditions. More generally, water has a very rich **phase diagram**, with more than ten **crystalline polymorphs** [Chaplin, 2017]. The complete diagram is shown in Fig. 1.2.

The most common crystalline structure is called “**ordinary**” or “**hexagonal ice**”, and is denoted *Ih*. It results from highly directional **weak interactions** between a hydroxyl group from a water molecule, and a hydrogen atom from a neighboring molecule, called “**hydrogen bonds**” [Maréchal, 2006]. In ordinary ice, each molecule is involved in four hydrogen bonds organized in a **tetrahedral network** (see Fig. 1.3). However, even if hydrogen bonds are weak interactions, their energy – around  $20 \text{ kJ} \cdot \text{mol}^{-1}$  – is higher than thermal agitation energy at room temperature ( $R \cdot T \approx 2.5 \text{ kJ} \cdot \text{mol}^{-1}$ ) and the latent heat of fusion of water

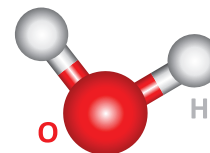
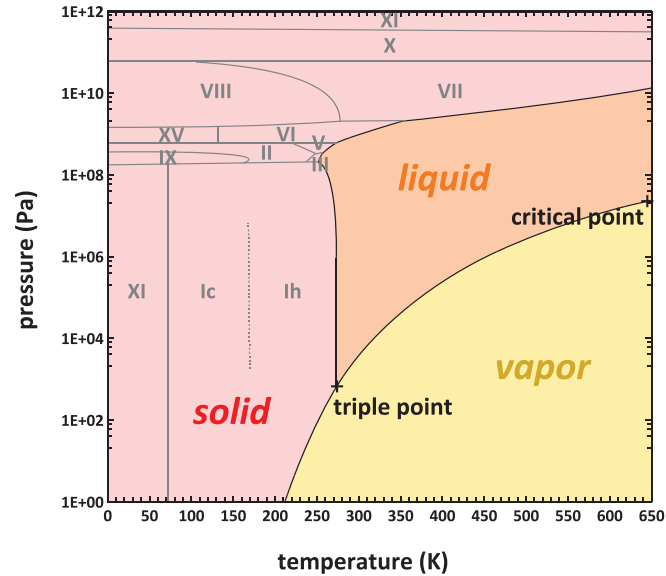


**Figure 1.1** ▲  
The water molecule  $\text{H}_2\text{O}$ .

See Chap. 2 for a microscopic description of hydrogen bonds.

**Figure 1.2** ▶  
The phase diagram of water (adapted from [Chaplin, 2017]). Only stable phases are represented. Roman numbers denote the different crystalline polymorphs.



( $6 \text{ kJ} \cdot \text{mol}^{-1}$ ). Consequently, this hydrogen bond induced tetrahedral structure subsists locally in liquid water. About 63 % of hydrogen bonds still exists in liquid water at 273 K, and about 30 % at 373 K. However, rotation of water molecules due to thermal agitation in liquid state easily breaks this structure, which is consequently **short-lived** (typically a few picoseconds) [Teixeira, 1993].

**Figure 1.3** ▶  
The structure of ordinary ice. A fully developed hydrogen bond network links each molecule to four neighbors – two as hydrogen donor and two as hydrogen acceptor – giving a tetrahedral environment to oxygen atoms.

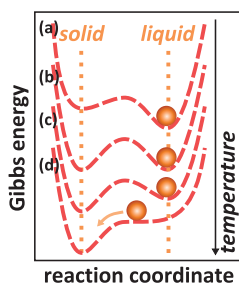
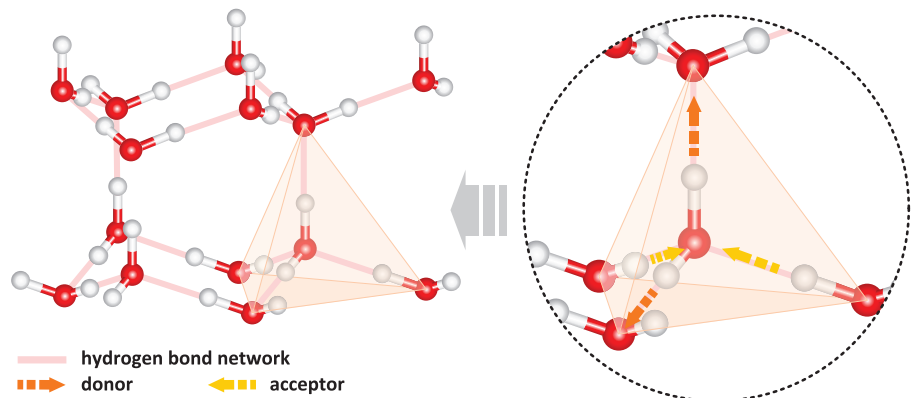


**Figure 1.5** ▲  
Phase transition and metastability. The phase transition temperature corresponds to a change of minimum in the energy landscape (b), but the transition cannot occur while the energy barrier is not crossed. Below a critical temperature near the homogeneous nucleation temperature, the liquid state becomes unstable (d) and crystallization occurs.

Due to the high orientational order induced by hydrogen bonds, at 273 K, ice is less dense than liquid water. Moreover, the destruction of this network in the liquid state when the temperature is increased tends to increase the density. But this effect is counterbalanced by repulsion induced by thermal agitation, resulting in the existence of a **maximum of density** of liquid water around 277 K. This constitutes one of more than seventy-three **anomalous properties** of water in comparison with other liquids (see Fig. 1.4). Understanding this peculiar behavior still constitutes a topical subject within the scientific community [Chaplin, 2017, Pallares et al., 2016, Gonzalez et al., 2016]. As hydrogen bonds play an increasing role in water structure and dynamics when the temperature is decreased below the maximum of density, substantial interest has been devoted to **supercooled water** [DeBenedetti, 2003, Angell, 2002].

## 1.2 The water “liquid phase” diagram

“Supercooled water” denotes water that remains in a liquid state below the temperature of fusion. It is a **metastable state**, since it is not the state predicted by thermodynamics. As every phase transitions, liquid-solid transition needs an **energy barrier** to be overpassed to occur (see Fig. 1.5). While this energy barrier is not reached, water remains liquid. However, the liquid state cannot theoretically exist below a limit temperature, called **homogeneous**

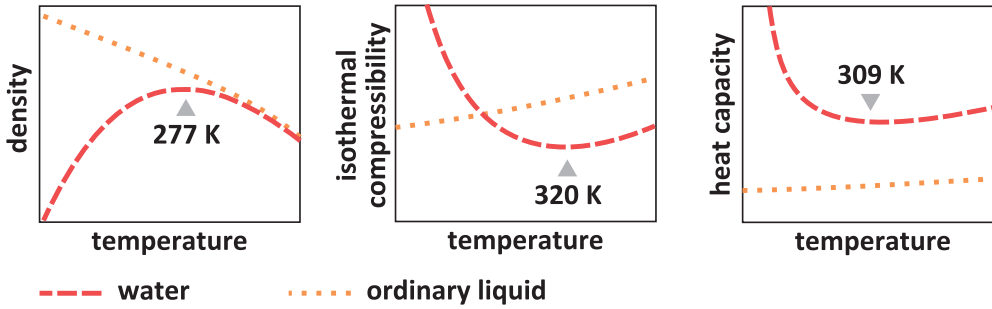


**Figure 1.4** ◀ Examples of abnormal properties of liquid water. Compared to other liquids, water shows numerous anomalies, including the existence of a density maximum and the increase of response functions (heat capacity, isothermal compressibility...) (adapted from [Debenedetti, 2003]).

**nucleation temperature**, corresponding to the temperature at which energy fluctuations becomes higher than the energy barrier. On a molecular point of view, thermal fluctuations create solid nuclei inside the liquid. Below a critical radius, those germs are unstable and disappear fast, but at higher radius, they grow up until the liquid is completely crystalized. The nucleation rate increases when the temperature is lowered, becoming very high at the homogeneous nucleation temperature [Diu et al., 2007]. At normal pressure, the homogeneous nucleation temperature of water is 231 K [Debenedetti, 2003]. However, if water is cooled on a timescale short compared to the crystal growth timescale (about 10 ps for a 3 μm liquid droplet), one gets a **frozen phase**, which is amorphous: it is the **glassy state**, and is denoted LDA (**Low Density Amorphous**) [Huang and Bartell, 1995, Sellberg et al., 2014]. It suggests a glass transition can occur in water. However, due to very high cooling rate required to reach this amorphous state, it is hard to perform any measurement to investigate such a transformation. Starting from the glassy state and increasing the temperature, a melted state has been observed at 136 K before the nucleation of (Ic) ice at 150 K. Thus, 136 K is usually mentioned as the **glass transition temperature** of water [Debenedetti, 2003], but no transition from liquid to solid has been observed up to now and the existence of such a transition is still under debate [Pallares et al., 2016, Singh et al., 2016, Overduin and Patey, 2015, Amann-Winkel et al., 2016]. Other authors predict a glass transition around 165 K [Angell, 2002]. The domain between the two nucleation temperatures is called “**no man’s land**” since it cannot be studied experimentally. Note that researchers use sometimes confinement or mixtures to explore the “no man’s land”. We will give more details about this point later.

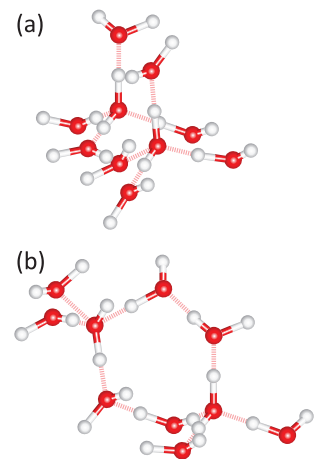


**Figure 1.6** ▲ Liquid water polyamorphism. Schematic view of what could be LDL (a) and HDL (b) local structures.

Various theories try to explain the transition from liquid to amorphous phases, *i.e.* what happens in the “no man’s land”. Another amorphous solid state can be reached by cooling liquid water under high pressure, and is denoted HDA (**High Density Amorphous**). By varying the pressure, it is possible to go from one amorphous phase to the other through a first order phase transition. Based on these observations, Poole et al. suggest the existence of two liquid phases, denoted LDL and HDL (**Low / High Density Liquid**) associated to the two solid phases (see Fig. 1.6), and separated by a phase transition line which ends by a critical point in the “no man’s land” [Poole et al., 1992]. It is the **polyamorphism of liquid**

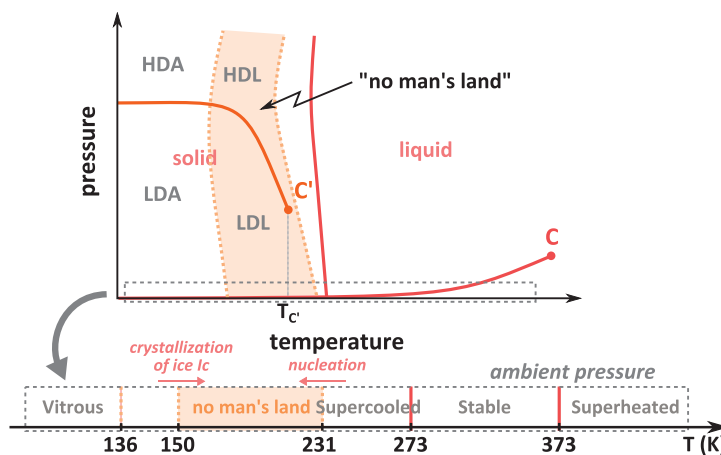


**Figure 1.7** ◀ The “liquid phase” diagram of water, according to the second critical point model [Tanaka, 1996]. Water is seen as a mixture of two liquids (LDL and HDL) separated by a phase transition line that ends by a critical point C’ in the “no man’s land”. At higher temperatures, the two liquid phases cannot be distinguished anymore, like liquid and vapor above the usual critical point C.

**water.** For temperatures higher than this critical point – and thus for all temperatures that

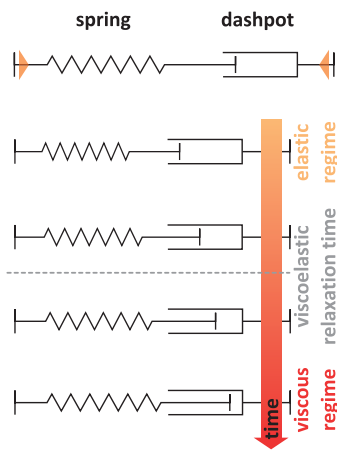


**Figure 1.8** ▲ The Maxwell relaxation time. The fluid is modelled by a combination of a spring and a dashpot. When a stress is applied, the spring first supports the whole deformation (elastic regime). Then, it relaxes and the dashpot starts to move. Finally, the spring recovers its original length and the deformation is fully supported by the dashpot (viscous regime).

See Chap. 2 for a discussion about intermolecular interactions.

can be explored experimentally – those two phases cannot be distinguished. The exact position of the critical point (and its existence) vary from an author to another [Debenedetti, 2003, Tanaka, 1996]. A schematic view of the metastable phase diagram according to this theory is given on figure 1.7. Even if this model agrees with various numerical and spectroscopic studies, it does not meet general approval [Smith et al., 2005]. One way to show the existence of a glass transition and to characterize it is to compare the dynamics of water with other glass-formers. To do so, two approaches can be considered: see water as a liquid, or see it as a solid.

### 1.3 Viscoelasticity of water

Many materials display a viscoelastic behavior: they are elastic – *i.e.* they behave like solids – at short times, whereas they are viscous – *i.e.* they flow – at longer times. The distinction between liquid and solid is only conditioned by the timescale considered, the temperature and the level of stress applied to the material: under normal conditions, the Earth's mantle is solid at our timescale but flows on geological timescales, whereas water is liquid at our timescale and responds elastically at the picosecond scale [Oswald, 2009]. The characteristic time that separates elastic and viscous behavior is called the **Maxwell relaxation time** and is usually denoted  $\tau_M$  (see Fig. 1.8). Glass formers are well known examples of such materials: at low temperature, they are glassy on typical experimental timescales, *i.e.* solids, whereas they are viscous liquids above the glass transition temperature  $T_g$ .

#### 1.3.1 Viscous approach

The most common approach to study the dynamics of a glass former liquid is to look at its viscous behavior. One distinguishes **strong liquids** where interatomic interactions are mainly covalent, and **fragile liquids** where interatomic interactions are mainly ionic or Van der Waals [Barrat and Hansen, 2003]. Common dynamical observables such as shear viscosity or relaxation times, generically denoted  $X$ , follow an **Arrhenius** dependency with respect to temperature  $T$  for strong liquids,

$$X = X_0 \cdot \exp\left(\frac{A}{T}\right), \quad \blacksquare \quad (1.1)$$

with  $A > 0$ , whereas fragile liquids are characterized by a faster increase. Several models have been reported in the literature to describe this behavior. The most common are the **Vogel-Tammann-Fulcher (VTF) law** (1.2a), the **Speedy-Angell (SA) law** (1.2b) and the **Bässler (B) law** (1.2c) [Debenedetti and Stillinger, 2001, Angell, 2002, Bässler, 1987]:

$$X = X_0 \cdot \exp\left(\frac{A}{T - T_f}\right), \quad \blacksquare \quad (1.2a)$$

$$X = X_0 \cdot \left(\frac{T}{T_f} - 1\right)^{-\gamma}, \quad \blacksquare \quad (1.2b)$$

$$X = X_0 \cdot \exp\left(\left(\frac{T_f}{T}\right)^2\right). \quad \blacksquare \quad (1.2c)$$

Within some hypotheses, the VTF law can be interpreted in the scope of Adam-Gibbs theory of liquid dynamics [Adam and Gibbs, 1965], whereas the SA law can be interpreted in the scope of stability limit conjecture at a thermodynamics level, or of mode-coupling theory at a dynamics level [Debenedetti, 2003, Dehaoui et al., 2015]. Those two laws are sometimes criticized because they introduce a singularity of  $X$  for a finite temperature  $T_f \neq 0$ , which has no physical basis. To this point of view, they should not be used to describe high values of  $X$ , and the third law should be preferred [Gotze and Sjogren, 1992]. However, the agreement with data is usually better with SA or VTF [Dehaoui et al., 2015, Gotze and Sjogren, 1992]. Comparison of the accuracy of those two latter is still a very active topic of research, as discussed below.

In water, molecules are linked by hydrogen bonds, so that water may be considered as a fragile liquid. Several experimental groups have focused on viscosity and diffusion to investigate the dynamics of supercooled water. Smith et al. [Smith et al., 2000] fitted the self-diffusion coefficient of amorphous solid water (ASW) thin films between 150 and 160 K in

combination with supercooled water values between 238 and 273 K and found a very good agreement with VTF law, whereas SA law failed to cover the whole range of temperature. Dehaoui et al. [Dehaoui et al., 2015] reported measurements of shear viscosity of water between 239 and 293 K and found a better agreement with SA law, although deviations from VTF law were small. Similar conclusions may be drawn from the study of structural relaxation times, although their definition may be ambiguous. Using quasi-elastic neutron scattering between 253 and 293 K, Chen et al. [Chen et al., 1982, Teixeira et al., 1985] identified two relaxation times: a rotational relaxation time, following an Arrhenius law, and a translational relaxation time, with a non-Arrhenius behavior. According to NMR measurements, the latter followed the SA law for pressures lower than 1.5 kbar, whereas it followed the VTF law for higher pressures [Lang et al., 1984]. Rønne et al. [Rønne and Keiding, 2002] showed that dielectric relaxation also splits into two relaxation times, whereas Bertolini et al. [Bertolini et al., 1982] and Torre et al. [Torre et al., 2004] found a unique relaxation time, with an Arrhenius behavior for the former and a SA behavior for the latter.

Molecular simulations studies led to similar discrepancies. Using TIP5P and ST2 water models, Kumar et al. [Kumar et al., 2007] found a unique relaxation time with non-Arrhenius behavior, as well as Móron et al. with the SPC force field [Morón et al., 2016], whereas Gallo et al. [Gallo et al., 1996], using the SPC/E water model, identified two relaxation times, one with an Arrhenius behavior, and the other with a SA behavior.

Finally, at low temperatures, a fragile-to-strong dynamical crossover around 228 K has been reported experimentally in confined water [Mallamace et al., 2006, Chen et al., 2006, Liu et al., 2006], *i.e.* the dynamics switches from a non-Arrhenius to an Arrhenius behavior below 228 K. Nevertheless, the existence of such a crossover in bulk water is in contrast with the experimental results of Smith et al. [Smith et al., 2000], showing a similar fragile behavior in supercooled water and in amorphous solid water at lower temperatures. Moreover, the 228 K crossover temperature reported experimentally is below homogeneous nucleation temperature. Therefore, a fragile-to-strong transition is hard to observe in bulk water, at least under atmospheric pressure.

This great variety of results could partly originate in the choice of different observables to characterize the dynamics of supercooled water. Most previous experimental and numerical studies focused on structural relaxation times, assuming that they provided an information equivalent to the viscosity, which is much more difficult to measure. However, recent work observed that viscosity and structural relaxation time were not equivalent in a model glass former [Shi et al., 2013], raising doubts on the generality of previous studies of supercooled water dynamics focusing on relaxation times. This issue is of particular importance if one aims to probe deviations from the Stokes-Einstein (SE) relation at low temperatures [Hansen and McDonald, 2013]:

$$D \propto \frac{k_B \cdot T}{\eta}. \quad \blacksquare \quad (1.3)$$

This equation links the self-diffusion  $D$  and the shear-viscosity  $\eta$  of simple liquids. The deviations are interpreted as a signature of the appearance of dynamical heterogeneities in supercooled liquids when approaching the glass transition [Ediger, 2000, Berthier, 2011]. Most of the numerical works to date have considered the so called  $\alpha$ -relaxation time  $\tau_\alpha$  as a proxy of the shear viscosity, but as already noticed in [Shi et al., 2013], this may lead to wrong estimates of the departure from the SE relation, departure which results from the different temperature dependence of the two observables  $\eta$  and  $\tau_\alpha$ . A numerical investigation on this problem is proposed in Chap. 3.

The  $\alpha$ -relaxation time will be defined in Chap. 3.

### 1.3.2 Elastic models

Another approach is to look at the elastic properties of water, *i.e.* its short timescales dynamics. Very few works addressed the connection between the slow dynamics and short time elastic properties of water. Recently, Klameth and Vogel discussed a connection between the  $\alpha$ -relaxation time and the high frequency shear modulus on the basis of Schweizer's elastic model [Klameth and Vogel, 2015]. We can also mention the study by Ciamarra et al.,

which does not concern specifically water, but a model glass former displaying a density maximum, as observed in water [Ciamarra and Sollich, 2015].

The common idea behind elastic models is the following [Dyre et al., 1996, Dyre, 2006, Puosi and Leporini, 2012a]. Collective relaxation processes such as flow events are infrequent in the supercooled liquid and occur on long time-scales, consisting in local molecular rearrangements characterized by an effective activation energy  $E_a(T)$ . Elastic models relate the activation energy to the elastic properties of the supercooled liquid calculated on short – picosecond – time scales. In the shoving model for instance, the activation energy is proportional to the work  $W$  necessary to shove the surrounding of a given molecule, so that flow can occur. The work  $W$  depends on the elastic properties of the supercooled liquid, as described by the shear modulus, denoted  $G$ , and the bulk modulus, denoted  $K$ . If the local structure around a rearranging region has a spherical symmetry, the rearrangement consists in a purely shear deformation [Dyre and Olsen, 2004]. Consequently, the observables characterizing the slow dynamics, including the shear viscosity  $\eta$  or the collective structural relaxation time  $\tau_\alpha$  – generally denoted  $X$  in the following, should be expressed as:

$$\begin{cases} X = X_0 \cdot \exp\left(\frac{E_a(T)}{k_B \cdot T}\right), \\ E_a(T) = \lambda \cdot G_p(T) \cdot a^3 \end{cases} \quad \blacksquare \quad (1.4)$$

where  $k_B$  denotes Boltzmann's constant,  $T$  is the temperature,  $a$  denotes a molecular length,  $G_p(T)$  is the high frequency plateau shear modulus and  $\lambda$  is a dimensionless number which takes values close to one (see Ref. [Dyre, 2006] for a review of the various models leading to this expression). Another popular version of the elastic models emphasizes correlations between the slow dynamics and the mean square displacement (Hall-Wolynes equation) [Ciamarra and Sollich, 2015, Ottochian et al., 2009]:

$$X = X_0 \cdot \exp\left(\frac{a^2}{2 \cdot \langle u^2(T) \rangle}\right). \quad \blacksquare \quad (1.5)$$

where  $\langle u^2(T) \rangle$  is the vibrational mean square displacement. Elastic models, in their two versions, proved to provide a good description of various systems including metallic, polymer and colloid glasses [Wang, 2012, Mattsson et al., 2009, Puosi and Leporini, 2012a, Hecksher and Dyre, 2015], but showed also some limitations, as in the case of oxide glasses [Potuzak et al., 2013]. We will see in Chap. 3 to what extent those models apply to water.

If water can be easily found around us in a pure form, it is also largely present with solvated species, like ions. We will see now to what extent those ions can influence the properties of water.

## 2 Salt water

### 2.1 Solvation and structure

When one puts a solid into liquid water, this solid can undergo no change, or can sometimes be dispersed inside the liquid without necessarily implying any chemical transformation of the liquid. In that case, one says the solid **dissolves**. This phenomenon is a consequence of both liquid and solid properties. For example, ionic solids (also called salts in the following) easily dissolve in water [Atkins and de Paula, 2010]. We will mainly focus on salts made of monoatomic ions in this section, although several considerations are more general.

Dissolution is generally described as a three steps process [Miomandre et al., 2011] (slightly different mechanisms have been recently suggested, see *e.g.* [Liu et al., 2011]): (i) **solid ionization**, *i.e.* the formation of ion pairs inside the liquid, (ii) **ion pair dissociation**, and (iii) **ion solvation**. All these steps come from electrostatic interactions between the solvent and ions. Under the attraction of the dipole of water molecules, ions located on the surface of the solid are dissociated from the crystal lattice. Then, water – which has a high dielectric constant ( $\epsilon_r = 78.5$ ) – can go between ions and the solid or between the two ions of a pair,

See Chap. 3 for a discussion about the distinction between the plateau shear modulus and the shear modulus at infinite frequency.

and **screens** the Coulombic interactions between them. This enables thus ions to go further together and disperses them inside the liquid. Of course, solvation can occur only if the final solution has a lower energy than the crystal itself.

From these interactions results a particular organization of water molecules around ions. It is the **hydration sphere**, or **hydration shell**. This organization depends on the anionic or cationic nature of ions, since the dipole of water molecules is oriented so that the oxygen atom – due to its high electronegativity – is close to cations, and the hydrogen atoms are close to anions (*see* Fig. 1.9). The spatial extension of the hydration sphere and the number of molecules surrounding the ion – *i.e.* the **coordination** of the ion – and the interaction strength depend on the ionic charge, polarizability and size, the concentration of the salt inside the solution, the temperature, *etc.*, and affect the distribution of hydrogen bonds between water molecules with respect to pure water [Marcus, 2009]. Surprisingly, the effects of ions on water structure can be completely different from one ion to another. Some ions tend to increase the liquid structure, *i.e.* to increase the mean reticulation level of the hydrogen bond network – one speaks about “**structure-makers**” or **kosmotropic ions** – whereas others tend to destroy this structure – on speaks about “**structure-breakers**” or **chaotropic ions** [Chaplin, 2017]. We will use this notion of chaotropy/kosmotropy induced by ions in the following, but the influence of ions beyond the hydration shell does not meet general approval [Marcus, 2009, Tobias and Hemminger, 2008].

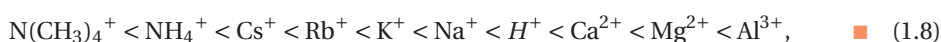
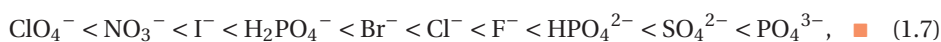
To have a better idea of the way an ion can increase or decrease the structure of water, we can consider the following example [Chaplin, 2017]. For big enough ions, the hydration sphere can form a regular cluster of water molecules, called clathrate. For this kind of structure, one can observe a conformational equilibrium between a convex conformation and a puckered conformation (*see* Fig. 1.10). The convex conformation fits particularly well to the tetrahedral organization of water molecules, and thus, reinforces this structure. In the opposite, the puckered conformation highly disturbs the tetrahedral organization, and thus, the global structure of the liquid. Depending on the nature of ions, the balance between the two forms is shifted to one conformation or to the other one, giving rise, in average, to a chaotropic or kosmotropic effect.

The salt concentration plays also a key role on these effects, since it affects the amount of water that is implied in a hydration sphere. The distance  $d$  between two ions in a solution of concentration  $c$  can be evaluated using [Marcus, 2009]:

$$d \approx \frac{0.94}{\sqrt[3]{c}}, \quad \blacksquare \quad (1.6)$$

where  $d$  is expressed in nanometers, and  $c$  is expressed in  $\text{mol} \cdot \text{L}^{-1}$ . Since the average extension of a water molecule is 3 nm, one estimates that hydration spheres merge for 2 M solutions in the case of monovalent ions. There is thus (i) almost no more “free” water molecules at higher concentrations, and (ii) hydration spheres are disturbed by overlapping.

The chaotropic/kosmotropic behavior of ions corresponds approximatively to **Hoffmeister series**:



with chaotropes on the left and kosmotropes on the right, although some permutations have been reported [Nucci and Vanderkooi, 2008]. A table of ionic radii is given in Table 1.2 at the end of the chapter. However, in a solution, an ion cannot be considered without its counter-ion. Generally speaking, it is admitted that anion effects predominate [Tobias and Hemminger, 2008], but the effects of a salt over the structure of water results from a balance between the two ions. Thus, a solvated salt can be kosmotropic, neutral or chaotropic depending on the relative chaotropic/kosmotropic effect of ions. We will see in Chap. 5 the effect of the solvation of some salts on the distribution of oxygen atoms in liquid water.

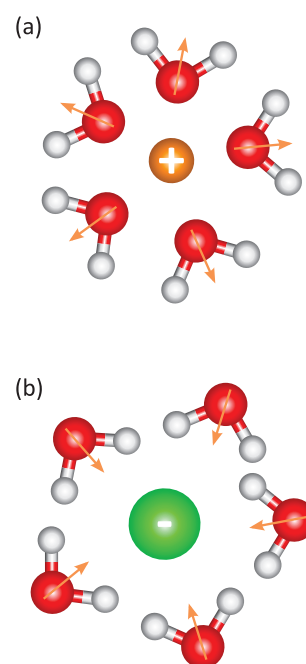


**Figure 1.9** ▲ Cartoon of the organization of water molecules inside the hydration sphere of a cation (a) and an anion (b). Arrows denote the dipole moment of molecules.

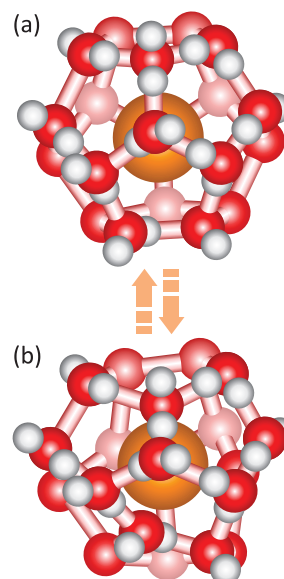


**Figure 1.10** ▲ The convex (a) and puckered (b) conformations of water clathrate formed around big ions. Pink lines correspond to hydrogen bonds.

Those structure modifications have, of course, some consequences on the dynamics of water. Among these effects, one can mention the so-called colligative properties of water (decrease of the fusion temperature, decrease of the vapor pressure, osmosis...) or the modification of hydrodynamics transport properties (self-diffusion of water, shear viscosity...). We will study more precisely those effects in the remaining of this section.

## 2.2 Colligative properties

### 2.2.1 Decrease of the fusion temperature

It is a well-known effect: adding sodium chloride on roads in winter prevents water from freezing at 0 °C. In a water-salt mixture, the entropy of water is decreased with respect to pure water, which decreases the chemical potential of water. This means more energy is needed to transit from the liquid phase to the solid phase, which reduces the fusion temperature of water. Thus, the liquid phase remains stable at lower temperature than when it is pure [Chaplin, 2017]. Moreover, on a kinetic point of view, in some cases, the presence of solvated species can prevent the formation of big solid germs, and thus prevent the growing of the crystal phase [Kim and Yethiraj, 2008]. In that case, water is easier to supercool.

### 2.2.2 Decrease of the vapor pressure

One can also observe a decrease of the vapor pressure. The basic idea is close to the previous case. The vapor pressure of water is the partial pressure of water vapor present in the surrounding of liquid water when both phases are in equilibrium. The increase of the entropy of water due to ion mixing must be overcome to remove one molecule from the liquid phase and vaporize it, that lowers the vapor pressure. At low ionic concentrations, the increase of entropy, and thus, the reduction of the vapor pressure, mainly depends on the ionic fraction, independently of the nature of the salt. At higher concentrations, water-salt interactions must be considered [Chaplin, 2017].

This property is used in practice to adjust the humidity rate in small volumes. The relative humidity (RH), expressed in percent, is defined as the ratio between the water partial pressure  $p_{\text{H}_2\text{O}}$  and the equilibrium vapor pressure  $p_{\text{H}_2\text{O}}^*$  of pure water at the same temperature:

$$\text{RH} = 100 \cdot \frac{p_{\text{H}_2\text{O}}}{p_{\text{H}_2\text{O}}^*}. \quad \blacksquare \quad (1.9)$$

Since, for a given salt, the relative humidity depends on the concentration of the salt, it is more convenient to use saturated solutions. One can thus find tables with the relative humidity associated to a saturated solution of various salts [Lide, 1997]. Another commonly used method is to use water-glycerol mixtures with various mass fraction of glycerol (see Fig. 1.11) [Forney and Brandl, 1992]. We will use this method to control the hydration of clay samples in next chapters.

### 2.2.3 Osmosis

One consider two reservoirs filled with salt water with different concentrations, and separated by a membrane that enables only water molecules to go from one reservoir to the other. The membrane can be a “real” membrane, or the entrance of a nano-channel, as in the case of the interlayer space of clays. It appears a flux of water across the membrane to homogenize the concentrations: this is the phenomenon of osmosis (see Fig. 1.12). To avoid this displacement of water, one must apply a pressure, called **osmotic pressure**  $\Pi$ , on the low concentration liquid. This pressure is a thermodynamic quantity that depends only on the salt concentration  $c$  (in the limit of low concentrations) and the temperature  $T$ , according to the Van’t Hoff’s law [Chaplin, 2017, Atkins and de Paula, 2010]:

$$\Pi = c \cdot R \cdot T, \quad \blacksquare \quad (1.10)$$

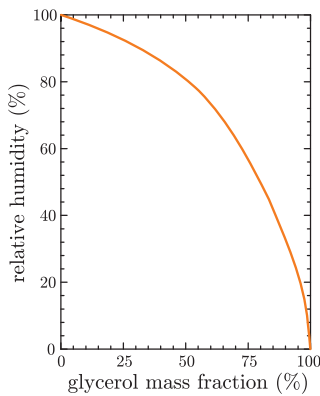


**Figure 1.11** ▲ Evolution of the relative humidity of a gas phase in equilibrium with a liquid water-glycerol mixture at 298 K with respect to the glycerol mass fraction (from [Forney and Brandl, 1992]).

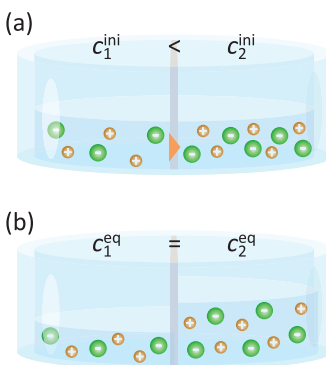


**Figure 1.12** ▲ Cartoon of water displacement under a salt concentration gradient (osmosis).

where  $R$  denotes the perfect gas constant. In the case of high salt concentrations, a corrective factor must be added in this expression. The osmotic pressure is a colligative property. On the contrary, the intensity of the flux is a kinetic quantity that depends mainly on the properties of the membrane and the concentration difference between the two reservoirs [Alleva et al., 2012]. Osmotic flows play a key role in nanofluidic channels, as we will see later.

### 2.3 Hydrodynamic transport

We already mentioned ions diffuse in a solution under a gradient of concentration. They can also migrate when an external electric field is applied. But ions also affect the solvent dynamics. In this last paragraph about ions, we will focus on this last effect.

Due to their (dis)ordering effects on the structure of liquid water, ions can enhance or reduce water molecule mobility in their vicinity, and thus modify the global viscoelastic properties of the liquid with respect to pure water. The shear viscosity of electrolytes has been extensively studied experimentally in the limit of low concentrations [Abdulagatov et al., 2006, Nakai et al., 1996, Goldsack and Franchetto, 1977], but not numerically. Within the limit of low concentrations, experimental data can be well described using the Jones-Dole equation [Marcus, 2009]:

$$\eta = \eta_{\text{solvent}} \cdot (1 + A \cdot \sqrt{c} + B \cdot c), \quad (1.11)$$

where  $\eta_{\text{solvent}}$  is the shear-viscosity of pure water, and  $A$  and  $B$  are coefficients related to the salt.  $A$  can be computed theoretically from solvent and ions properties and  $B$  is an empirical coefficient. A large amount of experiments have been devoted to the determination of  $B$  for various salts [Abdulagatov et al., 2006, Nakai et al., 1996, Goldsack and Franchetto, 1977]. It is usually assumed that salts with a positive  $B$  are kosmotropic, while those with a negative  $B$  are chaotropic [Marcus, 2009, Goldsack and Franchetto, 1977]. The evolution of the shear viscosity of water with respect to the concentration of various alkali metal halides is shown in Fig. 1.13. According to the Jones-Dole equation,  $A \cdot \sqrt{c}$  should be negligible at high

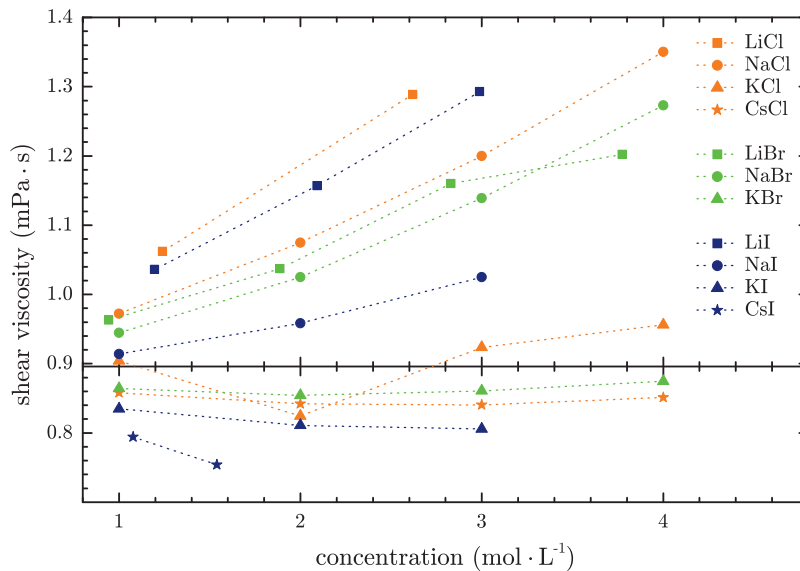
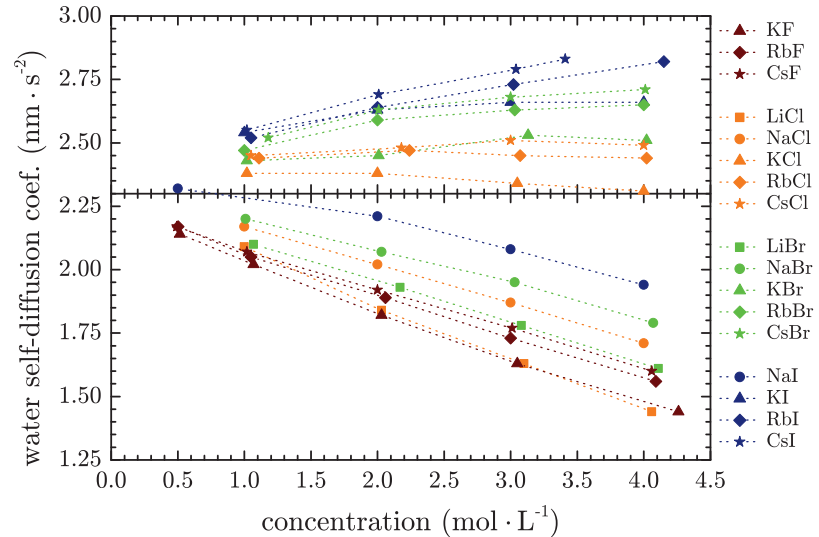


**Figure 1.13** ◀ Evolution of the shear viscosity of various alkali metal halide solutions with respect to the concentration. Molarities were assimilated to molalities when molarities were not available (from Refs. [Abdulagatov et al., 2006, Kestin et al., 1981b, Kestin et al., 1981a, Nakai et al., 1996, Zaytsev and Aseyev, 1992, Goldsack and Franchetto, 1977, Isono, 1984]).

concentrations. Indeed, for all salts considered here, experimental data are well described by an affine relation. Consequently, the slope of the curves directly gives the sign of  $B$ , and thus, the kosmotropic/chaotropic tendency of the salt. Using this assumption, lithium and sodium halides are kosmotropic, whereas cesium iodide is chaotropic. The trend for potassium halides and cesium chloride is not that clear and we can consider those salts having a neutral effect on the shear viscosity. Generally speaking, the kosmotropic effect is more pronounced as the size of ions decreases, whereas large ions are rather chaotropic.

A similar behavior is observed for the self-diffusion coefficient of water. Its evolution with respect to the concentration of various alkali metal halides is shown in Fig. 1.14.

**Figure 1.14** ▶ Evolution of the self-diffusion coefficient of water for various alkali metal halide solutions with respect to the concentration (from Ref. [Müller and Hertz, 1996]).



According to experimental data, lithium and sodium based salts decrease the self diffusion of water (that should correspond to a more structured liquid, so a kosmotropic effect), whereas potassium, rubidium and iodine increase it (that should correspond to a less structured liquid, so a chaotropic effect). Moreover, except for small cations, the evolution of the self diffusion coefficient with respect to the salt concentration only slightly depends on the nature of the cation: for a given anion, curves corresponding to potassium, rubidium and cesium are very close one to each other. Note that the structure making/breaking predictions are similar but not identical depending on the observable used (here the shear viscosity or the self diffusion coefficient). This is a general trend and it constitutes a major limit in the description of ions in terms of effects on the hydrogen bond network [Marcus, 2009]. We will study the influence of salts on the viscoelastic properties of water in Chap. 5.

### 3 Confined water

Up to now, we considered water in the bulk without any constraint from its container. However, in nature, there are many cases where water is **confined**, *i.e.* enclosed in a volume whose at least one dimension is smaller than 100 nm [Sparreboom et al., 2009]. It is for example the case inside some porous minerals, or inside biologic tissues. Those materials can lie inside an aqueous medium or can be filled with water due to **capillary condensation** under a humid atmosphere [Charlaix and Ciccotti, 2010]. Confinement implies an increased role of **surface phenomena** on the properties of the liquid, that can be completely modified with respect to bulk water [Sparreboom et al., 2009, Bocquet and Tabeling, 2014, Bocquet and Charlaix, 2010]. The aim of this section is to introduce the formalism and the main effects of confinement on the structure of liquid water and its hydrodynamics properties [Sparreboom et al., 2009, Bocquet and Tabeling, 2014, Bocquet and Charlaix, 2010, Chaplin, 2010].

#### 3.1 Structure of confined water

##### 3.1.1 Water-surface interactions: hydrophobicity, hydrophilicity

Interactions between water molecules and a solid surface can have two different nature: electrostatic (including Van der Waals interactions) and hydrogen bonds. We will explain the molecular origin of those interactions in the next chapter. As water is a polar molecule, it interacts more with a polar surface than with a non-polar surface. For neutral solids, a surface is polar when it is made of a stack of atoms with very different electronegativity. Due to the presence of the surface that ends the periodicity of the solid structure, an electrostatic instability raises at the surface, that is stabilized by a reorganisation of the charge

distribution [Goniakowski et al., 2007]. Polar surfaces also include solids with a net charge, such as clay layers. However, as we will see, the nature of the surface is not the only factor that controls the interactions. The geometry of the interface can also play a key role [Falk et al., 2010, Chaplin, 2010].

Let us first consider a non-polar surface, neglecting all geometry-related issues. The interactions between water and the surface are mainly Van der Waals, and thus are weak with respect to intermolecular hydrogen bonds. Consequently, the interactions with the surface do not directly drive the structure of interfacial water. One speaks about **hydrophobic surface**. However, as the presence of the wall removes water molecules from the neighboring of interfacial molecules, water near the surface undergoes molecular frustration: molecules cannot form as many hydrogen bonds than in the bulk. It results from this (i) a preferential orientation of molecules near the surface, and (ii) the hydrogen bonds formed are stronger. Thus, water molecules are locally more structured. The main example of hydrophobic confinement medium is carbon nanotube (see Fig. 1.15). It also constitutes a good example of the influence of the geometry. When the radius of the tube is decreased, the curvature of the water/solid interface is increased. Thus, the average distance between carbon atoms and water molecules decreases (the number of carbon atom in the first neighbor shell of a given water molecule increases up to 36 atoms per molecule) and Van der Waals interactions are stronger. So, for diameters smaller than 1.1 nm where a single molecule file is present, there are strong interactions between the tube and water molecules. We will mention later some implications on the dynamics of water.

Let us consider now a polar surface. The influence of a polar surface on the structure of the liquid highly depends on the chemical composition of the surface. The latter can form bonds with water molecules that are weaker or stronger than inter-molecular hydrogen bonds. The existence of strong hydrogen bonds with the surface tends to weaken the energy of O–H bonds that lies near the surface. Moreover, as in the case of ions with their hydration sphere, the solid surface orders molecules in a specific orientation. Then, due to cooperative effects, the perturbation induced by the surface can extend over several molecular sizes (typically over 1 nm, *i.e.* three molecular sizes). In addition, the interactions with the surface induce a **layering** of water molecules, with strong oscillations of the density profile with respect to the distance to the wall. Such a surface is said to be **hydrophilic**. The main examples of hydrophilic confinement media are porous silicates and aluminosilicates such as Vycor, MCM-41 or clays (see Fig. 1.16). However, the most striking effects happen when electrolytes are present inside pores, as we will see in the next section.

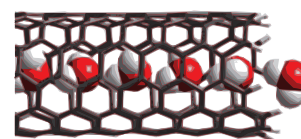


**Figure 1.15** ▲ Cartoon of a single wall carbon nanotube filled with a single file of water molecules (adapted from [Ma et al., 2017]).

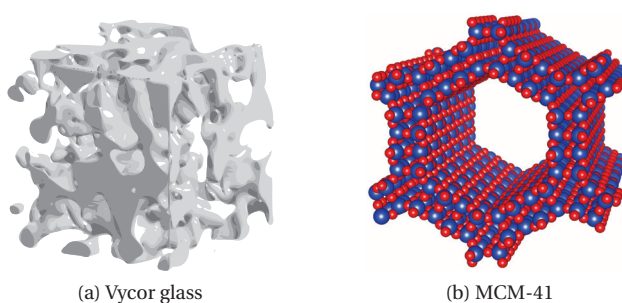


**Figure 1.16** ◀ Cartoon of the structure of Vycor glass (a) and mesoporous MCM-41 silica (b). Red: O; blue: Si. Vycor glass is a silica matrix with randomly distributed pores, whereas MCM-41 is made of regularly organized parallel channels (adapted from [Pellenq et al., 2001, Gusev, 2017]).

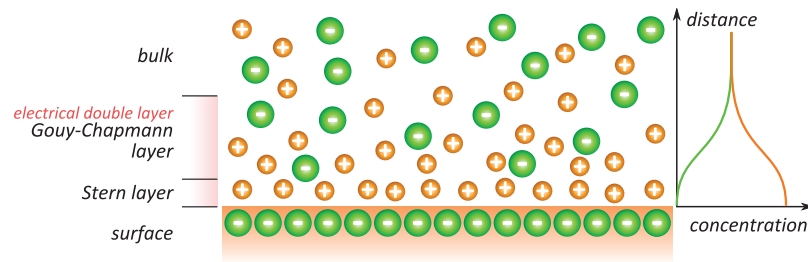
### 3.1.2 Charge distribution in salt water

When the confining medium has a charge surface and there are ions inside water, an **electrical double layer** (usually abbreviated EDL) of opposed charge is formed to screen the surface charge. The charge surface can be intrinsic to the material, as in the case of clay layers, or can be induced by the proximity of the electrolyte. Actually, when a solid is immersed inside an electrolyte, its surface acquires a surface charge due to various mechanisms such as the dissociation of chemical groups on the surface in the case of hydrophobic surfaces, or the adsorption of ionic species on hydrophobic surfaces [Israelachvili, 2011]. In the following, to simplify the discussion, we will consider a surface with a negative charge. Of course,

the discussion holds in the case of positively charged surface but signs of charges must be inverted.

The EDL is divided into two parts: the **Stern layer** and the **Gouy-Chapmann layer**. Far from the interface, the solution is homogeneous, with an equal concentration of anions and cations. The Stern layer is constituted by a layer of cations adsorbed on the solid surface, whereas the Gouy-Chapmann layer is a diffuse layer with a concentration gradient. The number of cations decreases progressively up to the bulk value with respect to the distance to the interface, whereas the number of anions increases progressively (see Fig. 1.17). It plays an important role in the hydrodynamic transport properties, especially when the

**Figure 1.17** ▶  
Electrical double layer near a negatively charged surface. The qualitative evolution of the concentration of anions (green) and cations (orange) across the Stern and the Gouy-Chapmann layers is shown on the right graph.



confinement induces an overlap between the electrical double layers of the different surfaces. We will give a few examples later.

Another important effect of confinement concerns phase transitions. That is what we are going to discuss in the upcoming paragraph.

### 3.1.3 Phases and phase transitions

Confinement influences the phase transitions of water in different manners [Chaplin, 2010, Lee et al., 2010b]. On a thermodynamics point of view – as in the case of a solvated salt – confinement affects the entropy of the liquid. Disorder induced by the interface increases the entropy, which decreases the heat of fusion and thus the melting temperature. The melting point depression becomes larger as the pore size decreases and the interfacial energy (the surface tension)  $\gamma$  increases. For a spherical pore of diameter  $d$ , the melting temperature  $T_m$  of confined water is well evaluated by the **Gibbs-Thompson equation**:

$$T_m = T_m^\circ \cdot \left( 1 - \frac{4 \cdot \gamma \cdot \cos(\phi)}{d \cdot \rho_c \cdot \Delta H_m^\circ} \right), \quad \blacksquare \quad (1.12)$$

where  $T_m^\circ$  denotes the bulk melting temperature,  $\Delta H_m^\circ$  is the bulk heat of fusion,  $\rho_c$  is the ice density and  $\phi$  is the liquid-solid contact angle (see Fig. 1.18). However, the opposite phenomenon is sometimes observed when the ice phase is particularly stabilized by water surface interactions (*i.e.* the organization of water molecules induced by the surface corresponds to those of ice). Moreover, since  $\phi$  usually shows a hysteretic behavior, the melting temperature can be different from the crystallization temperature.

To these thermodynamic effects, one must also add kinetic effects: confinement perturbs solid germs nucleation and their growth. Since the crystallites growth cannot occur beyond the limits of pores, the global crystallisation of the confined liquid is mostly driven by solid germs nucleation and can thus extend over a relatively large range of temperatures. Moreover, **heterogeneous nucleation** (*i.e.* from surfaces or foreign germs) dominates in small pores, whereas **homogeneous nucleation** (*i.e.* from an ice germ) dominates in large pores.

Researchers used the melting temperature depression and the nucleation delay to explore experimentally a range of temperatures that includes the “no man’s land”. However, it is questionable to consider the phase diagram of confined water as an extension of the phase diagram of bulk water due to surface effects. Using various confining media, a transition from a fragile behavior to a strong behavior has been observed at low temperatures (below 190 or 225 K depending on the considered medium). Other studies revealed a liquid-liquid transition at 240 K and a glass transition at 165 K (see Ref. [Chaplin, 2010] for a review).

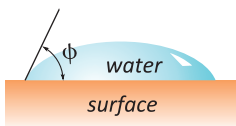


**Figure 1.18** ▲  
Definition of the contact angle  $\phi$  for a droplet of liquid on top of a solid surface.

The structure of the ice formed during the crystallization process depends on the geometry of the confining medium. In this respect, in some cases, it is possible to observe directly cubic ice nucleation instead of hexagonal ice. In addition, for 1-d or 2-d confinements, one can observe structures that are not present in the phase diagram of bulk water, as, for example, the so-called “zig-zag” 1-d structure of water inside carbon nanotubes.

As we have given the main implications of confinement on the structure of water, we will now look at its consequences in terms of dynamics.

## 3.2 Hydrodynamics in confined media: notions of nanofluidics

### 3.2.1 Slippage

Generally speaking, the equations of hydrodynamics hold to describe the behavior of confined water, except at very short distances from the wall (typically distances lower than 1 nm) [Sparreboom et al., 2009]. However, the traditional **no-slip boundary condition** – *i.e.* the continuity of the velocity at the solid–fluid interface – does not hold at small scales. Extrapolating the bulk fluid velocity profile up to the interface, a tangential **velocity slip**  $v_{\text{slip}}$  is observed. To characterize this slippage phenomenon, two observables are usually defined [Bocquet and Barrat, 2007]. One defines the **interfacial friction coefficient**  $\lambda$  so that:

$$\sigma = \lambda \cdot v_{\text{slip}}, \quad \blacksquare \quad (1.13)$$

where  $\sigma$  is the shear stress applied by the liquid on the solid surface. One can also define the **slip length**  $b$  as the distance to the wall beyond which the linear extrapolation of the velocity profile satisfies the no-slip condition (see Fig. 1.19). This length can be expressed as:

$$b = \frac{\eta}{\lambda}, \quad \blacksquare \quad (1.14)$$

where  $\eta$  denotes the shear viscosity of the bulk liquid. When the slip length is smaller than the typical molecular size, one says there is no slip. It is the case for water friction over a hydrophilic surface. On a hydrophobic surface, the slip length ranges from tens of nanometers up to tens of micrometers inside carbon nanotubes [Sendner et al., 2009, Falk et al., 2010, Falk et al., 2012] (although these latter orders of magnitude are strongly debated, with more recent work reporting slip lengths of hundreds of nanometers only [Secchi et al., 2016]). In this latter case, the curvature of the interface smooths at water molecule scale the corrugation of the energy landscape created by the solid surface, that explains the low friction [Falk et al., 2010, Falk et al., 2012]. Recent studies also suggest that slippage is enhanced by some coupling between the flow and surface phonons of the nanotube [Ma et al., 2015, Bocquet and Netz, 2015]. However, other factors can influence the dynamics near the interface. A slight increase in the corrugation of the energy landscape of the surface due to the presence of partial charges on atoms, for a given geometry, considerably decreases the slip length. This has been recently shown by comparing slippage on graphene and boron nitride sheets [Tocci et al., 2014].

High slippage enables fast flow of water. For a channel of typical size  $h$ , the flow rate is increased by a factor  $1 + C \cdot b/h$ , where  $C$  is a dimensionless number close to 1 and depending on the pore geometry [Sparreboom et al., 2009]. This fast transport property is of particular interest when there is an electrolyte inside water, as explained below.

### 3.2.2 Electro-osmotic transport

Let us consider a nanometric channel with polar surfaces subject to an external electrostatic potential parallel to the surfaces. Under this potential, the EDL undergoes an electric force, that makes ions migrating inside the channel. The displacement of ions creates a global flow of the fluid due to its viscosity, that is called **electro-osmotic flow** (EOF). This flow is enhanced in case of slippage by a factor  $1 + b/h_{\text{edl}}$  where  $h_{\text{edl}}$  denotes the thickness of the EDL [Sparreboom et al., 2009]. This kind of flow opens perspectives in terms

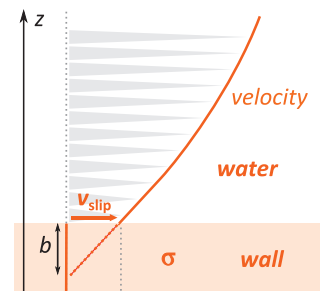


**Figure 1.19** ▲ Velocity profile of a fluid sheared between two identical solid walls. Slippage is characterized by the slip length  $b$ .

of energy conversion [Siria et al., 2013, Ren and Stein, 2008]. The idea is to use a related phenomena, called reverse electro dialysis. Taking advantage of a concentration gradient, for example near estuaries, a flow of salt water passes through the channel, inducing an electric potential parallel to the surfaces. The channel can thus be used as a power supply. It is the so-called “blue energy”. Fast transport due to slippage should improve the efficiency of the conversion. However, benefits from nanofluidic devices are debated [Bakli and Chakraborty, 2015, Majumder et al., 2015, Maduar et al., 2015, Bonthuis et al., 2011].

### 3.2.3 Permselectivity

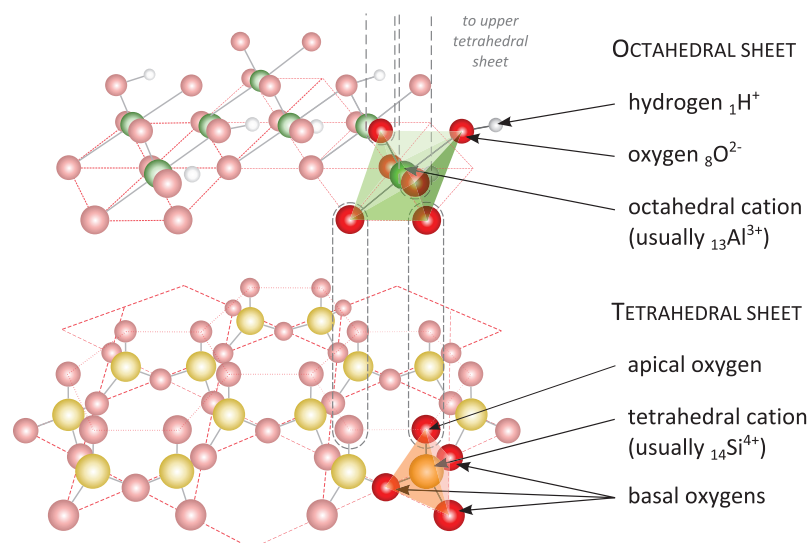
Another possible application of nanofluidic channels concerns filtering. To make the discussion simpler, we again consider a negatively charged surface. As we already discussed, there is a deficit of anions near the surface. Their concentration then increases progressively with respect to the distance to the wall. If the channel is narrow enough, the cumulative effects of walls prevent anions to lie inside the channel. Then, one get a channel that is impermeable to anions, but permeable to cations and water molecules. This phenomenon is called **permselectivity** [Sparreboom et al., 2009]. Most expectations come from biomimetic. Living organisms possess membranes (*e.g.* aquaporin) with an efficiency largely exceeding that of commercial ones in terms of both permeability, selectivity and energy cost [Murata et al., 2000, Gravelle et al., 2013, de Groot and Grubmüller, 2001, de Groot and Grubmüller, 2005, Sui et al., 2001]. Reproducing artificially such nanofluidic devices could enable to cure diseases due to aquaporin failings [de Groot and Grubmüller, 2005], but also – among many examples – to design membranes to improve fuel cells efficiency or desalination processes [Heiranian et al., 2015, Cohen-Tanugi and Grossman, 2012].

## 4 Water confined in clays

### 4.1 Clay structure

Clay materials [Mott, 1988, Auerbach et al., 2004] belong to the **phyllosilicate** – or **sheet silicate** – family. The term “clay” basically applies only to phyllosilicates of small size and presenting good ability of dispersion in water. These materials have a **layered structure**, and each layer is divided in several **sheets**. Those sheets can be **tetrahedral (T)** or **octahedral (O)**. Tetrahedral sheets are constituted by a bidimensional network of  $\text{SiO}_4$  tetrahedrons.

**Figure 1.20** ▶  
Structure of a clay layer, with detail of a T sheet and a O sheet.



Each tetrahedron shares the three oxygen atoms from its basis with the three neighboring tetrahedrons. Those atoms are called **basal oxygens** and are coplanar, forming a kind of honeycomb structure. The fourth oxygen atom is called **apical oxygen**. All apical oxygens

are also coplanar and have an hexagonal arrangement. Octahedral sheets are made of a bidimensional network of octahedrons with oxygens on the vertex and a metallic cation in the middle (or a vacancy).

A layer can be made whether by a T and a O sheet (TO layer), or by a O sheet surrounded by two T sheets (TOT layer). The O sheets share some of their oxygen atoms with apical oxygens from T sheets (see Fig. 1.20). One distinguishes **trioctahedral clays** where there is a metallic ion (generally  $Mg^{2+}$ ) in each octahedron, and **dioctahedral clays** where only two thirds of the octahedrons are filled (generally by  $Al^{3+}$ ). Such a structure is neutral, but in practice, several metallic cations inside tetrahedrons or octahedrons are substituted by cations with lower valence. For example,  $Si^{4+}$  can be substituted by  $Al^{3+}$  or  $Fe^{3+}$ . Due to these defects, layers have a negative net charge, called **interlayer charge**. This charge is balanced by absorbing cations – called **interlayer cations** – on the layer surface. The substitutions also slightly deform the layers. Interlayer cations behave as bridges that stick layers together, giving a 3-d structure to the material (see Fig. 1.21).

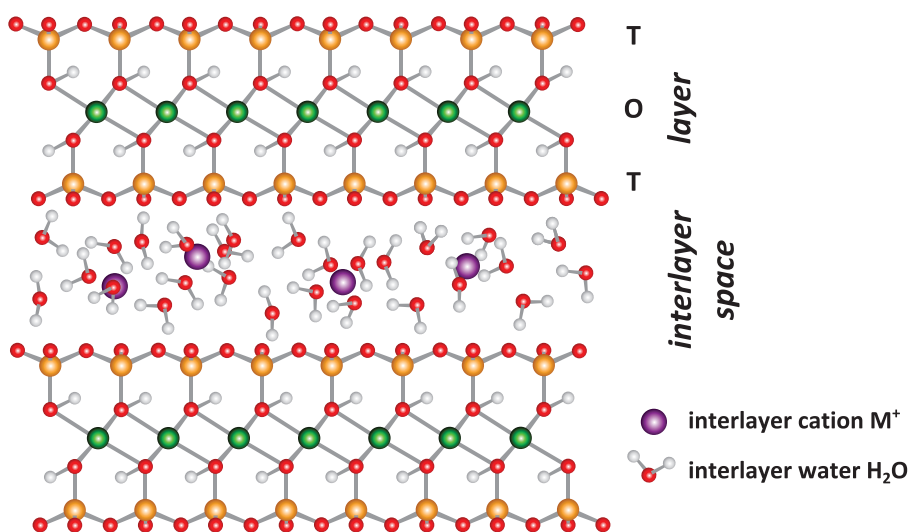


**Figure 1.21** ◀ Layers staking in clay materials and interlayer space. Water molecules and interlayer cations do not occupy their effective position on the cartoon.

Depending on the nature of the layers, the value of the interlayer charge and its localization inside the layers, phyllosilicates will adopt various behavior. Especially, some clays can adsorb water inside the interlayer space whereas micas cannot due to their higher interlayer charge. A classification of the main families of phyllosilicates is given in Table 1.1. In this study, we will focus on Montmorillonite clays, that belong to the smectite family. In those clays, the interlayer space can adsorb water, implying a swelling of the structure. For this reason, one speaks about “**swelling clays**”. We will also study some Illite clays – whose interlayer space cannot adsorb water – as reference for non-hydrated interlayer space.

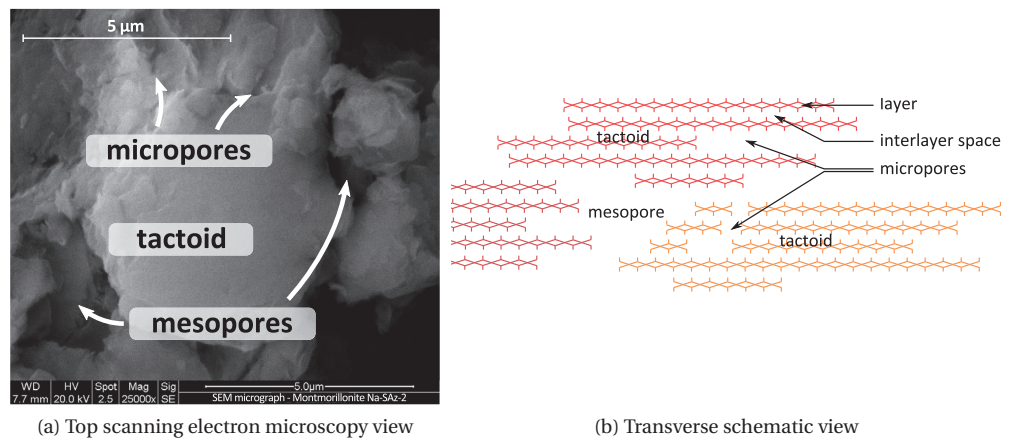
Successive layers have various size, so that the overall structure is irregular, with a couple of holes between layers. Those holes are called **micropores**. Moreover, due to those irregularities, stacks of layers become unstable above a critical thickness. Thus, layers form aggregates, called **tactoids**. The space available between tactoids is called **mesopores**. The typical size of layers is 1 nm thick and 1  $\mu m$  width. Micropores are nanometric size, whereas the size of tactoids and mesopores range from tens of nanometers to micrometers [Cases et al., 1992]. A general view of the pore structure is shown in Fig. 1.22. All pores (interlayer space, micropores and mesopores) can adsorb water, respectively called **interlayer**, **interporal** and **mesoporal water** in the following. Note that a slightly different description of the structuration is sometimes considered: according to this description, tactoids are locally ordered in micrometric aggregates. One then distinguishes mesopores that correspond to intertactoid space, whose size is typically tens of nanometers, and mesopores that correspond to interaggregate space, whose size is micrometric [Carrier et al., 2013]. In this dissertation, we will not do this distinction.

Depending on the pore type, water is more or less structured. Interlayer water could have a density higher than bulk water, whereas microporal and mesoporal water could have a density lower than bulk water [Tardy et al., 1999]. However, the structure of absorbed water is

Family	Layer	Interlayer charge	Interlayer space/distance (pm)	Octahedral sheet composition	Examples
kaolinite-serpentine	TO	$x \approx 0$	empty	dioctahedral	kaolinite
			720	dioctahedral	dickite
			H <sub>2</sub> O 720-1010 empty	trioctahedral	Halloysite lizardite
talcpyrophyllite	TOT	$x \approx 0$	empty	dioctahedral	pyrophyllite
			930	trioctahedral	talc
smectite	TOT	$x \in [0.6; 1.2]$	hydrated cations	dioctahedral	montmorillonite
			960-1500	trioctahedral	beidellite hectorite saponite
vermiculite	TOT	$x \in [1.2; 1.8]$	hydrated cations	dioctahedral	dioctahedral vermiculite
			1200-1500	trioctahedral	trioctahedral vermiculite
mica	TOT	$x \approx 2$	dehydrated cations	dioctahedral	muscovite
			1000	dioctahedral	celadonite phlogopite biotite
brittle mica	TOT	$x \approx 4$	dehydrated cations	dioctahedral	margarite
			732	trioctahedral	clintonite
illite	TOT	$x \in [1.2; 1.7]$	dehydrated cations	dioctahedral	illite
chlorite	TOT-O	variable	brucite-like layer	di/dioctahedral	donbassite
			1400	di/trioctahedral	sudoite
				tri/trioctahedral	chamosite

**Table 1.** Classification of phyllosilicates (adapted from [1]). The layers are ordered according to the interlayer charge, the interlayer space, the conventional interlayer distance, the crystal unit (in some cases) and sometimes the color.

**Figure 1.22** ▶ Multiscale porous structure of smectite-type clays. The SEM micrograph was realized in WW3, Erlangen, Germany, using a Quanta 200 microscope by FEI® on a Na-SAz-2 montmorillonite in the (001) (top) direction.



not fully understood yet. One reason is that one cannot study only one kind of water inside a hydrated clay. However, varying the relative humidity of surrounding atmosphere enables to modify the relative water population of pores, as we will see in the next paragraph.

## 4.2 Swelling processes

Various processes take part to clay swelling, that highly depends on the structure of the mineral itself – *i.e.* the size and the organization of tactoids – the interlayer charge and its localization over the layers, and the nature of interlayer cations. This mechanism is, as the porosity, multiscale. We will be interested in this study in **sodium-exchanged clays**, *i.e.* clays whose interlayer cation has been substituted by sodium.

The macroscopic expansion or shrinkage of clays is a major issue in several civil engineering processes. It causes instabilities of soils that can lead to the destruction of buildings, and oil well-bores. One estimates that damages due to clays swelling costs several billions of euros each year [Boek et al., 1995].

Two main processes are responsible of clay swelling: **intercrystalline swelling** and **osmotic swelling** [Cases et al., 1992]. Intercrystalline swelling corresponds to the expansion of the crystal due to the adsorption of several (between one and four) layers of water at layer surfaces (including interlayer space) or around cations. Due to this process, the interlayer space can grow from 10 to 18 Å approximatively [Ferrage et al., 2005, Villar et al., 2012, Holmboe et al., 2012]. Osmotic swelling corresponds to the water flux induced by the difference of ion concentration between the interlayer space and the clay surface. The existence of osmotic swelling results from the competition between two effects. From an electrostatic point of view, there is an attractive force between layers and cations, that tends to bring layers closer. On the opposite, on a thermodynamical point of view, the osmotic pressure is repulsive, since the salt “concentration” is much higher inside the interlayer space than outside. Depending on the layer charge surface and the valence of cations, the attractive or the repulsive contribution dominates. In the former case, one observes osmotic swelling with a large expansion of the interlayer space up to 40 Å, or a partial or complete exfoliation of the layers [Meleshyn and Bunnenberg, 2005, Michot et al., 2004], whereas in the latter case, it is inhibited. This is what happens when the interlayer cation is divalent. Strong forces acting between ions and layers prevent osmotic swelling, with a maximum interlayer space of about 19 Å [Holmboe et al., 2012, Michot et al., 2013]. Potassium also acts as a swelling inhibitor due to preferred interaction with the layer surface instead of hydration [Boeck et al., 1995]. Note that osmotic swelling can also be observed in mesopores.

Cases et al. first gave a global consistent picture of the different mechanisms involved [Cases et al., 1992, Bérend et al., 1995, Cases et al., 1997]. This description has then been refined [Ferrage et al., 2005] but also recently debated [Salles et al., 2010], which shows that swelling is still an open question. Based on an extensive analysis of X-ray diffraction data, nitrogen and water absorption isotherms, and calorimetric measurements, the authors suggest the following scheme. At low relative humidity (less than 16 %), water **adsorbs** mainly on **external surfaces** of tactoids. Then, interlayer hydration begins, with an alternated formation of a water layer on the **external surface**, then in the **interlayer**, then a second layer on external surface, *etc.*. The first layer of water in the interlayer space is filled around 50 % of humidity. Osmotic swelling begins around relative humidity close to 72 %, while the second adsorbed layer is not complete. At 90 % of relative humidity, the second layer is completed in only about 73 % of interlayer spaces and a third layer is formed in approximatively 15 % of interlayer spaces. The range of humidity higher than 50 % also corresponds to the filling of **mesopores**. During the hydration process, the overall structure of the clay is reorganized, with a partial exfoliation that reduces the size of tactoids from 20 to 6 clay layers during the first stages of the hydration.

**Desorption** follows a slightly different scheme. First the desorption of water from mesopores and external surfaces occurs down to 72 % of humidity. Then, three water layer configurations disappear below 50 % of humidity, two water layer configurations disappear below 25 %, with also desorption of all water mainly bond to layer surfaces, and finally, water bonded to interlayer cations desorbs at 5 % of humidity.

The influence of mesopore hydration on the swelling of clay is not clear. In the case of sodium-exchanged clays, various authors predict a shrinkage of mesopores upon hydration of the clay, due to the structural reorganization mentioned above [Massat et al., 2016]. This is consistent with Environmental Scanning Electron Microscopy (ESEM) measurements, which show that the global swelling is mainly due to interlayer swelling [Carrier et al., 2013].

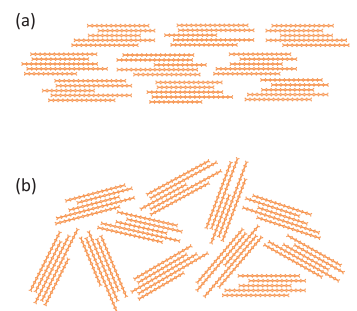


**Figure 1.23** ▲ Ordered (a) and disordered (b) stacking of tactoids.

On the contrary, other authors predict a swelling of mesopores [Salles et al., 2010]. A possible explanation to resolve this discrepancy is a high dependence of mesopore hydration on the ordering of tactoids. Randomly organized tactoids could imply a swelling of mesopores, whereas the latter shrink upon hydration when tactoids are regularly ordered (see Fig. 1.23).

Since adsorption and desorption do not occur in the same order for the different hydration states, one can modify the relative amount of water in the various pores working at different points of the adsorption/desorption isotherm. We will try to use this property to discriminate the structure and dynamics corresponding to the different confinement areas in Chap. 6.

### 4.3 Water structure and dynamics

**Structure.** Numerous studies have been devoted to the analysis of the structure of water adsorbed in clay minerals, both experimentally – using *e.g.* neutron scattering or infrared scattering – and numerically – using molecular dynamics or Monte-Carlo simulations. In particular, a lot of work focus on the arrangement of water molecules and cations inside the interlayer space, in comparison with what happens in bulk water [Skipper et al., 2006, Skipper et al., 1991, Skipper et al., 1995]. Here we discuss briefly the case of small alkali ions (lithium, sodium, potassium) exchanged clays (associated ionic radii are given in Table 1.2 at the end of the chapter). We first focus on the arrangement of cations. The solvation energy of lithium, sodium, and potassium increase with the size, and their solvation shell in bulk water is constituted respectively of 5, 6 and 6 water molecules. When no water is adsorbed inside the interlayer space, cations are mainly trapped inside the hexagonal cavities of the layer siloxane surfaces. Interestingly, in the presence of two layers of water, the distribution of oxygen atoms around those ions remains almost unmodified within the first hydration shell, but some oxygen atoms from water molecules can be replaced by basal oxygen atoms of the clay layers depending on the relative affinity of ions with the clay surface and water molecules. Indeed, as we mentioned in section 4.1, the coordination of cations depends on the delocalization of the layer charge [Chang et al., 1997, Skipper et al., 2006, Skipper et al., 1995, Mignon et al., 2010]. One distinguishes three states of coordination for interlayer cations (see Fig. 1.24) [Sposito et al., 1999]:

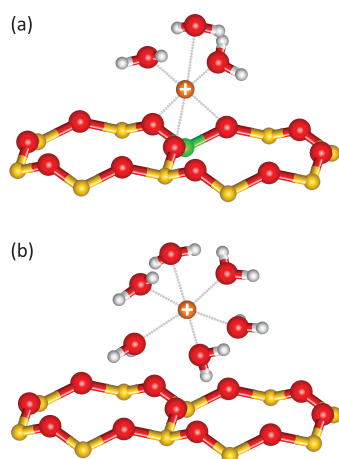


**Figure 1.24** ▲  
Cartoon of an inner-sphere surface complex (a) and an outer-sphere surface complex (b) formed by the interlayer cation on the layer (siloxane) surface (adapted from [Sposito et al., 1999]).

- **diffuse complex:** the cation is solvated by water without significant effect of the layer surfaces;
- **outer-sphere surface complex:** the cation interacts weakly with the surfaces, and water molecules lie between the cation and the clay layer (see Fig. 1.24b);
- **inner-sphere surface complex:** the cation interacts strongly with the surface, without any water molecule between the cation and the clay layer (see Fig. 1.24a).

Lithium forms an outer-sphere surface complex, wherever the layer charge is localized. Sodium forms an outer-sphere complex near an octahedral substitution whereas it forms an inner-sphere surface complex near a tetrahedral substitution. Potassium only forms inner-sphere surface complexes [Chang et al., 1997, Skipper et al., 2006, Skipper et al., 1995, Mignon et al., 2010]. In the case of inner-sphere surface complexes, three water molecules are typically substituted by basal oxygens within the first solvation shell. A similar trend has been reported for sodium when only one water layer is adsorbed inside the interlayer space [Skipper et al., 1995].

We focus now on the global arrangement of water molecules. When two (or more) water layers are adsorbed inside the interlayer space, the water structure is like those of salt water we introduced previously [Sposito and Prost, 1982], but suffers from a slight weakening at longer distances [Skipper et al., 2006]. The clay surface is basically hydrophobic, but substitutions confer a hydrophilic behavior. Thus, a strong layering parallel to the layers is observed, as we saw in the previous section near hydrophilic surfaces [Skipper et al., 2006, Rotenberg et al., 2010]. Molecules at the interface are oriented by the electric field created by the net charge of the crystal layers, and can form hydrogen bonds with both basal oxygens and other molecules. One hydrogen atom is directed to the surface, whereas the

other one interacts with other molecules [Skipper et al., 2006]. When only one layer of water molecules is adsorbed, the structure is somehow more disordered, but oxygen atoms concentrate in the mid-plane of the interlayer space whereas hydrogen atoms are directed to the layer surfaces [Boeck et al., 1995].

In a similar manner as the structure, we will see now that transport properties are not that much affected by the confinement.

**Hydrodynamics transport.** The slip length of water over an uncharged clay layer is about 4.1 Å, which is slightly above the molecular size (typically 3 Å), whereas it falls to 1.5 Å for Montmorillonites due to the net charge of the layers, conferring to the clay hydrophilic properties [Botan et al., 2011, Botan et al., 2013]. Surprisingly, this hydrophilic behavior does not influence that much the hydrodynamics properties of confined water when more than one water layer is adsorbed in the interlayer space. According to various experiments such as neutron scattering of conductimetry and various calculations, the self-diffusion coefficients of cations and water molecules inside the interlayer space are typically reduced by a factor between 2 and 4 with respect to bulk water, but remain of the same order of magnitude [Salles et al., 2015, Ngouana W and Kalinichev, 2014, Malikova et al., 2005]. A similar trend is observed for the shear viscosity, with a slight increase inside the interlayer space with respect to bulk water [Botan et al., 2011]. Cations forming inner-sphere surface complexes, as Cs<sup>+</sup> and K<sup>+</sup>, diffuse slightly slower than the one forming outer-sphere surface complexes, as Li<sup>+</sup> and Na<sup>+</sup>. For the two latter, the self-diffusion coefficient in the interlayer space is almost equal to the one in bulk water. Logically, in mesopores where water is less confined, self-diffusion coefficients are almost identical to those in bulk water [Salles et al., 2015]. However, at macroscopic scale, the self-diffusion of water is lowered by about one order of magnitude with respect to interlayer water, due to the exchange dynamics between mesopores and interlayer space [Marry et al., 2002, Salles et al., 2015]. We will investigate numerically those transport properties in the case of a sodium exchanged Montmorillonite in Chap. 6.

**Low temperature dynamics.** Several recent studies focus on the temperature behavior of water confined in clay minerals. Gailhanou [Gailhanou, 2005], using Differential Scanning Calorimetry, reported between one and three phase transitions. At low water content, a unique phase transition is observed, extending from 150 and 250 K, associated to a glass transition of confined water. At higher water contents, two additional phase transitions appear: one between 240 and 273 K, and the other between 273 and 290 K. The first one is explained by a second glass transition, or by the crystallization of water confined in the narrowest pores. For the second one, it is suggested it could correspond also to crystallization of water in some pores. Maheshwari et al. [Maheshwari et al., 2013], using Positron Annihilation Spectroscopy, Dielectric Relaxation Spectroscopy, Differential Scanning Calorimetry and Nuclear Magnetic Resonance, reported two phase transitions for water confined in clay minerals: one between 274 and 286 K and the other between 240 and 245 K. The first one is associated with an increase of free volume and an alteration of the hydrogen-bond network. It has been interpreted as a freezing of water molecules hydrogen-bonded to the layer surfaces. The other one is associated to a fragile-to-strong crossover and was explained by a partial freezing of remaining confined water. Between those two transitions, confined water behaves almost like a liquid. Fleury et al. [Fleury et al., 2013], using Low-Field Nuclear Magnetic Resonance, reported two transitions: a water surface freezing between 263 and 273 K and another transition around 243 K. Finally, Salles et al. [Salles et al., 2010], using calorimetry, reported solidification of water adsorbed in nanometric mesopores between around 243 and 253 K, whereas water present in larger mesopores at high hydration states freezes around 269 K. In summary, all these studies agree to attribute two phase transitions for confined water, one around 273 K, and another one around 240 K. The interpretations of those transitions differ, but in each case, the transitions do not concern weakly-bound interlayer water. According to Salles et al., those water molecules cannot freeze. Only Gailhanou reported a transition around 190 K, interpreting it as a glass transition of water molecules. It is not inconsistent with other studies if one assumes this transition concerns weakly-bound interlayer water. We will try to go further on this point in Chap. 6.

As we saw, even if water confined in clay minerals has been extensively studied during the

last decades, many open questions remain, especially in terms of dynamics. We will try to give some elements to answer to these questions in Chap. 6. Before that, we will analyze separately the various elements that constitutes water confined in clay minerals: water (Chap. 3), confinement (Chap. 4) and ions (Chap. 5).

## 5 Appendix: Table of effective ionic radii

several  
n, 1976,

Ion	Coordination	Ionic radius (Å)	Ion	Coordination	Ionic radius (Å)
Al <sup>3+</sup>	4	0.39	K <sup>+</sup>	9	1.55
Al <sup>3+</sup>	5	0.48	K <sup>+</sup>	10	1.59
Al <sup>3+</sup>	6	0.54	K <sup>+</sup>	12	1.64
Br <sup>-</sup>	6	1.96	Li <sup>+</sup>	4	0.59
Ca <sup>2+</sup>	6	1	Li <sup>+</sup>	6	0.76
Ca <sup>2+</sup>	7	1.06	Li <sup>+</sup>	8	0.92
Ca <sup>2+</sup>	8	1.12	Mg <sup>2+</sup>	4	0.57
Ca <sup>2+</sup>	9	1.18	Mg <sup>2+</sup>	5	0.66
Ca <sup>2+</sup>	10	1.23	Mg <sup>2+</sup>	6	0.72
Ca <sup>2+</sup>	12	1.34	Mg <sup>2+</sup>	8	0.89
Cl <sup>-</sup>	6	1.81	Na <sup>+</sup>	4	0.99
Cs <sup>+</sup>	6	1.67	Na <sup>+</sup>	5	1
Cs <sup>+</sup>	8	1.74	Na <sup>+</sup>	6	1.02
Cs <sup>+</sup>	9	1.78	Na <sup>+</sup>	7	1.12
Cs <sup>+</sup>	10	1.81	Na <sup>+</sup>	8	1.18
Cs <sup>+</sup>	11	1.85	Na <sup>+</sup>	9	1.24
Cs <sup>+</sup>	12	1.88	Na <sup>+</sup>	12	1.39
F <sup>-</sup>	2	1.29	Rb <sup>+</sup>	6	1.52
F <sup>-</sup>	3	1.3	Rb <sup>+</sup>	7	1.56
F <sup>-</sup>	4	1.31	Rb <sup>+</sup>	8	1.61
F <sup>-</sup>	6	1.33	Rb <sup>+</sup>	9	1.63
H <sup>+</sup>	1	-0.38	Rb <sup>+</sup>	10	1.66
H <sup>+</sup>	2	-0.18	Rb <sup>+</sup>	11	1.69
I <sup>-</sup>	6	2.2	Rb <sup>+</sup>	12	1.72
K <sup>+</sup>	4	1.37	Rb <sup>+</sup>	14	1.83
K <sup>+</sup>	6	1.38			
K <sup>+</sup>	7	1.46			
K <sup>+</sup>	8	1.51			



## Chapter 2

# Probing water from electrons to bulk: numerical and experimental methods

### Outline

1	Atoms and molecules . . . . .	25
1.1	Atoms . . . . .	25
1.2	Molecules . . . . .	26
1.3	Beyond the molecule: molecular interactions . . . . .	27
2	Infrared absorption spectroscopy . . . . .	27
2.1	Theory (with applications to water) . . . . .	27
2.2	Instrumentation . . . . .	30
3	Classical and ab initio molecular dynamics . . . . .	34
3.1	Molecular dynamics . . . . .	34
3.2	Computing forces (I): density functional theory . . . . .	39
3.3	Computing forces (II): point charge force fields . . . . .	41

## 1 Atoms and molecules

At the human scale, matter looks continuous, but at the nanometer scale, it is made of numerous atoms and molecules. From atoms and their interaction originate all phenomena at macroscopic scale. Linking what occurs at one scale with what happens at another constitutes the main work of a great number of chemists and physicists. In this section, we will recall some basics of atomic and molecular physics that will be useful to understand what comes next [Atkins and de Paula, 2010, Atkins and Friedman, 2011].

### 1.1 Atoms

An atom is constituted by electrons that gravitate around a nucleus. In all this dissertation, we will not consider the structure of the nucleus. The closest electrons to the nucleus are tightly bound with it and are called **core electrons**. Electrons from external shells are easier to pull off and are mostly responsible for the reactivity of the atom. They are called **valence electrons**.

Quantum mechanics teaches us two important properties of electrons: (i) one cannot know precisely at the same time their velocity and their position (it is also true for light nucleus like hydrogen and helium, and, in a less extend, for others) – it is the **Heisenberg's uncertainty principle** – and (ii) the energy of an electron is **quantified**. From (i), it results that electron cannot be described by its position, but rather by a field of **probability of presence**, using its **wavefunction**  $\psi$ , with  $|\psi|^2 \cdot d\tau$  the probability for the electron to lie in the

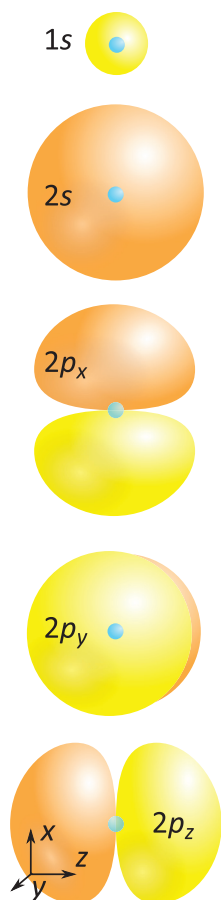


**Figure 2.1** ▲ Approximate shape of the spatial distribution of the probability of presence of the electron around the nucleus (in blue) for the first energy levels, represented by isodensity surfaces.

volume  $d\tau$ . From (ii), the wavefunction  $\psi$  cannot have a random form. A specific wavefunction corresponds to each energy level. For hydrogenoid ions – *i.e.* ions with only one electron – these wavefunctions are called **atomic orbitals**, denoted  $1s, 2s, 2p, 3s, 3p, 3d$  (see figure 2.1)... Energies  $E_i$  and wavefunctions  $\psi_i$  of each energy level  $i$  are solutions of the **stationary Schrödinger equation**:

$$\mathcal{H}\psi_i = E_i \cdot \psi_i. \quad \blacksquare \quad (2.1)$$

$\mathcal{H}$  is the Hamiltonian operator of the system, expressing the kinetic energy of both nucleus and electron and the Coulombic interaction between the electron and the nucleus:

$$\mathcal{H} = -\frac{\hbar^2}{2 \cdot m_n} \cdot \vec{\nabla}^2 - \frac{\hbar^2}{2 \cdot m_e} \cdot \vec{\nabla}^2 - \frac{Z \cdot e^2}{4 \cdot \pi \cdot \epsilon_0 \cdot \|\vec{r}_n - \vec{r}_e\|}, \quad \blacksquare \quad (2.2)$$

where  $\hbar$  is the reduced Planck constant,  $m_n$  and  $\vec{r}_n$  (*resp.*  $m_e$  and  $\vec{r}_e$ ) are the mass and the position of the nucleus (*resp.* the electron),  $Z$  is the atomic number of the atom, and  $\epsilon_0$  is the vacuum permittivity. For polyelectronic atoms and ions, since electrons dynamics are coupled, one cannot anymore define atomic orbitals, *i.e.* mono-electronic wavefunctions (solutions of the Schrödinger equation depend of all degrees of freedom at the same time) and electronic levels are **shifted**. In practice, such wavefunctions are nevertheless defined: it is the **orbital approximation**. We will see later some consequences of this approximation. However, a few rules must be respected to build the many-electron wavefunction, *e.g.* to respect the fact that electrons are **indistinguishable**. The repartition of electrons over the different energy levels constitutes the electronic configuration of the atom and controls the energy required to remove or to add an electron from / to the atom, and thus, it controls the ability of the atom to form a molecule and the properties of resulting chemical bonds.

## 1.2 Molecules

Similarly to the coupling between electrons inside an atom, coupling between two atoms affects the distribution of electronic energy levels of the pair. If the energy of the system is lower than the sum of the energies of the two isolated atoms, then one says there is a constructive overlap of atomic orbitals; a **chemical bond** is formed.

A nucleus/nucleus term must then be added in the Hamiltonian with respect to eq. (2.2). Due to this term, even for the simplest molecular structure, the analysis of the Schrödinger equation to evaluate the energy levels and associated wavefunctions becomes much harder. However, since nuclei are much heavier than electrons ( $m_n \approx 2000 \cdot m_e$ ), they move very slowly. A classical hypothesis consists in considering that nuclei are stationary at the electron dynamics timescale. It is the **Born-Oppenheimer approximation**. Thus, one has to consider (i) electronic energy levels that are solutions of the Schrödinger equation for a given position of nuclei, and (ii) rotational and vibrational energy levels associated to the dynamics of nuclei. Under this hypothesis, the wavefunction can first be approximated as a linear combination of atomic orbitals in the Schrödinger equation. This enables to get an approximation of the energy levels and the electron distribution, that can be used as initial guess in molecular simulations. Once the electronic structure is known, the rotational and vibrational energy levels can be computed using either classical or quantum mechanics. For example, in the case of *ab initio* molecular dynamics (see further), forces applied on nuclei are computed from the electronic structure, and then, the displacement of nuclei is determined using classical mechanics. Rotational and vibrational energy levels characterize the molecular structure and its environment. They can be measured *e.g.* using infrared absorption spectroscopy. We will go back on this point in the next section.

Depending on the electronic configuration of the atoms that constitute the molecular structure and its geometry, the molecule can be **polarized**. The distribution of electrons can also be modified by an external electric field and induce a dipolar moment. In that case, one says the molecule is **polarizable**. From those polarity and polarizability properties originate low energy electrostatic interactions between molecules, which play a key role in the structure and dynamics of condensed phases, as detailed in the next section.

### 1.3 Beyond the molecule: molecular interactions

Interactions between (induced or permanent) dipoles are called **Van der Waals interactions**. Among those interactions, those between two permanent dipoles are called **Keesom** interactions, those between a permanent dipole and an induced dipole are called **Debye** interactions, and those between two induced dipoles are called **London**, or **dispersive**, interactions. The latter require some comments. Due to quantum fluctuations, *i.e.* transient occupation of excited energy levels by electrons, the electronic clouds of molecules can be temporary polarized. The resulting dipole direction is *a priori* random. However, since electrons interact, the dipole moments of neighboring molecules are correlated and the resulting interaction leads to an attractive force between atoms. From this interaction, one can explain the condensation of dihydrogen or argon at low temperature. Thus, the London interaction is very important and is a purely quantum property resulting from electronic structure fluctuations. Since only the ground-state wavefunction is considered within the Born-Oppenheimer approximation, the existence of excited states, and thus of quantum fluctuations and London interaction, cannot be rendered by these approaches, constituting a major limit to them. We will go back to this point at the end of this chapter.

All these interactions can be expressed in the following form:

$$V = -\frac{C}{r^6}, \quad \blacksquare \quad (2.3)$$

where  $C$  is a constant and  $r$  denotes the distance between the two molecules. Another important interaction is the so called “**hydrogen bond**”. It is the interaction between a A–H group of a molecule with a B atom from another molecule, where A and B denotes very electronegative atoms – mainly nitrogen, oxygen and fluor. From this interaction, it results a slightly constructive overlap between the orbitals of the *three* atoms A, B and H, which is thus directional. The associated energy lies between the energy of a covalent bond and a Van der Waals interaction. As we already saw in the previous chapter, this interaction plays a key role in water structure and dynamics.

## 2 Infrared absorption spectroscopy

### 2.1 Theory (with applications to water)

As we mentioned in the previous section, energy levels can be associated to vibrations and rotations of nuclei inside a molecule. For example, in the case of an isolated diatomic molecule, the vibrational energy levels correspond in a rough approximation to the energy levels of the harmonic oscillator introduced in all quantum mechanics textbooks. The transition energy between those levels usually fall inside the infrared domain. Thus, the study of infrared radiation absorption by molecular structures constitutes a precious analysis tool. A system constituted by  $N$  atoms has  $3 \cdot N$  degrees of freedom in which  $3 \cdot N - 6$  are **vibrational** degrees of freedom, and 3 are **rotational** degrees of freedom. These  $3 \cdot N - 6$  vibrations are coupled, but can be expressed in terms of  $3 \cdot N - 6$  uncoupled **collective vibrations**, called **eigenmodes** (or **phonons**) of the system [Atkins and de Paula, 2010, Atkins and Friedman, 2011, Griffiths and De Haseth, 2007]. These collective vibrations affect notably the position of only a small number of localized atoms. It can be for example a functional group of a molecule. Consequently, it is of common use to characterize and call those vibrations in terms of the local rearrangement they make, even if all atoms move a little bit. For instance, in the case of water, one speaks about symmetric and antisymmetric stretching modes of O–H bonds, or H–O–H stretching mode [Atkins and de Paula, 2010].

Each eigenmode is not necessary associated with a **light absorption process**. A system can absorb or emit an electromagnetic wave of frequency  $\nu_0$  only if it has – at least transiently – a dipole oscillating at a frequency  $\nu$  close to  $\nu_0$  (see the theory of oscillating dipoles in any electromagnetism textbook for details). Thus, in the specific case of infrared absorption, vibration modes must induce a **variation of the dipole moment** of the system. The mode is then said “infrared active”. It is the same with rotational modes. Those conditions are the so-called **selection rules** [Atkins and de Paula, 2010, Atkins and Friedman, 2011, Griffiths and

In the specific case of linear molecules, there are  $3 \cdot N - 5$  internal degrees of freedom since the rotation around the axis of the system does not change the system.

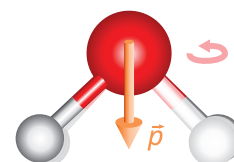
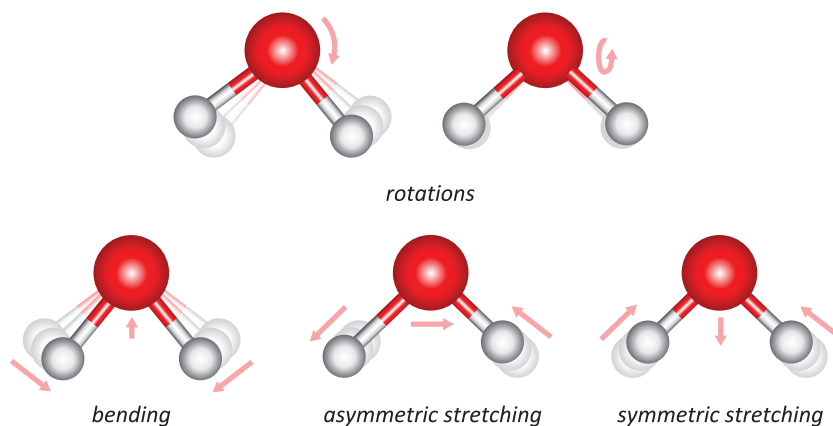


**Figure 2.2** ▲ Rotation around  $z$ -axis does not change the dipole moment of the molecule and thus is infrared inactive.

De Haseth, 2007]. Consider for example an isolated water molecule. It has three atoms that are not aligned, so it has three rotational modes and three vibrational modes. The rotation around the  $z$ -axis (see Fig. 2.2) does not affect the dipole moment of the molecule. Thus, this mode is not infrared active. All other modes are active, and are represented on figure 2.3. More generally, a systematic study of the **symmetries and invariances** of a molecular structure enables to predict which modes are active or not [Atkins and de Paula, 2010, Atkins and Friedman, 2011]. In liquid water, all molecules are coupled. Vibration modes corresponding

**Figure 2.3** ▶ Rotational and vibrational modes of a single water molecule that are infrared active.



mostly to molecular rotations are called **libration** modes. Moreover, the coupling between molecules removes degeneracy of molecular energy levels. As the number of molecules is huge (on the order of magnitude of  $10^{23}$ ), the energy gap between successive levels goes to zero and one obtains a **continuous spectrum** [Atkins and de Paula, 2010, Atkins and Friedman, 2011, Griffiths and De Haseth, 2007].

The absorption of infrared radiation by a sample can be expressed in terms of its **absorbance**  $A$ , defined as:

$$A(\nu) = -\log\left(\frac{I(\nu)}{I_0(\nu)}\right), \quad \blacksquare \quad (2.4)$$

where  $I(\nu)$  and  $I_0(\nu)$  denote respectively the intensity of the radiation at wave-number  $\nu$  after passing through the sample and after using the same path but without the sample. The absorbance is related to the number of absorbing species  $i$  via the **Beer-Lambert's law**:

$$A(\nu) = \sum_i \alpha_i(\nu) \cdot l \cdot c_i, \quad \blacksquare \quad (2.5)$$

where  $l$  is the thickness of the sample,  $\alpha_i$  is the absorptivity of species  $i$ , and  $c_i$  is its molar concentration. The product  $l \cdot c_i$  (apart from a surface factor) give the amount of specie  $i$ . Thus, for a given set of experimental conditions (so at constant  $\alpha_i$ ), the absorbance is directly proportionnal to  $l \cdot c_i$  and can thus be used to follow the evolution of the amount of the different species.

Figure 2.4 gives the infrared absorption spectrum of liquid water at ambient conditions. Libration, bending and stretching modes appear as three distinct large bands located in the mid-infrared domain. Libration is located around  $600 \text{ cm}^{-1}$ , bending around  $\nu_2 = 1650 \text{ cm}^{-1}$ , and stretching around  $3400 \text{ cm}^{-1}$ . The latter is usually deconvoluted in three (or more) contributions using Gaussians, located approximatively at  $3250 \text{ cm}^{-1}$ ,  $\nu_1 = 3450 \text{ cm}^{-1}$  and  $\nu_3 = 3600 \text{ cm}^{-1}$  [Brubach et al., 2005]. Different hypotheses have been made to assign these contributions. Based on the evolution of the spectrum with the temperature, some authors suggest a link between the frequency and the **connectivity of molecules**. Per this hypothesis, the first peak corresponds to fully (or highly) H-bonded molecules, the second one to intermediately H-bonded molecules, and the third one to poorly H-bonded molecules [Brubach et al., 2005, Mallamace et al., 2007]. Another explanation is to assign bands around  $\nu_1$  and  $\nu_3$  respectively to **asymmetric** and **symmetric stretching** of O-H bonds, and the band at  $3250 \text{ cm}^{-1} \approx 2 \cdot \nu_2$  to an overtone of the bending band, enhanced

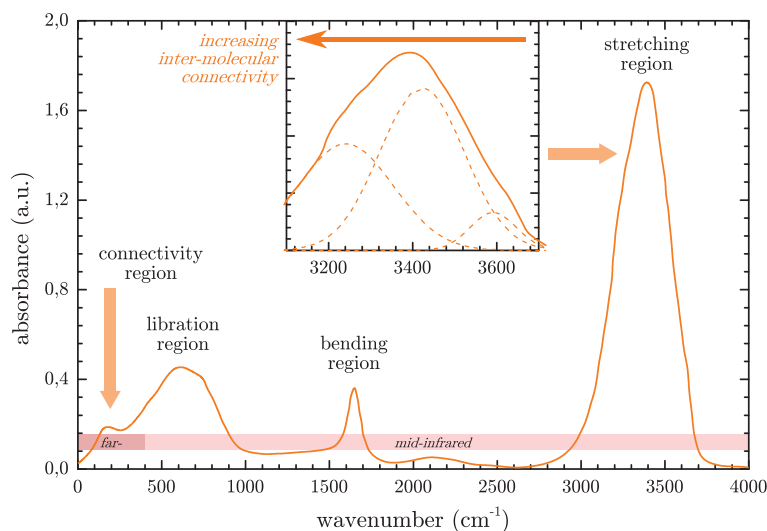


**Figure 2.4** ◀ Liquid water far- and mid-infrared absorption spectrum at ambient conditions (from [Hasegawa and Tanimura, 2011]). It is constituted by three main components, corresponding to libration, bending and stretching modes of water molecules. A shoulder on the libration band in the far-infrared region corresponds to inter-molecular vibrations. Inset: the stretching band can be deconvoluted in three contributions, corresponding (from low to high wavenumbers) to strongly, moderately and poorly H-bonded water molecules.

by the proximity of the stretching bands (**Fermi resonance**) [Dalla Bernardina, 2015]. The slight band around  $2200\text{ cm}^{-1}$  is usually assigned to an overtone between stretching and libration bands. Finally the shoulder at  $200\text{ cm}^{-1}$  is assigned to inter-molecular vibrations and are usually called **connectivity bands**. It corresponds to the longitudinal motion of the hydrogen atom between the two oxygens of a hydrogen bond. One also speaks about “H-bond stretching mode” [Brubach et al., 2005].

We also present briefly the spectra of ordinary ice and vapor on figures 2.5 and 2.6 respectively. The spectrum of ice is characterized by a narrowing of the different contributions

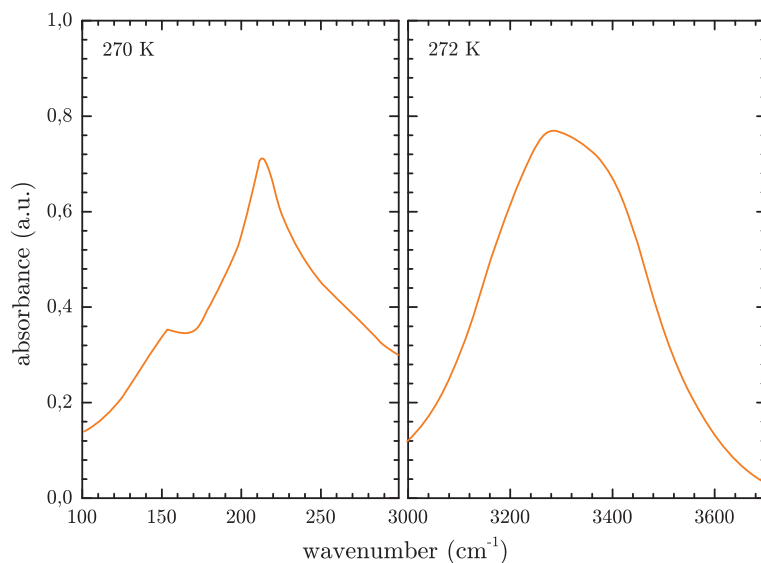


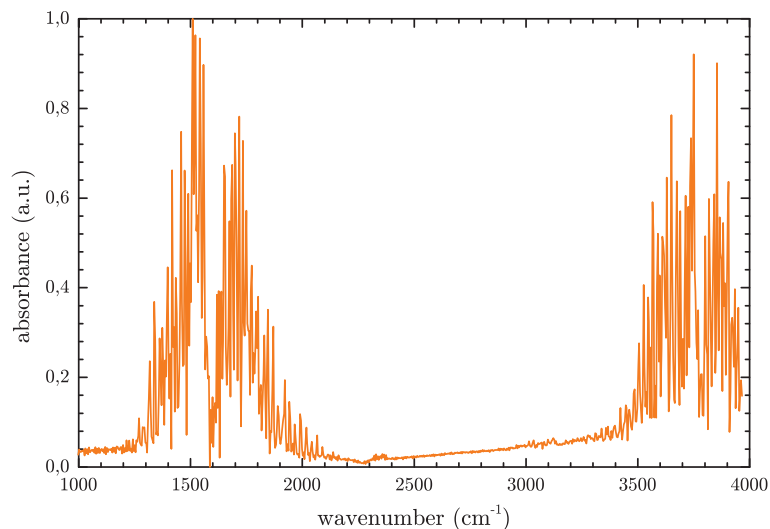
**Figure 2.5** ◀ Ordinary (hexagonal) ice far- and mid-infrared absorption spectrum near  $0\text{ °C}$  (from [Le Caër et al., 2014]). The mid-infrared absorption spectrum is slightly shifted at lower wavenumbers, with an increase of the intensity of the  $3250\text{ cm}^{-1}$ , due to the increase of fully H-bonded water molecules with crystallization. The far-infrared absorption is made of two sharp contributions around  $160$  and  $230\text{ cm}^{-1}$  corresponding to H-bond stretching vibrations in two different directions of space.

of the liquid spectrum upon cooling. The stretching bands are slightly shifted to lower wavenumbers, and the intensity of the  $3250\text{ cm}^{-1}$  contribution increases with decreasing temperature, due to the increase of the population of fully H-bonded water molecules between liquid and ice structures. Two sharp peaks also appear on the far-infrared (FIR) absorption spectrum, corresponding both to H-bond stretching modes in two different directions of space since water molecules have different orientations inside the ordinary ice structure [Le Caër et al., 2014].

The spectrum of vapor is easy to recognize since the three broad bands that appear on the liquid spectrum are replaced by series of regularly spaced thin peaks, that characterize gaseous phases [Atkins and de Paula, 2010, Atkins and Friedman, 2011, Griffiths and De Haseth, 2007]. The series in the bending and stretching regions (*cf.* Fig. 2.6) correspond to **rotational-vibrational** modes, *i.e.* coupling between vibrational modes and low fre-

**Figure 2.6** ▶

Water vapor infrared absorption spectrum (from [NIST, 2017]). The spectrum is characterized by the presence of two series of regularly spaced thin peaks corresponding to coupling between rotational and bending or stretching modes of O-H bonds. The series approximately lie in the bending and stretching regions of the liquid spectrum. Another similar series of peaks corresponding to pure rotational modes lies in the libration region (not shown here).



quency rotational modes, since in gaseous phase, water molecules can rotate freely (which is not the case in the other phases due to neighboring molecules). The series at lower frequency corresponds to pure rotational modes. Even if we do not directly deal with water vapor in the present study, this spectrum is of importance since there is water vapor everywhere in the atmosphere (especially when trying to hydrate a sample!) and thus this spectrum contributes to the overall absorption and must be subtracted from the absorbance.

Now that we have the key theoretical elements of infrared absorption phenomena, we can see how to record in practice an absorption spectrum.

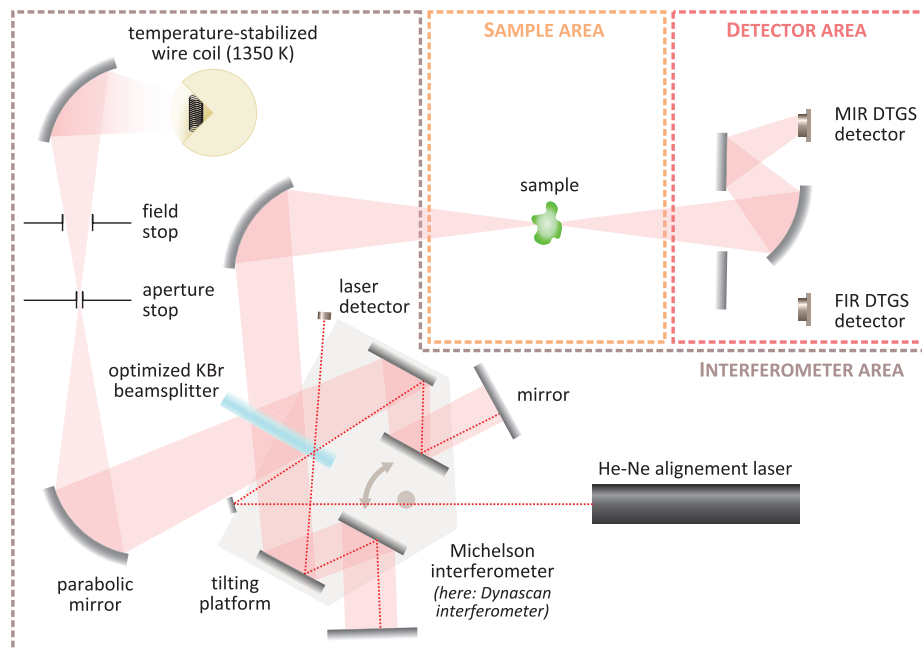
## 2.2 Instrumentation

### 2.2.1 Description of Fourier Transform Spectrometers

The principle of a laboratory Fourier Transform spectrometer is illustrated on figure 2.7. An

**Figure 2.7** ▶

Principle of a Fourier Transform Spectrometer (here a Spectrum GX by Perkin Elmer®). See main text for details. On this model, a patented Dynascan interferometer is used instead of a conventional Michelson interferometer. The principle is almost the same, except that the optical path is varied by tilting a platform holding intermediate mirrors positioned along the optical path instead of translating one of the two limit mirrors.



infrared radiation with a wide spectrum is produced by heating a metallic wire. Then, using a **Michelson interferometer** (or equivalent), a spectral component of the incident beam is isolated and directed to the sample area. Collimation of the beam is realized using parabolic metallic mirrors, as standard glass lenses absorb most of infrared radiations. Changing

the relative distance between the mirrors of the two arms of the interferometer enables to scan the complete spectrum of the source. Then, if the spectrometer is used in **transmission** mode – which is the most common way to record an infrared spectrum – light passes through the sample, and the time evolution of the intensity of the light beam is recorded using a detector sensitive to infrared radiations. The **energy spectrum**  $I(\nu)$  of the light is then obtained by calculating the **Fourier Transform** of the recorded signal. The Fourier transform operation requires many precautions in terms of sampling. A complete description of the signal processing procedure is beyond the scope of the present manuscript and can be found in textbooks [Griffiths and De Haseth, 2007]. Recording the energy spectrum with and without the sample, one can then calculate the **absorption spectrum**, using formula (2.4). The global intensity of the beam can be adjusted by changing the field stop diameter in order not to saturate the detector. The aperture stop controls the divergence of the beam, and thus, the spectral width of light after passing through the interferometer for a given position of the mirrors. It consequently controls the **resolution** of the spectrum. The alignment of the mirrors of the interferometer is continuously controlled (and corrected if necessary) using the interference pattern produced by a laser beam passing through the interferometer.

For the present study, three different standard commercial spectrometers were used: a Spectrum GX by Perkin-Elmer® at CeCoMO, Villeurbanne, France, a Nicolet iS10 by Thermo Scientific® at WW3, Erlangen, Germany, and a IFS125HR by Bruker® at Synchrotron Soleil, Saint-Aubin, France (see Fig. 2.8). The first one was used for mid-infrared (MIR) measurements and some far-infrared (FIR) tests, the second one was used for MIR measurements, and the third one was used for FIR measurements.

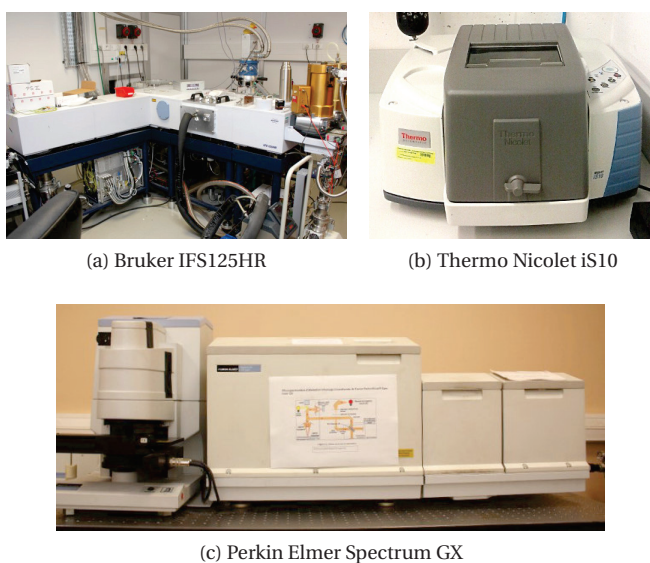
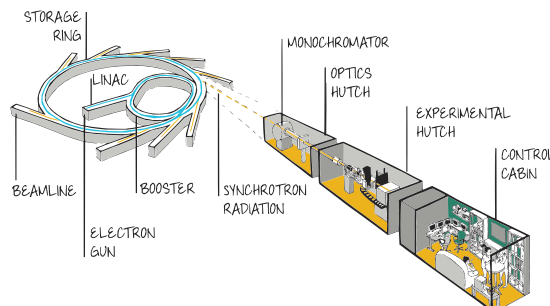


**Figure 2.8** ◀  
Photographs of the different spectrometers used in this study.

Thermal IR sources suffer from a lack of intensity and stability in the FIR domain [Griffiths and De Haseth, 2007]. Moreover, atmospheric water vapor highly absorbs in this domain, and standard laboratory deuterated triglycine sulfate (DTGS) detectors are not very sensitive. For all these reasons, it is a delicate task to perform FIR measurements using a standard laboratory equipment. To avoid those troubles, we took benefits from **synchrotron radiation** and the associated high quality equipment to investigate FIR absorption. Measurements were performed on the AILES beamline of synchrotron Soleil, Saint-Aubin, France. In a synchrotron, a current of free electrons (500 mA in Soleil) circulates inside a storage ring. The infrared radiation is produced by accelerating the electron beam using a bending magnet (see Fig. 2.9) [Dalla Bernardina, 2015, Synchrotron Soleil, 2017]. The produced radiation has a broad spectrum, extending from terahertz (THz) domain to X-rays. Most of the time, only X-rays are used in synchrotrons. In that case, a monochromator is used to select the spectral range of interest. For the AILES beamline, the THz and IR components of the radiation are simply extracted using a mirror. The radiation has a high and very stable intensity that suits very well for measurements. This radiation is then directed inside a Bruker

IFS125HR spectrometer. This is a high precision spectrometer used in vacuum to prevent atmospheric absorption, and used in combination with a helium-cooled **silicon bolometer**. This kind of thermal detector is between one and two decades more sensitive than standard DTGS detectors. A 6  $\mu\text{m}$ -thick Mylar (polyethylene terephthalate) beamsplitter, that allows measurements from 20 to 600  $\text{cm}^{-1}$ , was used.

**Figure 2.9** ▶ Use of the synchrotron radiation as an IR source. The IR radiation is produced by accelerating the electron beam with a bending magnet placed on the storage ring. Both pictures are taken from [Synchrotron Soleil, 2017].



(a) Cartoon of a standard Synchrotron beamline



(b) A bending magnet

MIR measurements were performed using a standard thermal source, in combination with a room temperature DTGS detector and a potassium bromide (KBr) beamsplitter, allowing measurements from 370 to 7800  $\text{cm}^{-1}$  or from 400 to 4000  $\text{cm}^{-1}$  depending on the spectrometer used.

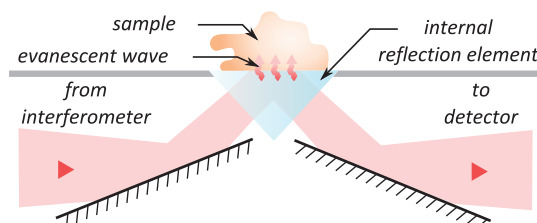
Synchrotron measurements were performed using the standard transmission method, by depositing the sample over a diamond window, that is almost transparent in all the IR domain. All other measurements were performed using the **Attenuated Total Reflection (ATR)** method, as described in the following paragraph.

## 2.2.2 Attenuated Total Reflection (ATR)

Attenuated Total Reflection is a technique that enables to study the **surface** of a material. The principle is the following. Using some mirrors, the IR beam is directed on an IR transparent crystal, called **Internal Reflection Element (IRE)**. This crystal is bevel-cut, so that the incident beam is normal to the incidence surface. The sample is deposited on the top surface of the crystal. The IR beam undergoes a **total reflection** on the top surface of the crystal, and the is directed to the detectors. During the reflection, an **evanescent wave** is created at the crystal/sample interface and the sample can absorb a part of the radiation (see Fig. 2.10).

IR lenses are also used on some systems but not on those studied there.

**Figure 2.10** ▶ Principle of ATR measurements.



The **penetration depth** of the wave through the sample, and thus the thickness of the analyzed area, denoted  $e$ , depends on the wavenumber and the relative **refraction indexes**  $n_1$  and  $n_2$  of the IRE and the sample, per the formula [Griffiths and De Haseth, 2007]:

$$e(\nu) = \frac{1}{2 \cdot \pi \cdot \nu \cdot n_1(\nu) \cdot \sqrt{\sin^2(\theta) - \left(\frac{n_2(\nu)}{n_1(\nu)}\right)^2}}, \quad \blacksquare \quad (2.6)$$

where  $\theta$  is the incidence angle on the sample, equal to 45° here. Since depth of penetration depends on the wavenumber, the absorption spectrum obtained using ATR is not identical to the one obtained by transmission. However, within a good approximation, the

transmission-equivalent absorbance  $A$  can be calculated using [Griffiths and De Haseth, 2007]:

$$A(\nu) = A_{\text{ATR}}(\nu) \cdot \nu, \quad \blacksquare \quad (2.7)$$

and thus, measurements performed using those two methods can be easily compared.

This technique is of particular interest for thin films. However, it is also commonly used for homogeneous highly absorbing solid or liquid materials: without any precaution, such samples would fully absorb the IR radiation in the transmission configuration, whereas it is only partially absorbed using ATR, since the IR beam only interacts with a thin layer of the sample. Since it is easy to use, it has become nowadays a standard method for IR investigations.

Two ATR accessories were used for measurements: a Silvergate accessory by Specac<sup>®</sup> and a DuraSamplIR II accessory by SensIR<sup>®</sup>. The IRE of the Silvergate accessory is a germanium crystal, enabling measurements from 550 to 5100  $\text{cm}^{-1}$  when used in combination with the Spectrum GX spectrometer, whereas the IRE of the DuraSamplIR II is a diamond, enabling measurements from 400 to 4000  $\text{cm}^{-1}$  when used in combination with the Nicolet iS10 spectrometer. Since the refraction indexes of germanium and diamond are different, the depth of penetration is not the same (less than 1  $\mu\text{m}$  with germanium and about 2  $\mu\text{m}$  with diamond), but this is not a problem here since we study only homogeneous thick materials. We are also developing another setup using a GladiATR accessory by Pike<sup>®</sup> to be used in combination with the Spectrum GX spectrometer. The IRE is made of diamond and is sealed on a temperature-regulated plate. It should in the end enable measurements from 160 to 7800  $\text{cm}^{-1}$ , between -196 and +210  $^{\circ}\text{C}$  [Müller et al., 2016]. Photographs of the different modules are shown on fig 2.11.

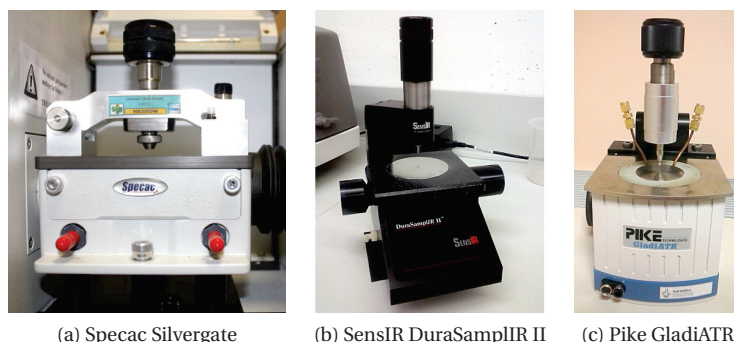


**Figure 2.11** ◀ Photographs of the different ATR accessories used in this study. The IRE of the Silvergate (a) is made of germanium whereas those of the DuraSamplIR II (b) and the GladiATR (c) are made of diamond.

Having a good contact between the sample and the IRE is essential for ATR measurements. For liquids, it is not a problem. In the case of clay samples, this was achieved by depositing a droplet of clay dispersed in water on the crystal surface and by letting it dry overnight.

### 2.2.3 Humidity and temperature control

Two setups were used to control the humidity and/or the temperature around the sample: a homemade atmospheric pressure humidity controller for ATR measurements, and the vacuum humidity controller of the AILES beamline used in combination with a helium closed-circuit cryostat for transmission measurements. The first setup consists in a closed air circuit (see Fig. 2.12). A lid isolates the sample area from atmosphere over the ATR accessory. Then, using a simple membrane air pump, the humidity of the air surrounding the sample is controlled by passing through a water-glycerol mixture. As explained in Chap. 1, depending on the relative ratio of water and glycerol, one can adjust the equilibrium vapor partial pressure, and thus the relative humidity. The main advantages of this setup is that it is cheap and easy to use, and the IR beam does not pass through the humid area, avoiding parasite absorption. Moreover, this setup should fit in the future the temperature controlled ATR to have both humidity and temperature control. One disadvantage is that low humidity ratios are hard to access: a slight variation of the amount of water in the mixture highly modifies the equilibrium vapor pressure at low water contents.

The lid is maintained over the sample using the anvil of the ATR accessory.

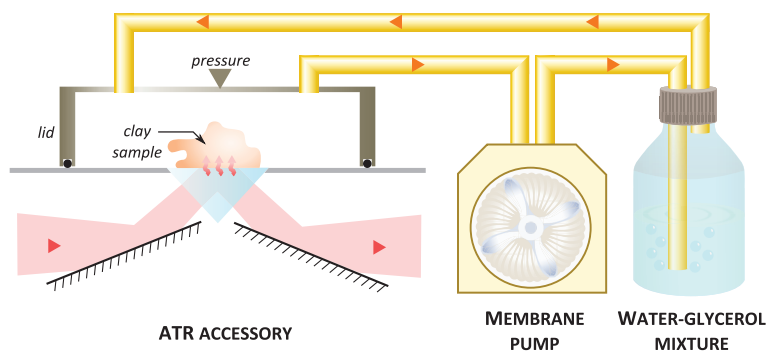
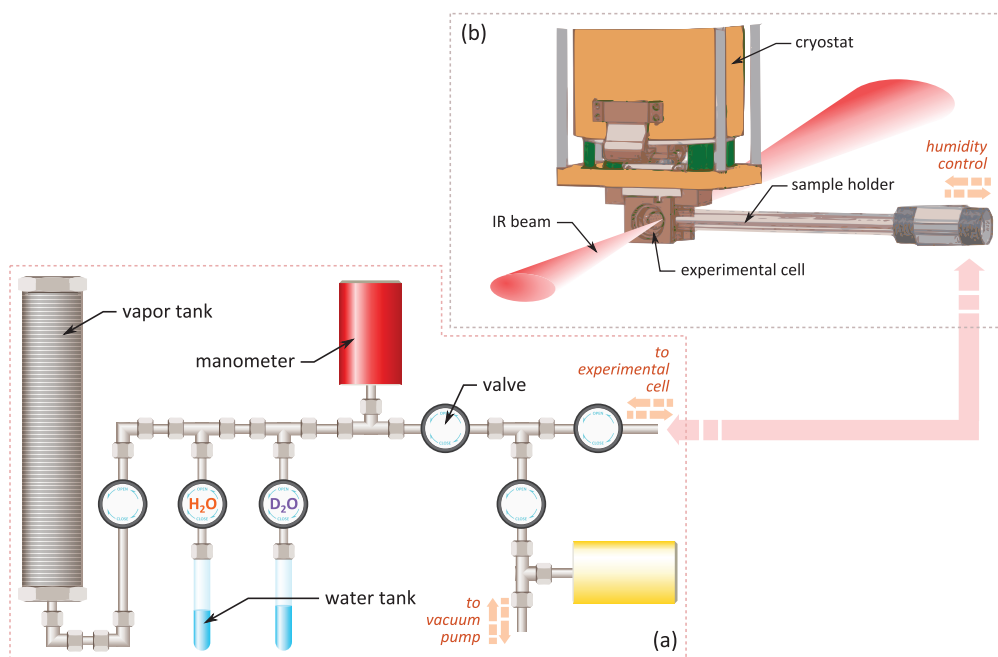


Figure 2  
Homema  
ATR mea

Figure 2.13 ▶  
Vacuum humidity (a) and temperature (b) controllers for transmission measurements. Picture (b) was freely adapted from [Dalla Bernardina et al., 2014]



The second setup (see Fig. 2.13) is made of a vacuum chamber enclosed by polypropylene (IR transparent) windows positioned on the beam path [Dalla Bernardina et al., 2014]. A water reservoir and a vacuum pump are plugged on the chamber, and isolated from the cell by valves. First the chamber is purged of all air and water until a high vacuum of  $10^{-4}$  mbar is obtained. Then, the humidity can be adjusted by opening one of the two valves to add or remove water vapor. The vapor pressure can be directly followed using precision manometers since water is the only gas present in the chamber. A vapor tank enables to increase the volume of the setup to make the adjustment of the vapor pressure easier. The main advantage of this setup is to enable to work at any water pressure with a high flexibility (in the first setup, the corresponding water-glycerol mixture must be prepared), and low humidity rates can be easily reached very quickly. The main disadvantage is that there is vapor on the beam path, which implies post-corrections on spectra. Moreover, water can freeze on the windows of the cell and thus on the beam path during low temperature measurements. On this setup, the temperature of the sample can be regulated down to 4 K using a helium closed-circuit cryostat coupled to a resistor and a PID controller.

Low temperature and humidity controlled measurements are reported in Chap. 6. The end of the chapter is devoted to molecular simulations.

## 3 Classical and ab initio molecular dynamics

### 3.1 Molecular dynamics

#### 3.1.1 Basic principles

Molecular dynamics methods [Frenkel and Smit, 2001, Allen and Tildesley, 1989] are **computer simulations** that aim to reproduce the dynamics of a system at the **atomic scale**. Basically, the system is modelled by a set of points, each point representing an atom, or at least its nucleus, with a mass and a charge (possibly zero, and possibly delocalized). The motion of these points is then described using the laws of **classical mechanics**, using a discrete representation of time. Note that, in some cases, nuclear motion can be computed using quantum mechanics. This is for example the case of the so-called Path Integral Molecular Dynamics (PIMD) formalism, but such methods are beyond the scope of this manuscript [Marx and Parrinello, 1996]. Thus, the routine of a molecular dynamics calculation is structured as follows:

1. for a given set of atomic positions at timestep  $t_i$ , compute the forces between atoms;
2. integrate the equations of motion to get positions at timestep  $t_{i+1} = t_i + dt$ ;
3. iterate.

The computation of forces can be performed using different methods. We will present two of them in the next two sections. For the moment, we just assume that we succeeded to get the total force  $f_j(t_i)$  acting on atom  $j$  at timestep  $t_i$ . The standard approach to integrate the equations of motion is to use the **Verlet algorithm**. This algorithm is based on a Taylor expansion of the atomic coordinates  $\vec{r}_j$  with respect to time. By combining:

$$\vec{r}_j(t_i + dt) = \vec{r}_j(t_i) + dt \cdot \frac{d\vec{r}_j}{dt}(t_i) + \frac{(dt)^2}{2} \cdot \frac{d^2\vec{r}_j}{dt^2}(t_i) + \frac{(dt)^3}{6} \cdot \frac{d^3\vec{r}_j}{dt^3}(t_i) + O((dt)^4) \quad \blacksquare \quad (2.8)$$

and:

$$\vec{r}_j(t_i - dt) = \vec{r}_j(t_i) - dt \cdot \frac{d\vec{r}_j}{dt}(t_i) + \frac{(dt)^2}{2} \cdot \frac{d^2\vec{r}_j}{dt^2}(t_i) - \frac{(dt)^3}{6} \cdot \frac{d^3\vec{r}_j}{dt^3}(t_i) + O((dt)^4), \quad \blacksquare \quad (2.9)$$

one gets:

$$\begin{aligned} \vec{r}_j(t_i + dt) &= 2 \cdot \vec{r}_j(t_i) - \vec{r}_j(t_i - dt) + (dt)^2 \cdot \frac{d^2\vec{r}_j}{dt^2}(t_i) + O((dt)^4) \\ &= 2 \cdot \vec{r}_j(t_i) - \vec{r}_j(t_i - dt) + \frac{\vec{f}_j(t_i)}{m_j} \cdot (dt)^2 + O((dt)^4), \end{aligned} \quad \blacksquare \quad (2.10)$$

where we replaced the second time derivative of the position by the force acting on the atom of mass  $m_j$  using the second Newton law. The position  $\vec{r}_j$  at timestep  $t_{i+1}$  can be thus be expressed as a function of atomic coordinates and forces at timesteps  $t_i$  and  $t_{i-1}$ . By subtracting the two Taylor expansions, one gets a similar expression for the atomic velocities:

$$\vec{v}_j(t_i) = \frac{\vec{r}_j(t_i + dt) - \vec{r}_j(t_i - dt)}{2 \cdot dt} + O((dt)^2). \quad \blacksquare \quad (2.11)$$

It can be surprising to see that this relation uses the positions at timestep  $t_{i+1}$  to compute the velocities at timestep  $t_i$ . However, as the velocities are not required to compute the positions, it is not a problem. Typical timestep used in the case of aqueous systems are 0.5 or 1 fs. This is necessary in particular for water since hydrogen atoms are light and thus move quite fast with respect to other atoms. This algorithm ensures a good stability of the energy of the system during the simulation. Thus, as the energy, the volume and the number of particles in the system are constant, such algorithm mimics the **microcanonical statistical ensemble** and is usually referred to as *NVE* simulation.

Note that the molecular dynamics library used in the present study (LAMMPS) uses a variant of this algorithm, called "velocity Verlet algorithm".

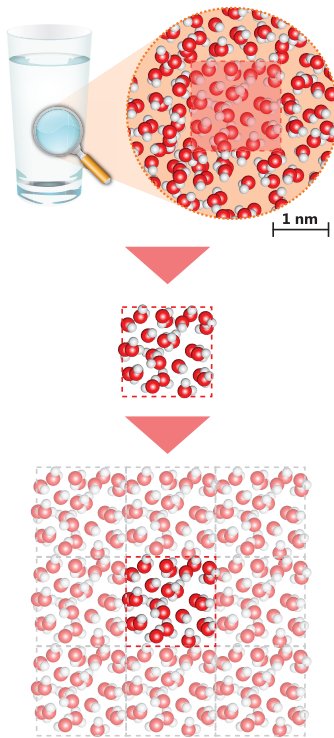
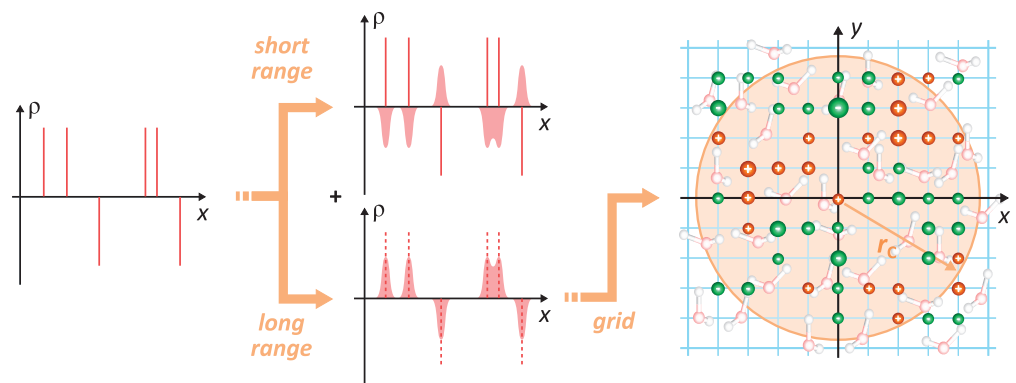


**Figure 2.14** ▲  
Cartoon of the construction of a molecular dynamics system. To mimic a real system, one isolates a small part of it and reproduces it periodically at infinite.

**Figure 2.15** ►  
PPPM method applied to Coulombic interactions. The distribution of punctual charges (the atomic partial charges, Dirac distributions) is superimposed to a smooth distribution with opposite charge. This distribution creates a short-ranged potential so that interactions can be computed using a cutoff. Then using the superposition principle, an opposite term is added to the distribution to get back the real distribution. This distribution creates a long-ranged smooth potential. To calculate its effect, the distribution is sampled over a grid and transposed in Fourier space where it generates a short-ranged potential that is also evaluated using a cutoff.



For the moment, we did not assess the question of “experimental” conditions. In a real experiment the system has an environment which controls its temperature and volume or pressure. It is the object of the next paragraph.

### 3.1.2 Reproducing experimental conditions with thermostats and barostats

Various methods have been developed to mimic **thermostats** and/or **barostat** to reproduce different statistical ensembles and simulate real experimental conditions. The most popular are the thermostat by **Nose and Hoover** and the barostat by **Hoover and Andersen** [Martyna et al., 1994]. Those two algorithms were respectively used in calculations to reproduce the **isothermal-isochoric ensemble** ( $NVT$ ) or the **isothermal-isobaric ensemble** ( $NpT$ ).

First, we need to define the temperature and the pressure of the system from an atomic point of view. From the **equipartition theorem**, one knows that each degree of freedom has

The computational cost of molecular dynamics depends, of course, on the size of the system, *i.e.* the number of atoms, and it also depends on the complexity of the method used to compute forces. In the simplest cases, the maximum number of atoms used in a simulation can reach one million. Typical simple simulations will use about one hundred thousand atoms which corresponds to a typical system size below 100 nm. It rises two main problems: first, it is far from a real macroscopic system, and one can expect **finite size effects** to influence the dynamics of the system, and secondly, one must find **boundary conditions** that do not add spurious effects. To limit those problems, the system is duplicated periodically in all directions to mimic an infinite size system (see figure 2.14). It means that one only needs to compute the positions of the  $N$  atoms of the simulation box, but the interactions with atoms from all replicas are taken into account in the calculation. But considering an infinite size system immediately introduces a new problem: interactions cannot be computed for an infinite number of atoms.

Two different strategies are used in practice to avoid that. In the case of **short-ranged interactions** (for example, Van der Waals interactions whose amplitude is proportional to  $1/r^6$  where  $r$  is the distance between atoms), one approach is to use a **cutoff radius**. This means that interactions are only computed between atoms separated by a distance lower than the cutoff, and the **long-tail part** of the interaction is neglected. In the case of **long-ranged interactions** (for example, Coulombic interactions decrease like  $1/r$ ), this approximation cannot stand. In that case, a common way to calculate long-ranged interactions is to use the so-called **Particle-Particle Particle-Mesh (PPPM) method**, or the **Ewald method**. The basic idea is the same. Here we describe only the PPPM method that was mostly used in the present work, in the case of Coulombic interactions. The distribution of charges is decomposed, using the superposition principle, in a “purely” short-ranged part and a “purely” long-ranged part. The short-ranged part can be then computed as explained before using a cutoff. The long-ranged part, which is rather smooth at the simulation box length scale, is sampled on a grid. Then the charge distribution is transposed in the Fourier space where interactions are short-ranged, and can be computed using a cutoff. The method is illustrated on figure 2.15.

an average energy equal to  $k_B \cdot T/2$ , with  $k_B$  the Boltzmann constant. Since a 3-d isolated system made of  $N$  punctual atoms has  $3 \cdot N - 3$  degrees of freedom, the temperature of the system can be evaluated from the total kinetic energy – and thus from the atomic velocities – of the system following the formula:

$$\frac{3 \cdot N - 3}{2} \cdot k_B \cdot T = \frac{1}{2} \cdot \sum_{j=1}^N m_j \cdot \vec{v}_j^2. \quad \blacksquare \quad (2.12)$$

Pressure is usually evaluated using the **virial equation**, based on forces acting on atoms and their position:

$$p = \frac{N \cdot k_B \cdot T}{V} + \frac{1}{3 \cdot V} \cdot \sum_{j=1}^N \sum_{k=1}^j \vec{f}_{jk} \cdot \vec{r}_{jk}, \quad \blacksquare \quad (2.13)$$

where  $\vec{f}_{jk}$  and  $\vec{r}_{jk}$  denote respectively the force acting and the distance between atoms  $j$  and  $k$  (for pairwise interactions).

Now that we have a way to compute the temperature and the pressure using atomic coordinates and velocities, we can see how to fix them. The method by Nose and Hoover consists in adding a **fictitious degree of freedom** to the system, with its own mass and momentum, that can exchange kinetic energy with other degrees of freedom – so other atoms – to adjust the temperature of the system. The coupling is realized by adding a force acting on atoms, the momentum is adjusted on the fly at each timestep to get the correct temperature, and the mass governs the inertia of the thermostat. This mass must be adjusted so that the typical evolution timescale of the temperature of the system approaches molecular timescales. If this typical timescale is too long, the system will need a long time to equilibrate, and the system will not be thermostatted efficiently (for instance heat generated in flow conditions will not be removed fast enough). On the contrary, if this time is too short, the dynamics of the system will be affected by the thermostat, and the dynamics may become unstable. In a similar manner, the method by Hoover and Andersen adds a fictitious degree of freedom that couples with the volume of the system, *i.e.* the simulation box size. In this case, the momentum associated to this degree of freedom is adjusted to get the right pressure.

In all calculations performed here, the implementation of these methods is achieved using the Martyna *et al.* formulation [Martyna et al., 1994], which is based on the Verlet algorithm.

### 3.1.3 Structural and dynamical measurements

Numerous structural and dynamical observables can be calculated from atomic coordinates, velocities and pair forces. We already met two examples in the previous paragraph: the temperature and the pressure of the system. In the following paragraph, we will see how to compute some other quantities that will be useful in the next chapters. Generally speaking, measurements are performed in the  $NVE$  ensemble after a sufficient equilibration time in the  $NpT$  ensemble to ensure the system reaches a steady state. However, they can change from one measurement to another, we will systematically precise in the upcoming chapter the conditions used for the corresponding calculations.

**Structural measurements** The simplest structural observable is the **mass density** of the system. It is computed as the ratio between the global mass of particles lying inside the simulation box over the volume of the box. This is of course an important information but it tells us nothing about the **local structure** of the system. The latter can be described using the so-called **radial distribution function**, denoted  $g(r)$  [Frenkel and Smit, 2001]. This observable, which can be obtained using X-ray or neutron diffusion, gives the evolution of the local density of the system with respect to the distance to a given atom. This means, for a given tolerance  $dr$ ,  $g(r)$  is computed as the density of the volume enclosed between the spheres centered on the reference atom and of radius  $r$  and  $r + dr$  (see Fig. 2.16). Partial  $g(r)$  can also be computed, for example to get the distribution of oxygen-oxygen distances inside water.

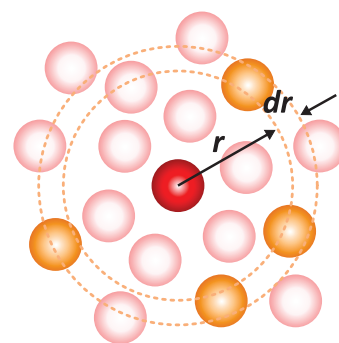


**Figure 2.16** ▲ Evaluation of  $g(r)$  relative to the red atom.

**Viscoelasticity.** We will later focus on various other bulk observables, including the **self-diffusion coefficient** of water  $D$ , its **shear viscosity**  $\eta$  and **high frequency elastic modulus**  $G$ . The self-diffusion coefficient  $D$  can be computed at equilibrium from the slope of the atomic **mean square displacement** versus time curve at long times (*i.e.* in diffusive regime) [Frenkel and Smit, 2001]:

$$D = \frac{1}{6} \cdot \lim_{t \rightarrow \infty} \frac{d \langle (\vec{r}(t) - \vec{r}(0))^2 \rangle}{dt}. \quad \blacksquare \quad (2.14)$$

Since  $D$  is highly influenced by **long-ranged hydrodynamic interactions**, it depends on the simulation box size. To subtract these finite size effects,  $D$  can be extrapolated for an infinite box size using the scaling relation [Yeh and Hummer, 2004, Tazi et al., 2012]:

$$D(L) = D_\infty + \frac{\xi}{L}, \quad \blacksquare \quad (2.15)$$

where  $L$  is the length of the simulation box and  $\xi$  is a constant that depends for example on the viscosity and the temperature. No box size effects are observed for the other quantities considered here, as detailed for instance in Chap. 3.

The shear viscosity can be calculated – at equilibrium – within the **Green-Kubo formalism** [Frenkel and Smit, 2001]:

$$\eta = \frac{V}{k_B \cdot T} \cdot \int_0^\infty \langle p_{ij}(0) \cdot p_{ij}(t) \rangle \cdot dt, \quad \blacksquare \quad (2.16)$$

where  $p_{ij}$  is one of the five independent components of the traceless stress tensor:  $p_{xy}$ ,  $p_{xz}$ ,  $p_{yz}$ ,  $(p_{xx} - p_{yy})/2$  and  $(p_{yy} - p_{zz})/2$  [Alfe and Gillan, 1998],  $V$  the volume of the simulation box,  $k_B$  the Boltzmann's constant and  $\langle \cdot \rangle$  denotes an ensemble average over the different replicas. Of course, one cannot perform an infinite time measurement. That means the integral must be computed over a finite time interval, that must be long enough so that the result is converged, *i.e.* invariant when longer time domains are used.

The viscosity can also be computed within **stationary shear flow conditions**. Let us consider the fluid is enclosed between two rigid parallel walls moving with opposite tangential velocities. The viscosity can be computed from the **shear rate**  $\dot{\gamma}$  of the fluid (obtained as the slope of the fluid velocity versus distance to walls) and the **shear stress**  $\sigma$  applied on the walls (*i.e.* the total force acting between water and wall atoms per unit of surface in the direction of the flow) as (see Fig. 2.17):

$$\eta = \frac{\sigma}{\dot{\gamma}}. \quad \blacksquare \quad (2.17)$$

Finally, the **Maxwell viscoelastic relaxation time**  $\tau_M$  and the infinite frequency shear modulus can be extracted from the equilibrium autocorrelation function of the stress tensor components by fitting it with a **stretched exponential decay**:

$$\frac{V}{k_B \cdot T} \cdot \langle p_{ij}(0) \cdot p_{ij}(t) \rangle = G_\infty \cdot \exp\left(\left(-\frac{t}{\tau_M}\right)^\gamma\right). \quad \blacksquare \quad (2.18)$$

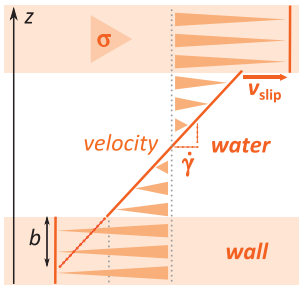


**Figure 2.17** ▲  
Evaluation of  $\eta$  and interfacial properties under stationary flow.

We will also focus on **surface hydrodynamics properties**, such as the **slip length**  $b$  and the **interfacial friction coefficient**  $\lambda$ . As in the case of the shear viscosity, those observables can be computed at equilibrium or under stationary flow. Under flow, the friction coefficient  $\lambda$  is calculated from the **slip velocity**  $v_{\text{slip}}$ , *i.e.* the tangential velocity jump at the liquid-solid interface, and the shear stress  $\sigma$  applied to the walls per  $\sigma = \lambda \cdot v_{\text{slip}}$  (see Fig. 2.17). At equilibrium, the friction coefficient is calculated using the Green-Kubo formula by Bocquet and Barrat [Bocquet and Barrat, 1994]:

$$\lambda = \frac{1}{A \cdot k_B \cdot T} \cdot \int_0^\infty (dt \cdot \langle \vec{F}_w^\parallel(0) \cdot \vec{F}_w^\parallel(t) \rangle), \quad \blacksquare \quad (2.19)$$

where  $A$  denotes the surface of the wall and  $\vec{F}_w^\parallel$  the total tangential force applied to the wall. Then in both cases, the slip length is obtained using  $b = \eta/\lambda$ , with  $\eta$  the shear viscosity of the liquid, determined using one of the methods previously mentioned.

**Vibrational properties** Vibrational properties computation can be of great interest to help identification of the components of experimental spectra. The **IR absorption spectrum** can be approximated numerically using the molecular dipole moments  $\vec{\mu}$  [Thomas et al., 2013]:

$$A(\nu) \propto m \cdot \nu^2 \cdot \int_0^\infty \langle \vec{\mu}(\tau) \cdot \vec{\mu}(t + \tau) \rangle_\tau \cdot e^{i \cdot \nu \cdot t} \cdot dt, \quad \blacksquare \quad (2.20)$$

where  $A(\nu)$  denotes the absorbance at the frequency  $\nu$ ,  $m$  the reduced mass of molecules and  $\langle \cdot \rangle_\tau$  denotes a time-average. Then, using the Wiener-Khintchine theorem, this formula can be simplified in the following way:

$$A(\nu) \propto m \cdot \nu^2 \cdot \sum_{\alpha}^{\{x,y,z\}} |\mathcal{F}[\mu_\alpha(t)]|^2, \quad \blacksquare \quad (2.21)$$

where  $\mathcal{F}[X]$  is the time Fourier transform of  $X$ . As we will see at the end of this section, the charge of the oxygen atom is not localized at the same position as the atom when using the TIP4P/2005f force field for calculations. In that case, the dipole moment of water molecules is post-processed from atomic coordinates using the real position of the charges. Then the absorption spectra are calculated using a homemade routine based on the FFTW3 library [Frigo and Johnson, 2005].

Another related quantity is the **vibrational density of state** (VDOS). It corresponds to the vibrational spectra of the system, without any selection rule. It can be obtained experimentally from neutron scattering experiments, and can be approximated numerically in a similar manner as the infrared spectrum, using the atomic velocities instead of the molecular dipole moments [Thomas et al., 2013].

We already mentioned several times the forces acting between atoms. We will now see how to compute them.

## 3.2 Computing forces (I): density functional theory

Density functional theory consists in computing the **potential energy surface** of the atoms – and thus the forces – directly from the **electronic structure**. It means consequently that this structure must be computed for each set of atomic positions, so, at each iteration. We will first give the main ideas of this method, then say a few words about its implementation, and finally review briefly its use with water. We refer the reader to textbooks such as Refs. [Sholl and Steckel, 2011, Koch and Holthausen, 2015] for more details on density functional theory.

### 3.2.1 Density functional theory in a nutshell

**Electron density.** We saw previously that electrons are described by wave-functions. For a system of  $M$  atoms and a total of  $N$  electrons, an accurate determination of the electron distribution would consist in solving a  $(N + M)$ -body problem. We said this is practically impossible for a single molecule, thus, this is also impossible for a more complex system. This problem must consequently be simplified. Since we want to determine the electron distribution for a given set of nucleus positions, we implicitly work within the framework of the **Born-Oppenheimer approximation**. Two other major approximations are that we consider the system is in its **ground-state** and express the ground-state wavefunction as a product of mono-electronic wavefunctions (**orbital approximation**). We already showed this means neglecting electronic structure fluctuations, that play a key role in molecular interactions (dispersion interaction).

Within those approximations, the electron distribution is expressed in terms of its **density function**:

$$n(\vec{r}) = 2 \cdot \sum_{i=1}^N \psi_i^*(\vec{r}) \cdot \psi_i(\vec{r}), \quad \blacksquare \quad (2.22)$$

where  $\psi_i$  is the mono-electronic wave-function associated to the  $i^{\text{th}}$  electron. The density functional theory relies on two theorems, by **Kohn and Hohenberg**:

1. the ground-state energy from Schrödinger's equation is a unique functional of the electronic density;
2. the electronic density that minimizes the energy of the functional is the true electron density corresponding to the full solution of the Schrödinger equation.

This means one can express the energy of the system by a **functional** of  $n(\vec{r})$  and that, when this functional is known, the electron density can be determined by minimizing this functional. From this, density functional theory can be summarized in an unique question: what is this functional? There is no answer and it must be postulated.

**Energy functional.** Re-expressing the Schrödinger equation in terms of mono-electronic wave-functions  $\psi_i$ , one gets the so-called **Kohn and Sham equations**:

$$\left[ -\frac{\hbar^2}{2 \cdot m_e} \cdot \vec{\nabla}^2 + V(\vec{r}) + e^2 \cdot \int \frac{n(\vec{r}')}{|\vec{r} - \vec{r}'|} \cdot d\vec{r}' + \frac{\delta E_{XC}(\vec{r})}{\delta n(\vec{r})} \right] \psi_i(\vec{r}) = E_i \cdot \psi_i(\vec{r}). \quad \blacksquare \quad (2.23)$$

The terms in brackets constitute the **energy functional**. From the Schrödinger equation, we recognize the kinetic energy within the first term, and the second term contains Coulombic interactions between the electron and the nucleus. The two other terms correspond to electron-electron interactions. The first is called the **Hartree potential** and represents the Coulombic repulsion between electrons (including electron with itself), and the second is called **exchange-correlation functional** and contains all other information about electron interactions, including the correction of the self-interaction term present in the Hartree potential. But as we already said, no one knows how to express this term. Defining efficient exchange-correlation functionals is a very active field of research. It exists many families of such functionals corresponding to various approximations, called Local-Density Approximation (LDA), Generalized-Gradient Approximation (GGA), meta-GGA..., corresponding to various degrees of refinement. Of course, the most refinement are included inside the functional, the most precise it is expected to be, but also the most computational cost is required.

In various systems and especially in water, a major issue is to describe correctly dispersion interactions. There are mainly two ways to do so: by refining the exchange-correlation functional with respect to electron correlation – this kind of functional is called **dispersion-inclusive functional** – or by applying corrections to the potential energy surface after the DFT calculation using a standard functional (by adding for example  $1/r^6$  terms) – one speaks in that case of **dispersion-corrected functional**.

For the moment, we said nothing about the way to calculate the electron density. We will give some elements in the next paragraph.

### 3.2.2 Implementation

The Kohn and Sham equations are resolved iteratively through a **self-consistent field** approach:

1. define a trial electronic density  $n_0(\vec{r})$ ;
2. determine the corresponding mono-electronic wavefunctions using the Kohn and Sham equations;
3. compute the new electronic density  $n_1(\vec{r})$ ;
4. if  $n_0(\vec{r})$  and  $n_1(\vec{r})$  are identical, then it is the ground-state electron density; otherwise, update  $n_0(\vec{r})$  and iterate.

Various methods are used in practice to save computational time during this procedure. First, only the wavefunctions of valence electrons are directly computed. Core electrons are considered through a so-called **pseudo-potential** directly added to the electron density. Secondly, both wave-functions and electron density are projected on **basis of trial functions**. In the present study, we used the CP2K/Quickstep library for DFT calculations [VandeVondele et al., 2005a]. This library uses the **Gaussian and Plane-Wave method** (GPW).

The basis used for the electron density is made of a family of Gaussians, whereas the one used for the wavefunctions is made of plane-waves. Bases have a finite size, that implies wavefunctions and electron density have a finite precision. The precision of the bases is setup in the calculation by specifying the spatial frequency  $k_{\text{cut}}$  of the finest plane-wave. In practice, this frequency is given in terms of **energy cutoff**:  $E_{\text{cut}} = \hbar^2 \cdot k_{\text{cut}}^2 / (2 \cdot m_e)$ . A high cutoff means a high computational cost, but a low cutoff can induce a non-negligible error in the energy calculation. Thus, the energy cutoff value must be optimized for each calculation so that it is the lowest value that gives converged results, *i.e.* results do not change if a higher value is used.

### 3.2.3 DFT and water

We conclude this section by a brief review of the use of DFT to describe water. Since the pioneering work by Car and Parrinello [Car and Parrinello, 1985, Laasonen et al., 1993, Sprik et al., 1996], DFT has been used to describe a great variety of phenomena implying aqueous systems, such as reactivity [Tocci and Michaelides, 2014, Sulpizi et al., 2012, Mundy and Kuo, 2006, Joly et al., 2016], friction [Tocci et al., 2014] or structure and dynamics [Lee et al., 2014, Ambrosetti et al., 2012, Cicero et al., 2008, Pedroza et al., 2015, Feibelman, 2013, Demontis et al., 2013, Rana and Chandra, 2013, Mignon et al., 2010] near a solid-liquid interface, liquid/vapor equilibrium [McGrath et al., 2006, Kuo et al., 2006, Baer et al., 2011, Choudhuri and Chandra, 2014, Kühne et al., 2010, Kuo and Mundy, 2004], water dissociation and ionic transport [Tuckerman et al., 2002, Tuckerman et al., 2006, Chen et al., 2002b, Megyes et al., 2008, Chen et al., 2002a, Buch et al., 2007, Baer et al., 2014, Asthagiri et al., 2004, Baer and Mundy, 2011, Tuckerman et al., 1995, Baer and Mundy, 2013, Bankura et al., 2013]. Extensive work has also been performed to characterize the performance of exchange-correlation functionals to describe liquid water and clusters of molecules [Klimeš and Michaelides, 2012, Gillan et al., 2016], using different static observables like the liquid density [Spura et al., 2015, Miceli et al., 2015, Gaiduk et al., 2015, Del Ben et al., 2013, McGrath et al., 2011], the pair correlation function [Alfè et al., 2014, Wang et al., 2011, VandeVondele et al., 2005b, Todorova et al., 2006], the hydrogen bond angle distribution [DiStasio Jr et al., 2014, Møgelhøj et al., 2011], but also dynamical observables like the self diffusion coefficient [Corsetti et al., 2013, Ma et al., 2012, Jonchiere et al., 2011] or the infrared absorption spectrum [Lee and Tuckerman, 2007, Grossman et al., 2004, Zhang et al., 2011]. It is well known that simple GGA functionals like BLYP or PBE over-structure water and under-predict the density and self diffusion [Gaiduk et al., 2015, Wang et al., 2011, DiStasio Jr et al., 2014]. Various approaches have been tested to improve those results, such as including dispersion terms in the functional [Spura et al., 2015, Wang et al., 2011, Schmidt et al., 2009, McGrath et al., 2011], nuclear quantum effects (NQE) (through the use of the path integral formalism [Spura et al., 2015], or replacing H<sub>2</sub>O molecules by D<sub>2</sub>O for which nuclear quantum effects are much lower [DiStasio Jr et al., 2014, Gaiduk et al., 2015, Todorova et al., 2006]), or a fraction of exact exchange through hybrid functionals [Zhang et al., 2011, DiStasio Jr et al., 2014, Gaiduk et al., 2015, Todorova et al., 2006]. In each case, an improvement is observed, but the self diffusion coefficient remains too low. Moreover, cumulative inclusion of both NQE and dispersion improves negligibly the accuracy of calculations with respect to calculations where only dispersion is taken into account [Spura et al., 2015]. Another common approach is to increase the temperature with respect to experiments to compensate the slow dynamics observed. The temperature is generally chosen to reproduce a particular property of water (eg. the crystallization temperature [Yoo et al., 2009], the liquid density or diffusivity [Gaiduk et al., 2015, Joly et al., 2016] or the radial distribution function [Gaiduk et al., 2015, Jonchiere et al., 2011]) or to compensate NQE [DiStasio Jr et al., 2014], but highly depends on the functional and system considered. Thus, one can question the validity of this approach for heterogeneous systems. Moreover, for composite systems, the density is not necessarily equal to the bulk density, so that constant volume calculations might not be suitable. In Chap. 3, we will investigate the accuracy of constant pressure methods to describe the structure and dynamics of water.

### 3.3 Computing forces (II): point charge force fields

The potential energy surface computation using DFT requires at each timestep to solve Kohn and Sham equations using the iterative procedure previously described. That represents a lot of computational time. Thus, DFT can be applied only to small systems (typically a few hundred atoms) and very short times (typically a few tens of picoseconds). Even with such a small system, a simple molecular dynamics shear viscosity calculation typically lasts one month using 64 cores CPU. This considerably limits the possibilities of the method. For this reason, the use of classical force fields to compute the potential energy surface is very popular and the development of new force fields is still an active field of research. In this section, we will describe the key elements that constitutes force fields [Frenkel and Smit, 2001, Allen and Tildesley, 1989, Plimpton et al., 2005] and mention a couple of popular water models.

The key point of force fields approaches is the interaction energy between a group (*e.g.* a pair) of atoms has a fixed form that only depends on the relative positions of atoms within the group. There is thus no equation to solve to compute the potential energy surface. Thus, what is achieved within typically one minute using DFT requires only a fraction of second using force fields. For molecular systems, one distinguishes **intermolecular interactions** and **intramolecular interactions**. Most of the time, molecules are considered as rigid bodies, and thus intra-molecular interactions are not considered.

#### 3.3.1 Intermolecular interactions

Intermolecular interactions include Van der Waals interactions, hydrogen bonds, short-ranged electronic shell repulsion, and – if needed – Coulombic interactions.

Let us first consider non-Coulombic interactions. Generally speaking, interactions are usually decomposed as a sum of 2-, 3-, 4-body... terms. Most of the time, the 2-body term is the only term considered in the development. Thus, a common-use way to mimic interactions is to apply a **Lennard-Jones potential** between pairs of atoms (see Fig. 2.18):

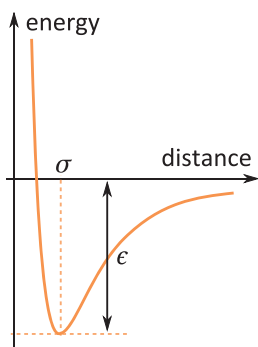


Figure 2.18 ▲  
The Lennard-Jones potential.

$$U_{LJ}(r_{ij}) = 4 \cdot \epsilon \cdot \left( \left( \frac{\sigma}{r_{ij}} \right)^{12} - \left( \frac{\sigma}{r_{ij}} \right)^6 \right), \quad \blacksquare \quad (2.24)$$

where  $r_{ij}$  is the distance between atoms  $i$  and  $j$ , and  $\epsilon$  and  $\sigma$  are constants depending on the type of atom considered. For an isolated pair of atoms,  $\sigma$  denotes the equilibrium distance between atoms and  $\epsilon$  the binding energy. The second term corresponds to Van der Waals interactions, whereas the first term is empirical and mimics short range repulsion.

Instead of defining  $\epsilon$  and  $\sigma$  for each pairs of atoms involved in the system, one usually defines atomic  $\epsilon$  and  $\sigma$  values. Pair values are then computed using so-called **mixing rules**. Here we use **Lorentz-Berthelot mixing rules**:

$$\begin{cases} \epsilon_{ij} = \sqrt{\epsilon_i \cdot \epsilon_j} \\ \sigma_{ij} = \frac{\sigma_i + \sigma_j}{2} \end{cases}, \quad \blacksquare \quad (2.25)$$

where  $x_i$  and  $x_j$  denote atomic values and  $x_{ij}$  denotes pair value. The determination of  $\epsilon$  and  $\sigma$  can be based on quantum mechanics calculations or can be empirical (for example adjusted to reproduce a specific property of the system).

The interaction potential can have a different form and include three-body (or more-body) terms, giving rise to an infinite variety of possible forcefields.

Coulombic interactions acts as two-body terms, using the standard formula:

$$U_{\text{coul}}(r_{ij}) = \frac{q_i \cdot q_j}{4 \cdot \pi \cdot \epsilon \cdot r_{ij}}. \quad \blacksquare \quad (2.26)$$

For monoatomic entities, there is *a priori* no trouble in the definition of  $q$  values. But in the case of polyatomic structures, one must attribute **partial charges** to atoms. As in the case of the Lennard-Jones parameters, this can be achieved using quantum mechanics calculations or empirically.

The potential energy surface is then computed as the sum of all contributions (Coulombic and non-Coulombic), eventually applying cutoffs as explained in section 3.1. The computational cost depends on the complexity of non-Coulombic interaction terms that are used. Typical simulations include between 10000 and 100000 atoms, during 1 million timesteps (*i.e.* 1 ns).

### 3.3.2 Intramolecular interactions

As we mentioned, a common approach is to consider a molecule as a rigid body. In that case, a specific algorithm, as for example the SHAKE method [Ryckaert et al., 1977], is required to compute the displacement of the molecule from the average atomic interactions. As we will consider flexible molecules, we will not develop this point. Details can be found in many textbooks [Frenkel and Smit, 2001, Allen and Tildesley, 1989].

Intramolecular interactions include, of course, all the terms previously mentioned. Those are treated exactly as in the case of intermolecular interactions. Here we only focus on terms that are specific to molecules.

Chemical bonds can be described using various ways. The most popular way is to model the bond by a harmonic spring, *i.e.* a harmonic potential:

$$U_{\text{harm}} = k \cdot (r_{ij} - r_0)^2, \quad \blacksquare \quad (2.27)$$

with  $k$  the strength of the spring and  $r_0$  its equilibrium length. Another popular way including anharmonicity is to use a Morse potential (see Fig. 2.19):

$$U_{\text{morse}} = D \cdot (1 - e^{-\alpha \cdot (r_{ij} - r_0)})^2, \quad \blacksquare \quad (2.28)$$

with  $\alpha$  and  $D$  two constants. Again,  $k$ ,  $r_0$ ,  $\alpha$  and  $D$  can be computed or chosen empirically.

For molecules with more than two atoms, as bonds are strongly coupled, three- (angles) or four-body (dihedral) terms can be added to the global interaction potential. For example, in water molecules, three body terms can be considered adding a harmonic potential on the HOH angle.

In some cases, the polarizability of the electronic shell of atoms can be considered, to create so-called polarizable force fields. Those force fields require more computational resources and are not considered in the present study. As we saw, the different terms that constitute force fields can be empirical, to reproduce a specific property of the system. For this reason, the geometry of molecules does not necessarily represent the real geometry. This is particularly true concerning water models, as we will see now.

### 3.3.3 A few water force fields

Various geometries have been considered to model numerically a water molecule [Guillot, 2002] (see Fig. 2.20). Of course, water can be modelled using three point charges for its three atoms (see Fig. 2.20a). It is the case of the very popular SPC (Simple Point Charge) force field [Berendsen et al., 1981] and its derivatives (SPC/f [Teleman et al., 1987], SPC/E [Berendsen et al., 1987]...), or the TIP3P [Jorgensen et al., 1983] (Transferable Intermolecular Potential 3 Points) force field. But it is common to change this geometry to consider the two oxygen lone pairs of electrons. This is achieved by delocalizing the charge of the oxygen atom on one or two massless points located on the HOH bisector in the case of one point, or organized in a tetrahedral geometry with hydrogen atoms in the case of two points. The geometry with one massless point (see Fig. 2.20b) gave rise to the TIP4P force field family (TIP4P [Jorgensen and Madura, 1985], TIP4P/Ew [Horn et al., 2004], TIP4P/2005 [Abascal and Vega, 2005], TIP4P/2005f [González and Abascal, 2011], E3B [Kumar and Skinner, 2008, Tainter et al., 2015] (Explicit Three Body)...), whereas the geometry with two massless sites (see Fig. 2.20d) is used in the TIP5P [Mahoney and Jorgensen, 2000] force field. Interestingly, although the TIP5P geometry seems to mimic more closely the real charge distribution in water molecules, the best results are obtained with models from the TIP4P family [Vega et al., 2009].

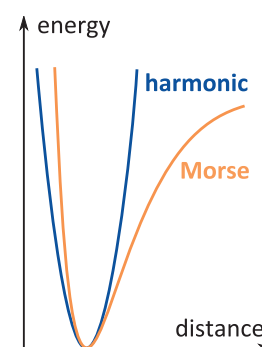
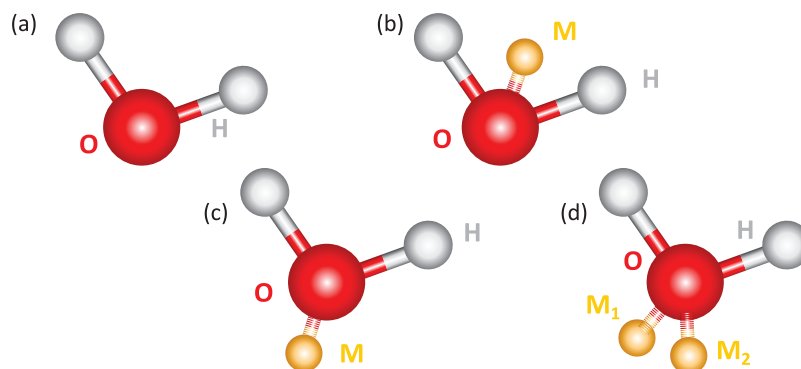
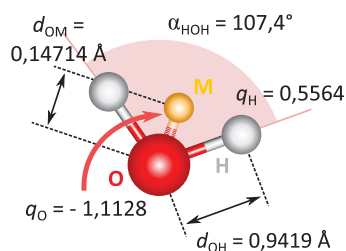


Figure 2.19 ▲ The harmonic and Morse potentials.



**Figure 2**  
Geometry  
for differ  
massless  
the oxyge  
of the ox



**Figure 2.21** ▲  
Geometry of the TIP4P/2005f wa-  
ter molecule.

The development of water force field reached a milestone a decade ago, with the apparition of amazingly accurate models. Those are the TIP4P/2005 force field, and two related models: the rigid E3B model and the flexible TIP4P/2005f model. Those two latter are considered as the most accurate existing force fields to this day [Vega et al., 2009, Vega, 2015, Tainter et al., 2015], and we will see in the next chapters some proofs concerning the TIP4P/2005f force field. Nevertheless, we will also see that they have limits. Those three models have the geometry (b) shown on figure 2.20. In the TIP4P/2005 force field, molecules are rigid and interact through a Lennard-Jones potential applied between oxygen atoms only (and of course a Coulombic potential) [Abascal and Vega, 2005]. In its flexible derivative, the TIP4P/2005f force field, O–H bonds are modeled using a Morse potential and three-body interactions are considered by applying a harmonic potential to HOH angles [González and Abascal, 2011]. The E3B model use the TIP4P force field parametrization (the same as TIP4P/2005 but with other parameters), and add two and three body intermolecular corrections to the pair Lennard-Jones potential [Kumar and Skinner, 2008, Tainter et al., 2015].

All the following study will be performed using the TIP4P/2005f force field. We summarized its parameters in Table 2.1 and figure 2.21. Details about the parametrization of the other models mentioned can be found in the corresponding referenced papers.

**Table 2.1** ►  
TIP4P/2005f force field geome-  
try and parameters and compar-  
ison to tabulated geometry of  
water molecules in liquid phase  
at room temperature/atmospheric  
pressure (from [González and Abas-  
cal, 2011]).

Parameter	TIP4P/2005f	Experiments
$M_O$ ( $\text{g} \cdot \text{mol}^{-1}$ )	15.9994	15.9994
$M_H$ ( $\text{g} \cdot \text{mol}^{-1}$ )	1.008	1.008
$q_O$	$-1.1128 \cdot e$	–
$q_H$	$0.5564 \cdot e$	–
$d_{OH}$ (Å)	0.9419	0.9584
$d_{OM}$ (Å)	1.147144	–
$\alpha_{HOH}$ (°)	107.4	104.45
$\epsilon_{OO}$ ( $\text{kcal} \cdot \text{mol}^{-1}$ )	18.52	–
$\epsilon_{HH}$ ( $\text{kcal} \cdot \text{mol}^{-1}$ )	0.0	–
$\sigma_{OO}$ (Å)	3.1644	–
$\sigma_{HH}$	0.0	–
$r_c^{LJ}$ (Å)	9.0	–
$r_c^{Coul}$ (Å)	8.5	–
$k_{HOH}$ ( $\text{kcal} \cdot \text{mol}^{-1} \cdot \text{rad}^{-2}$ )	43.95435	–
$D_{OH}$ ( $\text{kcal} \cdot \text{mol}^{-1}$ )	103.389	–
$\beta_{OH}$ ( $\text{nm}^{-1}$ )	22.87	–

Since this model is very recent, its accuracy has not been assessed on a large variety of experimental conditions. Especially, shear viscosity has not been assessed at low temperatures. We will present our work on these questions in Chap. 3.

## Chapter 3

# Viscoelastic properties of pure liquid water

<i>Outline</i>	
1	Long time dynamics of water: water as a viscous liquid . . . . . 45
1.1	Computational details . . . . . 46
1.2	Structural relaxation times . . . . . 46
1.3	Shear viscosity . . . . . 48
1.4	Stokes-Einstein relation . . . . . 49
1.5	Summary . . . . . 52
2	Links with the short time dynamics: from viscous liquid to elastic solid . . . . . 52
2.1	Numerical methods . . . . . 52
2.2	Slow dynamics vs elastic modulus . . . . . 53
2.3	Hall-Wolynes equation . . . . . 54
2.4	Summary . . . . . 55
3	Towards a consideration of quantum effects: ab initio approach . . 55
3.1	Aim of the study and methods . . . . . 55
3.2	Pulay stress correction . . . . . 56
3.3	Structural and dynamical predictions . . . . . 57
4	Conclusion . . . . . 60

The aim of the following numerical study is first to assess the accuracy of empirical and ab initio molecular simulations to describe the viscoelastic properties of pure liquid water, secondly to provide a reference for following studies on heterogeneous systems, and thirdly to analyse the behaviour of various dynamical observables at low temperature, in order – for example – to investigate on the debated glass transition of water. The first part will be devoted to a classical study of the **long time** dynamics of water, in the second part we discuss the connection to the **short time** dynamics, and in the third part, we test the accuracy of **ab initio methods** in order to assess the role of quantum effects.

## 1 Long time dynamics of water: water as a viscous liquid

Using molecular dynamics simulations, we propose here to analyze the temperature dependence of both the shear viscosity and the structural relaxation times on a range of temperatures much larger than the one used in experiments and confront our results to empirical models in order to get a consistent picture of the dynamics of water at low temperatures.

## 1.1 Computational details

All calculations were performed using the LAMMPS simulation package [Plimpton, 1995]. Water molecules interacted through the TIP4P/2005f force field [González and Abascal, 2011] introduced in chapter 1. Two sets of calculations were performed: (i) equilibrium calculations and (ii) steady-state shear calculations. Due to the flexibility of molecular bonding, a small timestep was required; 1 fs was used for all calculations. For equilibrium calculations, eight different box sizes were used from  $8 \times 8 \times 8$  to  $22 \times 22 \times 22$  molecules, with periodic boundary conditions. For each box size, four replicas of the system with different initial atomic coordinates and velocities were equilibrated in the isotherm-isobaric ensemble during a time that varied from 40 ps for the highest temperatures to 100 ps for the lowest temperatures using a Langevin thermostat [Schneider and Stoll, 1978] and a Hoover and Andersen barostat [Martyna et al., 1994], making in total thirty-two replicas at each temperature. The temperature was varied from 360 K to 228 K by 3 K steps, using each time the final configuration from the previous temperature as initial state to save computation time. The pressure was fixed at 1 atm. For steady-state shear calculations, 8228 water molecules were enclosed between two walls made of a face-centered cubic Lennard-Jones rigid crystal, with periodic boundary conditions in the two directions parallel to the walls. Opposite tangential velocities of 40, 70 and 100 m/s were applied to the wall to shear the fluid, with a 1 ns preliminary run to reach the steady state. The temperature was controlled using a Nose-Hoover thermostat [Martyna et al., 1994] in the same range as for the equilibrium measurements, but was changed by 15 K steps, except two extra calculations at 230 and 235 K. The pressure was set by applying normal forces on the walls. All data points reported in the following discussion are averaged over the values obtained for each replica of the system, and error bars are estimated as the standard error of those data sets.

## 1.2 Structural relaxation times

We introduce first the coherent intermediate scattering function,  $F(q, t)$ , defined by:

$$F(q, t) = \frac{\langle \rho(\vec{q}, t) \cdot \rho(-\vec{q}, 0) \rangle}{\langle \rho(\vec{q}, 0) \cdot \rho(-\vec{q}, 0) \rangle}, \quad \blacksquare \quad (3.1)$$

where  $\rho(\vec{q}, t)$  is the space Fourier transform of the density of the system at time  $t$  evaluated for each direction with  $\vec{q}$  the wave vector corresponding to the first maximum in the static structure factor [Kumar et al., 2007].  $F(q, t)$  was calculated during 10 ps and averaged over 100 ps for each replica of the system. This function was fitted by a double exponential decay to extract the  $\alpha$ - and  $\beta$ -relaxation times (see inset in Fig. 3.2):

$$F(q, t) = (1 - a) \cdot \exp\left(-\frac{t}{\tau_\alpha}\right) + a \cdot \exp\left(-\frac{t}{\tau_\beta}\right). \quad \blacksquare \quad (3.2)$$

The coherent intermediate scattering function is usually fitted by stretched exponentials, and gives one or two relaxation times. In the present case, Fig. 3.1 reveals a two-timescales process. As illustrated in the inset of Fig. 3.2, the best agreement with calculated values was obtained using two simple exponential functions, Eq. (3.2), instead of stretched exponentials, with one decay time following a VTF / SA behavior and the other one an Arrhenius behavior, as in the case of  $\alpha$ - and  $\beta$ -relaxations of common glass-formers. Those two decay times were consequently identified with  $\tau_\alpha$  and  $\tau_\beta$ .  $\alpha$ - and  $\beta$ -relaxation processes decouple at very high temperature, around 350 K, that is, near the boiling temperature, as shown on Fig. 3.2. Such  $\alpha/\beta$  transition is usually observed in the supercooled regime of glass-formers [Debenedetti and Stillinger, 2001]. This implies that water may have a supercooled-like dynamics at much higher temperatures than its melting temperature, which is consistent with the fact that, as already mentioned, several water anomalies occur at quite high temperature. Note also that the  $\beta$ -relaxation time follows an Arrhenius law with a negative activation energy. Staib et al. [Staib and Hynes, 1993] reported that, contrary to other molecular liquids, the relaxation time of O–H stretching modes from an excited state to the fundamental state increases with temperature in the case of water, due to the weakening of the hydrogen bonds. Assuming  $\beta$ -relaxation process is mainly related to bond stretching,

$\alpha$  and  $\beta$  relaxations denote respectively collective and local relaxations of the system.

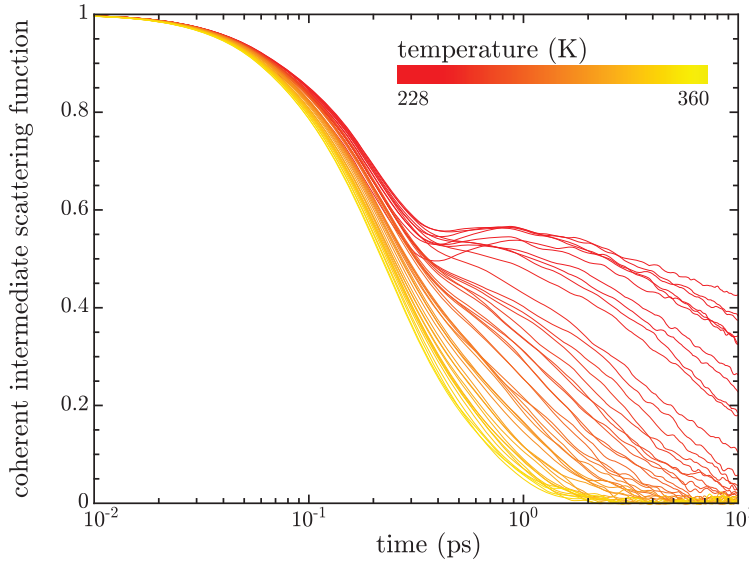


**Figure 3.1** ◀ Coherent intermediate scattering functions for different temperatures. At low temperatures, the decay process splits into a two-timescales decay.

this could explain this surprising behavior. Actually, O–H vibrational relaxation times measured by Lock et al. [Lock et al., 2002] are in very good agreement with our calculated values of  $\tau_\beta$ , which confirms this hypothesis (see Fig. 3.2).

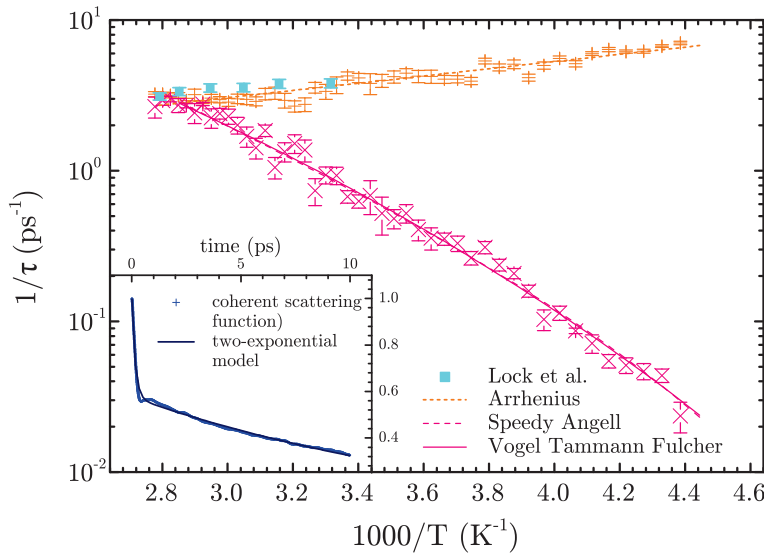


**Figure 3.2** ◀ Water  $\alpha$ - and  $\beta$ -relaxation times computed with the TIP4P/2005f force field (points). For temperatures lower than 350 K, the relaxation function, observed through the coherent intermediate scattering function decay, splits into a slow ( $\alpha$ ) and a fast ( $\beta$ ) relaxations (see inset), the former following an inverted Arrhenius behavior, and the latter following a non-Arrhenius behavior. Both SA and VTF laws (lines) are in good agreement with the simulation data for the  $\alpha$ -relaxation time. Experimental data by Lock et al. [Lock et al., 2002] of the O–H vibrational relaxation time are also plotted for comparison.

Regarding the evolution of the  $\alpha$ -relaxation time with temperature, the calculated values can be fitted by both VTF and SA laws, without significant differences over the range of temperature studied here. However, by defining the glass transition temperature  $T_g$  as the temperature at which  $\tau_\alpha$  reaches 100 s [Debenedetti and Stillinger, 2001], and by assuming the fits using these laws can be extrapolated down to the glass transition, their predictions are very different: the VTF law predicts  $T_g = 119 \pm 10$  K, whereas the SA law predicts  $T_g = 178 \pm 13$  K. The  $T_g$  predicted by VTF law is slightly lower than the lowest tabulated value, 135 K [Debenedetti, 2003], whereas SA gives a much higher value. Another way to characterize a glass-forming liquid is to calculate its fragility index  $m$ . To give a good definition of this index is not trivial, as explained by Angell [Angell, 2002]. Here, we use:

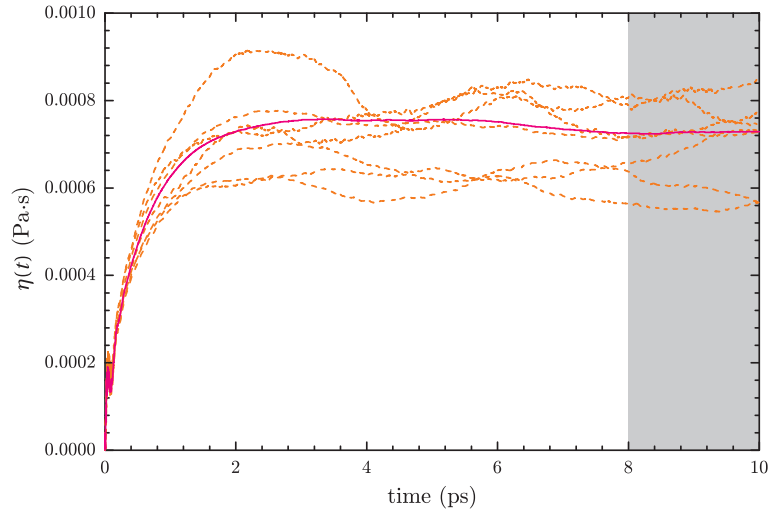
$$m = -\frac{T_g}{\ln(10)} \cdot \left( \frac{\partial \ln(X)}{\partial T} \right)_{T_g}, \quad \blacksquare \quad (3.3)$$

where  $X$  can be the shear viscosity or the  $\alpha$ -relaxation time. According to this definition, VTF law gives  $m \approx 55$ , which is consistent with a highly fragile behavior, and SA law gives  $m \approx 16650$  which is much higher than usual fragility values. Assuming the definition (3.3) is

valid whatever the model is used to extrapolate the values of  $\tau_\alpha$  at low temperatures [Mauro et al., 2009], that suggests that, for our study, the extrapolated data obtained with VTF law are more realistic than those using SA law. However, one must consider this result with caution, since the definition of  $m$  has been initially derived for VTF law, and might be not suitable for SA law. We will therefore consider only the fragility index provided by the VTF law in the following. To conclude, despite the same accuracy between the two laws to describe computed values of  $\alpha$ -relaxation time, their predictions in term of glass transition temperature are very different.

### 1.3 Shear viscosity

**Figure 3.3** ► Variations of the Green-Kubo integrals (Eq. (3.5)) with time at 300 K. Dashed curves correspond to a small set of representative integrals calculated for isolated replicas, whereas the plain curve corresponds to the integral averaged over all 160 independent Green-Kubo curves. The value of viscosity is obtained by averaging the plateau value over the last 2 ps.



To go beyond this relaxation study, we also looked at the behavior of the shear viscosity with respect to temperature and compared the picture of the glass transition given by both approaches. This method is used by a few experimentalists to investigate supercooled liquids, but is almost not used by theoreticians, probably due to the poor convergence of viscosity calculations. As we already mentioned, two sets of calculations were performed: (i) equilibrium calculations and (ii) steady-state shear calculations. We first briefly justify the validity of those two approaches, especially in terms of convergence.

For equilibrium calculations, the shear viscosity was computed using the Green-Kubo formalism:

$$\eta = \lim_{t \rightarrow \infty} \eta(t), \quad \blacksquare \quad (3.4)$$

with

$$\eta(t) = \frac{V}{k_B \cdot T} \cdot \int_0^t \langle p_{\alpha\beta}(0) \cdot p_{\alpha\beta}(u) \rangle \cdot du, \quad \blacksquare \quad (3.5)$$

where  $\langle \dots \rangle$  denotes an ensemble average, and  $\alpha\beta$  is one of the five independent components of the traceless stress tensor (see Chap. 2). To get convergence, we averaged the values obtained for 160 independent Green-Kubo integrals (see previous paragraph) for each temperature, as illustrated in Fig. 3.3. Then, we estimated the error associated with the average value by taking the standard deviation of this set of values, divided by the root mean square of the number of values in the set (standard error). The time interval on which the integrals are calculated were adjusted to ensure that a plateau is reached for each temperature.

For steady-state shear calculations, the shear viscosity is then given by:

$$\eta = \frac{\sigma}{\dot{\gamma}}, \quad \blacksquare \quad (3.6)$$

where  $\sigma$  and  $\dot{\gamma}$  denote the shear stress applied to the walls and the imposed shear rate, respectively. Both quantities were averaged over 1 ns. Three replica of the system were used

at each temperature, applying shear velocities of  $\pm 40, 70$  and  $100 \text{ m} \cdot \text{s}^{-1}$  to the walls. As shown in the Fig. 3.4, we checked the linearity of the shear stress with respect to the shear rate to control that the simulations remained in the linear response regime. The values of viscosities reported are averages of the values obtained for each replica. The error is then calculated as the standard error over those values.

The two sets of calculations (Green-Kubo and steady-state shear) are found to be consistent and show an excellent agreement with experimental data by Osipov et al. [Osipov et al., 1977], as shown in the inset of Fig. 3.5. The agreement is also very satisfactory with the data by Dehaoui et al. [Dehaoui et al., 2015], and by Hallett et al. [Hallett, 1963] (whose data are very close to those by Dehaoui et al.). This shows the accuracy of TIP4P/2005f force field to describe the slow dynamics of supercooled water. Like for the  $\alpha$ -relaxation time, the calculated values of the shear viscosity were fitted over the range of temperature 228 to 360 K since the  $\alpha/\beta$  transition shows that a supercooled-like regime extends over this full range of temperature. Again, both VTF and SA laws describe reasonably well our values, with a slightly lower reduced  $\chi^2$  for VTF law (see Fig. 3.5). We also tried to fit the data with Bässler law [Bässler, 1987], but it clearly deviates from our simulation results. In the case of shear viscosity, the glass transition temperature is conventionally defined as the temperature at which the viscosity reaches  $10^{12} \text{ Pa} \cdot \text{s}$ . Again, extrapolated VTF and SA laws give different predictions for this temperature:  $T_g = 189 \pm 21 \text{ K}$  for VTF, and  $T_g = 217 \pm 24 \text{ K}$  for SA. Regarding the fragility index, the VTF law for the viscosity gives  $m \approx 358$ , higher than the value calculated from  $\tau_\alpha$ . All the values for  $T_g$  and  $m$  are summarized in Table 3.1. Overall, the relaxation time and the shear viscosity exhibit different behaviors with respect to temperature, providing different estimations of the glass transition temperature and of the fragility index. This is in contrast with a standard assumption in the community [Kumar et al., 2007], although previous work evidenced such a decoupling in a model glass former [Shi et al., 2013].

	Shear viscosity		$\alpha$ -relaxation time	
	VTF	SA	VTF	SA
$T_g$	$189 \pm 21 \text{ K}$	$217 \pm 24 \text{ K}$	$119 \pm 10 \text{ K}$	$178 \pm 13 \text{ K}$
$m$	358	–	55	–

**Table 3.1** ◀ Values of the glass transition temperature  $T_g$  and the fragility index  $m$  estimated from shear viscosity and  $\alpha$ -relaxation time calculations, fitted by VTF and SA laws.

## 1.4 Stokes-Einstein relation

To compare the dynamics at low temperatures of both shear viscosity and  $\alpha$ -relaxation time and assess the reliability of the previous studies, we also looked at the coupling between on the one hand viscosity and self-diffusion, and on the other hand  $\alpha$ -relaxation time and self-

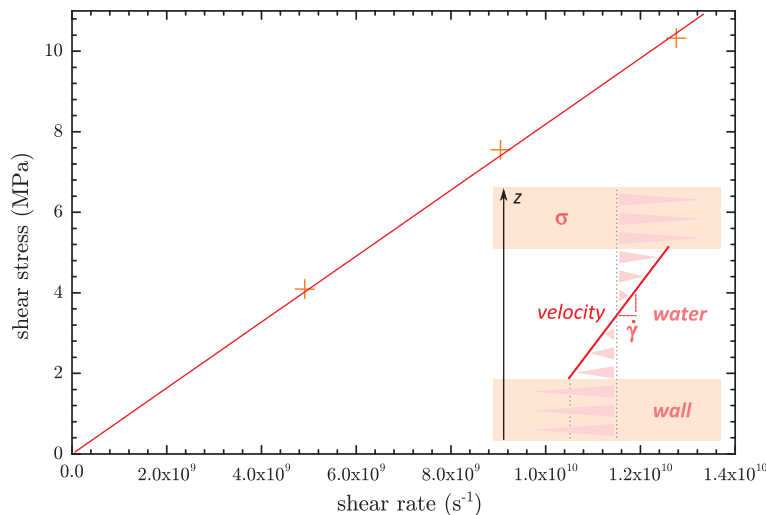
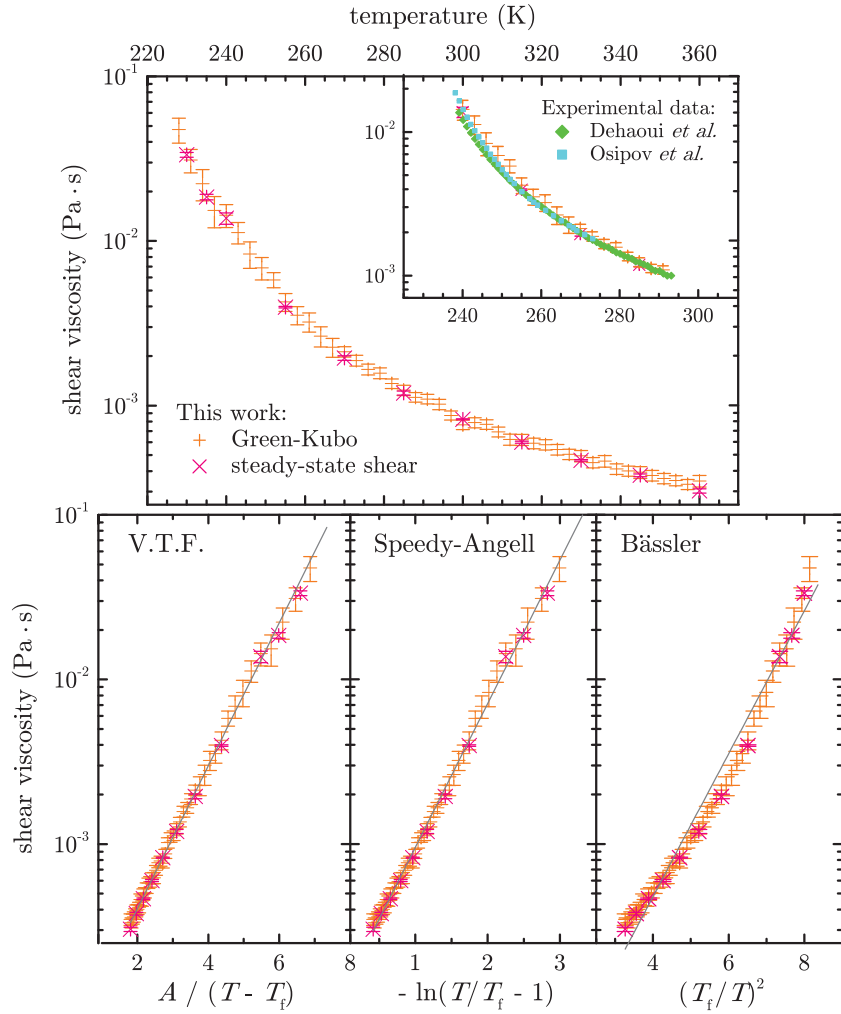


**Figure 3.4** ◀ Evolution of the shear stress with respect to the shear rate for different velocities applied to the walls. Points correspond to calculated values at 300 K. The line shows that all values are in the linear response regime.

**Figure 3.5** ▶

Water shear viscosity computed with the TIP4P/2005f force field using the Green-Kubo formalism (+) and stationary shear calculations (×). Both data sets are consistent and are in very good agreement with experimental values [Osipov et al., 1977, Dehaoui et al., 2015] (see inset). Fits by VTF, SA and Bässler laws (lines) are presented on separate bottom figures. The two first are in overall good agreement with the data, whereas the third one does not match.



diffusion, through the Stokes-Einstein (SE) relation [Hansen and McDonald, 2013]:

$$\frac{D \cdot \eta}{T} = \text{Cst}, \quad \blacksquare \quad (3.7)$$

or its equivalent for  $\alpha$ -relaxation time:

$$\frac{D \cdot \tau_\alpha}{T} = \text{Cst}'. \quad \blacksquare \quad (3.8)$$

To the best of our knowledge previous numerical work on supercooled water only considered the  $\alpha$ -relaxation time, we would like to compare here the predictions obtained with both observables, as it has been done previously for a model binary mixture [Shi et al., 2013]. The self-diffusion coefficient of bulk water computed with the TIP4P/2005f force field is in very good agreement with NMR measurements over a wide range of temperatures [Price et al., 1999], see Fig. 3.6, showing again the accuracy of this force field. The temperatures  $T_{SE}^\eta$  and  $T_{SE}^\alpha$  below which violations of the SE relation for viscosity and  $\alpha$ -relaxation time are observed are very different:  $T_{SE}^\eta$  is  $265 \pm 15$  K, whereas  $T_{SE}^\alpha$  is  $320 \pm 10$  K, as shown in Fig. 3.7 (top). Note that we tested another suggested correlation between viscosity and structural relaxation time,  $\tau_\alpha \propto \eta/T$  [Yamamoto and Onuki, 1998], leading to an alternative SE relation for the  $\alpha$ -relaxation time:  $D \cdot \tau_\alpha = \text{cst}$ . The temperature  $T_{SE,alt}^\alpha$  below which the alternative SE formula fails was well within the error bars of  $T_{SE}^\alpha$ . This confirms the fact that shear viscosity and  $\alpha$ -relaxation time behave differently at low temperatures in water.

However, even if those quantities are not equivalent, the glass transition is unique. Independently of the way the transition is approached, both quantities should predict similar glass transition temperatures. One needs consequently to go further.  $\alpha$ -relaxation time and

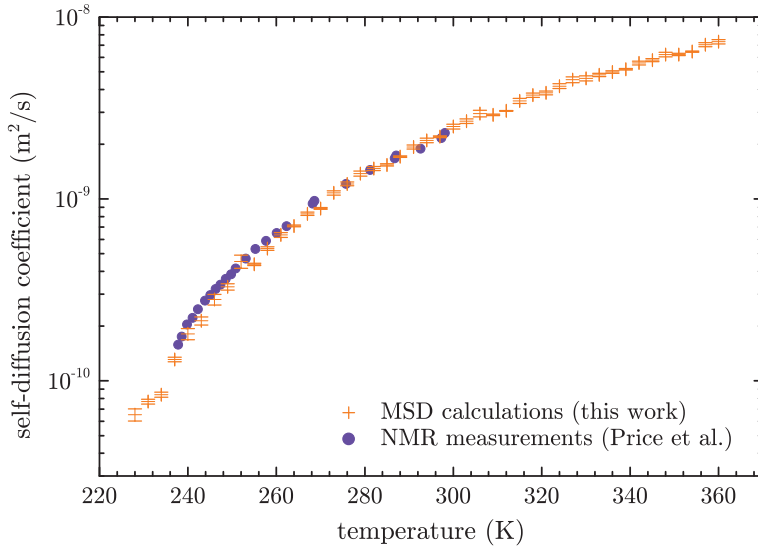


**Figure 3.6** ◀ Water self-diffusion coefficient computed with TIP4P/2005f forcefield (+) using the slope of the atomic mean square displacement in the diffusive regime. Calculated values are in very good agreement with NMR measurements (●) by Price et al. [Price et al., 1999].

shear viscosity refer to different physical quantities. To this point of view, it can be interesting to look at direct correlations between  $\alpha$ -relaxation time and a macroscopic time related with the viscosity: the Maxwell viscoelastic relaxation time  $\tau_M$ , defined as the ratio between the liquid shear viscosity  $\eta$  and the infinite frequency shear modulus  $G_\infty$ :

$$\tau_M = \frac{\eta}{G_\infty}. \quad \blacksquare \quad (3.9)$$

Those two timescales behave identically for temperatures higher than 285 K that is slightly lower than  $T_{SE}^\alpha$ , as shown in Fig. 3.7 (bottom), but are no more correlated for lower temperatures. A possible explanation for this decoupling at low temperatures is related to the different length scales probed by the two relaxation times [Berthier et al., 2004, Pastore et al., 2015]. Indeed, by definition the  $\alpha$  relaxation time calculated here corresponds to density fluctuations at the length scale  $2 \cdot \pi / k_{max}$ , where  $k_{max}$  is the wavevector corresponding to the first maximum of the static structure factor. This defines an almost temperature independent length scale which is comparable with the size of a water molecule. Conversely, the length scale relevant to shear viscosity depends on temperature. At high temperatures, the shear viscosity has an Arrhenius-like behaviour, and stress relaxation should occur through single molecule hopping. In this situation, the length scale probed by the shear viscosity is comparable with  $2 \cdot \pi / k_{max}$ , and the two relaxation times  $\tau_M$  and  $\tau_\alpha$  increase similarly on cooling. At lower temperatures, the dynamics becomes heterogeneous and stress relaxation should be cooperative and involves the relaxation of the cage formed by neighbouring molecules. Hence, the length scale probed by the viscosity should be larger than  $2 \cdot \pi / k_{max}$ . In conclusion, the heterogeneous dynamics, which is the hallmark of supercooled liquids, should explain the decoupling between  $\tau_M$  and  $\tau_\alpha$ .

Another, yet not contradictory, recent interpretation for this decoupling is due to Iwashita et al. who attribute the increase of shear viscosity at low temperatures in glass-formers in terms of local configurational excitations, and introduced a timescale  $\tau_{LC}$  for the evolution of local atomic connectivity [Iwashita et al., 2013]. They found that  $\tau_{LC}$  and  $\tau_M$  coincide for temperatures higher than  $T_A$  that corresponds to a strong-to-fragile transition temperature, *i.e.* a crossover between Arrhenius and non-Arrhenius behavior of the shear viscosity. This transition occurs at high temperatures and should not be confused with the fragile-to-strong transition observed in confined water at lower temperatures  $T < 228$  K. In the present case, we found a similar behavior for  $\tau_M$  and  $\tau_\alpha$  if we take  $T_A = 285$  K. Actually, the shear viscosity shows an Arrhenius behavior in Fig. 3.5 for temperatures higher than  $T_A$ . Consequently,  $T_A$  could indeed correspond to a strong-to-fragile crossover. As it is close to  $T_{SE}^\alpha$ , the decoupling between  $\alpha$ -relaxation time and self-diffusion coefficient might be explained by such a crossover. Reevaluation of the accuracy of VTF and SA laws by restricting data to temperatures lower than  $T_A$  does not affect significantly the predictions of the glass transition temperatures and fragility indexes: changes are within error bars. Thus, the existence

See Chap. 2 for the numerical determination of  $\tau_M$ . A discussion about the validity of the approach will be given in section 2.

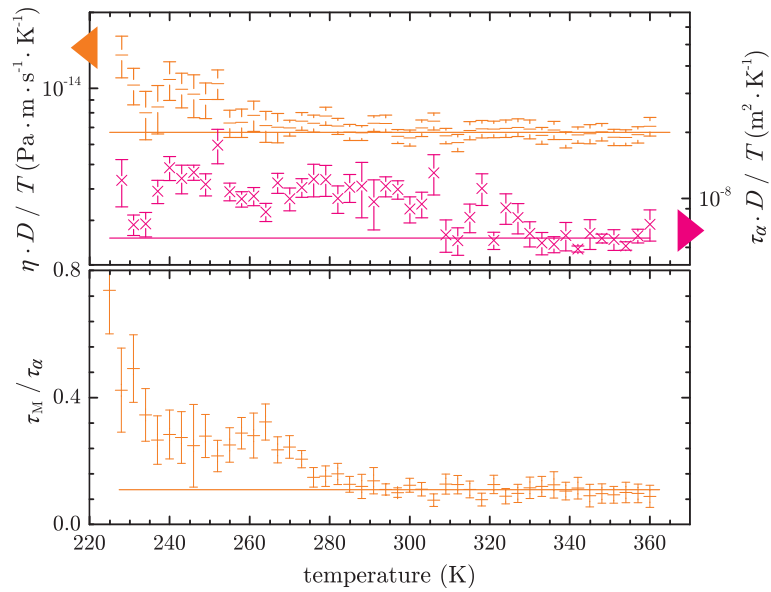


**Figure 3** Coupling parameter  $\eta \cdot D / T$ , relaxation time  $\tau_M$ , and the Stokes-Einstein relation parameter  $\tau_\alpha \cdot D / T$ . Top figure shows the ratio between shear viscosity and shear viscoelasticity are tested against the Stokes-Einstein relation is violated at lower than the viscosity, an  $\alpha$ -relaxation time. Bottom figure: microscopic (microscopic) compared. The relaxation time for temperature is a constant diagram.

of a strong-to-fragile transition does not explain the differences observed between the two observables.

### 1.5 Summary

In this section, we have shown that the TIP4P/2005*f* force field is very accurate to model hydrodynamic transport properties of supercooled water. It predicts two structural relaxation times, namely  $\alpha$ - and  $\beta$ -relaxation times, with a  $\alpha/\beta$  decoupling around 350 K, so that liquid water behaves like a supercooled liquid almost up to its boiling temperature. It is important to remark that in the present study, we are primarily concerned with the dynamics of supercooled water above the homogeneous nucleation temperature around 232 K. Therefore, we do not address any fragile-to-strong transition that may occur at lower temperatures, and which is observed under confinement [Mallamace et al., 2006, Liu et al., 2006, Chen et al., 2006]. Analyzing the  $\alpha$ -relaxation time and shear viscosity temperature dependence, we investigated the supercooled dynamics of water and compared with several empirical laws. VTF law gives glass transition temperatures that are closer to tabulated values than SA law, even if the two laws describe with a comparable accuracy the simulation data over the range of temperatures considered here. However, the viscosity and the  $\alpha$ -relaxation time behave differently with temperature, with a decoupling around 309 K that could correspond to a fragile-to-strong transition of water. This decoupling corresponds also to a violation of the Stokes-Einstein relation for the  $\alpha$ -relaxation time, whereas the Stokes-Einstein relation for shear viscosity is violated at a lower temperature (around 265 K).

## 2 Links with the short time dynamics: from viscous liquid to elastic solid

We introduced two “elastic” models in the chapter 1 to connect the slow and fast dynamics of glass-former liquids. In this section, we assess the validity of these models to describe the slow dynamics of supercooled water using molecular dynamics simulations. We consider the promising TIP4P/2005*f* force field as in the beginning of this chapter. We report a strong correlation between the  $\alpha$ -relaxation time and the high frequency shear modulus or the mean square displacement for the temperatures considered in this study. Conversely, elastic models perform well at low temperatures but, depending on the model and the observable, they can fail above a temperature on the order of 260 K. Interestingly, this temperature is close to the temperature where the Stokes-Einstein relation begins to be violated.

## 2.1 Numerical methods

Numerical methods used in this study are the same as those introduced in the first section of this chapter (see section 1.1).

## 2.2 Slow dynamics vs elastic modulus

We first look at direct correlations between the shear viscosity or the  $\alpha$ -relaxation time of liquid water with the high frequency shear modulus using Eq. (1.4). As a reminder, those equations are:

$$\begin{cases} X = X_0 \cdot \exp\left(\frac{E_a(T)}{k_B \cdot T}\right), \\ E_a(T) = \lambda \cdot G_p(T) \cdot a^3 \end{cases} \quad (3.10)$$

The plateau shear modulus  $G_p$  is traditionally defined as the value of the elastic modulus where the derivative of  $\log(G(t))$  is minimum [Puosi and Leporini, 2012a, Dyre and Wang, 2012]. To estimate the position of the plateau, one can look at the vibrational density of state of water. We calculated the VDOS using the TIP4P/2005f force field for various temperatures, as shown on Fig. 3.8. The position of the different bands introduced in Chap. 2

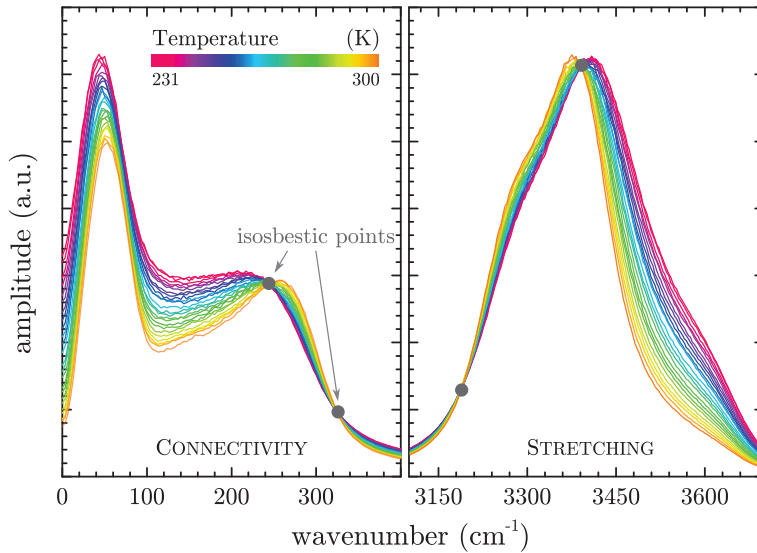


**Figure 3.8** ◀ Evolution of the vibrational density of states (VDOS) of water with respect to the temperature. Left: the connectivity region, obtained using the VDOS of oxygen atoms. Right: the intramolecular stretching region, obtained using the VDOS of hydrogen atoms.

is overall well reproduced. Especially, the connectivity band, at low wavenumbers, is associated with the hydrogen bond bending mode around  $50 \text{ cm}^{-1}$  and the hydrogen bond stretching mode around  $200 \text{ cm}^{-1}$  [Brubach et al., 2005]. The latter shifts from approximately 250 to  $200 \text{ cm}^{-1}$  when decreasing the temperature from 300 to 231 K. Note the presence of isosbestic points, indicating an equilibrium between weakly and strongly H-bonded liquids [Walrafen et al., 1986]. Using  $200 \text{ cm}^{-1}$  band as a probe for the typical timescale describing connectivity of molecules, the plateau should be located around 170 fs. However, due to zero wave vector optical phonon modes [Landry et al., 2008], the autocorrelation function of the stress tensor components strongly oscillates at short timescales, so that the plateau value  $G_p$  must be extrapolated. We fitted the stress autocorrelation function for  $t > 0.03 \text{ ps}$  using a stretched exponential functional form,

$$\langle \sigma_{\alpha\beta}(t) \cdot \sigma_{\alpha\beta}(0) \rangle = \frac{G_0 \cdot k_B \cdot T}{V} \cdot \exp\left(-\left(\frac{t}{\tau_M}\right)^\gamma\right), \quad (3.11)$$

where  $V$  denotes the volume of the system and  $T$  the temperature, which was found to give good results over long time scales for each temperature. In the following, we will therefore use the parameter  $G_0$  as a proxy to the high frequency plateau modulus  $G_p$ . Note that for the highest temperatures, extraction of  $G_0$  becomes difficult as the oscillations of the stress tensor auto-correlation function extend over a time interval longer than the decay time  $\tau_M$ .

The stretching exponent  $\gamma$  as a function of temperature is shown in Fig. 3.9. At high temperatures  $T > 280$  K, the exponent  $\gamma$  is close to 1 and the stress autocorrelation function can be well described by a single exponential. Below 280 K,  $\gamma$  decreases with cooling, indicating that a single Maxwell relaxation time can not describe stress relaxation at low temperatures, as also observed in Refs Furukawa and Tanaka, 2011, Kawasaki and Kim, 2017.

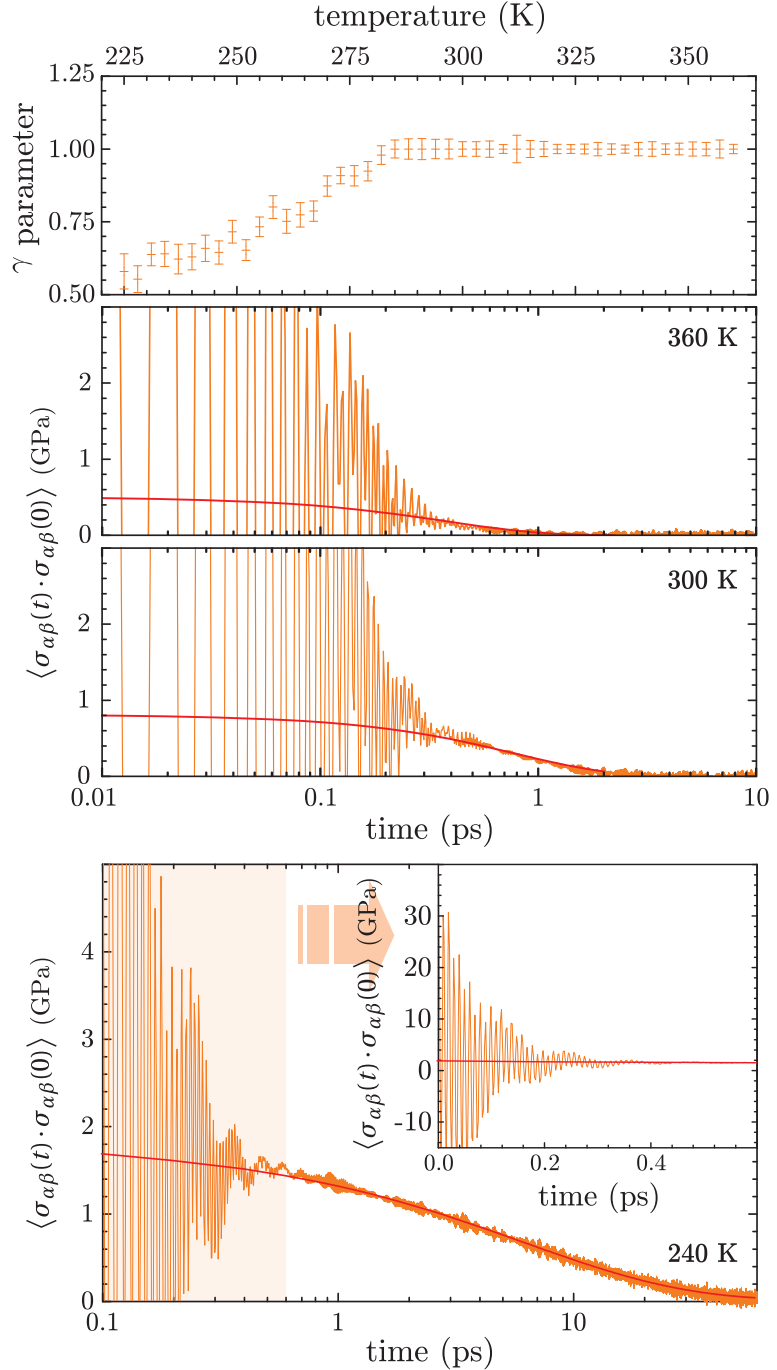
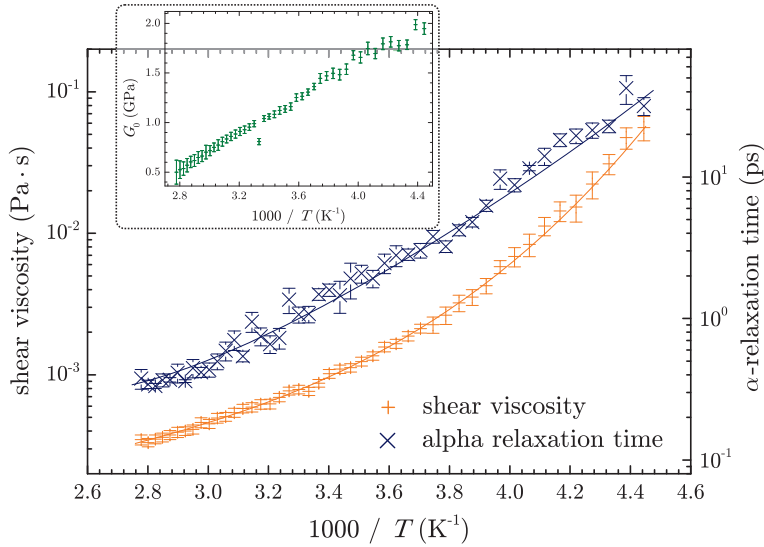


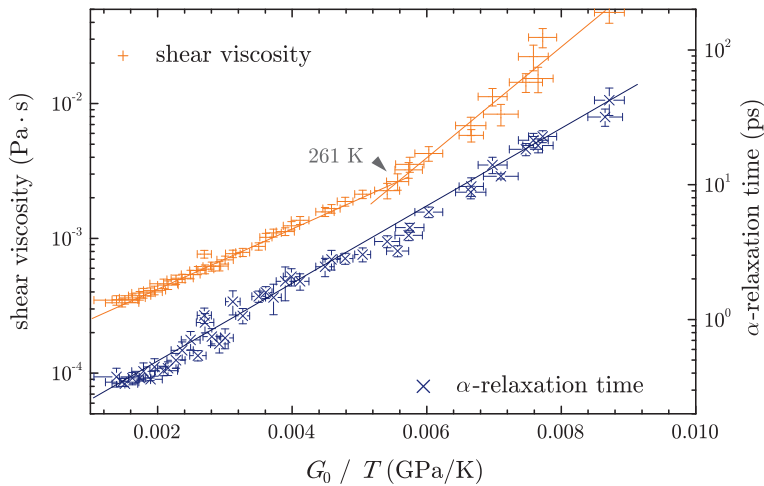
**Figure 3** Extraction of the stretching exponent  $\gamma$  from the stress autocorrelation function  $\langle \sigma_{\alpha\beta}(t) \cdot \sigma_{\alpha\beta}(0) \rangle$  at different temperatures. The stretching exponent  $\gamma$  is shown as a function of temperature. The stress autocorrelation function  $\langle \sigma_{\alpha\beta}(t) \cdot \sigma_{\alpha\beta}(0) \rangle$  is shown for 360 K, 300 K, and 240 K. The red solid lines represent the exponential fit to the data. The inset shows the high-frequency shear modulus  $G_0$  versus time (ps) for 240 K. The orange dots represent the data and the red line represents the fit.

As we showed in the first section, the TIP4P/2005f force field predicts a non-Arrhenius behavior for the shear viscosity and the  $\alpha$ -relaxation time, even if deviations to the Arrhenius law are smaller in the case of  $\alpha$ -relaxation time. Both observables are displayed in Fig. 3.10.

The evolution of the high frequency shear modulus is also reported in the inset of this figure. Interestingly, the shear modulus  $G_0$  decreases monotonously with increasing temperature. Therefore, the temperature dependence of  $G_0$  follows that of the plateau modulus  $G_p$ , and



$G_0$  is clearly distinct from the infinite frequency shear modulus  $G_\infty$  [Puosi and Leporini, 2012a, Dyre and Wang, 2012]. Using the initial value  $G_0$  of the stretched exponentials as a proxy of  $G_p$ , the agreement between elastic models and our calculations is only partial: for the shear viscosity, Eq. (1.4) does not fit well the simulation data over the whole temperature range analyzed, and two temperature domains can be distinguished, as shown in Fig. 3.11. In the two domains, Eq. (1.4) describes the correlation between  $G_0/T$  and the viscosity, but the parameter  $a$  is not the same at high and low temperatures. For  $T < 261$  K,  $a \approx 1.8$  Å, while for  $T > 261$  K,  $a \approx 1.5$  Å (assuming  $\lambda = 1$ ). The fact that the parameter  $a$  is larger at low temperatures may be explained by an increase of cooperativity, as discussed in the following paragraph. As for  $\alpha$ -relaxation time, Eq. (1.4) provides a good description of the slowing down of supercooled water with a single set of parameter  $a \approx 1.6$  Å over the entire temperature domain.

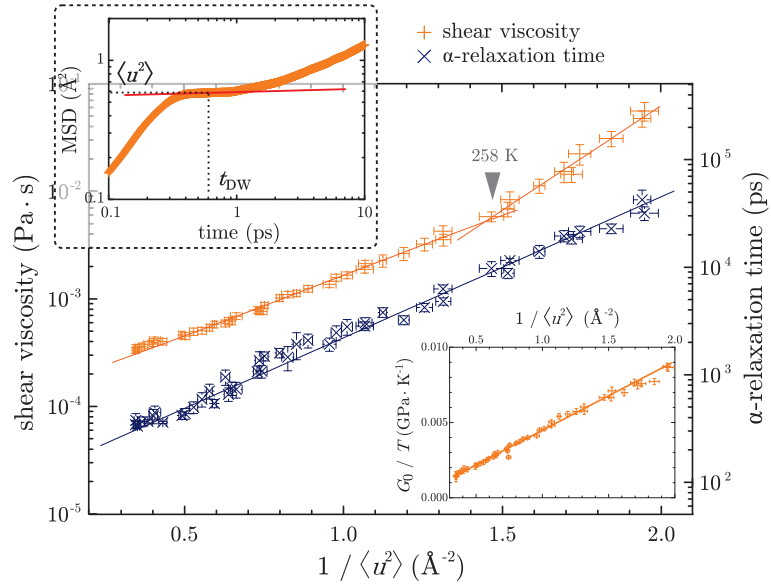


Interestingly, the temperature of transition between the high temperature and low temperature behavior of the viscosity is found to be close to 261 K, which corresponds to the temperature below which the self-diffusion coefficient  $D$  and the shear viscosity  $\eta$  decouple with respect to the Stokes-Einstein relation,  $D \cdot \eta \sim T$ , which we estimated to be  $265 \pm 15$  K and related to the appearance of dynamical heterogeneities in the previous section. The Stokes-Einstein relation describes a regime where particle motion is not cooperative and may be compared to a Brownian particle diffusing in a bath of neighbor molecules. Conversely, elastic models traditionally describe a situation where atomic motions involve collective displacements of the surrounding particles. However, here we saw that elastic models could still describe the slowing down of the dynamics at high temperatures, provided we

defined an effective length  $a$  which takes a smaller value as compared with the low temperature value. The fact that  $a$  is smaller at high temperatures could then be related to the loss of cooperativity. Therefore, two regimes emerge in the description of the dynamics in the framework of elastic models: a diffusive homogeneous regime at high temperature where molecule displacements are almost independent and the Stokes-Einstein relation is obeyed, and a low temperature regime where molecule motions are cooperative.

**Figure 3.12** ▶

Correlations between the shear viscosity /  $\alpha$ -relaxation time and the vibrational mean squared displacement. The vibrational mean squared displacement is determined as the value of the mean squared displacement of the center of mass of a water molecule when the slope is minimum (see top left inset). Similarly to the previous correlations with the elastic modulus, the  $\alpha$ -relaxation time is described by Eq. (3.12) over the whole temperature range, while a transition is observed at ca. 258 K for the shear viscosity. The inset shows the correlation between the vibrational mean squared displacement and the high frequency shear modulus.



### 2.3 Hall-Wolynes equation

We now assess the validity of the mean square displacement version of the elastic model, as described in Eq. (3.12), reminded here:

$$X = X_0 \cdot \exp\left(\frac{a^2}{2 \cdot \langle u^2(T) \rangle}\right). \quad \blacksquare \quad (3.12)$$

The quantity of interest here is the vibrational mean squared displacement, which can be accessed through the mean square displacement  $\langle r^2(t) \rangle$ , as illustrated in the top inset of Fig. 3.12. In a dense system, molecules move ballistically at short times while they diffuse at long times:  $\langle r^2(t) \rangle = 6 \cdot D \cdot t$  where  $D$  is the diffusion coefficient. At intermediate time scales, the mean square displacement of a molecule is limited by the presence of neighbouring molecules. As seen in fig. 3.12, at these intermediate time scales the MSD has a minimum slope, which corresponds to the time  $t_{DW}$  when the particle shoves its neighbors. The corresponding value of the MSD is called mean square vibrational amplitude or Debye-Waller (DW) factor [Puosi and Leporini, 2012a, Dyre and Olsen, 2004], and denoted  $\langle u^2 \rangle$  in the following.

Since the pioneering work of Buchenau and Zorn [Buchenau and Zorn, 1992], Eq. (3.12) has been shown to hold in many systems [Larini et al., 2008, Puosi and Leporini, 2012b, Ciamarra and Sollich, 2015]. For supercooled water, Fig. 3.12 reports a good agreement between Eq. (3.12) and our simulation data at low temperatures. As for the previous elastic model, we find two different behaviors depending on the observable  $X$ . If  $X$  is the  $\alpha$ -relaxation time, the agreement extends over the whole range of temperatures analyzed, with a molecular length  $a = 1.62 \text{ \AA}$ . In the case of the shear viscosity, two regimes with different molecular lengths appear ( $a = 1.97 \text{ \AA}$  at low temperature and  $a = 1.48 \text{ \AA}$  at high temperature), with a crossover temperature close to 258 K. This crossover temperature is very close to the one determined in the previous approach. The equivalence between the two approaches discussed is confirmed by the inset of Fig. 3.12, which demonstrates the good correlation between  $G_0/T$  and the MSD. The difference of behavior between the shear viscosity and the  $\alpha$ -relaxation time is not surprising, and can be related to the decoupling between these two observables observed at low temperatures (see previous section and Ref. Shi et al., 2013).

The relevance of the vibrational MSD  $\langle u^2 \rangle$  is supposed to hold while  $\tau_\alpha$  is lower than  $t_{DW}$  [Larini et al., 2008], which corresponds to a temperature much higher than the crossover temperature  $T = 258$  K. Actually, the activation energy associated with the two versions of the elastic models at this threshold temperature is close to the energy of a hydrogen bond (*ca.* 20 kJ/mol), which could explain the change of regime at high temperatures: the connectivity of water molecules is mainly due to hydrogen bonds. At high temperature, thermal motion breaks the hydrogen bond network, so that the local tetragonal structure is short lived, and molecular displacements are no longer collective [Kawasaki and Kim, 2017]. Again, an interesting point is that elastic models are valid when the Stokes-Einstein relation  $D \cdot \eta / T = \text{Cst}$  breaks down, *i.e.* below  $265 \pm 15$  K for the TIP4P/2005f force field (see previous section). The breakdown of the Stokes-Einstein relation is usually associated with the rise of dynamical heterogeneities. Likewise, heterogeneous structural relaxation is connected with the experimental test of the Hall-Wolynes equation [Larini et al., 2008].

Before concluding, we should say a word about the role of quantum effects in the dynamics of supercooled water. Indeed, our simulations are fully classical and one may ask the relevance of quantum effects to describe the slow dynamics of water. These include the description of the nuclear degrees of motion, the hydrogen bond network but also the temperature dependence of the mean square displacement. We have already shown that the TIP4P/2005f potential reproduces accurately the shear viscosity of supercooled water (see previous section). It would be interesting to measure the elastic properties of supercooled water at low temperatures, to see if the TIP4P/2005f potential can also describe the temperature dependence of the shear modulus, or the vibrational mean square displacement. This would allow us to conclude whether quantum effects do play a significant role in the slow dynamics of water, or if they play a negligible role due to compensation effects. If quantum effects turn out to be important, demanding ab initio simulations could be unavoidable to investigate supercooled water dynamics [Ceriotti et al., 2016, Gillan et al., 2016, DiStasio Jr et al., 2014].

## 2.4 Summary

We show here that the long time dynamics of liquid water at low temperatures is highly correlated with its short time elastic properties, quantified by the shear modulus at high frequency. In particular, it is surprising to see that in spite of the numerous anomalies of water, elastic models perform as well as for simple glass formers including metallic glasses or supercooled polymers. Moreover, for the viscosity, two different temperature regimes with different effective molecular lengths are observed, and the crossover temperature is close to the one where the Stokes-Einstein relation starts to be violated. These results call for experimental investigation of the high frequency shear modulus of supercooled water using *e.g.* inelastic X-ray scattering. Looking for correlations between the elastic modulus and the shear viscosity measured at low temperatures may also help in assessing the role of quantum effects which are not considered in our classical approach.

# 3 Towards a consideration of quantum effects: ab initio approach

## 3.1 Aim of the study and methods

We reviewed in Chap. 2 some challenges of density functional theory (DFT) in the context of aqueous systems. In this last section, the aim is to characterize the accuracy of DFT to describe liquid water, to see in what extent this method could be used in the future to investigate the role of quantum effects on the dynamics of water. We report density calculations in the isothermal-isobaric ensemble ( $NpT$ ) of liquid water as a function of temperature for three different functionals including or corrected with dispersion terms. We then look at different commonly used observables to evaluate the accuracy of the different functionals: the radial distribution function, the hydrogen bond angles distribution, and the self diffusion coefficient at room temperature. We also estimate the value of the shear viscosity, which to

this day has been sparsely considered using AIMD [Kühne et al., 2009]. For density calculations, we propose a method to fully compensate the incompleteness of the basis set in the stress tensor evaluation whatever the kinetic energy cutoff is used for the calculation.

All calculations are performed using the CP2K/Quickstep method [VandeVondele et al., 2005a] (CP2K 2.5.1), with a 400 Ry kinetic energy cutoff, molecularly optimized short range double zeta valence polarized basis set by VandeVondele et al. [VandeVondele and Hutter, 2007] for the wave functions representations and PBE-optimized pseudopotentials by Goedecker, Teter and Hutter [Goedecker et al., 1996, Hartwigsen et al., 1998, Krack, 2005]. We used three functionals including or corrected with dispersion terms: two dispersion-inclusive functionals (optB88-vdW [Becke, 1988, Klimeš et al., 2009] and VdW-DF2 [Lee et al., 2010a]) and also one dispersion-corrected functional (PBE-D3 [Grimme et al., 2010, Grimme et al., 2011]). No correction was applied to compensate NQE.

A 64 molecules simulation box was used for all calculations presented in the following. Note that we thoroughly tested the influence of the box size, which we found, as we will discuss later, to be negligible compared to the error bars associated to the estimation of the different observables, in agreement with previous studies [Grossman et al., 2004, Sit and Marzari, 2005]. For structure calculations, the system is first equilibrated during 7 ps in the  $NpT$  ensemble with a standard Nose-Hoover thermostat [Martyna et al., 1994] and a Hoover and Andersen barostat [Martyna et al., 1994] (1 bar) and then, the density, the RDF and the OOO angle distributions are averaged over 3 ps. For dynamic calculations, the system was first pre-equilibrated using classical molecular dynamics at the average density value obtained by  $NpT$  calculations, and then equilibrated during 10 ps in the isotherm-isochoric ( $NVT$ ) ensemble using AIMD at 300 K. 60 ps runs in  $NVT$  ensemble were finally used for the self diffusion and the shear viscosity calculations.

### 3.2 Pulay stress correction

For a volume fluctuating system, the calculation of the total energy and thus of its stress tensor components, generally depends on the kinetic energy cutoff or the number of plane waves used, except if the calculation is fully converged with respect to the basis set employed to represent the wave functions. The difference between the real stress and the calculated one is called Pulay stress [Gaiduk et al., 2015, Bernasconi et al., 1995]. Different strategies have been used to correct it, including functional corrections [Bernasconi et al., 1995], use of a high energy cutoff [McGrath et al., 2006], or of a complete basis set [Ma et al., 2012, Lee and Tuckerman, 2007, Lee and Tuckerman, 2006]. Here, we adapt the method proposed by Froyen et al. [Froyen and Cohen, 1986], by correcting the pressure at each step of the molecular dynamics loop according to the following formula:

$$p = p_{E_c} + \frac{2}{3} \cdot \frac{E_c}{V} \cdot \left( \frac{\partial E}{\partial E_c} \right)_V, \quad \blacksquare \quad (3.13)$$

where  $p_{E_c}$  denotes the pressure calculated at constant kinetic energy cutoff,  $E_c$  the energy cutoff,  $V$  the volume,  $E$  the total energy and  $()_V$  indicates that the derivative is estimated at constant volume. The second term corresponds to the Pulay stress, and can be evaluated through a first order development of the total energy with respect to the energy cutoff:

$$\frac{\partial E}{\partial E_c}(E_c) \approx \frac{E(E_c + \delta E_c) - E(E_c - \delta E_c)}{2 \cdot \delta E_c}, \quad \blacksquare \quad (3.14)$$

where  $E(E_c + \delta E_c)$  and  $E(E_c - \delta E_c)$  are determined by performing the energy calculation with the same configuration of the system for two different values of the energy cutoff. This correction suppresses the influence of the energy cutoff, whatever the value used for the calculation, as shown in Fig. 3.13 for a static configuration of the system with the optB88-vdW functional.

The integrating scheme we used is thus the following:

1. Calculate the atomic forces, energy and the pressure at 400 Ry, and the energy of the system for two extra energy cutoff (350 and 450 Ry) with CP2K/Quickstep.

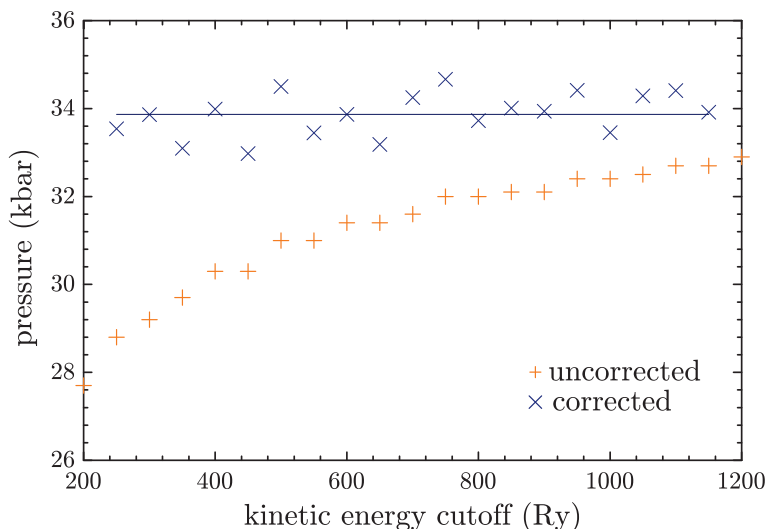


**Figure 3.13** ◀ Influence of the kinetic energy cutoff on the calculated pressure with and without Pulay stress correction. Without correction, the absolute error varies between 1.2 kbars for the highest cutoff value allowed by CP2K (1200 Ry) and 5 kbars for 200 Ry. No influence of the cutoff value is observed when the Pulay stress correction is applied, even if the pressure fluctuates over an interval of ca. 1 kbar.

2. Calculate the corrected pressure at 400 Ry by expanding the derivative  $(\partial E/\partial E_c)_V$  for the three energy cutoff values.
3. Integrate the equation of motion in the  $NpT$  ensemble with the corrected pressure using atomic forces calculated with 400 Ry energy cutoff.
4. Iterate.

This procedure is automated with a homemade software, using the standard algorithm by Martyna et al. [Martyna et al., 1994] for  $NpT$  integration.

### 3.3 Structural and dynamical predictions

#### 3.3.1 Density

Compared to empirical molecular dynamics, simulation boxes and simulation times are much smaller in AIMD. It raises some questions about the accuracy of the approach. We first discuss the influence of the simulation box size and the simulation time in the case of density measurements.

The influence of the simulation box size on the density calculations is evaluated using empirical molecular dynamics. Calculations were performed using the LAMMPS simulation package [Plimpton, 1995], using the TIP4P/2005f force field [González and Abascal, 2011] for water, with the same parameters as in previous sections. Eight different box sizes were used from  $3 \times 3 \times 3$  to  $10 \times 10 \times 10$  molecules, with periodic boundary conditions. For each box size, the system was equilibrated in the isotherm-isobaric ensemble during 500 ps using a Nose and Hoover thermostat [Martyna et al., 1994] and a Hoover and Andersen barostat [Martyna et al., 1994], as in the case of AIMD calculations, then the density was averaged over 2 ns using the same thermostat/barostat. The temperature was fixed at 300 K and the pressure at 1 atm. The evolution of the equilibrium density with respect to the simulation box size is given in Fig. 3.14.

The relative error due to finite box size effects is systematically lower than 0.4 %. Especially, in the case of a  $4 \times 4 \times 4 = 64$  molecules simulation box, which is the size considered in the present study, the error is about 0.3 %. This is, as we will see, completely negligible with respect to the error bars associated to the present AIMD density calculations. Thus, finite size effects do not affect the present density measurements.

Another striking point is the time used in the previous calculations to evaluate the density. It is several orders of magnitude larger than the time used for AIMD calculations. It raises questions about the convergence of the AIMD calculations. As explained previously, for each temperature, the system was equilibrated first during 7 ps. Then, the density was

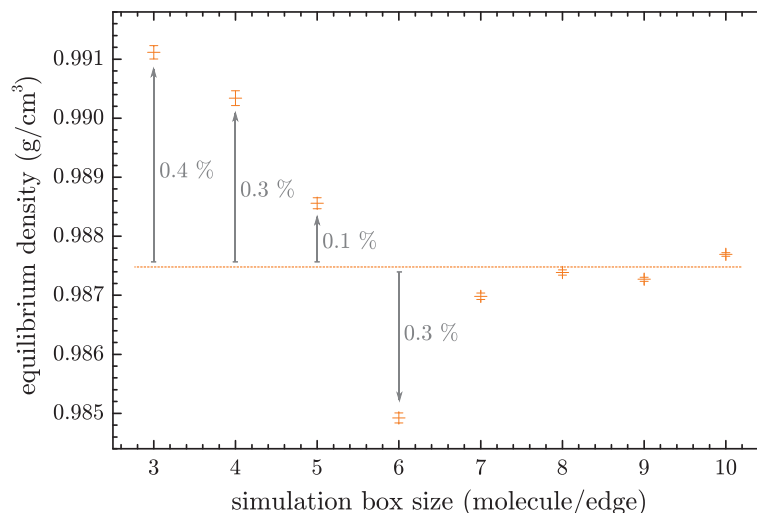


**Figure 3**  
Evolution  
respect t  
using em  
The box  
of numb  
of the si  
line repre  
tained ov  
and grey  
error with

averaged over 3 ps. In order to evaluate the validity of this approach and its accuracy, 5 additional picoseconds were used for a couple of temperatures. Then, a running average over 3 ps intervals was calculated. A typical averaged curve is shown in Fig. 3.15.

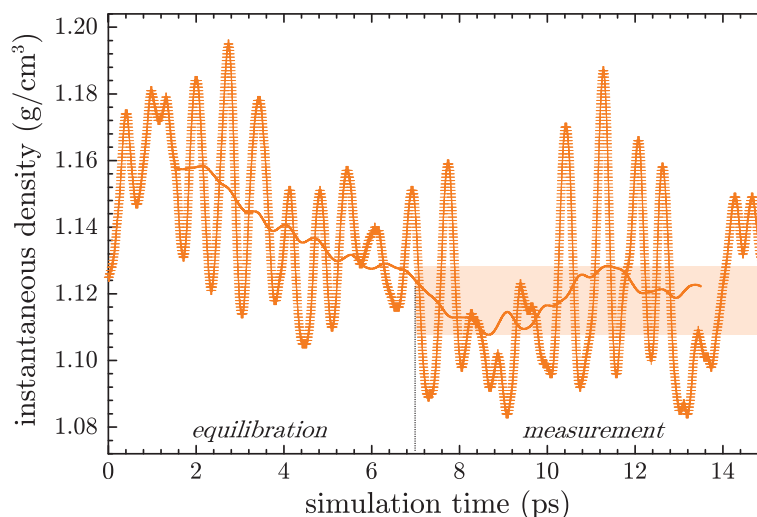


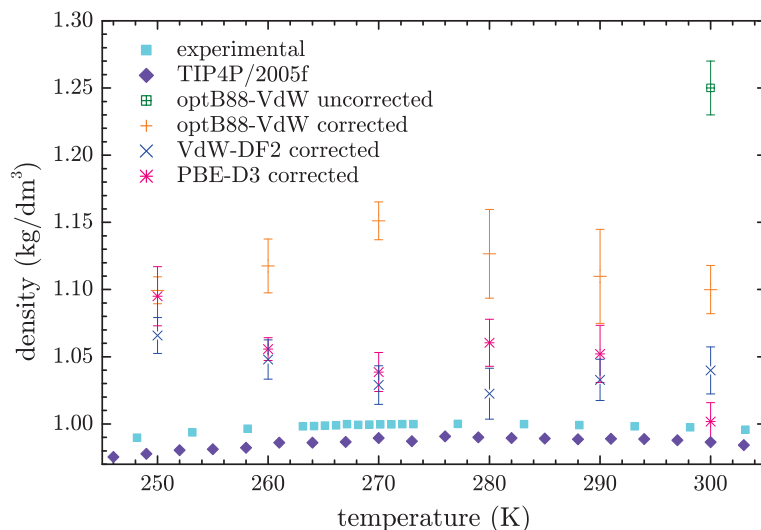
**Figure 3**  
Evolution  
the simu  
molecular  
respond t  
of the d  
curve con  
erage ov  
shaded  
amplitude  
averaged  
time.

The instantaneous density strongly oscillates. However, looking at the time evolution of the averaged curve, the density value oscillates in a relatively narrow interval. We can thus consider that the simulation time gives a reasonable estimation of the density. The amplitude of the oscillations of the averaged curve (*i.e.* the width of the shaded area in Fig. 3.15) is used as error bar.

We now move to the results. We first look at the influence of the Pulay stress correction. With the optB88-vdW functional, the density obtained with Pulay stress correction is much closer to experiments than without correction: the relative error decreases from 25 % without correction to 9 % with correction at 300 K, as shown in Fig. 3.16. Thus the Pulay stress correction improves greatly the accuracy of the calculation using this functional. However, even with the correction, the density is higher than in experiments. This is something usually observed for dispersion functionals [Ma et al., 2012, Gaiduk et al., 2015]. Nevertheless, using different functionals with this correction, at 300 K, the density obtained with the VdW-DF2 functional is better, with ca. 4 % relative error, and the value obtained with PBE-D3 is in quantitative agreement with experiments within error bars.

Another way to assess the accuracy of the different functionals is to look on their ability to reproduce the overall temperature dependence of the density instead of the absolute values at a given temperature. From this point of view, the optB88-vdW functional reproduces the

maximum of density of liquid water around 270 K, which is close to the experimental value (277 K) [Kell, 1975].



On the contrary, the VdW-DF2 functional predicts a minimum of density around 280 K whereas the PBE-D3 functional predicts a non-monotonic temperature dependency of the density. Both evolutions differ qualitatively from experiments and thus are nonrealistic. However, these conclusions must be considered cautiously since the variations are hardly higher than the error bars.

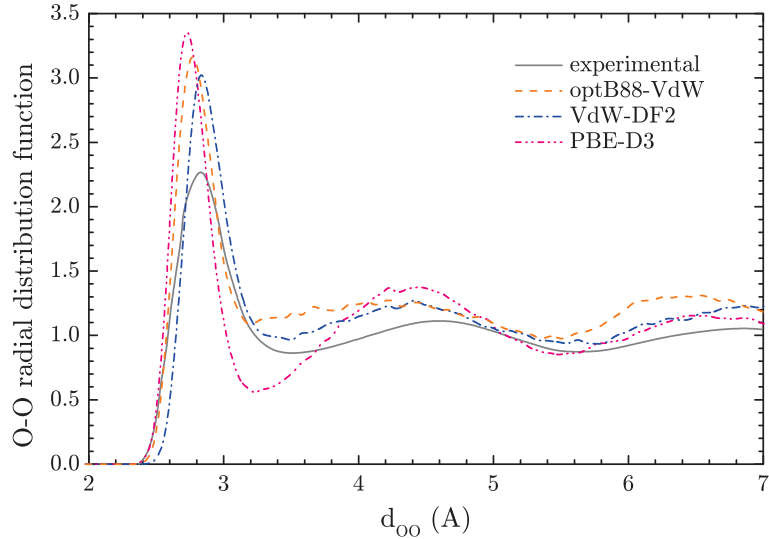
### 3.3.2 Local structure

We then considered the oxygen-oxygen radial distribution function (RDF) and the oxygen-oxygen-oxygen angle distribution function ( $p_{000}$ ) of the first coordination shell in the case of pressure-corrected calculations, as shown in Figs. 3.17 and 3.18. For the latter, the angle distribution was computed only for atoms separated by a distance lower than those corresponding to the first minimum of the RDF. The three functionals predict quite different atomic distributions. The position of the first peak of the RDF is overall well reproduced by the three functionals, but its amplitude is overestimated in each case. The three functionals also underestimate the position of the second peak. In the case of the optB88-vdW and VdW-DF2 functionals, the amplitude of the second peak is similar to the experimental value, whereas it is over-pronounced in the case of PBE-D3. Then, the three functionals predicts a similar amplitude for the third peak, that is slightly overestimated. However, in the case of PBE-D3 and VdW-DF2, the experimental curve is well reproduced in terms of position, whereas the optB88-vdW functional underestimates this position. Therefore, the three functionals lead to an over-structured liquid phase at ambient temperature. In comparison with RDF obtained with dispersion-inclusive functionals with the density fixed at its experimental value (see Ref. Møgelhøj et al., 2011), the amplitude is increased, but the second and third peaks are closer to the experimental curve. In terms of RDF, VdW-DF2 appears to be the most accurate functional with respect to experiments, with results similar to those obtained by Lee and Tuckerman [Lee and Tuckerman, 2006]. OptB88-vdW is slightly less accurate, whereas PBE-D3 differs strongly from the experimental curve within the first and second coordination spheres.

The trend is the same concerning the angle distributions. The position of the maximum of the distribution is well reproduced by the optB88-vdW and VdW-DF2 functionals, and slightly overestimated by the PBE-D3 functional. In the case of optB88-vdW and PBE-D3, the distribution is thinner than the experimental one, with a poor restitution of its shoulders. VdW-DF2 gives a distribution closer to experiments, with a good restitution of the shoulder at low angles, but it underestimates the one at high angles. Note that the shape of the curves highly depends on the criterion used to evaluate the distribution. For example, the method proposed by Soper *et al.* [Soper, 2007] leads to a smaller cutoff radius for

**Figure 3.17** ▶

Comparison of the experimental oxygen-oxygen radial distribution function at 300 K [Soper, 2007] with the prediction of different functionals. All functionals over-structure the liquid, with a much higher first peak than experiments. The second peak is shifted up, but the amplitude is similar to the experimental curve.

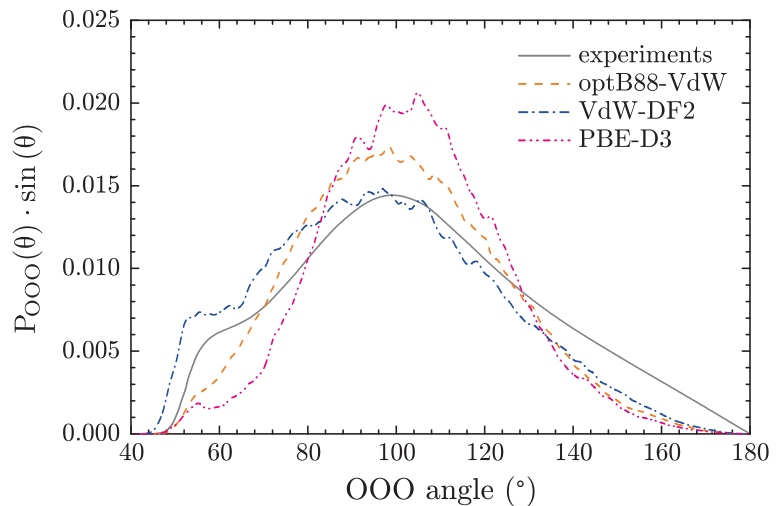


O-O pairs selection, and the distribution obtained are much thinner, without any shoulder, whatever the functional is used.

The width of the distribution obtained with optB88-vdW and PBE-D3 is similar to those obtained working at the experimental density with various functionals including functionals without any correction of dispersion contributions and hybrid functionals [DiStasio Jr et al., 2014], whereas VdW-DF2 leads to a much better agreement with the experimental curve. Moreover, the present distributions, obtained working at the equilibrium density predicted by the functional reproduce quite accurately the position of the maximum of the distribution, whereas it is systematically largely shifted when the experimental density is used, even using hybrid functionals [DiStasio Jr et al., 2014]. According to Jonchiere *et al.* [Jonchiere et al., 2011], some dynamical properties such as the self diffusion of water molecules is strongly dependent on interactions over several molecular sizes. One can thus expect that the overall good restitution of the local structure of water observed through the RDF and the angle distribution, especially in the case of the VdW-DF2 functional, will lead to accurate values of the self diffusion coefficient and the shear viscosity.

**Figure 3.18** ▶

Comparison of the OOO angle distributions in the first coordination shell at 300 K for different functionals and experiments [Soper and Benmore, 2008]. The function  $p_{OOO}(\theta) \cdot \sin(\theta)$  is normalized to unit area over the  $[0^\circ; 180^\circ]$  range. All functionals show an over-structuring of the liquid with a poor restitution of the shoulder at high angles observed experimentally. The shoulder around  $60^\circ$  is also poorly reproduced by optB88-vdW and PBE-D3, but well reproduced by VdW-DF2. Moreover, the position of the maximum of the distribution is overall well reproduced.



### 3.3.3 Hydrodynamics

In order to characterize the dynamical response of the models mentioned above, we calculated the self diffusion coefficient and the shear viscosity of water. The diffusion coefficient was computed from the slope of the mean squared displacement of the center of mass  $\langle \alpha^2 \rangle$

of water molecules [Frenkel and Smit, 1996]:

$$D = \lim_{t \rightarrow \infty} \frac{1}{2} \cdot \frac{\partial \langle \alpha^2 \rangle}{\partial t}, \quad \blacksquare \quad (3.15)$$

where  $\alpha$  denotes  $x$ ,  $y$  or  $z$ , and the error was evaluated from the standard deviation of the values obtained for the three directions. The viscosity was computed using the Green-Kubo formalism [Frenkel and Smit, 1996]:

$$\eta = \frac{V}{k_B \cdot T} \cdot \int_0^\infty \langle p_{\alpha\beta}(t) \cdot p_{\alpha\beta}(0) \rangle \cdot dt, \quad \blacksquare \quad (3.16)$$

where  $V$  denotes the volume of the simulation box,  $k_B$  the Boltzmann's constant,  $T$  the temperature and  $p_{\alpha\beta}$  is one of the five independent shear components of the stress tensor [Alfe and Gillan, 1998]:  $p_{xy}$ ,  $p_{xz}$ ,  $p_{yz}$ ,  $(p_{xx} - p_{yy})/2$  and  $(p_{yy} - p_{zz})/2$ . Again, the error is evaluated from the standard deviation of the values obtained for the five components. As in the case of empirical calculations in the previous paragraph, the question of the convergence of the method must be assessed, especially considering the simulation time used here.

The evolution of the Green-Kubo integrals is given in Fig. 3.19 for one functional. Even

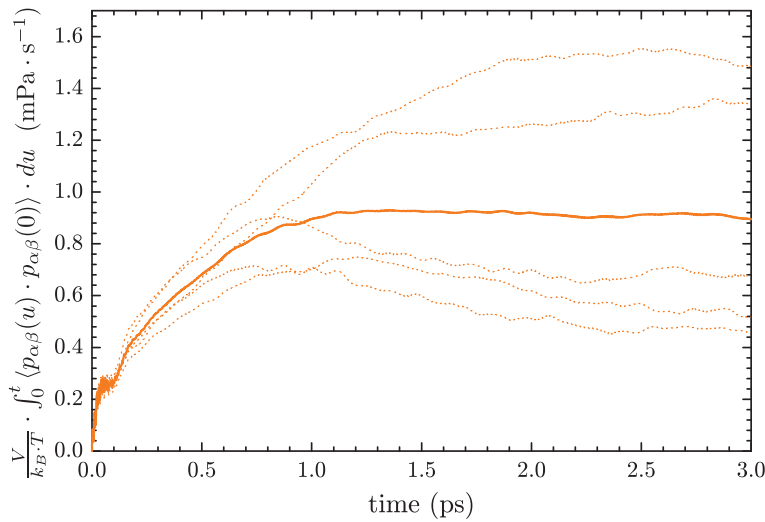


**Figure 3.19** ◀ Evolution of the Green-Kubo integrals with integration time. Dotted curves correspond to the different components  $\alpha\beta$  of the traceless stress tensor, and the plain curve correspond to the average over the five components.

though each component shows strong fluctuations, the averaged curve displays a well-defined plateau, that can be reasonably used as an estimation of the shear viscosity. The error bar is evaluated taking the standard deviation of the “plateau” values obtained for the five components.

Independently of the accuracy of the functional used for the calculation, the self diffusion coefficient strongly depends on the simulation box size due to hydrodynamics interactions [Zahn et al., 1997]. Yeh and Hummer [Yeh and Hummer, 2004] proposed a correction for those finite size effects, applied with success on water using various empirical force fields [Tazi et al., 2012]: the self diffusion coefficient corrected for finite size effects  $D_\infty$  can be derived from the calculated self diffusion coefficient  $D(L)$  obtained for a simulation box of size  $L$ , using:

$$D_\infty = D(L) + \frac{2.837 \cdot k_B \cdot T}{6 \cdot \pi \cdot \eta \cdot L}. \quad \blacksquare \quad (3.17)$$

This correction is critical in the case of AIMD calculations since the simulation box considered are very small. The values of  $D_\infty$  corresponding to the optB88-vdW and VdW-DF2 functionals are reported in Table 3.2, using the calculated viscosities for  $\eta$  in Eq. 3.17. Using the value of the density obtained without correction of the Pulay stress, the optB88-vdW functional strongly underestimates (by almost a factor 3) the self diffusion coefficient of water, in agreement with other studies [Miceli et al., 2015]. Using the corrected density, the self diffusion coefficient is strongly improved, but is still too low, with a relative error of 48 %

with respect to the tabulated value. The value obtained with PBE-D3 is much worse, which is surprising since this functional is the most accurate in terms of room temperature density. In contrast, the value obtained using the VdW-DF2 functional is in quantitative agreement with the tabulated value within the error bars, as in the case of the TIP4P/2005*f* force field, even if the error bar is much larger in the case of DFT.

Functional	$D$ ( $10^{-9} \text{ m} \cdot \text{s}^{-2}$ )	$D_{\infty}$ ( $10^{-9} \text{ m} \cdot \text{s}^{-2}$ )	$\eta$ (mPa·s)
optB88-vdW (uncorr.)	$0.64 \pm 0.10$	$1.06 \pm 0.24$	$1.20 \pm 0.20$
optB88-vdW (corr.)	$0.84 \pm 0.04$	$1.31 \pm 0.23$	$1.10 \pm 0.19$
VdW-DF2 (corr.)	$1.43 \pm 0.20$	$1.99 \pm 0.38$	$0.91 \pm 0.12$
PBE-D3 (corr.)	$0.27 \pm 0.06$	$0.29 \pm 0.10$	$3.6 \pm 1.1$
TIP4P/2005 <i>f</i>	–	$2.30 \pm 0.01$	$0.76 \pm 0.05$
experimental	–	2.3	0.896

As we already mentioned, the self diffusion coefficient was shown to be strongly influenced by long range interactions within the liquid [Jonchiere et al., 2011]. This includes dispersion interactions, which decrease slowly with the distance. The VdW-DF2 reproduces more accurately the overall shape of the water RDF and angles distribution than the optB88-vdW and PBE-D3 functionals, and especially the position and the amplitude of the third peak of the RDF. This is consistent with the present observation that the VdW-DF2 reproduces much better the self-diffusion of water than the optB88-vdW functional.

A similar trend is observed concerning the shear viscosity. For this observable, as mentioned in the first section of this chapter, no finite box size effect is expected. The optB88-vdW overestimates the shear viscosity of water when no correction is taken into account for the Pulay stress, with a relative error of 34 %, as shown in Table 3.2, whereas the error is reduced to 23 % with the correction. Again, PBE-D3 leads to a value that is very far from experiments. In contrast, the VdW-DF2 functional is in agreement with the experimental value, and gives a slightly better value than the TIP4P/2005*f* force field. The shear viscosity of water is mainly due to hydrogen bonding. So, it seems that using the density predicted by the functional improves the hydrogen bond structure and dynamics. The shear viscosity has only be scarcely considered using AIMD. The only value for bulk water to our knowledge, obtained without taking into account dispersion effects, is much higher than the different values obtained here [Kühne et al., 2009]. Thus, when used at their equilibrium density, the two dispersion functionals used here enable an accurate estimation of the shear viscosity.

### 3.3.4 Summary

We showed that accurate  $NpT$ -AIMD calculations are now feasible using moderate cut-off values. Correction for Pulay stress strongly improves the predictions of the calculations with respect to standard  $NpT$  calculations. The VdW-DF2 functional reproduces almost quantitatively various observables such as the room temperature density, the RDF, the self-diffusion coefficient, and the shear-viscosity. However, it gives a wrong temperature dependence of the liquid density (although the variations of density are not large as compared to uncertainties). Concerning this last point, the optB88-vdW functional gives better results, predicting a maximum of density close to its tabulated temperature, but the predictions for the other observables considered here are less accurate. This opens new insight for complex aqueous system studies, where the density of water cannot be a priori figured out, and should help to understand the role of quantum effects in the dynamics of liquid water.

## 4 Conclusion

In this chapter, we saw that the TIP4P/2005*f* force field describes accurately the long-time dynamics of water, and offers an interesting connection with short-time elastic properties of the liquid at low temperatures using the so-called elastic models. *Ab initio* approaches in the isothermal-isobaric ensemble, using the correction of the pressure introduced, also predicts accurately some properties of water, especially using the VdW-DF2 functional, and

**Table 3.2.** Comparison of the self-diffusion coefficient and shear viscosity for different functionals [calculated in the present work] and experimental values [calculated in the present work and tabulated values]. The values are given for the TIP4P/2005*f* force field (given for comparison).

should be used with benefits in the future to investigate the role of quantum effects in the dynamics of water. However, regarding the numerical cost of the approach, and its limited accuracy with respect to classical molecular dynamics using the TIP4P/2005*f* force field, the latter approach will be preferred to the former in the next chapters, dedicated to water based complex systems.



## Chapter 4

# Water hydrodynamics near a hydrophobic surface

### Outline

1	Aim of the study . . . . .	67
2	Simulations details . . . . .	67
3	Temperature dependence of the friction coefficient and the slip length . . . . .	68
4	Origin of the friction temperature dependence . . . . .	71
4.1	Structure of the liquid near the interface . . . . .	71
4.2	Corrugation of the solid surface . . . . .	73
4.3	Liquid and interface relaxation . . . . .	73
5	Summary and conclusion . . . . .	75

## 1 Aim of the study

We characterized in the previous chapter the dynamics of bulk water. In various media, including clays, water is surrounded by solid surfaces. We pointed out in Chap. 1 the particular properties of liquids near an interface, as for example friction/slippage, with its application to enhance the permeability of nano-channels. Fluid-solid friction is well known to be highly dependent of the temperature in the tribology community, especially in the case of complex fluids like polymers [Drda and Wang, 1995, Yoshizawa and Israelachvili, 1993]. Moreover, as we saw in Chap. 1 and 3, water exhibits many anomalous properties at low temperatures. However, most of the current knowledge about interfacial water concerns properties at room temperature. The aim of this chapter is – using classical molecular dynamics simulations – to investigate the low temperature hydrodynamic properties of water in the vicinity of a prototypical hydrophobic solid surface. We will first introduce the system used for the study, and then analyze the temperature dependence of both interfacial friction coefficient and slip length (see Fig. 4.1).

## 2 Simulations details

All simulations were performed using the LAMMPS package. The simulations boxes are the same as those used in the previous chapter for steady-state shear calculations, except they are here used for both equilibrium (using the Green-Kubo formalism) and nonequilibrium (steady-state shear) calculations. The solid surface is a generic apolar surface, made of a set of atoms localized on the nodes of a face cubic centered (fcc) lattice, with lattice parameter

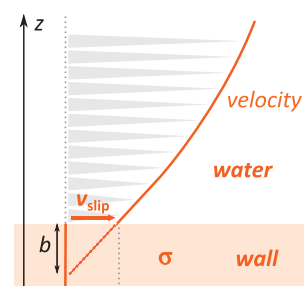


**Figure 4.1** ▲ Liquid-solid friction. Friction can be characterized by the friction coefficient  $\lambda = \sigma / v_{\text{slip}}$  or the slip length  $b = \eta / \lambda$ , where  $\eta$  denotes the shear viscosity of the liquid.

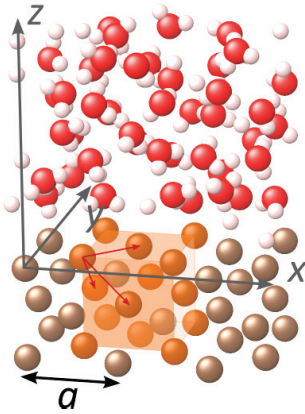


**Figure 4.2** ▲  
Partial screenshot of the simulation box. A fcc unit cell is highlighted.

$a = 5.34954 \text{ \AA}$  (see Fig. 4.2). The thickness of the solid is 5 atomic layers, *i.e.* about  $10.7 \text{ \AA}$ , that is higher than the cutoff radius value used to compute Lennard-Jones interactions (there is no Coulombic term since atoms are neutral), so the liquid sees a semi-infinite solid surface.

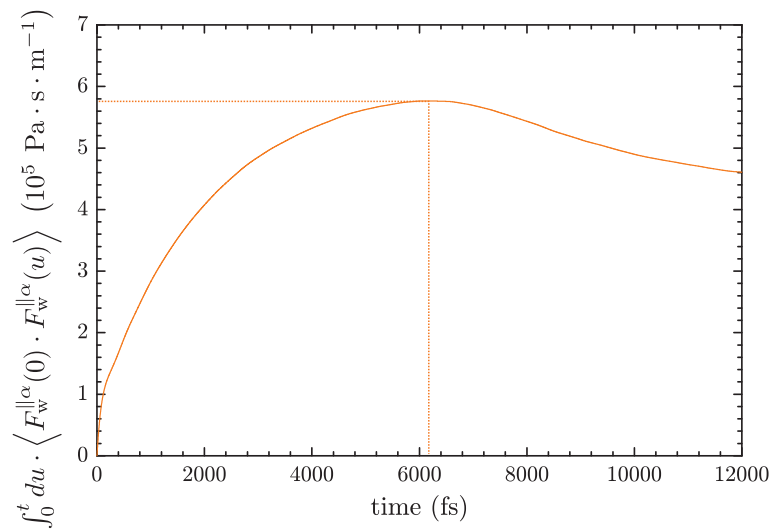
The walls are rigid, and interact with oxygen atoms through a Lennard-Jones potential with  $\epsilon_C = 0.164 \text{ kcal} \cdot \text{mol}^{-1}$  and  $\sigma_C = 3.37 \text{ \AA}$ . The thickness of the water layer is about  $50 \text{ \AA}$ . Thus, since confinement water recovers its structure above  $10 \text{ \AA}$  from the surface, no effect of confinement is expected here [Raviv et al., 2001, Li et al., 2007, Zhu et al., 2012, Zhang et al., 2013, Markesteijn et al., 2012]. The temperature is scanned from 225 to 360 K. In the case of steady-state shear calculations, for each wall velocity, the simulation was run during 1 ns to reach the steady-state, and then measurements were performed during 1 ns. For Green-Kubo calculations, the system was first equilibrated during 0.5 ns and then, three measurements of 1 ns were performed. In each case, a Nose-Hoover thermostat was applied to liquid atoms in the direction normal to the walls during the simulation. The pressure was fixed by applying a force normal to the wall on the solid surfaces during the whole simulation.

The shear-viscosity of the fluid, the friction coefficient and the slip length were computed using both equilibrium Green-Kubo formalism and nonequilibrium steady-state shear flow methods described in Chap. 2.

### 3 Temperature dependence of the friction coefficient and the slip length

As in the case of shear viscosity calculations, one must check the validity and consistency of both Green-Kubo and steady-state shear flow approaches. The typical time evolution of the Green-Kubo integral for the friction coefficient is shown in Fig. 4.3. Contrary to the Green-Kubo integral for the shear viscosity, the curve displays no plateau. The integral increases to a maximum value and then decreases, due to the finite thickness of the water layer [Joly et al., 2016]. We took the maximum value as the value of the friction coefficient, as it was done elsewhere [Joly et al., 2016]. This integral was evaluated in the two directions tangential to the walls, for each wall. It means 4 values of  $\lambda$  were obtained from each of the 3 replicas used. The values reported in the following for each temperature are averaged over those 12 values, and the error is computed as their statistical standard error.

**Figure 4.3** ►  
Typical shape of the Green-Kubo integral vs time curve (here at 240 K).



For steady-state shear flow calculations, we checked – using five different shear rates – that the friction coefficient did not depend on the shear rate. This was indeed the case, as shown on Fig. 4.4, except at high temperatures, at which friction values looked more dispersed. Consequently, for the highest temperatures, the friction coefficient was averaged only over

the two smallest shear rates, whereas it was averaged over the five shear rates for other temperatures. Again, the statistical standard error is used to estimate error bars.

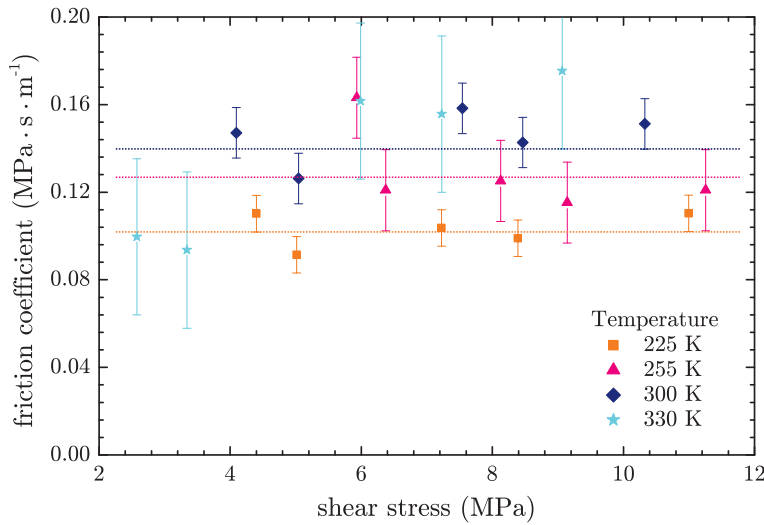


**Figure 4.4** ◀ Shear stress dependence of the friction coefficient for various temperatures. Dotted lines show average values.

The temperature dependence of the water-wall friction coefficient is reported in Fig. 4.5 for Green-Kubo and steady-state shear flow measurements. Both methods are in good agree-

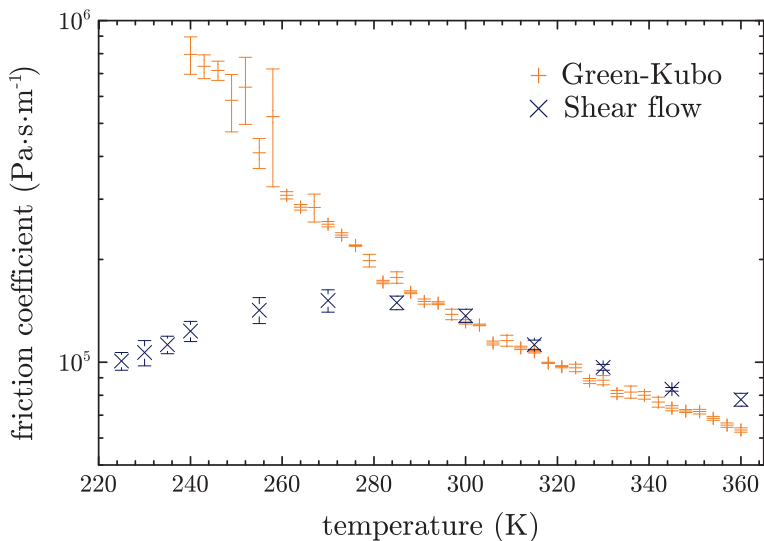


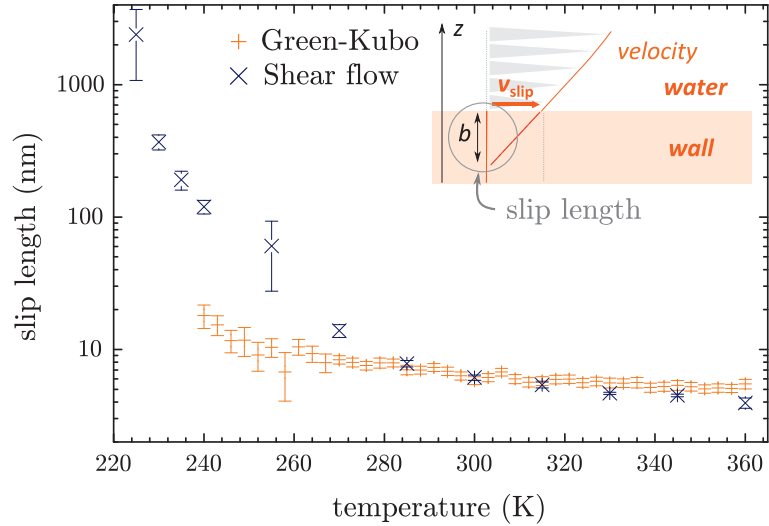
**Figure 4.5** ◀ Evolution of the water-wall friction coefficient with respect to the temperature for Green-Kubo (+) and steady-state shear flow (x) calculations.

ment for temperatures higher than 300 K and predict a slight decrease of the friction coefficient when the temperature increases (the slight difference at high temperatures is due to a misevaluation of the friction coefficient using the Green-Kubo method, since the limit of linear response regime is reached, as discussed previously). However, at lower temperatures, the two sets of measurements differ qualitatively: Green-Kubo calculations predict an increase of the friction coefficient at low temperatures, in the continuation of high temperature measurements, whereas steady-state shear flow calculations predict a non-monotonic evolution of the friction coefficient, with a slight decrease at low temperatures.

We also calculated the evolution of the slip length  $b = \eta/\lambda$  with the temperature using the shear viscosity measurements presented in Chap. 3 (see Fig. 4.6). Both methods predict an increase of the slip length at low temperatures, but as in the case of the friction coefficient, the two sets of measurements differ below 300 K, with a faster increase in the case of steady-state shear flow measurements.

There are two interesting points. First, whatever the method used, the slip length, defined as the ratio  $\eta/\lambda$ , increases at low temperatures. It means that, even for the Green-Kubo calculations which predicts an increase of the friction coefficient at low temperatures, the shear

**Figure 4.6** ▶ Evolution of the water-wall slip length with respect to the temperature for Green-Kubo (+) and steady-state shear flow (×) calculations.



viscosity increases faster than the friction coefficient. Secondly, considering steady-state shear flow calculations, we see that the slip length reaches high values in the supercooled regime. Especially, for moderately supercooled water, the slip length is found to be of the same order of magnitude that in the case of water/graphene friction at room temperature (between 30 and 80 nm depending on the authors [Kotsalis, 2008, Thomas and McGaughey, 2008, Falk et al., 2010]), and it reaches 1  $\mu\text{m}$  before the nucleation limit. Generally speaking, superlubricity implies complex liquids or superhydrophobic surfaces. This is not the case here, since we consider a simple liquid on a simple hydrophobic surface.

Such slip lengths may open new perspectives in the development of nanofluidic devices in a low temperature environment. Indeed, as explained in Chap. 1, slippage increases the water flux through a nanochannel of width  $L$  by a factor  $1 + C \cdot b/L$ , where  $C$  is a constant close to 1. Consequently, working at low temperatures would enable to considerably increase the hydrodynamic permeability of nanochannels.

However, since our two sets of measurements are in disagreement, we first need to solve this discrepancy. Especially, we must determine if the difference means one of the two approaches is not valid, or if it corresponds to two different regimes of friction (since one is at equilibrium and the other is not). This is the aim of the reminder of this chapter.

To check the role of the surface in this effect, we performed extra calculations (using Green-Kubo and steady-state shear flow methods) at 255 K replacing the model hydrophobic surface by two graphene sheets. The corresponding values of the friction coefficient and the slip length are given in Table 4.1. As in the case of the model hydrophobic surface, the val-

**Table 4.1** ▶ Water-graphene friction coefficient  $\lambda$  and slip length  $b$ .

	Green-Kubo	Shear flow
$\lambda$ ( $\text{Pa} \cdot \text{s} \cdot \text{m}^{-1}$ )	$(41.7 \pm 2.6) \cdot 10^3$	$(14.4 \pm 0.7) \cdot 10^3$
$b$ (nm)	$99 \pm 16$	$294 \pm 52$

ues of the slip length predicted by steady-state shear flow calculations are much higher than those predicted by Green-Kubo calculations. Moreover, the value of the slip length is much higher than on the model surface, consistently with room temperature measurements.

The existence of two friction coefficients is a well-known property of solid-solid friction: the interface can sustain a higher tangential force when the solids are not sliding one over the other than when they are sliding. This leads to the so called “stick-slip” motion when one solid is dragged over the other with a fluctuating moderate force, that disappears above some critical force – one then gets a “smooth sliding” regime. Here, Green-Kubo calculations would correspond to no effective sliding since the system is at equilibrium, whereas steady-state shear flow calculations would correspond to high velocity sliding. One can wonder thus to what extent a parallel can be made between the two friction coefficients observed here at low temperature and those traditionally observed in the case of solid-solid friction. Actually, various cases of transitions between different friction regimes have been

reported for fluid-solid friction. For example, for polymer melts, a transition from a “weak” slip regime – corresponding to desorption of molecules from the solid surface or partial disentanglement of polymer molecules between adsorbed molecules and other molecules – to a “strong” slip regime – corresponding to complete disentanglement of molecules at higher flow velocities – can be observed [Drda and Wang, 1995, Hatzikiriakos, 2015]. Another interesting example is molecularly thin films of a simple fluid. Stick-slip oscillations with a transition to a “smooth” slip regime above a critical temperature or a critical slip velocity have been reported and studied extensively [Israelachvili et al., 1990, Yoshizawa and Israelachvili, 1993, Gee et al., 1990]. In that case, the transition from a regime to another is explained by transitions from a highly ordered “solid-like” liquid that tends to stick the two solid surfaces together and a disordered “liquid-like” film that flows easily. At sufficiently high temperature or slip velocity, the ordered phase cannot nucleate anymore and one gets a “smooth” slip regime [Yoshizawa and Israelachvili, 1993]. In the present case, similarities with those two examples can be found. On the one hand, since supercooled water is an associated liquid, *i.e.* is highly reticulated by hydrogen bonds, it can behave to some extent like a polymer melt. On the other hand, a strong organization of molecules can occur near the crystal surface at low temperatures and can modify the sliding dynamics. In the next section, we will analyze the evolution of the structure of water near the walls with the temperature and its relaxation dynamics to try to understand to what extent those hypotheses can apply to water.

## 4 Origin of the friction temperature dependence

From the equilibrium Green-Kubo formula for liquid-solid friction [Bocquet and Barrat, 1994] (see Chap. 2),

$$\lambda = \frac{1}{A \cdot k_B \cdot T} \cdot \int_0^\infty dt \cdot \langle F_w^{\parallel\alpha}(0) \cdot F_w^{\parallel\alpha}(t) \rangle, \quad \blacksquare \quad (4.1)$$

where  $A$  denotes the surface of the wall and  $F_w^{\parallel\alpha}$  the total force applied to the wall in the direction  $\alpha$  tangential to the wall, one can decompose the friction coefficient as [Falk et al., 2010, Barrat et al., 1999]:

$$\lambda \approx \frac{\tau_F}{k_B \cdot T} \cdot \rho_1 \cdot f_{q_{\parallel}}^2 \cdot S(q_{\parallel}), \quad \blacksquare \quad (4.2)$$

where  $\tau_F$  is the decorrelation time of the tangential force acting between the wall and water,  $\rho_1$  is the surface density of water near the interface,  $f_{q_{\parallel}}$  is the roughness of the landscape created by the wall at a distance corresponding to the position of the first layer of water molecules, and  $S(q_{\parallel})$  is the 2-dimensional structure factor of water for the wavenumber corresponding to the transverse periodicity of the wall. Thus, this formula tells us that the interfacial friction depends on:

- solid and liquid structures near the interface;
- the amount of water at the interface;
- the temperature;
- the relaxation time of water-wall interactions.

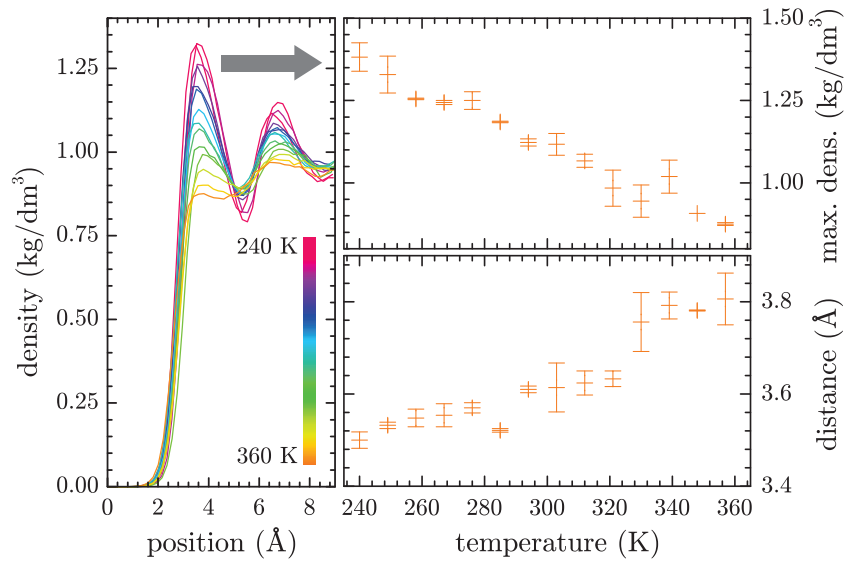
So, the friction is inversely proportional to the temperature and should consequently increase at low temperature, as it is observed for Green-Kubo calculations. Even if this formula is only valid for Green-Kubo calculations, it is interesting to analyze the different parameters that influences friction involved in this formula.

## 4.1 Structure of the liquid near the interface

### 4.1.1 Density

The evolution with temperature of the density profile, *i.e.* the variation of the density with the position in the direction normal to the walls, is shown in Fig. 4.7 (left). At high temperature, the profile is almost flat, as expected for a hydrophobic surface, whereas at low temperature, a strong layering is observed. We define the contact density  $\rho_1$  in Eq. (4.2) as the maximum of the first peak of the density profile. This value increases almost linearly when decreasing the temperature, as shown in Fig. 4.7 (top right). According to Eq. (4.2), this tends to increase the friction coefficient at low temperatures, as observed with Green-Kubo calculations. Performing the calculation of the density profile for both Green-Kubo and steady-state shear flow calculations, no difference is observed between the two sets of measurements. Thus, the evolution of the density cannot explain the different behavior reported.

**Figure 4.7** ▶ Evolution of water density near the surface with respect to temperature. Left: Evolution of density profile near the wall. The position reported corresponds to the distance to the wall. Top right: Temperature dependence of the maximum value of the density profile, *i.e.* the peak density of the first layer of water near the wall. Bottom right: Temperature dependence of the water-wall distance, evaluated as the distance between the solid surface atoms and the first maximum of the density profile.



At the same time a layering appears, the distance between the wall and the first water molecules layer decreases, as shown in Fig. 4.7 (bottom right). This might indicate an increase of water-wall interactions, and thus, of the friction. But again, since the same phenomenon is observed in both regimes, it cannot explain the difference.

### 4.1.2 2-d structure factor

The density profiles indicate a structuration of the fluid in the direction normal to the walls, but tells us nothing about a possible structuration in directions parallel to the walls. Especially, a partial crystallization of adsorbed molecules could explain a change of the regime of friction. To analyze the tangential structure of the liquid, we compute the 2-d structure factor of the fluid inside the first layer of water molecules near the solid surface.

The 2-d structure factor  $S$  is defined as [Falk et al., 2010]:

$$S(q) = \frac{1}{N} \cdot \left\langle \left( \sum_{j=1}^N \cos(\vec{q} \cdot \vec{x}_j) \right)^2 + \left( \sum_{j=1}^N \sin(\vec{q} \cdot \vec{x}_j) \right)^2 \right\rangle, \quad (4.3)$$

where  $\vec{q}$  is a vector of the reciprocal space in the directions parallel to the walls,  $\vec{x}_j$  denotes the 2-d position of the center-of-mass of water molecules inside the first layer, and  $\langle \dots \rangle$  denotes an average over all directions tangential to the walls. The evolution of the structure factor with the temperature is shown in Fig. 4.8. The structure factor shows oscillations that decrease at high wavenumbers. Moreover, the amplitude of the oscillations slightly increases when the temperature decreases. We also see high frequency oscillations at low wavenumbers, corresponding to the wavenumber associated to the cutoff radius used to

compute Lennard-Jones interactions, and which are consequently a purely numerical artifact.

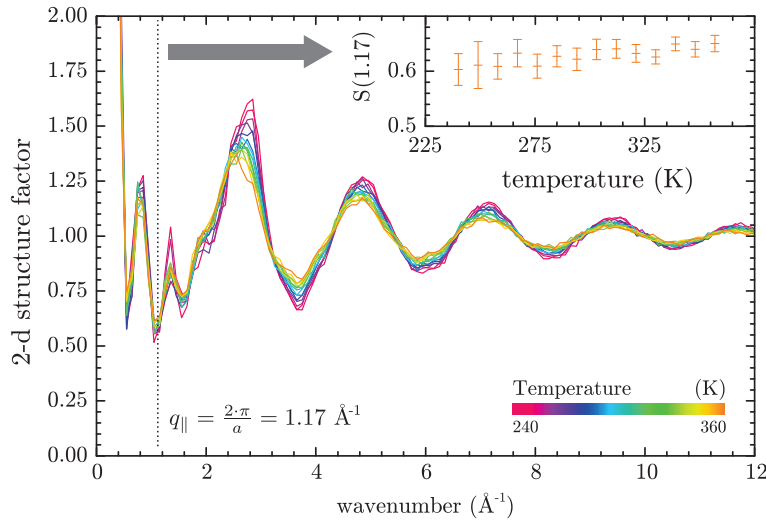


**Figure 4.8** ◀ Evolution of the 2-d structure factor of water near the interface with respect to the temperature in directions parallel to the walls. Inset: Temperature dependence of the 2-d structure factor for the wavevector corresponding to the periodicity of the lattice in the reciprocal space.

Since we are interested in the liquid structure commensurable to that of the wall (which will control friction), the structure factor is evaluated at  $q_{\parallel} = 2 \cdot \pi / a \approx 1.17 \text{ \AA}^{-1}$  with  $a$  the lattice parameter of the wall (see inset in Fig. 4.8). Unfortunately, this wavevector corresponds to the part of the curve that is perturbed by the cutoff radius. However, since  $q_{\parallel}$  corresponds to a minimum of the oscillations, the effect should be limited. The amplitude of the structure factor at  $q_{\parallel}$  only slightly decreases at low temperatures, which contributes to a decrease of the friction coefficient according to Eq. (4.2). However, the decrease is very small, showing a negligible effect of temperature on the transverse structuration of the fluid. Moreover, as in the case of the density, the evolution is exactly the same for Green-Kubo and steady-state shear flow measurements.

## 4.2 Corrugation of the solid surface

We mentioned previously that the distance between the first layer of water molecules and the wall decreases at low temperatures. That might affect the friction coefficient. In this paragraph, we compute the interfacial free energy to analyze the potential energy landscape created by the wall. The interfacial free energy is defined as:

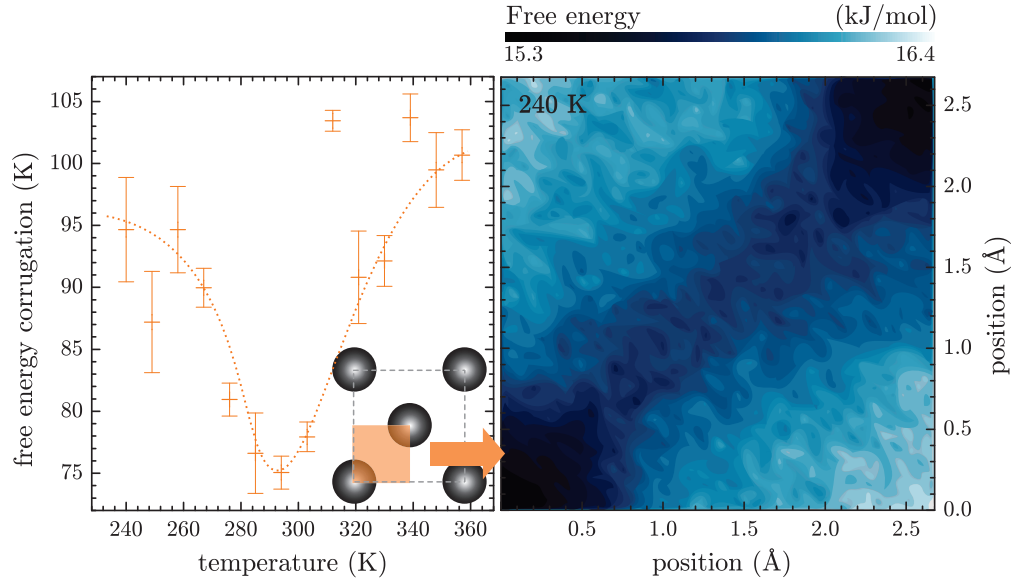
$$F(x, y) = -\frac{1}{\Delta z} \cdot \int_{z_{\text{wall}}}^{z_{\text{wall}} + \Delta z} dz \cdot k_B \cdot T \cdot \ln(p_O(x, y, z)), \quad \blacksquare \quad (4.4)$$

where  $x$  and  $y$  denote the coordinates in the direction tangential to the wall,  $z$  the coordinate in the direction normal to the wall,  $p_O$  is the oxygen atoms probability distribution function (pdf), and the integral is evaluated over the first water layers, by taking  $\Delta z = 10 \text{ \AA}$ . For each temperature, the oxygen atoms pdf is averaged over 200 ps. The typical evolution of the free energy with the position over a quarter of unit cell of the wall is shown in Fig. 4.9 (right). Then, the corrugation of this free energy landscape is computed as the difference between the minimum and maximum value, and reported in Fig. 4.9 (left). For more clarity, the energy corrugation is expressed in temperature unit.

The corrugation has a non-monotonous behavior, with a minimum around 300 K, showing a competition between (i) the decrease of the liquid-wall distance at low temperatures and (ii) the flatter of the surface density profile at high temperatures. It means that the surface is rougher at low and high temperatures than at intermediate temperatures, which disagrees with both Green-Kubo and steady-state shear flow calculations of the friction coefficient. Indeed, both methods predict a decrease of the friction coefficient at high temperatures, that should indicate a smoother surface. However, whatever the temperature is considered, the corrugation is extremely low compared to the thermal energy of the system. Consequently, the surface appears very smooth in the range of temperatures considered in

**Figure 4.9** ▶

Left: Evolution of the corrugation of the energy landscape created by the wall with respect to the temperature. Right: Typical shape of the energy landscape (here at 240 K).



the present study. Thus, the surface roughness does not explain the temperature dependence of the friction coefficient.

### 4.3 Liquid and interface relaxation

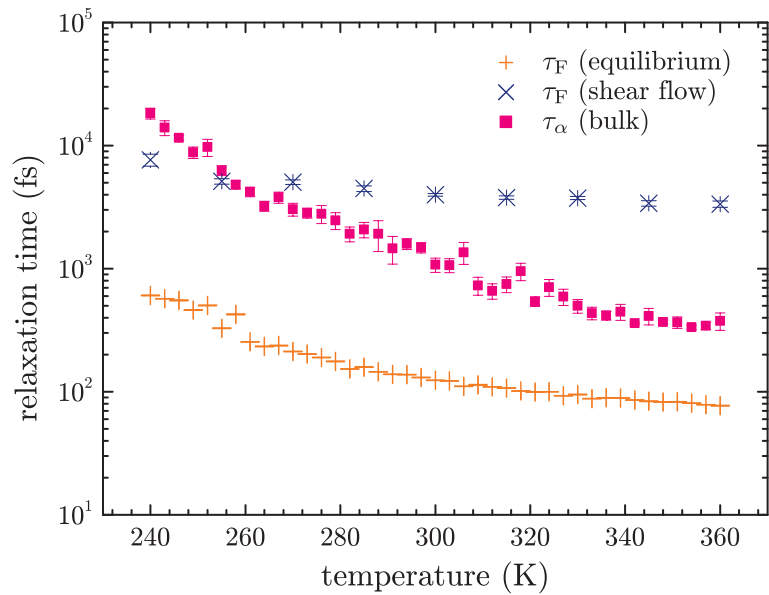
We finally probe directly the dynamics of the interface through the water-wall tangential force decorrelation time  $\tau_F$ , defined as the plateau value of the time-integral:

$$\tau_F = \int_0^\infty dt \cdot \frac{\langle \delta F_W^{\parallel\alpha}(0) \cdot \delta F_W^{\parallel\alpha}(t) \rangle}{\langle F_W^{\parallel\alpha}(0) \cdot F_W^{\parallel\alpha}(0) \rangle}, \quad (4.5)$$

with  $\delta F_W^{\parallel\alpha}(t) = F_W^{\parallel\alpha}(t) - \langle F_W^{\parallel\alpha} \rangle$ . The evolution of  $\tau_F$  with the temperature for both Green-Kubo and steady-state shear flow calculations is reported in Fig. 4.10.

**Figure 4.10** ▶

Evolution of the friction force relaxation time for both Green-Kubo (+) and steady-state shear flow (x) calculations. The curve corresponding to the  $\alpha$ -relaxation time of bulk water (see Chap. 3) is also plotted for comparison.



In both cases,  $\tau_F$  increases at low temperature: for Green-Kubo calculations, it is approximately multiplied by 10 with respect to the highest temperature considered here, whereas the increase is lower in the case of steady-state shear flow calculations. However, in the case of steady-state shear flow calculations, the decorrelation time is more than one order of

magnitude higher than in the case of Green-Kubo calculations, which, regarding Eq. (4.2), does not explain the lower values of the friction coefficient measured under steady-state shear flow.

We compare then this interfacial relaxation time to a liquid relaxation time, the  $\alpha$ -relaxation time, assuming its value in the vicinity of the wall is close to its bulk value. In the case of Green-Kubo calculations,  $\tau_F$  is much lower than  $\tau_\alpha$ , whereas in the case of shear flow calculations, both observables are of the same order of magnitude, with a crossover at low temperatures, as shown in Fig. 4.10. If the liquid relaxes more slowly than the interface, one can expect that the fluid appears frozen for the interface and the friction coefficient should decrease. However, in the present case, comparing  $\tau_F$  and  $\tau_\alpha$  at high temperatures, one would expect different friction regimes ( $\tau_\alpha$  is between the Green-Kubo and shear-flow values of  $\tau_F$ ) which is not consistent with the agreement observed between the two sets of friction coefficient measurements reported at high temperature. Nevertheless, looking only at steady-state shear flow calculations, the crossover between  $\tau_F$  and  $\tau_\alpha$  may indicate the system enters in a “solid friction” regime, that could explain the decrease of the friction coefficient.

## 5 Summary and conclusion

---

Using molecular dynamics, we computed the friction coefficient of water on a model hydrophobic surface. At low temperatures, an increase of the friction coefficient is observed for Green-Kubo calculations, whereas a decrease is observed for steady-state shear flow calculations. This decrease goes along with a rapid increase of the slip length, that opens new perspectives to develop very high permeability nano-channels working at low temperatures. By probing then the structure and dynamics of the interface using various observables, this surprising behavior might be due to a transition to a “solid friction” regime related to a crossover between the  $\alpha$ -relaxation time and the friction force decorrelation time at low temperature. However, we failed to explain the difference observed between Green-Kubo and steady-state shear flow calculations.

Steady-state shear flow calculations are based on a direct application of the definition of the friction coefficient. Moreover, we checked that calculations were performed within the linear response domain. Consequently, the validity of this approach should not be questionable. In contrast, concerning Green-Kubo calculations, the formula is based on fluctuations of the system at equilibrium. So, one can wonder if it is still valid in the supercooled regime, where the system is out of equilibrium in a thermodynamic point of view. The question is particularly relevant since both methods give similar results in the “stable” liquid domain, whereas they differ in the “metastable” domain. One must mention also that the Green-Kubo formula for liquid-solid friction is controversial [Petřavac and Harrowell, 2007]. In addition, further work should also check the influence of the thermostat, that can modify the dynamics of the system. However, the reason why the two methods differ only at low temperature remains an open question. An experimental investigation of the evolution of the slip length with the temperature in the supercooled domain – for example using Surface Force Apparatus of Atomic Force Microscopy – should help to solve these discrepancies and hopefully confirm the giant slippage that can be obtained at low temperature. One should also compute the friction coefficient at low temperatures for different interfacial energies (*i.e.* different water-wall  $\epsilon$  parameters in the Lennard-Jones potential) to see if giant slippage is also observed for wetting interfaces.



## Chapter 5

# Influence of dissolved salts on the transport and structural properties of water

### Outline

1	Molecular Dynamics in Electronic Continuum . . . . .	78
1.1	Principle . . . . .	78
1.2	Dielectric constant of TIP4P/2005f water . . . . .	78
1.3	Application, pros and cons of the method . . . . .	79
2	Force field optimization . . . . .	80
3	Molecular dynamics methods . . . . .	82
4	Application of the model . . . . .	82
4.1	Crystal structures . . . . .	82
4.2	Liquid structure . . . . .	82
4.3	Water self diffusion . . . . .	84
4.4	Shear viscosity . . . . .	85
4.5	Mid-infrared absorption spectrum . . . . .	87
5	Conclusion . . . . .	88

In a recent paper, Kim et al. [Kim et al., 2012] pointed out a common flaw of salt models. They studied the evolution of the self diffusion coefficient of water with respect to the concentration for nine alkali metal halides, using various ions and water force fields. Whatever the combination they used for the two models, they always observed a decrease of the self diffusion coefficient of water when the salt concentration is increased, whereas the three behavior – chaotrope, neutral and kosmotrope – were reported experimentally in terms of self diffusion (see Chap. 1). A possible explanation of this flaw might be the poor restitution of the dielectric properties of water by non-polarizable force fields, or the fact that ion polarizability is not taken into account. However, as shown by Kim et al. [Kim et al., 2012] using the AMOEBA force field, taking into account polarizability improves the quantitative agreement with experimental values of self diffusion but the evolution with respect to the salt concentration still differs qualitatively from experiments.

Since the publication of their work, several solutions have been suggested or challenged to eliminate this deficiency. In a recent paper about water models, Vega [Vega, 2015] suggested a fair restitution of water properties requires to “leave the dogma”, *i.e.* to use different simulation parameters to describe potential energy and dielectric properties of water. It means, for example, using charges different than  $\pm 1$  for univalent ions. This approach was tested by Kann and Skinner [Kann and Skinner, 2014] by scaling the charge of ions in order to compensate the difference between the calculated and tabulated dielectric constant of pure water. Using the model by Mao and Pappu [Mao and Pappu, 2012] for ions and various water models, they obtained a slight increase of the self diffusion coefficient of water in CsI solutions when the concentration is increased, in qualitative agreement with experiments,

but still far from a quantitative agreement. However, they did not adjust the Lennard-Jones parameters of the model with respect to the new charges, that could have improved their results. Ding et al. [Ding et al., 2014] obtained similar results using *ab initio* molecular dynamics. More recently two studies reached quantitative agreement between experiments and calculations: Li et al. [Li and Wang, 2015] using a non-polarizable model with a much more complex parametrization than standard water force fields, and Yao *et al.* [Yao et al., 2015] using a polarizable force field. However, both studies were limited to a reduced set of relatively small ions without pronounced chaotropic effects on self diffusion. Further work is therefore needed to check the transferability of those approaches over a larger set of salts.

In this chapter, we try to go further with Kann and Skinner approach [Kann and Skinner, 2014], using the promising TIP4P/2005f water force field [González and Abascal, 2011], since we showed in Chap. 3 that this force field reproduces accurately the self-diffusion coefficient and shear viscosity of water over a wide range of temperatures.

## 1 Molecular Dynamics in Electronic Continuum

### 1.1 Principle

The Kann and Skinner approach [Kann and Skinner, 2014] is based on the so-called Molecular Dynamics in Electronic Continuum (MDEC) method. We first introduce the principle of this method.

For a system of  $N$  charged particles in vacuum, the electrostatic interaction energy can be expressed as:

$$U_{\text{el}} = \frac{1}{2} \cdot \sum_{i=1}^N \sum_{j=1}^N \frac{q_i \cdot q_j}{4 \cdot \pi \cdot \epsilon_0 \cdot r_{ij}}, \quad \blacksquare \quad (5.1)$$

where the sums stand over all particles and  $r_{ij}$  denotes the distance between particles  $i$  and  $j$ .

The aim of MDEC is to model an homogeneous medium of relative dielectric constant  $\epsilon_r$ . To do so, one adjusts the charges of particles so that:

$$q_i^{\text{eff}} = \frac{q_i}{\sqrt{\epsilon_r}}, \quad \blacksquare \quad (5.2)$$

where  $q_i^{\text{eff}}$  denotes the new charge of the particle. The electrostatic interaction energy can thus be rewritten:

$$U_{\text{el}} = \frac{1}{2} \cdot \sum_{i=1}^N \sum_{j=1}^N \frac{q_i^{\text{eff}} \cdot q_j^{\text{eff}}}{4 \cdot \pi \cdot \epsilon_0 \cdot r_{ij}} = \frac{1}{2} \cdot \sum_{i=1}^N \sum_{j=1}^N \frac{q_i \cdot q_j}{4 \cdot \pi \cdot \epsilon_0 \cdot \epsilon_r \cdot r_{ij}}. \quad \blacksquare \quad (5.3)$$

The system is formally equivalent to  $N$  particles lying in a medium of relative dielectric constant  $\epsilon_r$ .

The same method can be applied to compensate the underestimation of the dielectric constant of water using nonpolarizable force fields. In that case, denoting  $\epsilon_{\text{ff}}$  the relative dielectric constant predicted by the force field, and  $\epsilon_r$  the tabulated “real” relative dielectric constant, one must define:

$$q_i^{\text{eff}} = q_i \cdot \sqrt{\frac{\epsilon_{\text{ff}}}{\epsilon_r}}. \quad \blacksquare \quad (5.4)$$

Thus, to apply this correction in the case of the TIP4P/2005f forcefield, one must first determine the associated dielectric constant.

## 1.2 Dielectric constant of TIP4P/2005f water

One considers a cubic box filled by  $16 \times 16 \times 16$  water molecules, with periodic boundary conditions. The relative dielectric constant of the system can be computed for the considered force field  $\epsilon_{\text{ff}}$  using:

$$\epsilon_{\text{ff}} = 1 + \frac{\langle \vec{M}^2 \rangle}{3 \cdot \epsilon_0 \cdot V \cdot k_B \cdot T}, \quad (5.5)$$

where  $\vec{M}$  denotes the total dipole moment of the system,  $V$  denotes the volume of the simulation box,  $k_B$  denotes the Boltzmann's constant and  $T$  denotes the temperature.

The total dipole moment can be written as the sum of the molecular dipole moments  $\vec{p}_i$ :

$$\vec{M} = \sum \vec{p}_i. \quad (5.6)$$

The dipole moment of a water molecule must be expressed considering the geometry of the TIP4P/2005f model (reminded in Fig. 5.1). Denoting  $H_1$  and  $H_2$  the two hydrogen atoms, one obtains :

$$\vec{p} = q_H \cdot \vec{OH}_1 + q_H \cdot \vec{OH}_2 + q_O \cdot \vec{OM} \quad (5.7)$$

with:

$$\vec{OM} = d_{\text{OM}}^{\text{rel}} \cdot (\vec{OH}_1 + \vec{OH}_2), \quad (5.8)$$

where  $d_{\text{OM}}^{\text{rel}} = 0.13194$  is a geometrical parameter of the force field. Considering thus that  $q_O = -2 \cdot q_H$ , one obtains :

$$\vec{p} \cdot \vec{e}_x = q_H \cdot (1 - 2 \cdot d_{\text{OM}}^{\text{rel}}) \cdot (x_{H_1} + x_{H_2} - 2 \cdot x_O), \quad (5.9)$$

so:

$$\vec{M} \cdot \vec{e}_x = q_H \cdot (1 - 2 \cdot d_{\text{OM}}^{\text{rel}}) \cdot \left( \sum_{\{H\}} x_H - 2 \cdot \sum_{\{O\}} x_O \right), \quad (5.10)$$

where the sums are respectively evaluated on all hydrogen atoms and all oxygen atoms.

By doing the simulations so, we found  $\epsilon_{\text{ff}} = 44.3 \pm 2.8$ , and thus,  $q_H^{\text{eff}} = 0.7513$ . This value of the relative dielectric constant is lower than those determined by Gonzales et al. (who found  $\epsilon_{\text{ff}} = 55.3$ ) but close to it.

## 1.3 Application, pros and cons of the method

Using the value of the effective charge previously calculated, we determined the corresponding Lennard-Jones parameters for all alkali metal halide salts following the approach by Mao and Pappu [Mao and Pappu, 2012] (see next section). The coefficient are summarized in Table 5.1.

	$\epsilon$ (kcal · mol <sup>-1</sup> )	$\sigma$ (Å)
Na	4.5145272	1.8147768
Cl	4.2717176	3.3764782

Those parameters lead to an overestimation of the self diffusion coefficient of water in a 4 M sodium chloride solution ( $(3.10 \pm 0.11) \cdot 10^{-9} \text{ m}^2 \cdot \text{s}^{-1}$ ), and predicts – for the first time using a Lennard-Joned force field – a strong chaotropic behavior for one salt. This shows that salts that enhance water self diffusion may be modeled using force fields. Unfortunately, in the case of sodium chloride, this is in qualitative disagreement with experiments. To solve this problem, we propose in the present work to treat the charge of ions as an empirical parameter, in the same manner as the Lennard-Jones parameters that describe non-Coulombic interactions between atoms. The charge is optimized using directly the water self diffusion coefficient as target observable, whereas Lennard-Jones parameters are optimized for

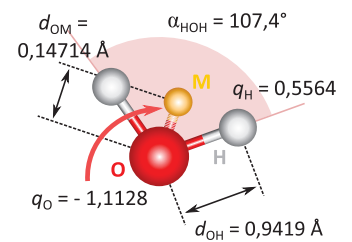


**Figure 5.1** ▲ The TIP4P/2005f water molecule. The partial charge of the oxygen atom is on a fictive massless site, denoted M, localized on the  $\widehat{HOH}$  bissector.

**Table 5.1** ◀ Optimized Lennard-Jones parameters obtained for  $z_{\text{eff}} = 0.9292$ .

each charge using the method previously mentioned. After a description of the optimization procedure, we test our new model for various structural and dynamical properties of salt solutions, including the water self diffusion, but also the shear viscosity and the infrared absorption spectrum, that are usually not considered. For each properties, we analyze its benefits and drawbacks. Especially, in the case of the infrared absorption spectrum, we realize both an experimental and numerical investigation of the influence of salts on the shape of the spectrum, and compare both results.

## 2 Force field optimization

The starting point of our approach is the method proposed by Mao and Pappu [Mao and Pappu, 2012]. The authors introduce an elegant and fast way to calculate the Lennard-Jones parameters of all alkali and halide ions based on the crystal structure of alkali metal halides at 0 K. Here we first summarize their method, introducing along the way the slight modifications needed for our model. All details can be found in their paper [Mao and Pappu, 2012].

The main idea is to minimize an error function measuring the deviation of calculated interionic distances – *i.e.* the distance between closest anion and cation pair – and lattice energies from their tabulated values for simple crystals with only one kind of anion and cation. The anion can be  $F^-$ ,  $Cl^-$ ,  $Br^-$  or  $I^-$ , whereas the cation can be  $Li^+$ ,  $Na^+$ ,  $K^+$ ,  $Rb^+$  or  $Cs^+$ . The interactions between ions in the crystal are modeled by a Coulombic potential and a Lennard-Jones potential. The lattice energy  $U$  can thus be written:

$$U = \frac{1}{2} \cdot \sum_{j \neq i} \left[ \frac{z_i \cdot z_j \cdot e^2}{4 \cdot \pi \cdot \epsilon_0 \cdot r_{ij}} + 4 \cdot \epsilon_{ij} \cdot \left( \left( \frac{\sigma_{ij}}{r_{ij}} \right)^{12} - \left( \frac{\sigma_{ij}}{r_{ij}} \right)^6 \right) \right], \quad \blacksquare \quad (5.11)$$

where the sum stands over all pairs of ions  $\{i, j\}$  with  $i \neq j$  and  $z_i$  denotes the valence of ion  $i$ ,  $e$  the electronic charge,  $\epsilon_0$  the vacuum permittivity,  $r_{ij}$  the distance between ions  $i$  and  $j$ , and  $\epsilon_{ij}$  and  $\sigma_{ij}$  the Lennard-Jones pair parameters, obtained from single ion parameters using the Lorentz-Berthelot mixing rules:  $\sigma_{ij} = (\sigma_i + \sigma_j)/2$  and  $\epsilon_{ij} = \sqrt{\epsilon_i \cdot \epsilon_j}$ . By putting together terms relative to the same ion and crossed terms, one gets:

$$U = -\frac{b_1 \cdot z_{\text{eff}} \cdot e^2}{4 \cdot \pi \cdot \epsilon_0 \cdot d} + \sum_{\{\alpha, \beta\}} 2 \cdot \epsilon_{\alpha\beta} \cdot \left( b_{12, \alpha\beta} \cdot \left( \frac{\sigma_{ij}}{r_{ij}} \right)^{12} - b_{6, \alpha\beta} \cdot \left( \frac{\sigma_{ij}}{r_{ij}} \right)^6 \right), \quad \blacksquare \quad (5.12)$$

where  $\{\alpha, \beta\}$  denotes one of the four cation (c) / anion (a) combinations  $\{c, c\}$ ,  $\{c, a\}$ ,  $\{a, c\}$  or  $\{a, a\}$ ,  $b_1$ ,  $b_{6, \alpha\beta}$  and  $b_{12, \alpha\beta}$  are constants that depend on the lattice structure,  $z_{\text{eff}}$  is the absolute valence of ions ( $z_{\text{eff}} = 1$  in the present case), and  $d$  is the interionic distance,  $d$  taken to minimize  $U$ . In practice,  $d$  is defined as the smallest positive root of the polynomial:

$$Q(d) = -\frac{64 \cdot b_1 \cdot z_{\text{eff}} \cdot e^2}{\pi \cdot \epsilon_0} \cdot d^{11} - 96 \cdot (b_{6, ca} \cdot \sqrt{\epsilon_c \cdot \epsilon_a} \cdot (\sigma_c + \sigma_a)^6 + 32 \cdot (b_{6, cc} \cdot \epsilon_c \cdot \sigma_c^6 + b_{6, aa} \cdot \epsilon_a \cdot \sigma_a^6)) \cdot d^6 + 3 \cdot (b_{12, ca} \cdot \sqrt{\epsilon_c \cdot \epsilon_a} \cdot (\sigma_c + \sigma_a)^{12} + 2048 \cdot (b_{12, cc} \cdot \epsilon_c \cdot \sigma_c^{12} + b_{12, aa} \cdot \epsilon_a \cdot \sigma_a^{12})). \quad \blacksquare \quad (5.13)$$

Among the twenty salts considered here, CsCl, CsBr, and CsI crystallize following the cesium chloride structure whereas the others have a rock-salt structure. The associated values of  $b_{6, \alpha\beta}$  and  $b_{12, \alpha\beta}$  can be easily computed since the sums converge fast.  $b_1$  is the Madelung

Cesium chloride structure		
$\alpha\beta$	cc / aa	ac / ca
$b_1$	1.762674773	
$b_{6,\alpha\beta}$	3.544561652	8.709106157
$b_{12,\alpha\beta}$	1.103849281	8.010339874
Rock-salt structure		
$\alpha\beta$	cc / aa	ac / ca
$b_1$	1.747564595	
$b_{6,\alpha\beta}$	1.806740118	6.595183822
$b_{12,\alpha\beta}$	0.1895606281	6.012588417

**Table 5.2** ◀  
Values of  $b_1$ ,  $b_{6,\alpha\beta}$  and  $b_{12,\alpha\beta}$  for the different structures.

constant and is thus tabulated (see *e.g.* Ref. [OEIS Foundation Inc., 2017]). All values are gathered in Table 5.2.

Having now a method to determine  $d$  and  $U$  for a given salt, one defines the error function for the whole set of salts:

$$\mathcal{F}(\{\epsilon_i, \sigma_i\}, z_{\text{eff}}) = \sqrt{\frac{1}{40} \cdot \sum_{\text{salts}} \%_{\text{rel}}^2(U) + \%_{\text{rel}}^2(d)}, \quad \blacksquare \quad (5.14)$$

with:

$$\%_{\text{rel}}(X) = \frac{X - X_{\text{tab}}}{X_{\text{tab}}}, \quad \blacksquare \quad (5.15)$$

where  $X_{\text{tab}}$  denotes the tabulated value for  $X$ . Tabulated values of  $U$  and  $d$  will be given in Table 5.4 of Results and Discussion section. For a given value of  $z_{\text{eff}}$ , one needs to find the set of Lennard-Jones parameters that minimize  $\mathcal{F}$ , and satisfy moreover a set of additional conditions, in order to respect the evolution of some properties of ions on a same column/line of the periodic table [Mao and Pappu, 2012] as *e.g.* the evolution of ionic radii (see Appendix of Chap. 1): (i)  $\sigma_j$  and  $\epsilon_j$  increase along a column of the periodic table, (ii) for a given line  $\sigma_c$  is smaller than  $\sigma_a$ , and (iii) for a given line,  $\epsilon_c \cdot \sigma_c^6$  is lower than  $\epsilon_a \cdot \sigma_a^6$ . The minimization procedure was implemented on Scilab 5.4.1 [Scilab Enterprises, 2012] using the integrated function for the determination of the roots of  $Q$  and the simple hill climbing algorithm [Wikipedia, 2017] for the minimization of  $\mathcal{F}$ .

Now come our contribution to the model. Up to now, the procedure is independent of the water model used and thus should be universal. What comes next depends on the force field used to describe water. In order to optimize the force field with respect to water self diffusion properties, the effective valence of ions  $z_{\text{eff}}$  is treated as an adjustable parameter. The idea is to build an error function in a similar manner than what was done before. Since we want to focus on the water self diffusion, it seems natural to make  $\mathcal{G}$  being minimal when the deviation between  $D([X])$  – the self diffusion coefficient of water in a solution containing a concentration  $[X]$  of salt  $X$  – and tabulated values is minimum. However, it would not be convenient since experimental reference data correspond to different sets of concentration depending on the salt. It would thus require to perform calculations with different concentrations for each salt. A possible solution to avoid this issue is to look at the variation of the self diffusion with respect to the concentration. Ignoring the point corresponding to pure water, the variation of the experimental water self diffusion with respect to the concentration is almost linear for each salt (see Fig. 5.3). It can thus be described using a model of the form  $D([X]) = m \cdot [X] + p$ , where  $m$  and  $p$  depend on the salt. An important issue when studying the influence of a salt on a given observable of water is that the water model can predict a value that differs from experiments for pure water. Thus, it necessarily affects values for salt water and their deviation from tabulated values. To avoid this problem, the quantity  $m/p$  is used to quantify the kosmotrope / chaotrope tendency of the salt. A high negative value means a high kosmotropic behavior, whereas a high positive value means a high chaotropic behavior, independently of the accuracy of the model to reproduce pure water self diffusion coefficient. Using the observable  $m/p$ , the error function takes the form:

$$\mathcal{G}(z_{\text{eff}}) = \sqrt{\sum_{\text{salts}} \%_{\text{rel}}^2\left(\frac{m}{p}\right)}, \quad \blacksquare \quad (5.16)$$

and has to be minimized with respect to  $z_{\text{eff}}$ . Four different concentrations were considered for calculations : 1, 2, 3 and 4 M. For each value of  $z_{\text{eff}}$ , each salt and each concentration, the computation of  $D$  requires a full set of molecular dynamics calculations, the evaluation of  $\mathcal{G}$  was restricted to four prototypical salts: LiCl, NaCl, KBr and CsI. The details about molecular dynamics calculations are given in the next section.

The minimization procedure is now the following. We consider a set of trial values for  $z_{\text{eff}}$  between 0.9 and 1 (in practice, we used 0.920, 0.941 and 0.955). For each trial value, the corresponding set of Lennard-Jones parameters are found. With those parameters, the value of  $D$  are calculated for the different salts and concentrations listed above using molecular dynamics. Then the corresponding value of  $m/p$  are determined. For each salt,  $m/p$  is extrapolated for each value of  $z_{\text{eff}}$  using a linear regression. Finally, injecting those extrapolations in  $\mathcal{G}$ ,  $z_{\text{eff}}$  is determined by minimizing  $\mathcal{G}$ . The procedure gives  $z_{\text{eff}} = 0.9292$ . The corresponding Lennard-Jones coefficients are gathered in Table 5.3.

**Table 5.3** ▶ Optimized Lennard-Jones parameters obtained for  $z_{\text{eff}} = 0.9292$ .

	$\epsilon$ (kcal·mol <sup>-1</sup> )	$\sigma$ (Å)
Li	0.6132788	1.7909036
Na	0.9188072	2.3347069
K	1.3412971	2.9252436
Rb	1.3412971	3.1805671
Cs	1.3412971	3.6020092
F	1.182328	2.4474882
Cl	1.2472496	3.3795668
Br	1.2472496	3.6674819
I	1.2472496	4.0834045

### 3 Molecular dynamics methods

All calculations were performed with the LAMMPS package [Plimpton, 1995], using the TIP4P/2005f force field [González and Abascal, 2011] for water. A 9.0 Å cutoff was used for Lennard-Jones interactions and a 8.5 Å cutoff was used for Coulombic interactions. The long range part of the Coulombic interactions was computed using the particle-particle particle-mesh (PPPM) method. Due to the flexibility of molecular bonding, a 1 fs timestep was used for all calculations. Eight different box sizes were used from 8 × 8 × 8 to 22 × 22 × 22 molecules, with periodic boundary conditions. Couples of randomly chosen molecules were alternately replaced by an anion or a cation in order to get the desired salt concentration. For each box size, four replicas of the system were first equilibrated in the isotherm-isobaric ensemble during 40 ps using a Langevin thermostat [Schneider and Stoll, 1978] and a Hoover and Andersen barostat [Martyna et al., 1994], making in total thirty-two replicas for one set of experimental conditions. The temperature was fixed at 300 K and the pressure at 1 atm. We then performed production runs in the microcanonical ensemble during 300 ps to extract three observables: the self diffusion coefficient  $D$ , the shear viscosity  $\eta$ , and the high frequency infrared (IR) absorption spectrum, using the method introduced in Chap. 2.

## 4 Application of the model

### 4.1 Crystal structures

From the Lennard-Jones parameters optimization process, we get directly the interionic distance and the lattice energies at 0 K for all alkali metal halides crystal structures. Results are given in Table 5.4. Overall, the agreement between calculated and tabulated values is excellent: relative errors are lower than 1 %. Interestingly, reducing the effective valence of ions improves crystal structure predictions since the values calculated here are much closer to tabulated values (in brackets in Table 5.4) than the one calculated by Mao and Pappu using the standard statement [Mao and Pappu, 2012]  $z_{\text{eff}} = 1$ .

	LiF	LiCl	LiBr	Lil
$-U$	251.7 (250.7)	207.7 (206.5)	196.1 (196.0)	180.9 (182.6)
$d$	2.009 (1.996)	2.530 (2.539)	2.705 (2.713)	2.969 (2.951)
	NaF	NaCl	NaBr	NaI
$-U$	221.1 (222.3)	188.5 (188.8)	180.5 (180.2)	169.9 (168.5)
$d$	2.306 (2.295)	2.791 (2.789)	2.946 (2.954)	3.178 (3.194)
	KF	KCl	KBr	KI
$-U$	199.1 (198.1)	170.8 (172.1)	164.2 (165.2)	155.9 (155.4)
$d$	2.633 (2.648)	3.118 (3.116)	3.268 (3.262)	3.487 (3.489)
	RbF	RbCl	RbBr	RbI
$-U$	191.2 (190.0)	164.3 (166.1)	158.1 (159.7)	150.2 (151.1)
$d$	2.765 (2.789)	3.250 (3.259)	3.400 (3.410)	3.617 (3.628)
	CsF	CsCl	CsBr	CsI
$-U$	179.7 (181.4)	161.2 (160.1)	155.5 (154.6)	147.7 (146.5)
$d$	2.988 (2.982)	3.529 (3.523)	3.678 (3.668)	3.906 (3.898)

**Table 5.4** ◀  
 Calculated and tabulated values of lattice energies  $U$  (kcal·mol<sup>-1</sup>) and interionic distances  $d$  (Å) of alkali metal halides. The first value is the calculated one using the Lennard-Jones parameters and the effective valence determined previously  $z_{\text{eff}} = 0.9292$ , and the value in brackets is the tabulated value, taken from [Mao and Pappu, 2012].

It could be interesting to analyze precisely other solid properties of alkali metal halides using our model, but as our aim is to focus on aqueous state properties, we directly move to the analysis of aqueous solutions with various concentrations.

## 4.2 Liquid structure

An important topic in the study of the effect of ion solvation on the associated structure of water is the oxygen-oxygen coordination. To this aim, we first analyze here the oxygen-oxygen (O–O) radial distribution function. To simplify the discussion, we will restrict ourselves to two limit case salts: lithium chloride (LiCl) will be treated as an example of kosmotrope, whereas potassium bromide (KBr) will be treated as an example of chaotrope. The curves corresponding to the different concentrations are gathered in Fig. 5.2.

The TIP4P/2005f force field is known to reproduce accurately the O–O radial distribution function [González and Abascal, 2011] at room temperature. Here, the first peak position is found to be at  $2.77 \pm 0.17$  Å. Interestingly, whatever the concentration used, the presence of solvated species does not affect this position, in agreement with neutron and X-ray diffraction experiments on sodium and potassium chloride solutions [Bouazizi et al., 2006, Mancinelli et al., 2007]. Moreover, a decrease of the amplitude of the peak is observed when the salt concentration is increased. It corresponds to the decrease of the mean number of oxygen atoms in their first coordination shell since a couple of them are replaced by ions. However, this decrease is only qualitatively reproduced: the decrease is more pronounced on experimental curves, and is accompanied by a broadening of the peak, due to the influence of ions hydration spheres [Mancinelli et al., 2007].

It is also interesting to look at other peaks, since the second peak of the O–O radial distribution function describes the local order of water, and is sometimes said to be the signature of the tetrahedral hydrogen bond network [Bouazizi et al., 2006]. Moreover, the self diffusion of water is influenced by molecular interactions beyond several molecular sizes [Jonchiere et al., 2011], and thus by the O–O distribution in the second and third coordination shells.

A progressive shift of the second peak to lower distances is observed for KBr solutions, whereas the shift is observed in the other direction for LiCl solutions. Since non-hydrogen bonded water molecules should be closer than hydrogen bonded molecules, the trend observed here are consistent with a chaotropic and kosmotropic behaviour respectively. Moreover, the trend observed for LiCl agrees with both X-ray and neutron diffraction data for NaCl [Bouazizi et al., 2006, Mancinelli et al., 2007], which is, like LiCl, a kosmotropic salt, whereas the trend observed for KBr agrees with neutron diffraction data [Mancinelli et al., 2007] for KCl which is, like KBr, a chaotropic salt.

In contrast with the second peak, using the present model, the third peak is found to shift to lower distances for both salts when the concentration is increased. This is also consistent with neutron diffraction data [Mancinelli et al., 2007], as shown in Fig. 5.2. Moreover, experimental curves are overall close to our simulated results at long distances (around the position of the third peak). Thus, the effect of ions, whether chaotropic or kosmotropic, on

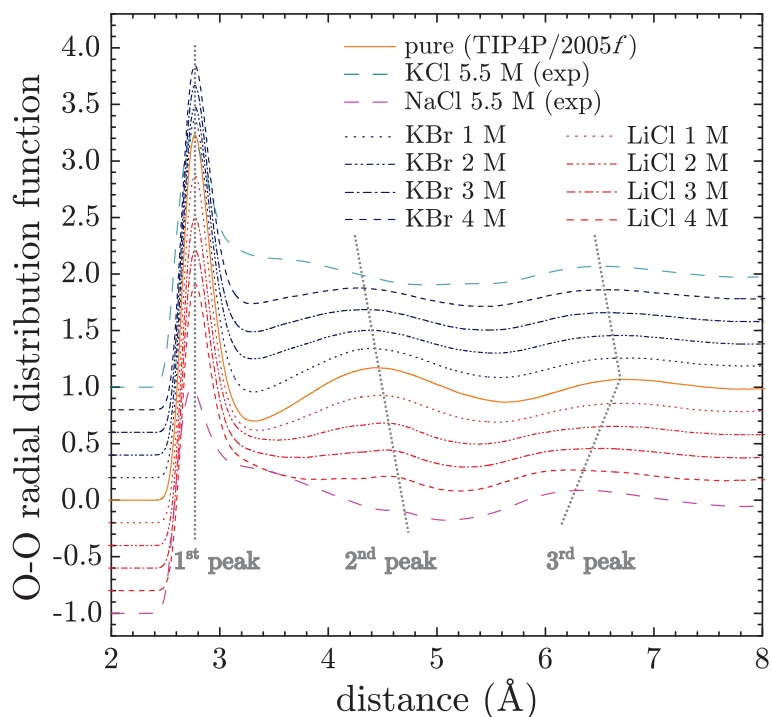


**Figure 5**  
Evolution of the O-O radial distribution function with respect to distance (Å) for various salt concentrations. The curves represent different salt concentrations: pure water (TIP4P/2005f), KCl 5.5 M (exp), NaCl 5.5 M (exp), KBr 1 M, 2 M, 3 M, 4 M, LiCl 1 M, 2 M, 3 M, 4 M. The first peak is at approximately 2.8 Å, the second peak is at approximately 4.5 Å, and the third peak is at approximately 6.5 Å. The amplitude of the first and second peaks increases with salt concentration, while the amplitude of the third peak remains relatively constant.

the local structure is accurately reproduced beyond the third coordination sphere or water molecules, whereas the agreement is only qualitative in the first and second coordination spheres.

An interesting point is that the third peak amplitude is not modified by the salts. This means thus that the (de)structuring effect of salts is limited. However, it is clear that the structure of water is altered beyond the first hydration shell since the radial distribution function differs from that of pure water further than the second peak. To this point of view, the present model reproduces well both the range and strength of the (de)structuration induced by ions.

### 4.3 Water self diffusion

The self diffusion coefficient of water has been computed for all alkali metal halides, except fluorides that suffered of numerical instabilities with the Morse potential used in the TIP4P/2005f force field to parametrize O-H bonds inside molecules. All calculations were corrected for finite size effects, as described in Chap. 2. The results are shown in Fig. 5.3 and compared to experimental data, when available. The self diffusion coefficient for pure water, computed in the same conditions than for salted solutions, but with twice more replicas of the system in order to reduce errors, is  $(2.30 \pm 0.01) \cdot 10^{-9} \text{ m}^2 \cdot \text{s}^{-1}$  which corresponds to the tabulated value [Krynicky et al., 1978]. Thus, calculated and tabulated values for salt solutions can be directly compared without any normalization.

According to experimental data, lithium and sodium based salts decrease the self diffusion of water (that should correspond to a more structured liquid), whereas potassium, rubidium and iodine increase it (that should correspond to a less structured liquid). Moreover, except for small cations, the evolution of the self diffusion coefficient with respect to the salt concentration only slightly depends on the nature of the cation, in agreement with previous studies: for a given anion, curves corresponding to potassium, rubidium and cesium are very close one to each other. The trend is well reproduced by our model in the case of lithium and sodium. Except for LiBr solutions with concentration higher than  $3 \text{ mol} \cdot \text{L}^{-1}$ , the differences between experimental and calculated values are within the error bars. However, our model fails to reproduce the increase of the self diffusion coefficient of water in the presence of chaotropic salts. In the case of chlorides whose influence on the self diffusion is small, calculated self diffusion coefficients slightly decrease with respect to the salt concentration, whereas for more chaotropic salts, calculated values remains approximately

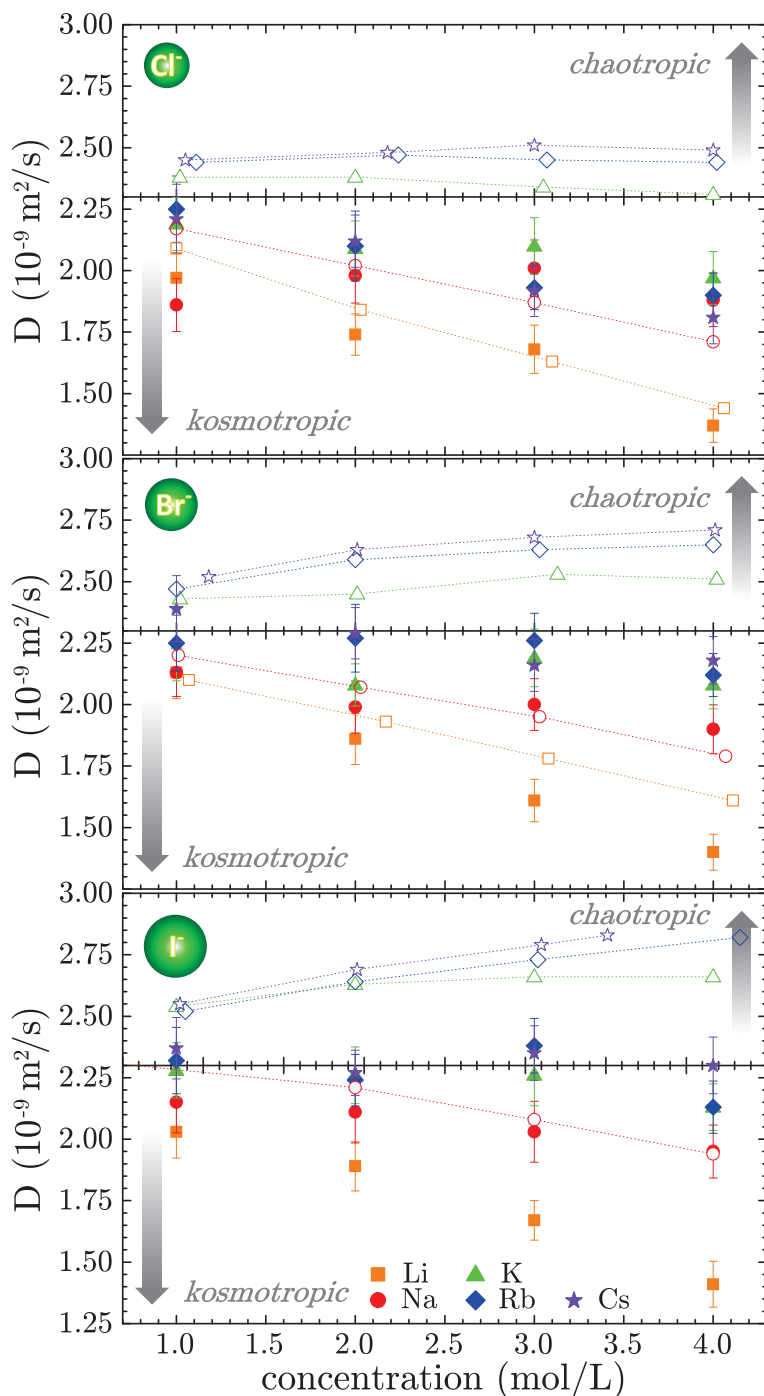


**Figure 5.3** ◀ Evolution of the water self diffusion coefficient with respect to the salt concentration. Filled symbols represent calculated values using our model at 300 K, and empty symbols represent tabulated values at 298 K (from Ref. [Müller and Hertz, 1996]). For clarity, values have been plotted on different graphs depending on the anion. Globally, the agreement between calculated and tabulated values is good for lithium and sodium based salts which are kosmotropic, whereas our model fails to reproduce tabulated values for others salts, that are mainly chaotropic.

constant with respect to the concentration. Despite of this strong failure of the model, the relative influence of the different salts is overall well restituted. Except for the chlorides, the set of points corresponding to the different cations are ordered in same way, and the dispersion of values for potassium, rubidium and iodine for a given halide is almost the same for tabulated and calculated values. Moreover, the overall accuracy of the present model to reproduce the self diffusion of salt water is similar to those of the model by Kann and Skinner [Kann and Skinner, 2014] or usual polarizable models [Kim et al., 2012], and is almost quantitative for salts involving small ions thanks to the accuracy of the TIP4P/2005f force field to reproduce the self diffusion of pure water.

## 4.4 Shear viscosity

The shear viscosity of electrolytes has been extensively studied experimentally in the limit of low concentrations [Abdulagatov et al., 2006, Nakai et al., 1996, Goldsack and Franchetto, 1977], but not numerically. Within the limit of low concentrations, experimental data can be well described using the Jones-Dole equation [Marcus, 2009]  $\eta/\eta_{\text{solvent}} = 1 + A \cdot \sqrt{c} + B \cdot c$ .  $A$  can be computed theoretically from solvent and ions properties and  $B$  is an empirical coefficient. A large amount of experiments have been devoted to the determination of  $B$  for various salts [Abdulagatov et al., 2006, Nakai et al., 1996, Goldsack and Franchetto, 1977]. It is usually assumed that salts with a positive  $B$  are kosmotropic, while those with a negative  $B$  are chaotropic [Marcus, 2009, Goldsack and Franchetto, 1977]. According to the Jones-Dole equation,  $A \cdot \sqrt{c}$  should be negligible at high concentrations. Indeed, for all salts considered here, our calculations are well described by an affine relation within error bars, even if a slight convexity seems to appear on all sets of points, as shown in Fig. 5.4. Consequently, the slope of the curves directly gives the sign of  $B$ , and thus, the kosmotropic/chaotropic tendency of the salt.

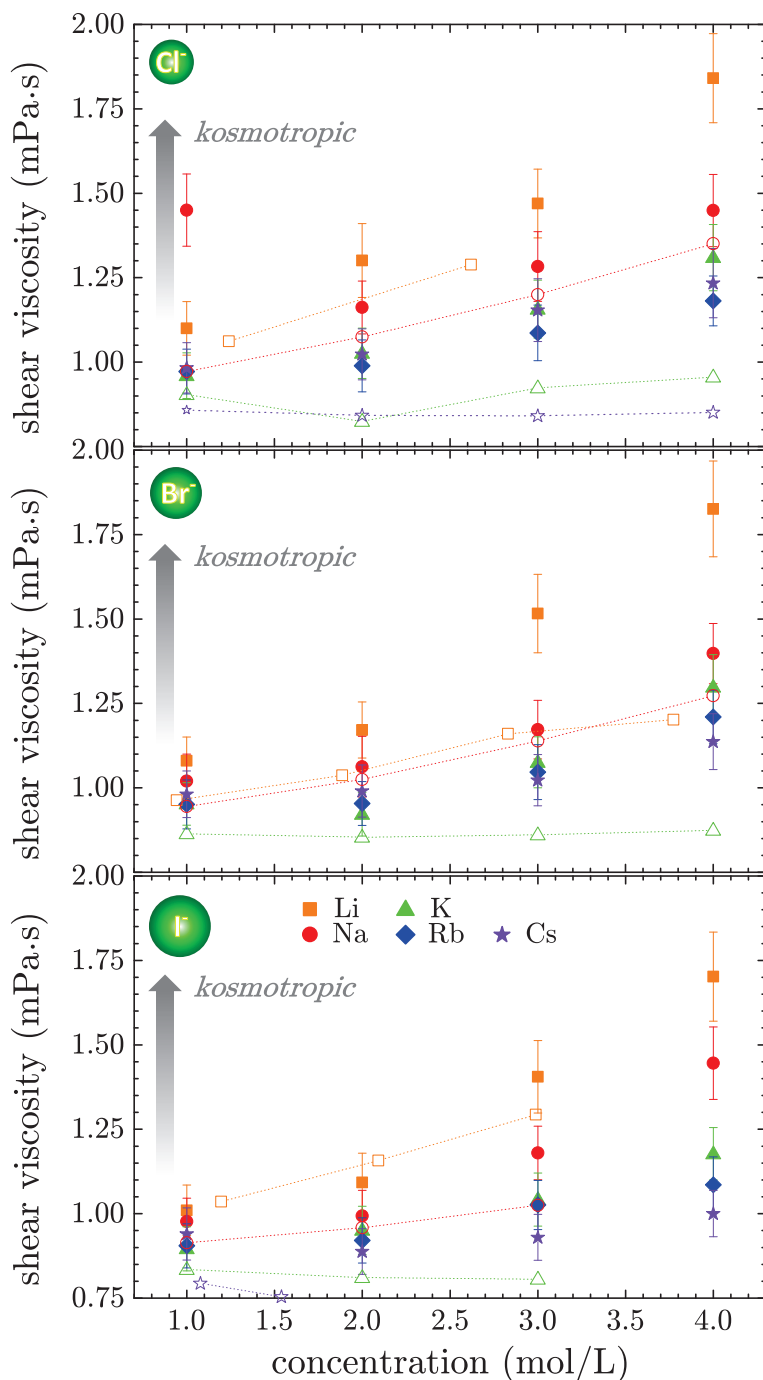
Using the TIP4P/2005*f* model, the shear viscosity of pure water at 300 K is  $0.76 \pm 0.05$  mPa·s, which is close to the tabulated value 0.896 mPa·s at 298.15 K [Harris and Woolf, 2004]. Thus, our values must be slightly underestimated with respect to experiments. We however apply no correction nor normalization on the graph of Fig. 5.4. Whatever the anion considered, the shear viscosity computed using the Green-Kubo method increases with respect to the concentration for lithium and sodium based salts, which corresponds to a positive  $B$  value, and thus, a kosmotropic tendency. This is – as in the case of the self diffusion – in qualitative agreement with experiments. The agreement is however better in the case of self diffusion: the increase of shear viscosity with respect to the concentration seems systematically overestimated. Calculations also predict positive  $B$  values for other salts, which is in qualitative disagreement with experiments, but in agreement with another recent numerical study [Hartkamp and Coasne, 2014]. Again, the model fails to reproduce the chaotropic behavior of salts. Note that the “saturation” of calculated values of the self diffusion coefficient of water near the pure water value for bromide and iodide is not observed in the case of shear viscosity. Even for the most chaotropic salts, the shear viscosity increases according to calculations. Recent models for salt water have not been employed to calculate the shear viscosity, so no comparison can be made between our model and other models.

## 4.5 Mid-infrared absorption spectrum

The infrared absorption spectrum of water represents the variations of dipole moments of water molecules induced by molecular vibrations, and is thus a dynamical observable. However, in the stretching region, as we already mentioned, the spectrum is also highly correlated to the structure of water (see Chap. 2). Brubach et al. [Brubach et al., 2005] suggested to deconvolute the stretching band (see Fig. 5.5) into three main contributions located approximatively around 3200, 3400 and 3600  $\text{cm}^{-1}$ , and corresponding respectively to highly (four H-bonds per molecule), intermediately (between one and three) and poorly hydrogen-bonded (no H-bond) water molecules [Brubach et al., 2005, Mallamace et al., 2007]. One or two additional Gaussians are sometimes used [Mallamace et al., 2007]. It is thus of particular interest to look at the influence of salts on the water spectrum. Rigid force fields only reconstitute the permanent dipole moment of water molecules. Due to its flexibility, the TIP4P/2005*f* force field [González and Abascal, 2011] also takes into account induced dipole moments, even if the electronic degrees of freedom are not considered. As in the radial distribution function analysis, LiCl will be treated as an example of kosmotrope, and KBr as an example of chaotrope.

Experimental spectra were recorded using a Nicolet iS10 Fourier Transform InfraRed (FTIR) Spectrometer by Thermo Scientific in conjunction with a single diamond Attenuated Total Reflectance (ATR) DuraSamplIR II accessory by SensIR. The standard tungsten source, KBr beam-splitter and DGTS detector were used. 40 scans with a 4  $\text{cm}^{-1}$  resolution were accumulated for each sample. The results are shown in Fig. 5.5.

The FTIR probe shows a large sensitivity to the salt concentration. In the case of KBr, the 3200  $\text{cm}^{-1}$  decreases when the concentration is increased, with only few modifications on

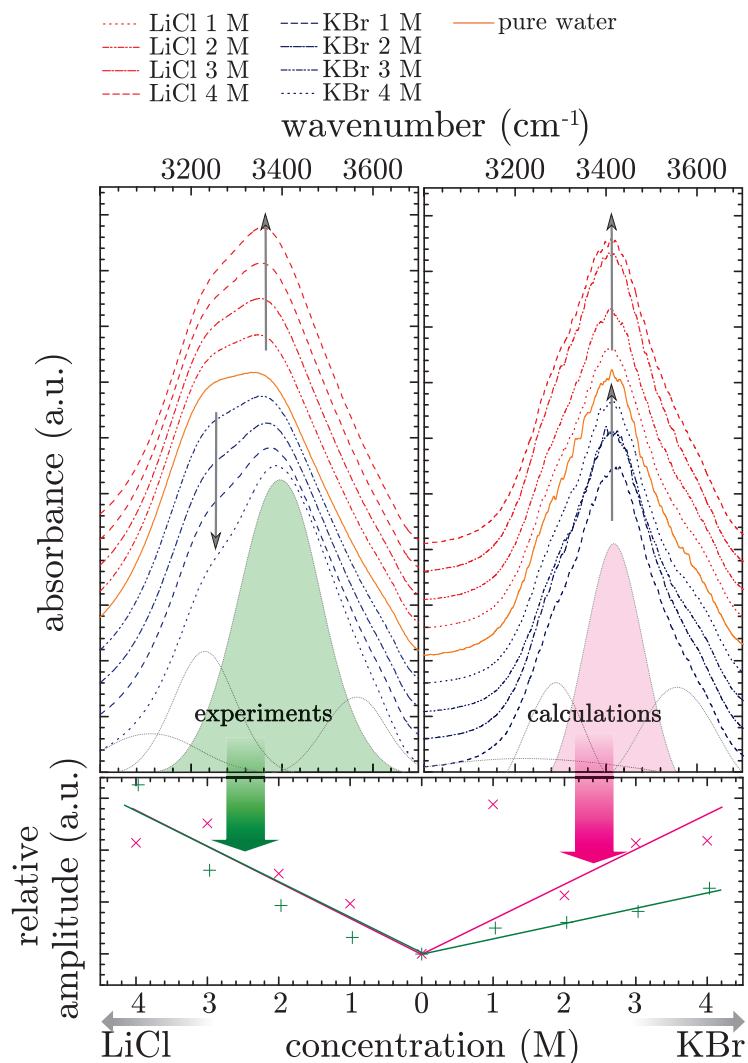


the other contributions, except a slight increase of the  $3400\text{ cm}^{-1}$  contribution, as shown on the bottom graph of Fig. 5.5. That means the population of highly H-bonded water molecules decreases when the concentration of KBr increases, with a partial transfer to intermediately H-bonded molecules. This is consistent with the chaotropic behavior of KBr. In contrast, for LiCl, only the  $3400\text{ cm}^{-1}$  band seems to be affected by adding salt, with a clear increase when the salt concentration is increased. That means the population of moderately H-bonded water molecules increases, without any change on the highly H-bonded water molecules population, which is consistent with the kosmotropic behavior of LiCl.

The TIP4P/2005f force field reproduces the different components of the O-H stretching spectrum of pure water, but each component is slightly shifted to higher frequencies. To simplify the discussion, we will speak about  $3200$ ,  $3400$  and  $3600\text{ cm}^{-1}$  components for the three highest bands (see deconvolution in Fig. 5.5) by reference to the experimental spectrum, even if the first frequency is closer to  $3300\text{ cm}^{-1}$ . When adding LiCl, the  $3200\text{ cm}^{-1}$

**Figure 5.5** ▶

Evolution of the experimental (left) and calculated (right) infrared absorption spectrum with respect to LiCl or KBr concentration in the O–H stretching region. LiCl is taken as an example of a kosmotropic salt, and KBr as an example of a chaotropic salt. A deconvolution using four Gaussians is suggested with dotted lines. All spectra were shifted for clarity. Bottom: evolution of the relative amplitude of the deconvoluted  $3400\text{ cm}^{-1}$  contribution with the salt concentration. The amplitude of the band is normalized with respect to those of pure water. Plain lines are eye-guides. Dotted lines are Gaussians.



component is only slightly affected, whereas the amplitude of the  $3400\text{ cm}^{-1}$  band increases with the concentration. This means that, at high concentration, as observed experimentally, the population of intermediately H-bonded molecules increases, without any evolution of the highly H-bonded molecules population. It corresponds to a kosmotropic behavior, which is consistent with experiments. When adding KBr, the same trend is observed for the two bands, and thus for intermediately and highly H-bonded water molecule populations. This means that, at high concentration, as observed experimentally, the population of intermediately H-bonded molecules increases, but since no evolution is observed for the  $3200\text{ cm}^{-1}$  component, it corresponds to a kosmotropic behavior, which is in disagreement with experiments, but in agreement with our previous observations using the self diffusion and the shear viscosity as probes. However, the FTIR probe give more informations: experimentally, KBr is found to affect both the intermediately and highly H-bonded molecule populations, whereas numerically, it only affects intermediately H-bonded molecules, with a overestimation of the increase of this contribution with respect to experiments, as shown on the bottom graph in Fig. 5.5. Consequently, our model fails to evaluate the population of four H-bonded molecules in the presence of KBr. More generally, it seems that the salt water model is not selective enough: it increases/decreases globally the average number of H-bonded molecules, so the overall structuration of the liquid, whereas in practice, ions affect the structure more specifically. A complete analysis of the hydrogen bond network using the TIP4P/2005*f* force field for pure and salt water may help to understand the failure of ion models to reproduce the structure and dynamics of salt water in the future.

## 5 Conclusion

---

Treating ionic charge as an adjustable parameter, we have developed a full set of parameters to model alkali metal halides in conjunction with the TIP4P/2005 $f$  force field. The local structure of water, probed through the oxygen-oxygen radial distribution function, is well restituted by the model, but hydrodynamic properties such as the self diffusion coefficient of water and the shear viscosity are only reproduced for small ion salts, *i.e.* lithium and sodium salts, that are kosmotropic. Moreover, through the analysis of the infrared absorption spectra of salt solutions, it appears that the point charge model fails to reconstitute the hydrogen bond distribution in water. This reinforces the idea that empirical non-polarizable force fields cannot reproduce fairly salt-water interactions. However, due to its flexibility, the TIP4P/2005 $f$  forcefield is slightly polarizable. Thus, considering our preliminary calculation of the self diffusion of water for sodium chloride solution with low charge ions mentioned in the introduction, we think that choosing a different routine based on liquid properties (see *e.g.* model by Horinek *et al.* [Horinek *et al.*, 2009]) to optimize the model could improve the overall agreement between calculations and experiments. In spite of the limitations of this model, the quantitative agreement with experiments for small ions due to the combined accuracy of the TIP4P/2005 $f$  and salt force fields should increase the benefits of molecular simulations to study heterogeneous systems such as for example nanofluidic devices or clay minerals. In particular, we will apply this model to describe interlayer cations in clays in Chap. 6.



 Chapter 6

# Structure and dynamics of water confined in clay minerals

## Outline

1	Evolution of the structure and connectivity of water adsorbed in clay minerals upon swelling . . . . .	91
1.1	Experimental methods . . . . .	92
1.2	Results . . . . .	93
1.3	Discussion . . . . .	98
1.4	Summary and conclusion . . . . .	102
2	Mono- and bi-layer configurations of interlayer water . . . . .	103
2.1	Numerical methods . . . . .	103
2.2	Identification of the stable mono- and bi-layer hydration configurations by molecular simulation . . . . .	104
2.3	Vibrational density of states of the mono- and bi-layer configurations . . . . .	105
3	Low temperature dynamics of confined water . . . . .	106
3.1	Water thermally induced migration and dynamics singularities . . . . .	106
3.2	Low temperature hydrodynamic properties of interlayer water . . . . .	110
4	Summary and conclusion . . . . .	111
5	Appendix: Temperature dependance of the far-infrared absorption spectrum for various hydration states . . . . .	113

This last chapter is dedicated to water adsorbed in clay minerals. As we explained in Chap. 1, the experimental investigation of the structural and dynamical properties of water adsorbed in clays is a delicate task due to the variety of scales implied. Performing for the first time extensive infrared adsorption measurements in the connectivity region, and coupling them to standard mid-infrared measurements, we will show that the infrared probe can be used as a standalone tool to characterize adsorbed water and the mechanisms of hydration and dehydration of clays. However, since the infrared spectrum of clay is complex, we will also show the efficiency and accuracy of molecular dynamics to refine the interpretation of spectra. Finally, we will apply both infrared and molecular dynamics probes to characterize the low temperature dynamics of confined water and propose a mechanism for water freezing inside clays.

## 1 Evolution of the structure and connectivity of water adsorbed in clay minerals upon swelling

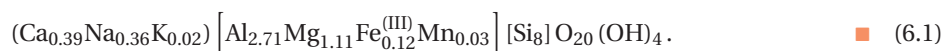
In the present study, we reinvestigate the hydration and dehydration processes of a sodium-exchanged montmorillonite clay using Fourier Transform infrared (FTIR) spectrometry in

both far- and mid-infrared domains, and try to analyze the evolution of the structure and connectivity of water molecules upon swelling. In Section 1.1, we will briefly present how samples were prepared for both far- and mid-infrared measurements. Then, in Section 1.2, we will present the evolution of the main components of the absorption spectrum in the different regions with respect to the relative humidity (RH), and discuss those evolutions in Section 1.3 to provide an attribution of the vibrational bands of montmorillonite in the far-infrared region and give a consistent picture of water adsorption and desorption mechanisms. We will see that the far infrared probe is specific to the adsorption sites of water, and is able to monitor the hydration mechanism at the various scales of porosity of clay minerals.

## 1.1 Experimental methods

### 1.1.1 Sample preparation

The clay used in this study is a natural montmorillonite SAz-2 from the Clay Mineral Society [Costanzo and Guggenheim, 2001]. The chemical formula is given by:



The interlayer charge – *i.e.* the net charge deficit per unit cell induced by isomorphous substitutions inside the clay layers – is  $1.16 \cdot e$ , with  $e$  the electronic charge, and is localized exclusively inside the octahedral sites of the clay layers. The sample was purified with respect to carbonates, organic matter and iron oxides following the procedure by Kittrick and Hope [Kittrick and Hope, 1963]. The interlayer cation was then exchanged with sodium using successive cycles of dispersion in a 1 mol/L sodium chloride solution and deionized water to remove excess ions. Finally, the clay was separated in four range of tactoids sizes – lower than 0.2  $\mu\text{m}$ , between 0.2 and 2  $\mu\text{m}$ , between 2 and 5  $\mu\text{m}$  and higher than 5  $\mu\text{m}$  – using various centrifugation and decantation cycles, following the procedure by Kittrick and Hope [Kittrick and Hope, 1963]. We qualitatively checked the result of particle-size separation using Scanning Electron Microscopy, as shown in Fig. 6.1. One can indeed observe an increase of the average size of the aggregates visible on the micrographs between the different pictures. In the following, all presented curves correspond to sample (a), *i.e.* clays particles smaller than 0.2  $\mu\text{m}$ . Curves corresponding to other samples displayed very similar behavior and are thus not shown for the sake of simplicity.

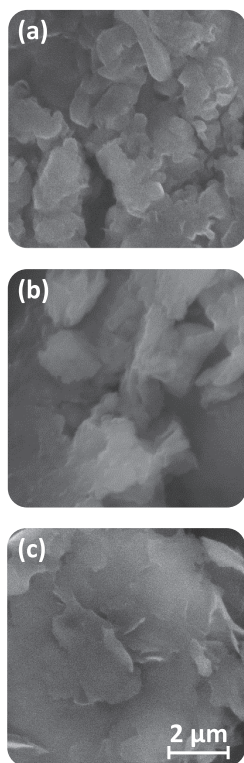


**Figure 6.1** ▲ Scanning Electron Micrographs (Secondary Electrons) of sodium-exchanged montmorillonite SAz-2 after particle size separation. From top to bottom: (a) smaller than 0.2  $\mu\text{m}$ , (b) between 0.2 and 2  $\mu\text{m}$  and (c) between 2 and 5  $\mu\text{m}$ .

### 1.1.2 Infrared absorption measurements

Infrared measurements were realized following the procedure described in Chap. 2. Far-infrared measurements were performed on the AILES beamline of Synchrotron Soleil, Saint-Aubin, France. Transmission spectra were recorded by averaging 200 scans from 100 to 680  $\text{cm}^{-1}$  with a resolution of 2  $\text{cm}^{-1}$ . The sample was dispersed in water, then a droplet of suspension was deposited over a diamond window, and let to evaporate. By doing so, a regular and a priori oriented (001) plans thin film was obtained. The sample was further dried from room conditions to RH = 0 in situ under vacuum during at least half an hour. Various RH values were used between 0 and 100 %. Before each measurement, we checked that the equilibrium was reached by following the evolution with time of the vapor pressure around the sample after the water injection/removal stopped inside the experimental cell.

Mid-infrared measurements were performed on a Thermo Nicolet iS10 spectrometer. Each spectrum was recorded by averaging 80 scans from 400 to 4000  $\text{cm}^{-1}$  with a resolution of 4  $\text{cm}^{-1}$ , using a single ATR accessory SensIR DuraSamplIR II. The sample was prepared in a similar manner than previously, except the droplet of clay suspension was deposited directly on the top-surface of the internal reflection element to get a good contact between the diamond and the clay thin film. All spectra were corrected following the formula  $A(\nu) \approx A_{\text{ATR}} \cdot \nu$  (see Chap. 2) to obtain transmission-equivalent spectra. The RH was varied from 0 to 100 % by step of 5 %.

## 1.2 Results

We present first the different results obtained in mid- and far-infrared domains, before discussing them in the next section.

### 1.2.1 Far-infrared measurements: connectivity region

The absorption spectrum of the Na-substituted montmorillonite SAz-2 is shown in Fig. 6.2 for various hydration states corresponding to different RH values among the adsorption branch of the water vapor adsorption isotherm (see Chap. 1). The absorbance was calculated using the absorption spectrum of the empty experimental cell as background. The

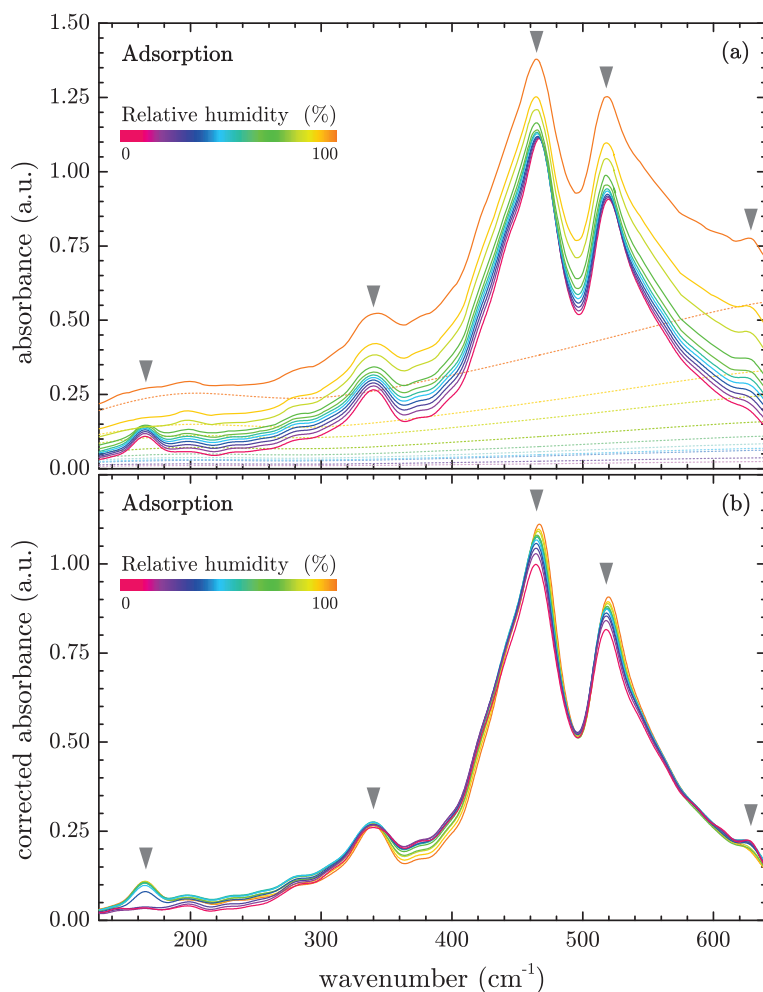


**Figure 6.2** ◀ (a) Evolution of the far-infrared absorption spectrum with RH during adsorption. Spectra are dominated by five main components (arrows) around 180, 340, 470, 520 and 630  $\text{cm}^{-1}$ . Dotted lines represent the part of the spectrum corresponding to “bulk-like” water. (b) Same spectra after subtraction of the “bulk-like” water component (dotted line of Fig. (a)).

spectrum appears complex, with many bands. However, five contributions predominate. They are located around 180, 340, 470, 520 and 630  $\text{cm}^{-1}$  (marked with gray arrows in Fig. 6.2). The two most intense contributions are localized at 470 and 520  $\text{cm}^{-1}$ . They are clearly identified in literature and corresponds to vibrations respectively associated with the deformation of Si–O–Si and Si–O–Al units in the clay layers [Madejová and Komadel, 2001, Boukili et al., 2003]. The other contributions have no clear assignment. We will suggest one in the discussion. Using a pumped bolometer working at 1.2 K, we also recorded the absorption spectrum down to 50  $\text{cm}^{-1}$  and saw no additional contribution. With increasing RH, one observes a strong evolution of the baseline, especially at high RH. Since it is generally assumed that water adsorbed in mesopores at high RH values behaves almost like bulk water (see, e.g. [Tardy et al., 1999] for a discussion about the evolution of the properties of water in mesopores with the water content), we tried to adjust the baseline using the absorption spectrum of pure bulk water  $A_{\text{bulk}}(\nu)$  (courtesy of J.B. Brubach) as described in the following. Since there should not be water adsorbed at 0 % of RH (referred as

the dry state in the following), the absorption spectrum corresponding to the dry state was subtracted to the others. Then, we calculated a coefficient  $\alpha(\text{RH})$  so that  $\alpha(\text{RH}) \cdot A_{\text{bulk}}(\nu)$  fits to the lower and upper wavenumber values of each spectrum  $A_{\text{clay}}(\nu, \text{RH}) - A_{\text{clay}}(\nu, 0)$ . The adjusted bulk spectra are shown with dotted lines in Fig. 6.2a, and the clay spectra after subtraction of this “bulk” component in Fig. 6.2b. It is noteworthy that the adjusted bulk spectra follow the shape of the clay spectra at low wavenumbers, *i.e.* between 130 and 240  $\text{cm}^{-1}$ . The trend is the same for the desorption branch. We rewrite the Beer-Lambert law [Atkins and de Paula, 2010]:

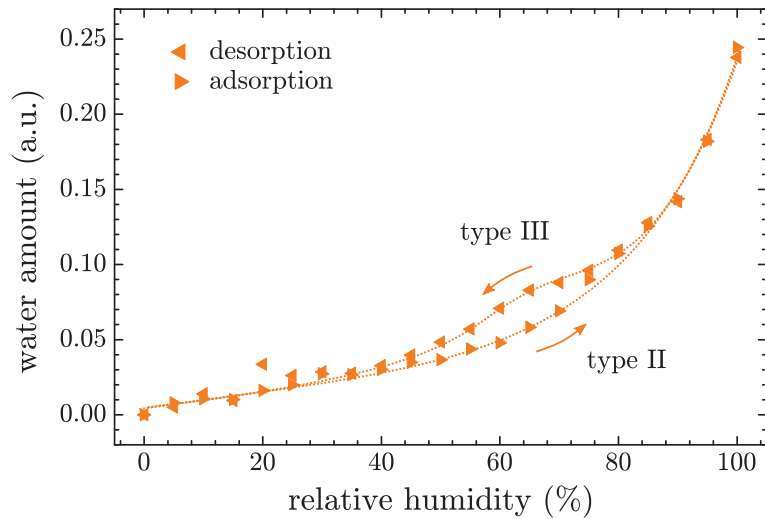
$$A(\nu) = \sum_i a_i(\nu) \cdot l \cdot c_i, \quad \blacksquare \quad (6.2)$$

with  $a_i(\nu)$  and  $c_i$  respectively the molar absorptivity and molar concentration of specie  $i$  and  $l$  the thickness of the sample, as a sum of “bulk-like” and other contributions:

$$A(\nu) = a_{\text{bulk}}(\nu) \cdot l \cdot c_{\text{bulk}} + \sum_{i \neq \text{bulk}} a_i(\nu) \cdot l \cdot c_i = a_{\text{bulk}}(\nu) \cdot \frac{n_{\text{bulk}}}{S} + \sum_{i \neq \text{bulk}} a_i(\nu) \cdot l \cdot c_i, \quad \blacksquare \quad (6.3)$$

where  $S$  is the surface of the sample (covered by the IR beam) and  $n_{\text{bulk}}$  is the amount of “bulk-like” water. Then, considering  $A_{\text{bulk}}(\nu)$  as a proxy of the molar absorptivity of water  $a_{\text{bulk}}(\nu)$ ,  $\alpha(\text{RH})$  is proportional to the amount of “bulk-like” water inside the sample at the corresponding RH.  $\alpha(\text{RH})$  is plotted for both adsorption and desorption branches in Fig. 6.3. The adsorption curve increases slowly at low RH, and more sharply at high RH. The desorp-

**Figure 6.3** ▶ “Bulk-like” water adsorption isotherm. According to the IUPAC classification, the adsorption curve corresponds to a type II isotherm, whereas the desorption curve corresponds to a type III isotherm. Dotted lines are guides for the eye.



tion curve match well with the adsorption curve at low and high RH values, but present an intermediate plateau between 80 and 60 % of RH. There is consequently a hysteresis on the adsorption isotherm. Using the classification of the IUPAC, the adsorption branch corresponds to an adsorption isotherm of type II, whereas the desorption branch corresponds to type III [Donohue and Aranovich, 1998]. We will discuss the implications of these particular shapes in the next section.

After subtraction of the “bulk-like” water contribution of all spectra (see Fig. 6.2b), the different bands show only small dependency to the hydration state. However, the Si–O–Si and Si–O–Al bands at 470 and 520  $\text{cm}^{-1}$  shift with the RH. It has been shown that the structure of the mineral, including those two bands, is highly sensitive to the presence of adsorbed water [Sposito and Prost, 1982, Yan et al., 1996, Kuligiewicz et al., 2015]. To emphasize the changes with respect to the dry state, the spectrum corresponding to the dry sample has been subtracted to the others. The evolution of the position of the remaining Si–O–Si and Si–O–Al bands is plotted in Fig. 6.4. Let us first consider the Si–O–Si deformation around 470  $\text{cm}^{-1}$ . The adsorption branch can be divided into three parts. Below 25 % of RH, the position of the band slightly decreases from 476 to 474  $\text{cm}^{-1}$ . Then, between approximately 25 % and 75 % of RH, the position remains constant, and finally, beyond 75 % of RH, it decreases from 474 to 472  $\text{cm}^{-1}$ . The desorption branch is somehow different since the

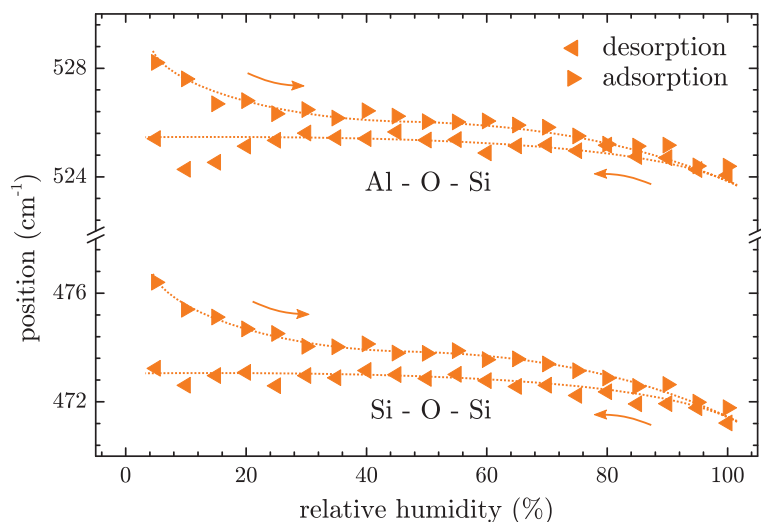


**Figure 6.4** ◀  
Evolution of the Si–O–Si and Si–O–Al deformation bands positions during adsorption and desorption of water. Both vibrational signatures behave similarly. At low RH during desorption, one does not recover the initial position of the bands, revealing some troubles to desorb water at low vapor pressures. Dotted lines are guides for the eye.

first step previously mentioned is not visible. The position increases slightly from 472 to 473  $\text{cm}^{-1}$  between 100 and 75 % of RH, and then remains constant. In addition, the plateau value is slightly shifted with respect to the adsorption branch. The same behavior is observed for the Si–O–Al deformation around 520  $\text{cm}^{-1}$ .

We now look at the band around 180  $\text{cm}^{-1}$ . Interestingly, this contribution is only visible at low RH values. The evolution of the amplitude of the band is reported in Fig. 6.5 for both adsorption and desorption branches. The position of the band and its half-height width do not change significantly with the RH. As in the previous case, the adsorption branch can be

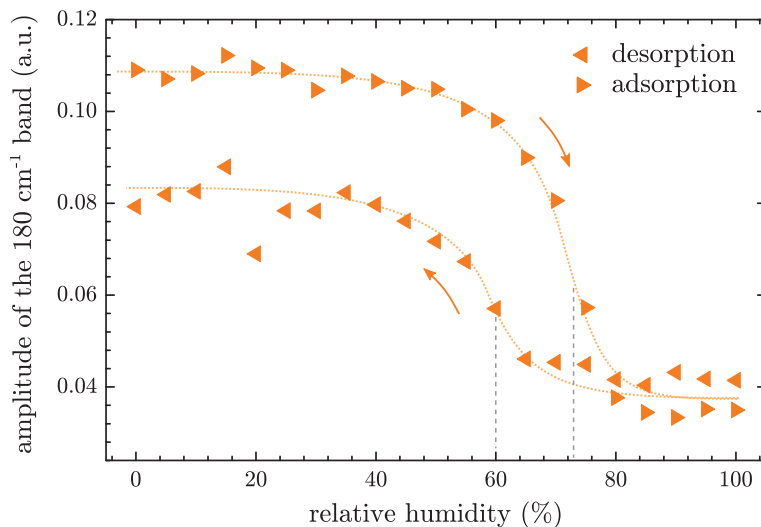


**Figure 6.5** ◀  
Evolution of the amplitude of the band around 180  $\text{cm}^{-1}$  with respect to the RH for both adsorption and desorption processes. Dotted lines are guides for the eye.

divided into three parts. First, the amplitude remains almost constant up to 60 % of RH. Then it strongly decreases between 60 and 80 % of RH, and it stabilizes at a constant value at higher RH. The desorption branch shows a bend between the low and high amplitude between 45 and 65 % of RH, revealing thus a strong hysteresis. Moreover, the plateau value at low RH is much lower than on the adsorption curve, meaning that the initial amplitude of the 180  $\text{cm}^{-1}$  band and thus the initial state of the clay is not recovered.

The band at 630  $\text{cm}^{-1}$  show a similar trend but the evolution of the amplitude of the peak is inverted: it increases instead of decreasing with respect to the RH. The curve reveals a similar bend as the 180  $\text{cm}^{-1}$  band, but the global evolution is less pronounced than the latter. Finally, looking at the band around 340  $\text{cm}^{-1}$ , there is no change of the position nor the amplitude with respect to the water content, but the half-height width slightly increases with RH in a similar manner to the amplitude of the 180  $\text{cm}^{-1}$  band (bend approximatively at the same position). However, since the evolution of the 340 and 630  $\text{cm}^{-1}$  contributions

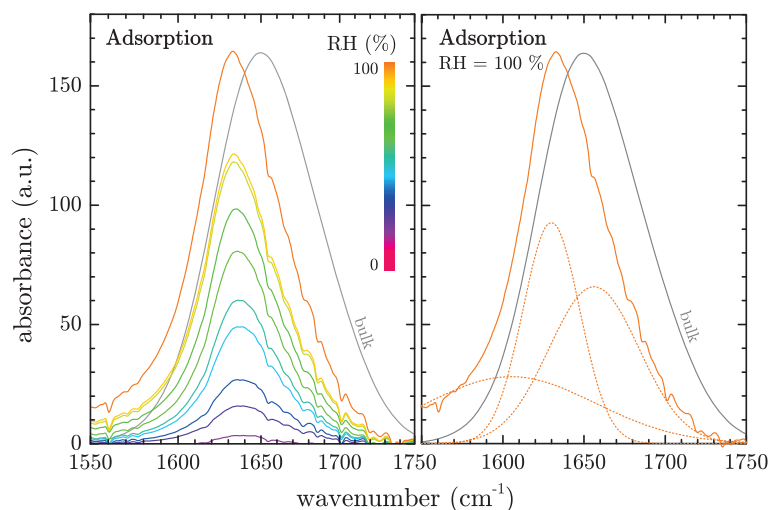
are small, it is difficult to separate the evolution upon swelling from noise and thus we will not use them in the following discussion.

### 1.2.2 Mid-infrared measurements (I): bending region

The “bending region” of the infrared absorption spectrum of Na-montmorillonite is given in Fig. 6.6 for different RH values along the adsorption curve. The spectral range is close to  $1650\text{ cm}^{-1}$ , which is the frequency of the bending motion of water molecules in bulk at ambient conditions [Bergonzi et al., 2014]. In this region, the spectrum of confined wa-

**Figure 6.6** ▶

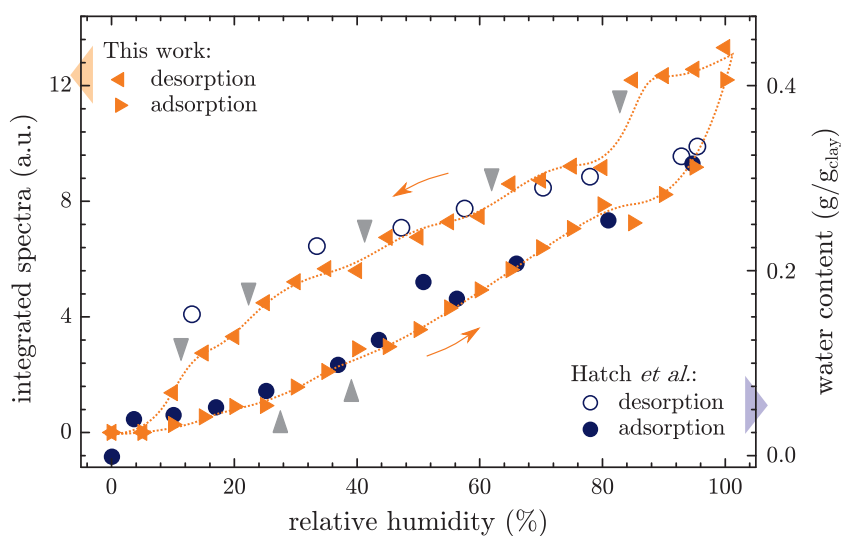
Left: Evolution of the bending mode of confined water with respect to the RH along the adsorption curve. To emphasize the evolution with respect to the dry state, the latter was subtracted to each spectrum. The grey curve corresponds to bulk water (courtesy of J.B. Brubach). Right: Deconvolution of the spectrum (at RH = 100 %) in three main Gaussian contributions, shown with dotted lines. Small negative lines that appear on the different spectra correspond to atmospheric water vapor.



ter is constituted, as in the case of bulk water, of a single well defined band. This band is however thinner than the one of bulk water and slightly shifted at lower frequencies. The band is deconvoluted using three Gaussians, one similar to the bulk water spectrum around  $1655\text{ cm}^{-1}$ , and two others of approximately equal weight (in terms of band area) at lower frequencies around  $1600$  and  $1620\text{ cm}^{-1}$ . Following the evolution of those three bands during hydration and dehydration of the clay sample, the amplitude of the three Gaussians evolves similarly. The evolution of the total area of the band (which should be proportional to the amount of absorbing species) is given in Fig. 6.7. During adsorption, at very low and

**Figure 6.7** ▶

Evolution of the total area of the bending band with respect to the RH along both adsorption and desorption curves. The area of each Gaussian presented in Fig. 6.6 show a similar trend. Dotted lines are guides for the eye. ATR experimental data by Hatch et al. [Hatch et al., 2012] are reported for comparison.



very high RH, the intensity of the band grows almost linearly. A plateau is observed around 85 % of RH, before a second growth regime, faster than the first one, up to the vapor saturation pressure. Small steps are visible at 25 % and 40 % of RH, but the precision of the measurements does not enable to be fully confident with their existence. The global shape

of this branch is in very good agreement with ATR measurements by Hatch et al. using a similar sample [Hatch et al., 2012], also reported in Fig. 6.7.

The desorption branch is a little bit more irregular, and shows a strong hysteresis. From 100 to 80 % of RH, the intensity of the band remains approximatively constant. Then, it decreases by steps with jumps around 80, 60, 40 and 20 % of RH. At 5 % of RH, one recovers the initial intensity.

### 1.2.3 Mid-infrared measurements (II): stretching region

The stretching region is the most commonly studied part of the clay spectrum. It refers to wavenumbers between 3000 and 3800  $\text{cm}^{-1}$ , where the stretching bands of O–H groups of water molecules lie in bulk water. The evolution of the adsorption spectrum in the stretching region in the case of clays is given in Fig. 6.8. After subtraction of the spectrum of the

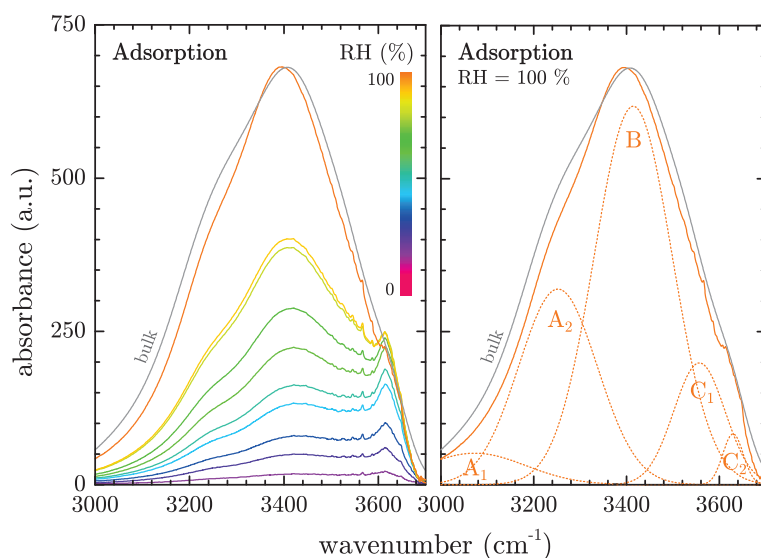
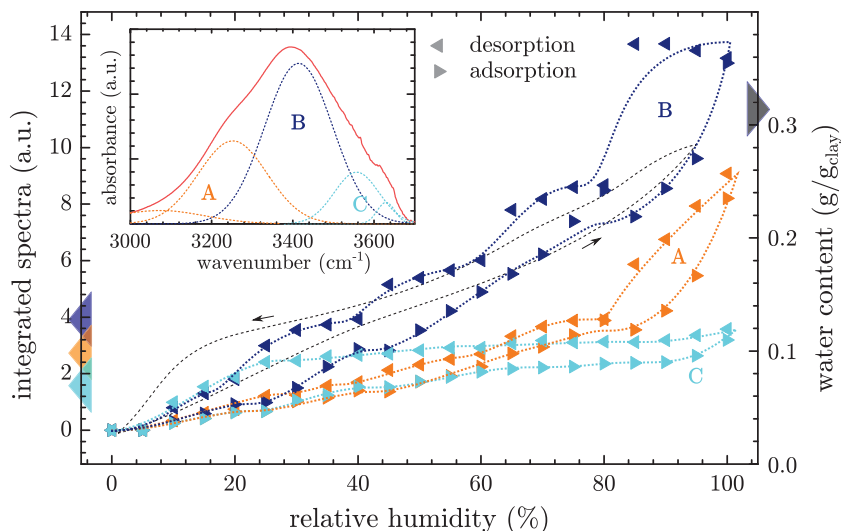


**Figure 6.8** ◀ Left: Evolution of the stretching modes of confined water with respect to the RH along the adsorption curve. To emphasize the evolution with respect to the dry state, the latter was subtracted to each spectrum. The grey curve corresponds to bulk water (courtesy of J.B. Brubach). Right: Deconvolution of the spectrum (at RH = 100 %) in five main Gaussian contributions, shown with dotted lines. Small teeth that appear on the different spectra correspond to atmospheric water vapor.

dry sample, the infrared adsorption spectra of hydrated Na-montmorillonite are very similar to the one of bulk water, except a high frequency contribution around 3620  $\text{cm}^{-1}$ , that tends to be negligible with respect to other contributions at high RH. Each spectrum was consequently deconvoluted following the scheme usually used for bulk water: four Gaussians centered around 3000, 3250, 3400 and 3550  $\text{cm}^{-1}$  were used (see Chap. 2), and a fifth Gaussian was used to describe the additional contribution at high frequency, around 3620  $\text{cm}^{-1}$ . These contributions can be associated to water molecules connectivity within the liquid. Following this approach, the bands at 3000 and 3250  $\text{cm}^{-1}$  are usually considered together – we will denote this as contribution *A* in the following – and it is the same for the bands at 3550 and 3620  $\text{cm}^{-1}$  – denoted contribution *C* in the following. The 3400  $\text{cm}^{-1}$  band will be denoted contribution *B*. Bands *A* correspond to highly H-bonded molecules (about 4 hydrogen bond per water molecule), band *B* corresponds to intermediately H-bonded molecules (between 2 and 3 hydrogen bond per molecule) and bands *C* correspond to poorly H-bonded molecules (1 or less hydrogen bond per molecule) [Brubach et al., 2005, Mallamace et al., 2007]. The evolution of the intensity (integrated bands) of those three contribution during both hydration and dehydration is shown in Fig. 6.9. Contributions *A* and *B* show a similar evolution with the RH, for both branches of the curves. The guide for the eyes of the *B* curve is, except minor changes, obtained by dilating the one of the *A* curve. Many steps appear on the curves, with well-defined jumps around 30 %, 60 % and 90 % of RH. Beyond 85 % of RH, the intensity increases faster, in a similar manner of what was observed in Fig. 6.3 for the “bulk-like” water contribution in the connectivity region. Desorption branches behave similarly to the bending band in Fig. 6.7, without any doubt this time concerning the presence jumps, located around 80 %, 60 %, 40 % and 20 % of RH. As in the case of the bending mode, the dry state is recovered at 5 % of RH. Contribution *C* looks simpler. It behaves like contributions *A* and *B* up to 60 % of RH among adsorption

**Figure 6.9** ▶

Evolution of the intensities of highly (A), intermediately (B) and poorly (C) H-bonded water molecule contributions in the stretching region with respect to the RH for both adsorption and desorption processes. Dotted lines are guides for the eye. Microgravimetry measurements of the water content, expressed in grams of water per gram of dry clay, from Xu et al. were reported (dashed line) for comparison [Xu et al., 2000].

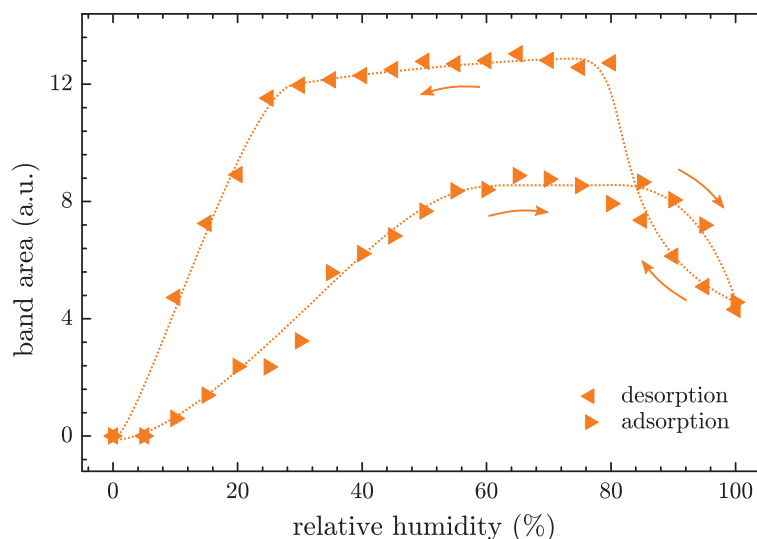


and then displays a large plateau from 60 to 90 % of RH and increases slightly at higher RH. The plateau is also visible and even larger on the desorption branch. It extends from 90 to 25 % of RH. Then the intensity decreases to its initial value.

To understand this particular behavior with respect to contributions A and B, we looked at the evolution of the intensity of the band at  $3620\text{ cm}^{-1}$ , that is specific to clays (whereas the others also appear on the spectrum of bulk water). Adsorption and desorption curves are plotted in Fig. 6.10. This band evolves in a completely different manner compared to the others. On the adsorption branch, the intensity increases almost linearly up to 55 % of RH, then it remains constant up to 85 % of RH and strongly decreases up to the vapor saturation pressure. The desorption branch evolves similarly, with a strong hysteresis. The intensity increases from 100 to 80 % of RH, then remains almost constant down to 25 % of RH and decreases to the initial value. We report the interpretation of this particular behavior in the discussion.

**Figure 6.10** ▶

Evolution of the area of the  $3620\text{ cm}^{-1}$  Gaussian contribution (see Fig. 6.8) with respect to the RH for both adsorption and desorption processes. Dotted lines are guides for the eye.



### 1.3 Discussion

#### 1.3.1 Band assignment in the connectivity region

As previously mentioned, among the five contributions that dominate the adsorption spectrum in the far-infrared region (here from  $130$  to  $640\text{ cm}^{-1}$ ), only two bands at  $470$  and  $520\text{ cm}^{-1}$  are clearly identified. They correspond respectively to the deformation of Si-O-Si

and Si–O–Al units in the clay layers [Madejová and Komadel, 2001, Boukili et al., 2003]. Here we propose an assignment for the other bands.

The band around  $180\text{ cm}^{-1}$  disappears at high RH. During swelling, both mesopores and interlayer space evolve, but however, the structure of mesopores should not change drastically: one only expect change of volume. On the contrary, the structure and dynamics inside the interlayer space strongly change [Sposito and Prost, 1982, Boek et al., 1995, Skipper et al., 2006]. Within the first stages of intercrystalline swelling, cations go out of the hexagonal cavities formed by the siloxane surface and interactions between successive layers and between layers and cations are screened by water molecules. Moreover, at high RH values, electric double layers are formed at each layer surface, inducing a repulsion between the surfaces and giving rise to osmotic swelling. Various translational modes are usually associated with the vibrations of the interlayer cation on the siloxane surface. It includes in-plane and out-of-plane modes. For example, in mica, out-of-plane vibrations of  $\text{K}^+$  were reported between  $136$  and  $152\text{ cm}^{-1}$  depending on the layer structure, whereas in-plane vibrations were reported between  $124$  and  $190\text{ cm}^{-1}$  [Prost et al., 1990, Laperche and Prost, 1991]. Both position and amplitude of these bands was shown to be affected by the nature of the interlayer cation, and the presence of substitutions in octahedral sites [Ishii et al., 1967, Laperche and Prost, 1991], probably due to the softening of interactions between layers and cations. In Na-exchanged montmorillonite SAz-2, the cation/layer interaction are indeed softer than in micas. Thus, the band at  $180\text{ cm}^{-1}$  could correspond to the in-plane translational modes of  $\text{Na}^+$  on the layer surface. Nevertheless, a precision must be added since in the case of montmorillonite, the interlayer cation is hydrated. Since isomorphic substitutions are purely localized in octahedral sheets in the present samples,  $\text{Na}^+$  is supposed to form outer-sphere surface complexes when more than one layer of water is adsorbed inside the interlayer space [Skipper et al., 2006]. Those outer-sphere complexes must reduce to inner-sphere complexes at lower water contents for steric reasons. Thus, we assign the band at  $180\text{ cm}^{-1}$  to in-plane translational mode of  $\text{Na}^+$  inner-sphere surface complexes at the surface of clay layers. This band disappears at high water contents, due to the increasing in-plane mobility of the cation with the progressive transition from inner-sphere to outer-sphere surface complexes after completion of the first hydration layer inside the interlayer space. This band should probably be modified/shifted when the inner-sphere surface complex is formed, which is not consistent with our observations at low RH. However, maybe there is some water adsorbed in the initial state. In that case, the inner-sphere complexes are already partially formed in our “dry” state. A cartoon of this vibration mode is given in Fig. 6.11. Interestingly, whatever the RH, no associated out-of-plane translational mode is observed. Maybe the strength of the interactions in the case of Na-exchanged montmorillonite is too weak, resulting in a broad and low-intensity band that does not appear clearly on the absorption spectrum.

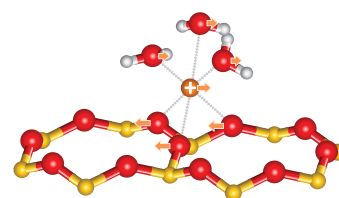


**Figure 6.11** ▲ Cartoon of the in-plane translational mode of the Na inner-sphere surface complex.

The band around  $340\text{ cm}^{-1}$  is almost not affected by hydration. The only modification is a slight enlarging at high RH, following a similar trend as the amplitude of the  $180\text{ cm}^{-1}$  band. Thus, the enlargement is probably related to the intracrystalline swelling within the interlayer space. In micas, a band at  $375\text{ cm}^{-1}$  was assigned to Si–O–Mg deformations [Jenkins, 1989]. Since outer-sphere surface complexes of  $\text{Na}^+$  are preferentially localized close to the siloxane hexagonal cavities on the top of substituted octahedral sites [Skipper et al., 2006, Mignon et al., 2010], it could correspond to the  $340\text{ cm}^{-1}$  band observed in the present work. The enlarging of the band is then due to a coupling between outer-sphere surface complexes and Mg atoms.

The band around  $630\text{ cm}^{-1}$  slightly grows during hydration, and its amplitude follow the same scheme as the  $180\text{ cm}^{-1}$  band (plateau up to RH = 60 %, fast evolution between 60 % and 80 %, plateau). Many bands in this region are assigned to Si–O–Al and Si–O–Mg vibrations in micas [Beran, 2002]. Using similar arguments as in the case of the  $340\text{ cm}^{-1}$  band, we may also assign this contribution to Si–O–Mg deformations. It is however difficult to say more.

### 1.3.2 Hydration of mesopores

As we already mentioned, it is usually admitted that water adsorbed in mesopores behave similarly to bulk water at high RH. The adsorption isotherm of “bulk-like” water shown in Fig. 6.3 corresponds indeed to type II and type III isotherms according to the classification of the IUPAC, which are prototypical isotherms for vapor adsorption in mesopores and macropores [Donohue and Aranovich, 1998]. Thus, this isotherm must represent mainly the contribution of mesopores within the global adsorption mechanism. The far-infrared adsorption spectrum of water is constituted by molecular libration as a very broad band centered around  $600\text{ cm}^{-1}$ , and connectivity as a shoulder of the previous band centered around  $200\text{ cm}^{-1}$  [Brubach et al., 2005]. Connectivity bands designate inter-molecular vibrations, and more precisely hydrogen bond stretching bands [Brubach et al., 2005]. Interestingly, since the bulk-water spectrum follows very well the absorption spectrum of the clay sample around  $200\text{ cm}^{-1}$ , as shown in Fig. 6.3, it means the water molecules connectivity is almost not affected inside mesopores, and on the opposite completely destroyed elsewhere (other water molecules do not contribute to the adsorption spectrum in the connectivity region).

Assuming this assignment of the “bulk-like” water isotherm, we see that water adsorption in mesopores begins at 0 % of RH, and the water content increases slowly and almost linearly up to 50 % of RH. The change in the slope beyond 50 % might be associated to mesopores swelling, which is consistent with the measurements by Salles et al., who found that mesopore swelling starts at 54 % of RH for another Na-montmorillonite [Salles et al., 2008]. Then, at high RH (beyond 85-90 %), the water content increases dramatically, that might correspond to the beginning of osmotic swelling, in consistency with another study [Salles et al., 2010]. This is however a little bit higher than the prediction by Cases et al. [Cases et al., 1992]. The shape of the adsorption branch, of type II, indicates weak interactions between water molecules and the surfaces. On the contrary, the shape of the desorption branch, of type III, indicates stronger interactions [Donohue and Aranovich, 1998]. It means that mesopore shrinkage is somehow more difficult than swelling. Cases et al. shown that intercrystalline swelling is accompanied by a restructuration of tactoids, and more precisely a diminution of the average number of clay layers per tactoids [Cases et al., 1992]. Thus, the hysteresis behavior observed between the swelling and shrinkage of mesopores might be due to a reconstruction of tactoids upon shrinkage, or some delay in the desorption of interlayer water, preventing the global shrinkage of the clay, and thus the shrinkage of mesopores. We will go back on this point later.

### 1.3.3 Hydration of interlayer cations and interlayer space

Information about the hydration of interlayer cations and interlayer space can be found in both far- and mid-infrared domains. We first discuss the far-infrared contributions. As we already mentioned, several bands in the connectivity region are sensitive to inner-sphere surface complexes. It includes the  $180\text{ cm}^{-1}$  that we assigned to in-plane translational mode of  $\text{Na}^+$  inner-sphere surface complex at the surface of clay layers. The evolution of this band consequently informs about the evolution of the population of such complexes, as explained in Section 1.3.1. Thus, at a RH of 60 %, inner-sphere surface complexes start to separate to the layer surface to form outer-sphere complexes. This correspond to the completion of the first hydration shell and the beginning of the formation of a second hydration shell inside the interlayer space. At a RH of 80 %, the band does not appear anymore on the spectrum, indicating the completion of the second hydration shell inside the interlayer space. During dehydration, the second hydration shell subsists down to 65 % of RH, where the intensity of the  $180\text{ cm}^{-1}$  starts to increase. The increase stops around 45 % of RH, but without recovering the initial value, meaning the desorption of the second hydration shell is incomplete. Hatch et al. argued that this non-reversibility can originate from traces of  $\text{Ca}^{2+}$  interlayer cations after sodium exchange process, since calcium is much more difficult to dehydrate than sodium [Hatch et al., 2012]. So, water molecules may stay bonded to  $\text{Ca}^{2+}$  ions at low hydration rates.

Cations preferentially remain near isomorphic substitution sites [Skipper et al., 2006], *i.e.* near Si-O-Mg or Si-O-Fe groups instead of Si-O-Al groups. This is consistent with the

presently observed behavior of the Si–O–Si and Si–O–Al bands at 470 and 520  $\text{cm}^{-1}$ , which show poor correlation with the 180  $\text{cm}^{-1}$  contribution. Since those groups cover the whole surface of the layers, they are of course correlated with intercrystalline swelling of the interlayer space. The slight shift of the two bands observed in Fig. 6.4 up to 25 % of RH should be related to the increase of the interlayer distance due to adsorption of first water molecules inside the interlayer space and formation of inner-sphere surface complexes with cations. Then the positions of the two bands show no sensitivity to the evolution of the interlayer distance during the adsorption of the first and second hydration shells. The final shift at RH higher than 80–85 % can be explained by the high decrease of the strength of interactions between layers when osmotic swelling starts, in consistency with our previous observations based on the evolution of the “bulk-like” water contribution. Moreover, as in the case of the “bulk-like” contribution, the desorption curve is really close to the absorption curve at high RH values. The hysteretic behavior and the absence of any curvature at low RH is consistent with our previous observation with the 180  $\text{cm}^{-1}$  band amplitude, and confirms the difficulty to recover the dry-state interlayer distance.

The mid-infrared region is much more complex to analyze. There is no evident separation of the contributions of the different adsorption sites. Substituting standard water by heavy water, Kuligiewicz et al. recently proved that the 3620  $\text{cm}^{-1}$  contribution visible on the absorption spectrum is related to both hydroxyl groups inside layers (also called constitution water) and hydration water, but the contribution of constitution water is only slightly affected by the hydration process [Kuligiewicz et al., 2015]. Consequently, since we subtracted the spectrum corresponding to the dry state to all spectra on Fig. 6.8, the contribution observed at 3620  $\text{cm}^{-1}$  should correspond only to hydration water. Therefore, the global area of the spectrum in the stretching region should include more or less all water molecules adsorbed in the sample, and must be correlated to the global water content of the clay. A first observation is that there is no crystalline order among adsorbed water. The spectrum is really similar to that of liquid bulk water and does not show the characteristic contributions of the spectrum of ice (see e.g. [Le Caër et al., 2014]). It was the same in the far-infrared region. Water adsorbed in clays is thus, at room temperature, liquid-like or amorphous. Then, the multi-step shape of the intensity curves displayed in Fig. 6.9 can be assimilated to standard water vapor adsorption isotherm plotted using, e.g. microgravimetry, even if our curves are more structured than those obtained using microgravimetry [Cases et al., 1992, Xu et al., 2000] (see Fig. 6.9). The curve by itself however does not give an accurate description of the global hydration mechanism due to the lack of sensitivity with respect to the various adsorption sites. The rapid increase of the global water content at high RH previously observed is here confirmed. To this extent, the evolution of the 3620  $\text{cm}^{-1}$  band is much more interesting. Kuligiewicz et al. assigned this band to interlayer water molecules bonded to the siloxane surface [Kuligiewicz et al., 2015]. Using this assignement, the progressive increase of the intensity of the peak up to about 55 % of RH can be explained by the progressive filling of the first hydration shell inside the interlayer space, consistently with our conclusions based on the 180  $\text{cm}^{-1}$  band. After the saturation of the siloxane surface, this contribution does not evolve anymore up to 80 % of RH. The strong decrease of the intensity of the band at higher RH confirms the beginning of osmotic swelling. The stretching spectrum also indicates the evolution of the average connectivity of water molecules. As shown in Fig. 6.12, according to the deconvolution of the stretching spectrum previously mentioned in terms of hydrogen bonding, the stretching frequency of O–H bonds of water molecules decreases progressively, departing from C band to contribute then to A band. This has to be associated with the increase of the interlayer distance, since water molecules become less constraint and can form hydrogen bonds with other molecules, acquiring a more “liquid-like” structure. The H-bond distribution at the vapor saturation pressure is however slightly different to those predicted by the percolation model [Stanley and Teixeira, 1980] for bulk water, which describes accurately the H-bond distribution from low to ambient temperature [Brubach et al., 2005]. The proportion of intermediately H-bonded molecules is much higher in confined water than in bulk water, whereas the population of highly H-bonded molecules is lower in confined water. On the contrary, the poorly H-bonded molecules ratio is well reproduced. At the end of dehydration, the population of poorly H-bonded molecules is higher than before hydration, which confirms that constrained interlayer water remains after at the end of

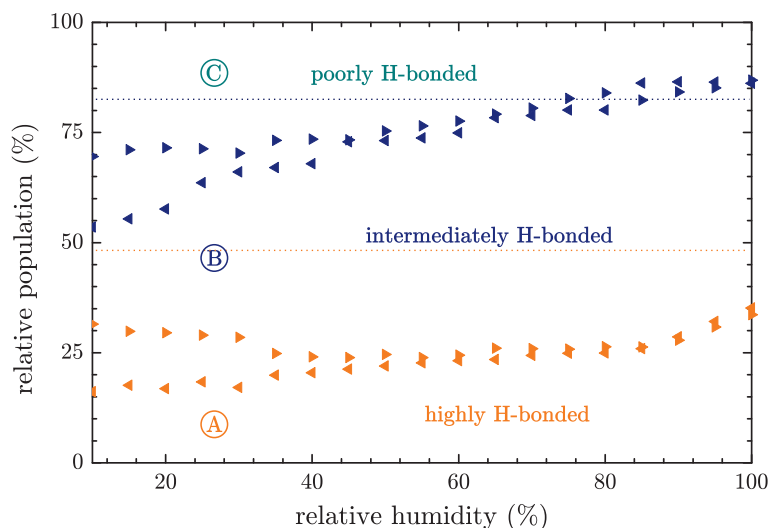


**Figure 6**  
Evolution of the A, B and C contributions (relative population) as a function of relative humidity. The data correspond to the desorption branch of the DSC curves (see Fig. 6.12) [Cases et al., 1980].

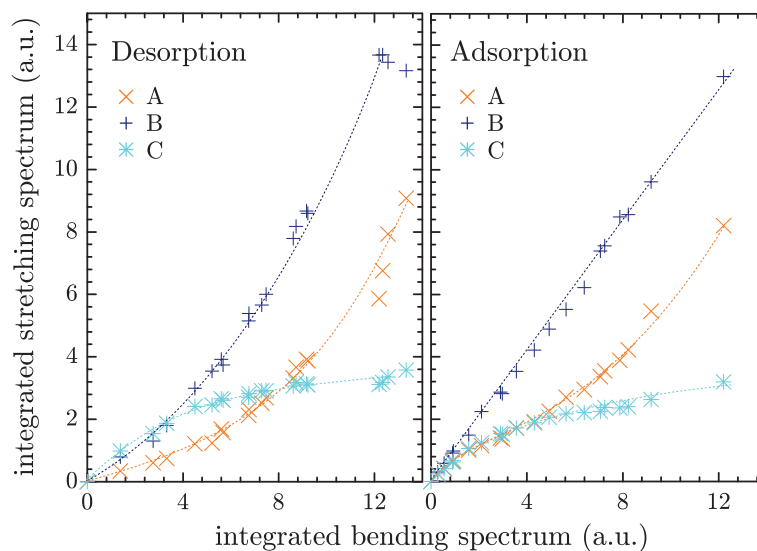
the desorption process.

The desorption branch shows, consistently with previous observations, that osmosis-driven shrinkage stops around 80 % of RH, and then, dehydration of the first hydration shell of interlayer space starts around 25 % of RH whereas there is no more interlayer water at 5 % of RH, which is in very good agreement with the scheme proposed by Cases et al. (see Chap. 1) [Cases et al., 1992].

Surprisingly, atmospheric dehydration performed with ATR measurements enabled to recover the dry state, whereas we failed in the case of dehydration under vacuum performed during transmission measurements. This might be explained by the fact that we waited for equilibration during a longer time in the case of ATR measurements, and that drying occurred under atmospheric pressure instead of vacuum (thus there was an external force applied on the layers, making the departure of water molecules easier and leading to smaller tactoids not so well oriented).

**Figure 6.13** ▶

Correlation between the area of the different contributions (A, B and C) of the stretching region and the area of the bending band, for both adsorption and desorption. Dotted lines are guides for the eye.



The absorption spectrum in the bending region is even harder to interpret, since all contributions behave similarly, as it can be observed in Fig. 6.7. It is however well correlated to the evolution of the B band of the stretching region, as shown in Fig. 6.13, especially during adsorption. The slight differences between the two spectral region might be due to the fact that water molecules strongly bonded to siloxane surfaces contribute less to the bending region, since bending is partially avoided by the constraints in the structure, as mentioned by Hatch et al. [Hatch et al., 2012]. It is however difficult to interpret more this curve.

## 1.4 Summary and conclusion

Using infrared absorption spectrometry as a unique probe, we succeeded to recover and complete, *e.g.* by precisizing the hydration mechanism of mesopores and the dynamics of cations, the hydration and dehydration schemes proposed by Cases et al. by combining X-ray diffraction, thermogravimetry, N<sub>2</sub> adsorption and calorimetry. During adsorption, mesopores are progressively filled up to 50 % of RH, and then starts to swell. In the meantime, one observes the intercrystalline swelling of interlayer space. At 25 % of RH, there are water molecules inside each interlayer space. Interlayer cations go out of siloxane cavities to form inner-sphere surface complexes. The first layer of interlayer water is completed around 60 % of RH, and the second layer around 80 % of RH, with a progressive weakening of interactions between interlayer cations and clay layers with the transition from inner- to outer-sphere surface complexes. At higher RH (80-85 %), intercrystalline swelling is replaced by osmotic swelling. Desorption follow a slightly different scheme, with complete dehydration of the second hydration shell of interlayer water around 25 % of RH, and of the first hydration shell around 5 % of RH. Dehydration of mesopores follow a similar path that hydration, with however a slight hysteresis. Whatever how constrained they are, water molecules never show any crystalline order at room temperature. Water structure inside mesopores was found to be very similar to those of bulk water in terms of connectivity of molecules, whereas this connectivity is almost destroyed for water adsorbed in other pores, indicating a more amorphous structure than liquid water.

The far-infrared spectrum turned out to be much easier to interpret than the mid-infrared spectrum, since its different contributions discriminate the different kinds of adsorption sites. Thus, with the improvement of internal sources and detectors of commercial spectrometers in the far-infrared domain, far-infrared absorption spectroscopy, using the present band assignement, opens perspectives for easy monitoring of the hydration and dehydration mechanisms in swelling clays, that could play an important role in the future in soil science. We will apply this method to analyse the thermal behavior of absorbed water in Section 3.

## 2 Mono- and bi-layer configurations of interlayer water

Although we identified signatures associated to the different hydration states of a clay sample, the study of the infrared absorption spectrum developed in the previous part is far from complete. The aim of this section is to show how molecular simulations can help to go further in the previous discussion.

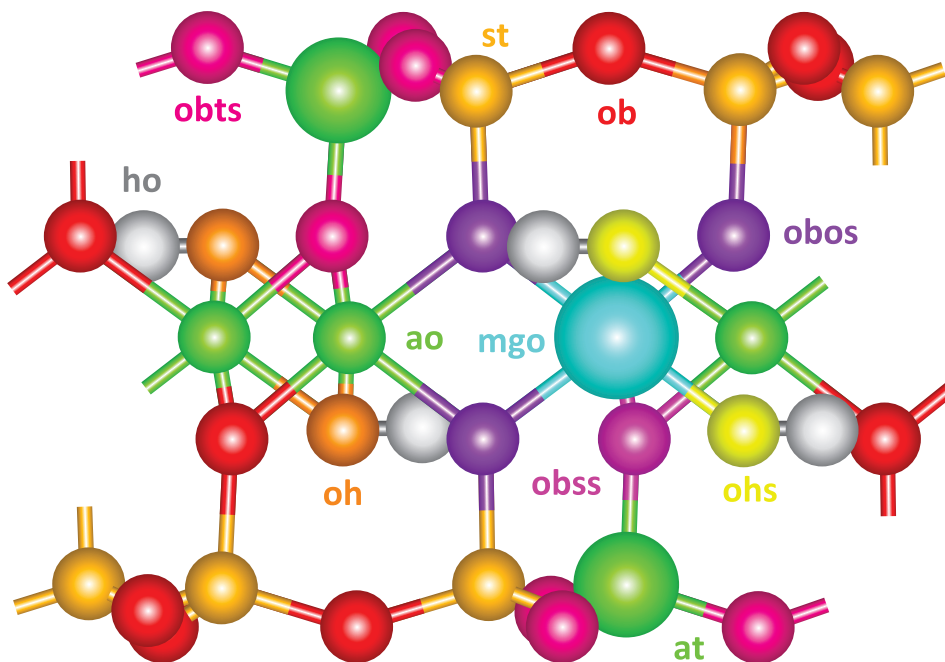
As mentioned in Chap. 1, the scale probed using molecular dynamics methods corresponds very well to the interlayer space. Consequently, we will focus only on the properties of interlayer water in the following.

### 2.1 Numerical methods

Clay layers are modeled using the ClayFF forcefield by Cygan et al. [Cygan et al., 2004] and its improvement ClayFF/M [Greathouse et al., 2009]. With this model, the clay layers are fully flexible. Atoms interact through a Lennard-Jones potential and Coulombic interactions. Moreover, a Morse potential is applied to O–H groups of layers (constitution water) and a harmonic potential is applied to angular displacement of M–O–H groups, with M the atom in octahedral sites connected to the hydroxyl group. To take into account the modifications induced by isomorphic substitutions, the charge of oxygen atoms depends on the nature of their surrounding atoms (see Fig. 6.14).

In order to reproduce experimental conditions, clay layers with the same chemical composition as montmorillonite SAz-2 were generated using a homemade routine. Octahedral substitutions were randomly distributed, and interlayer cations were fully exchanged with sodium. All simulations are performed using two clay layers (repeated periodically) of 12 × 8 crystal unit cells. The number of cations is adjusted to minimize the total charge of the simulation box.

**Figure 6.14** ▶ Parametrization of the ClayFF force field (adapted from [Ngouana W and Kalinichev, 2014]). Dark yellow: silicon (st); green: aluminum (ao/at); cyan: magnesium (mgo); grey: hydrogen (ho), red/purple/dark pink/light pink/light yellow: oxygen (o...). The different colors used for oxygen atoms correspond to different partial charges, depending on the nature of atoms in their surroundings.

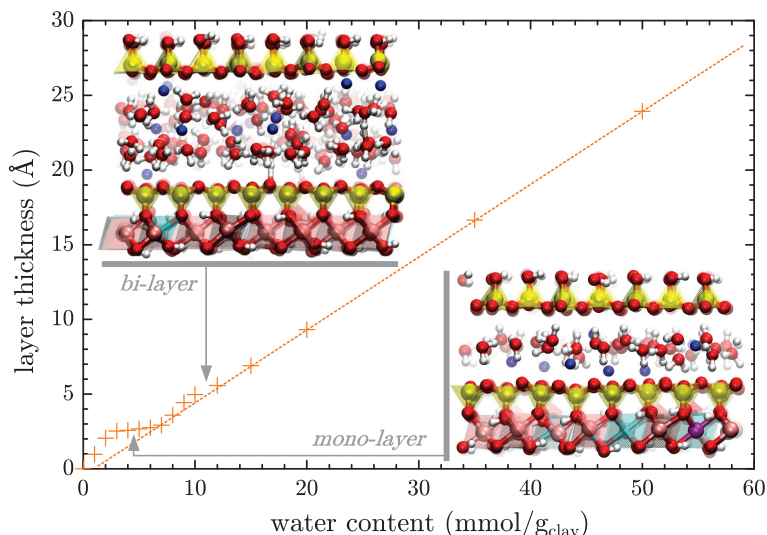


This force field was initially developed using the SPC/*f* [Teleman et al., 1987] forcefield for water. Here we use the TIP4P/2005*f* forcefield [González and Abascal, 2011], and the ion forcefield developed in Chap. 5 for sodium cations. No adjustment was performed on the other ClayFF parameters to fit to these changes.

Simulation boxes are first equilibrated for a fixed amount of water in  $NpT$  ensemble during 200 ps using an anisotropic global barostat to allow the system to relax independently in the three directions of space since the interlayer space is anisotropic. Then, the equilibrium thickness of the box (*i.e.* the dimension in the direction normal to the layers) is measured by averaging the size of the box in  $NpT$  ensemble during 1 ns and finally, the volume of the box is adjusted to this dimension and equilibrated in  $NVE$  ensemble during 1 ns. All measurements are then performed in  $NVE$  ensemble at the equilibrium volume, using a unique replica of the system.

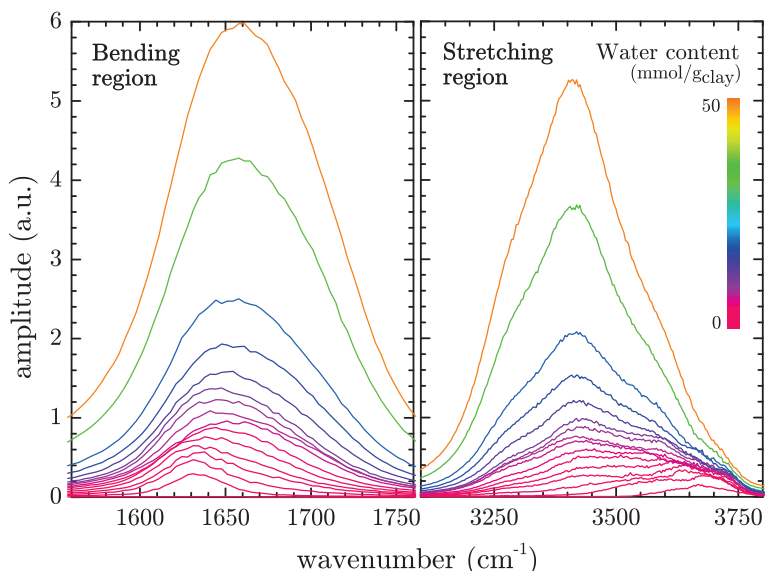
## 2.2 Identification of the stable mono- and bi-layer hydration configurations by molecular simulation

It is difficult to monitor experimentally the amount of water present in the interlayer space, because this water content is generally inhomogeneous. The interlayer space of clay is filled by a distribution of  $n$ -layer stable configurations of water molecules, with  $n = 1, 2, 3$  or 4, that can be estimated using X-ray diffraction (see *e.g.* [Cases et al., 1992]). This is thus of particular interest to analyze these  $n$ -layer configurations. Molecular simulations can isolate such configurations. To determine the water content associated to these configurations, the equilibrium thickness of the water layer was computed for various water content from 1 to 50 mmol of water per gram of dry clay (denoted mmol/g or mmol/g<sub>clay</sub> in the following). The evolution of the thickness with respect to the water content is shown in Fig. 6.15. The thickness increases linearly with the water content, except steps at low water contents, corresponding to stable configurations of interlayer water. The first step around 4-5 mmol/g is then identified as the mono-layer configuration, and the second one around 11-12 mmol/g is associated to the bi-layer configuration. In the following, the box with 5 mmol/g of water is used as a reference for the monolayer configuration and the box with 12 mmol/g is used as the reference for the bi-layer configuration.



### 2.3 Vibrational density of states of the mono- and bi-layer configurations

Now that we have identified the mono- and bi-layer configurations, we can analyze their contribution to the global water vibrational spectrum of clay. First, to check the validity of the model to reproduce the vibrational spectrum of clay, the evolution of the vibrational density of state (VDOS) is plotted for all water contents in Fig. 6.16 in both bending and stretching regions. It must be noticed that the VDOS and the infrared absorption spectrum



The VDOS was computed using the method presented in Chap. 2.

**Figure 6.16** ◀ Evolution of the calculated VDOS in the bending and stretching regions with respect to the water content. No normalization is applied.

should be different since there are selection rules in infrared spectrometry (see Chap. 2). Moreover, experimental spectra include all adsorbed water and also radiation absorbed by the mineral, whereas in the present case, the calculation is limited to the displacement of hydrogen atoms, probing thus vibrations of adsorbed water and constitution water. However, the spectra plotted in Fig. 6.16 are very similar to experimental infrared absorption spectra (see Figs. 6.6 and 6.8). Nevertheless, some differences can be observed with respect to experimental spectra. For example, the bending band shifts with the water content, which was not visible experimentally, probably due to the contribution of water molecules adsorbed in other pores. To go further in the discussion, we focus on the mono- and bi-layer configurations. Snapshots of those two configurations extracted from the simulations are shown in Fig. 6.17. We can see thus they correspond indeed to respectively one and two layers of water molecules inside the interlayer space. One can in addition notice the prefer-

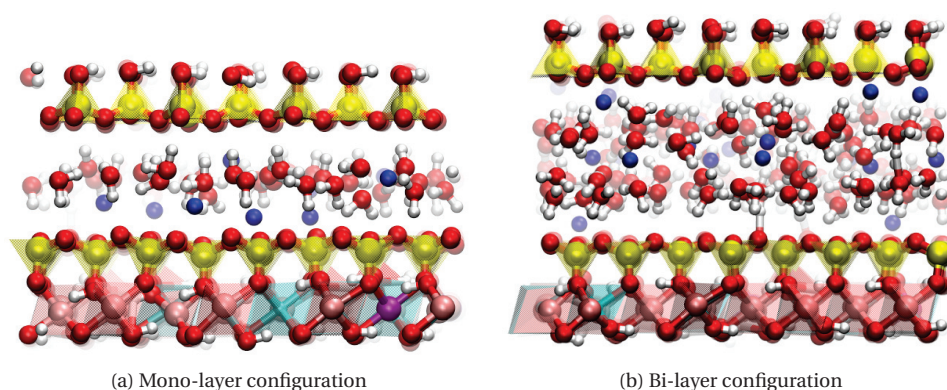
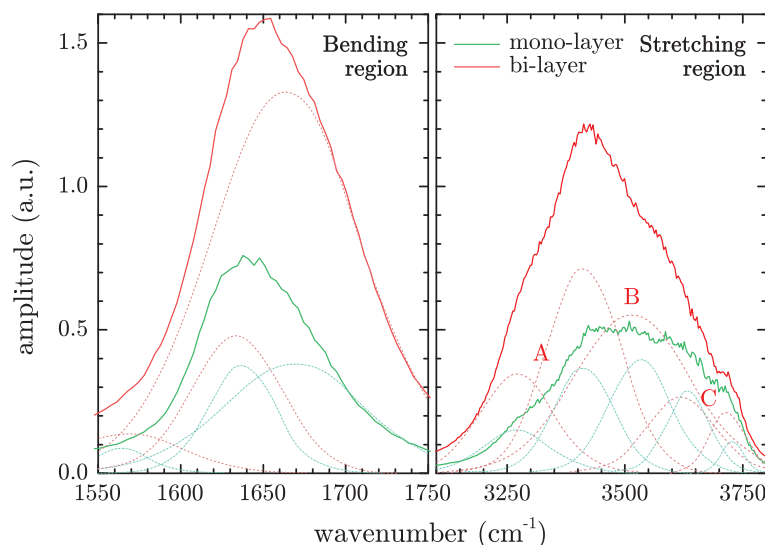


**Figure 6.17** Snapshot configurations of water molecules in the mono-layer (left) and bi-layer (right) configurations. The oxygen, hydrogen, silicon, and aluminum atoms are represented by red, white, yellow, and blue spheres, respectively.

entential orientation of water molecules near the solid surfaces with an O–H bond pointing to the clay layer, as previously mentioned (see Chap. 1).

The VDOS of these two configurations are plotted in Fig. 6.18. As in the case of experimental

**Figure 6.18** ▶ VDOS of the mono- and bi-layer configurations in the bending and stretching regions. A deconvolution with Gaussians is shown in dotted lines, using the same A/B/C classification as in the previous section for highly, intermediately and poorly H-bonded species respectively.



spectra, the VDOS in the bending and stretching regions can be respectively deconvoluted using three and five Gaussians. Looking first at the stretching region (6.18 (right)), the presence of five Gaussians with a non negligible amplitude shows that the three populations – poorly, intermediately and highly H-bonded – of water molecules are present even in the mono-layer configuration. Increasing the water content to form the bi-layer state, the amplitude of the fourth Gaussian increases less than the others. It means that the average connectivity of water molecules inside the interlayer space increases in the bi-layer state with respect to the mono-layer state.

In the bending region, the band is centered around the frequency of the second Gaussian in the mono-layer configuration, which was not observed in our infrared experiments, probably, as we already said, because of the contribution of water molecules in other pores. On the contrary, in the bi-layer configuration, the spectrum is largely dominated by the third contribution, leading to a shift of the band to higher wavenumbers. Additional calculations are necessary to interpret this shift, but should enable to learn much more about the dynamics of confined water and water-clay interactions.

## 3 Low temperature dynamics of confined water

### 3.1 Water thermally induced migration and dynamics singularities

We come back now on the experimental far-infrared absorption spectrum of clay and the attribution of its components proposed in Section 1. This aim of this section is to analyze the low temperature global dynamics of water and try to understand the phases transitions mentioned in Chap. 1.

#### 3.1.1 Experimental methods

The sample in the experimental setup used here are the same as those used in Section 1. The hydration cell is coupled to a helium cryostat to adjust the temperature, as explained in Chap. 2. The sample is first cooled down to 130 K. Then, the temperature is increased by steps of 5 K. Infrared spectra are recorded dynamically during the increase of the temperature. The temperature is monitored using a thermocouple positioned close to the sample. Its variation during the time of the measurement is lower than 2 K. Due to the thermal inertia of the cryostat, the temperature recorded near the sample is slightly lower to that of the cold head. However, this difference remains almost constant during all the experiment, as shown in Fig. 6.19. Consequently, no spurious effect due to the inertia of the cooling system is expected during the measurement.

Six series of measurements were recorded **with the same clay deposit**, on different points of the water adsorption or desorption isotherm: at 0, 30, 75 and 90 % of RH upon hydration, and at 75 and 30 % of RH upon dehydration. For each measurement, the sample was first equilibrated at the corresponding vapor pressure at room temperature, and then, was isolated from the hydration setup before cooling starts.

#### 3.1.2 Results

All measurements show a similar evolution of the absorption spectrum with the temperature. So, for the sake of simplicity, we only show curves corresponding to the sample equilibrated at RH = 30 % upon hydration. Moreover, for a given RH, except the contribution at  $170\text{ cm}^{-1}$  associated to Na inner-sphere complexes, the different spectral contributions mentioned in Section 1, *i.e.* bands at  $340$ ,  $470$ ,  $520$  and  $630\text{ cm}^{-1}$ , behave similarly when the temperature is increased. All these contributions were attributed to vibrations inside the clay layers, but were shown to be highly sensitive to the water content (see Section 1). The curve corresponding to the evolution of the height of the band at  $340\text{ cm}^{-1}$  is shown in Fig. 6.20. The global variation of the height of the peak appears complex. It increases from 130 to 250 K approximately in a linear way. Three points corresponding to an increase of the slope are visible at 150, 210 and 235 K approximately. Then, the curve decreases up to 275 K approximately, and increases again at higher temperature, with a slope similar to those corresponding to temperatures lower than 150 K. Moreover, the last segment looks in the continuation of the first one, as underlined by the dotted line in Fig. 6.20. The evolution of others layer bands are a little bit simpler, with no singularity between 150 and 250 K, but the global shape is almost the same.

All these slope changes should correspond to sample singularities with respect to the temperature. This is confirmed by the similarity between our measurements and heat capacity measurements on a similar clay sample by Gailhanou (see Fig. 6.20) [Gailhanou, 2005]. However, one must distinguish singularities associated to water and those associated to the mineral itself. To this extent, it can be interesting to look at the temperature evolution of a dehydrated sample. The evolution of the  $340\text{ cm}^{-1}$  band at RH = 0 % is also given in Fig. 6.20. We also reported some typical spectra recorded at various temperatures between 130 and 300 K at RH = 0 % in Fig. 6.21.

Various singularities are also present in the evolution of the height of the  $340\text{ cm}^{-1}$  band, but not as much as for RH = 30 %, and the shape of the curve is slightly different. There is no more slope break at 210 and 235 K, and the slope between 150 and 210 K is lower at RH = 0 % than at RH = 30 %. The decrease between 250 and 275 K is also lower at RH = 0 %, but

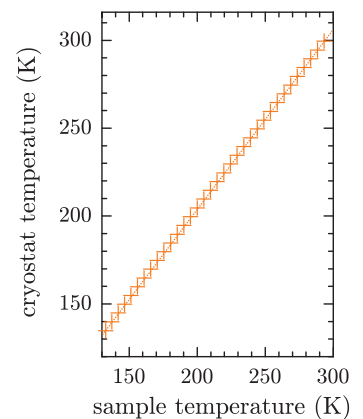


**Figure 6.19** ▲ Comparison of the temperature of the cold head of the cryostat and those measured near the sample.

The other spectra are shown in appendix at the end of this chapter.

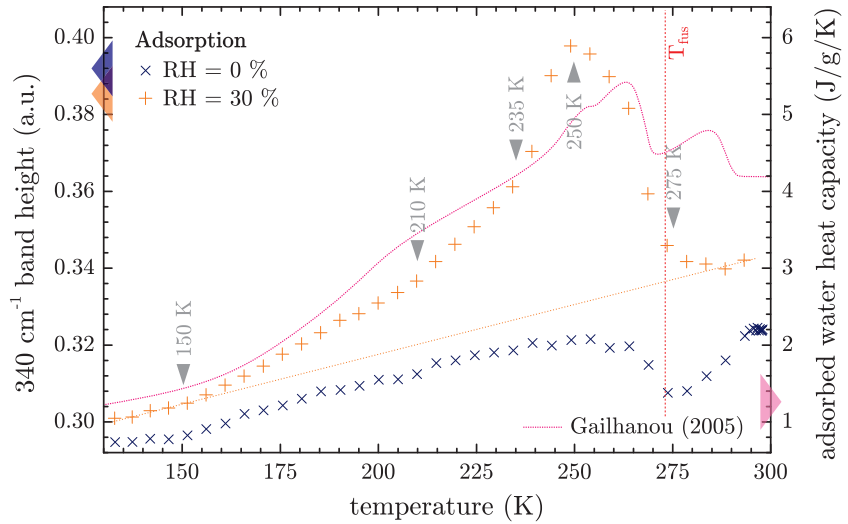
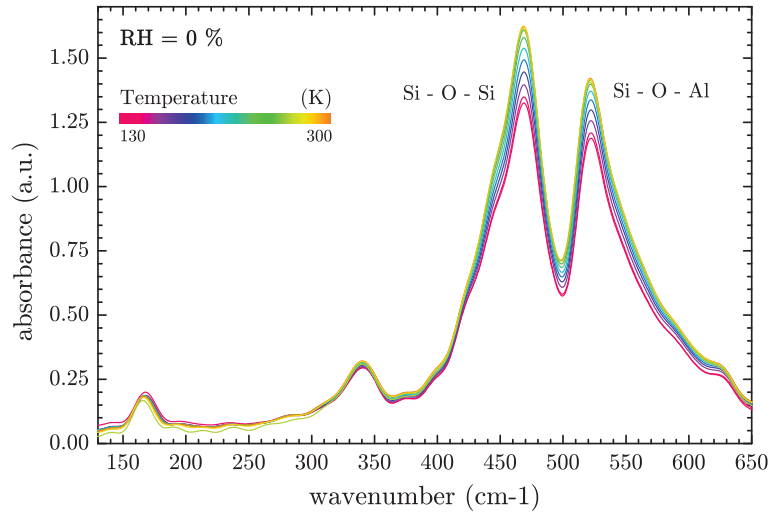


**Figure 6.20** Evolution of the 340 cm<sup>-1</sup> band height and adsorbed water heat capacity with temperature at RH = 30 %. The heat capacity is plotted from a similar experiment as in Gailhanou (2005) and is plotted for comparison.

**Figure 6.21** Evolution of the FIR adsorption spectrum with temperature at RH = 0 %.

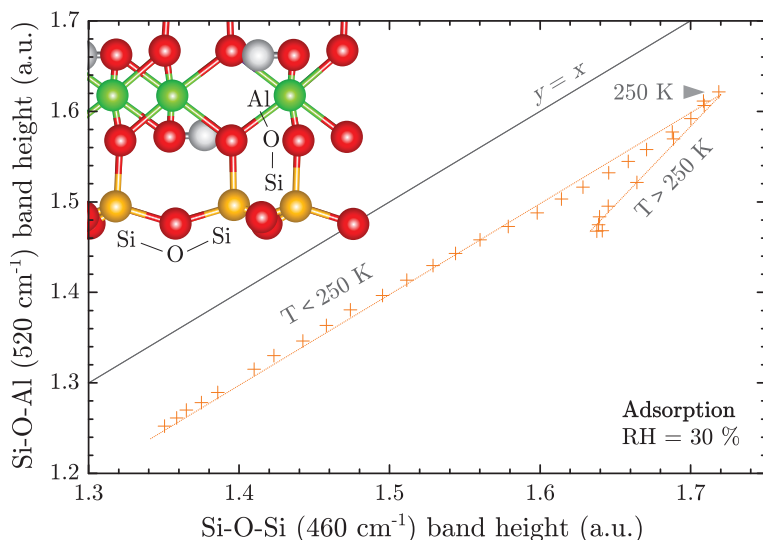


as in the case of the measurement at RH = 30 %, the curve increases at higher temperatures to reach a plateau that looks in the continuation of the curve at temperatures lower than 250 K. One must remember that room temperature measurements revealed the presence of some traces of water adsorbed in clay at RH = 0 % (see Section 1). Since the same sample is used for each RH value, the contribution of the mineral to the evolution of the spectrum with temperature should not change. Consequently, since the amplitude of variation are systematically lower at RH = 0 % than at RH = 30 %, all singularities can be associated to water.

To go further, we looked at direct correlations between the spectral contributions of clay at a given RH. Especially, as it can be seen on Fig. 6.21, the bands associated to Si–O–Si and Si–O–Al bending motions at 460 and 520 cm<sup>-1</sup> respectively highly depends on the temperature, even at RH = 0 %. So, the evolution of the height of the Si–O–Al band was plotted as a function of the height of the Si–O–Si band in Fig. 6.22. For temperatures lower than 250 K, the two bands behave the same: the ratio of the two bands evolves linearly with the temperature, with a slope close to unity. In contrast, at higher temperatures, the Si–O–Si band decreases more slowly than the Si–O–Al band. The same trend is observed at RH = 0 %, but the bend at high temperatures is much smaller. One can expect thus that the evolution observed below 250 K with a unity slope correspond to the thermal response of the mineral, whereas the bands are influenced by water at higher temperatures, and more precisely by interlayer water since the Si–O–Al and Si–O–Si groups cover surface of layers. We will try to discuss that later.

Finally, we also looked at the evolution of the band associated to interlayer cations, *i.e.* the

maximum  
50 cm<sup>-1</sup>)  
0 cm<sup>-1</sup>)  
spect to



band around 170 cm<sup>-1</sup>. The evolution of the height of the band with respect to the temperature is given in Fig. 6.23. The height of the band first increases fast up to 150 K, then goes back to its initial value abruptly and remains almost constant up to 235 K, where the band almost disappears. It reappears around 275 K and its height decreases up to room temperature. In addition, the segment between 275 and 300 K looks like a continuation of the curve at temperatures lower than 235 K. We will try to interpret this surprising behavior in the following section.

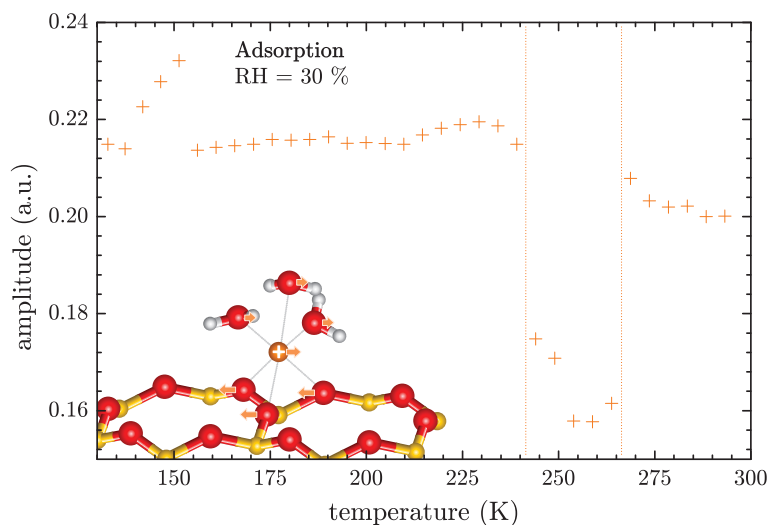


**Figure 6.23** Evolution of the height of the 170 cm<sup>-1</sup> band with the temperature.

### 3.1.3 Discussion

The fact that clay layers adsorption bands vary non-monotonically and that the interlayer cation band disappears transiently during the increase of the temperature is very surprising and constitutes a strong evidence that the low temperature dynamics of adsorbed water is highly complex.

First, it must be noticed that whatever the RH and the temperature considered, no band associated to ice is visible on the clay spectrum (see Chap 2 for the spectrum of ice). Moreover, there is no important change in the global shape of the spectrum that could indicate an important modification of the structure. Consequently, no crystallization is observed, even at high RH.

We associated in Section 1 the band at 170 cm<sup>-1</sup> to inner-sphere surface complexes inside the interlayer space, and we showed that this band disappears when the water content in-

side the interlayer space increases, due to the progressive transformation to outer-sphere surface complexes. Since the band is present at low temperatures (and looks in the continuation of the band at high temperatures), the transient disappearance of the band cannot be associated to some freezing. It does not mean that there is no freezing, but that freezing, if occurs, do not affect the shape of the spectrum. Consequently, the transient disappearance of the band should be associated to transient formation of outer-sphere surface complexes, and thus, a transient increase of the water content inside the interlayer space between 235 and 275 K. Since the global water content inside the experimental cell is fixed during the experiment, it means water moves from one adsorption site to another when the temperature increases.

As we discussed in the previous paragraph looking at the correlation between the Si–O–Si and the Si–O–Al bands in Fig. 6.22, the structure and/or dynamics of water at the surface of clay layers undergo some change between 250 and 300 K, whereas no singular behavior is noticed at lower temperatures. It could mean thus that water at the surface of layers is frozen below 250 K. More specifically, the curve in Fig. 6.22 shows no more evolution at temperatures higher than 275 K, so surface water melts between 250 and 275 K. This is consistent with the experimental observations by Maheshwari et al. and Fleury et al. [Maheshwari et al., 2013, Fleury et al., 2013] who observed a partial freezing of water at layer surfaces around 273 K.

In addition, the similar evolution of the absorption spectrum below 150 K and above 275 K, as shown with the dotted line in Fig. 6.20, might indicate that water is completely frozen below 150 K, since glassy state dynamics is in the continuation of the liquid state dynamics.

We associated the band at  $340\text{ cm}^{-1}$  to Si–O–Mg deformations inside the layers, and pointed out the fact that this band should be more sensitive to water close to interlayer cations since cations stay preferentially near substituted sites of layers, so close to Mg atoms in the present case. Thus, it seems natural to associate the singularity observed at 235 K in Fig. 6.20 to the disappearance of the  $170\text{ cm}^{-1}$  band at the same temperature. The disappearance of the band at  $170\text{ cm}^{-1}$  indicates an increase of the water content around ions and a swelling of the interlayer space below 235 K, but not above. This might be explained by a freezing of water around cations at lower temperatures, preventing thus clay swelling.

Then, between 150 and 235 K, the slow evolution of the band at  $340\text{ cm}^{-1}$  might be explained by the migration of some water molecules inside the interlayer space, and especially around cations, but this migration is limited because swelling is inhibited by the fact that cations are frozen. The slope increase at 210 K indicates the migration is somehow easier between 210 and 235 K, that can be explained by a partial melting of water bi-layer configurations in interlayer space.

### 3.1.4 Summary and conclusion

Putting together all elements discussed in the previous paragraph, we suggest the following mechanism. At temperatures lower than 150 K, water adsorbed in clay is completely frozen. Increasing the temperature, water in mesopores progressively melts from 150 to 210 K. Between 210 and 240 K, water in interlayer space with several adsorbed water layers partially melts whereas surface water and water around cations remains frozen, allowing migration of a few water molecules from mesopores to interlayer space. At 240 K, water found back mobility around interlayer cations, allowing larger expansion of interlayer space, and thus, migration of more water molecules from mesopores to interlayer space. This causes the disappearance of inner-sphere surface complexes. Then, from 250 K to 275 K, water at layer surfaces melts, with a partial re-balancing of water contents between mesopores and interlayer space, *i.e.* water migrates again from interlayer space to mesopores. Finally, at 275 K, there is no more frozen water and stable monolayer configurations inside interlayer space are recovered, with associated inner-sphere surface complexes.

We showed that temperature variations are associated with water migration between the different porosities. Water in each pore freeze at a more or less low temperature, without crystallization. It means thus water is in a glassy state. It is consistent with observations by Gailhanou, Maheshwari et al. and Fleury et al. [Gailhanou, 2005, Maheshwari et al.,

2013, Fleury et al., 2013], but in disagreement with assumptions by Salles et al. [Salles et al., 2010] who predict no freezing of interlayer water. Further study, for example using X-ray diffraction to follow directly the evolution of the interlayer space with temperature, are necessary to confirm the migration mechanism proposed here. Moreover, advanced molecular simulations could be used with interest to analyse the stability of a liquid-like phase inside the interlayer space at low temperatures through a nucleation analysis (see *e.g.* [Sosso et al., 2016]), but this is beyond the scope of the present dissertation.

### 3.2 Low temperature hydrodynamic properties of interlayer water

We showed in the previous part that there is no signature of crystallization of adsorbed water. However, the infrared probe fails to distinguish between “liquid-like” and “amorphous” (glassy) water. To this extent, simulations can give supplemental information. In this section, we come back on molecular dynamics simulations of interlayer water using the same routine as in Section 2, and perform steady-state shear flow calculations of the hydrodynamics properties of water and of the interface using the methods developed in Chaps. 3 and 4, with however a slight modification. Since the clay layers are flexible, the thermostat is applied to the walls (layers) instead of water. This avoids spurious effects in the dynamics due to the thermostat. To validate the method, all calculations are performed for a water content equal to 50 mmol/g, which is very high compared to experiments and corresponds to almost no confinement. Further work would consist in applying the same procedure to the bi-layer configuration to characterize the dynamics of interlayer water.

The evolution of the shear viscosity of interlayer water with the temperature is plotted in Fig. 6.24. The curve is very similar to that of bulk water, but is slightly shifted up. This is not

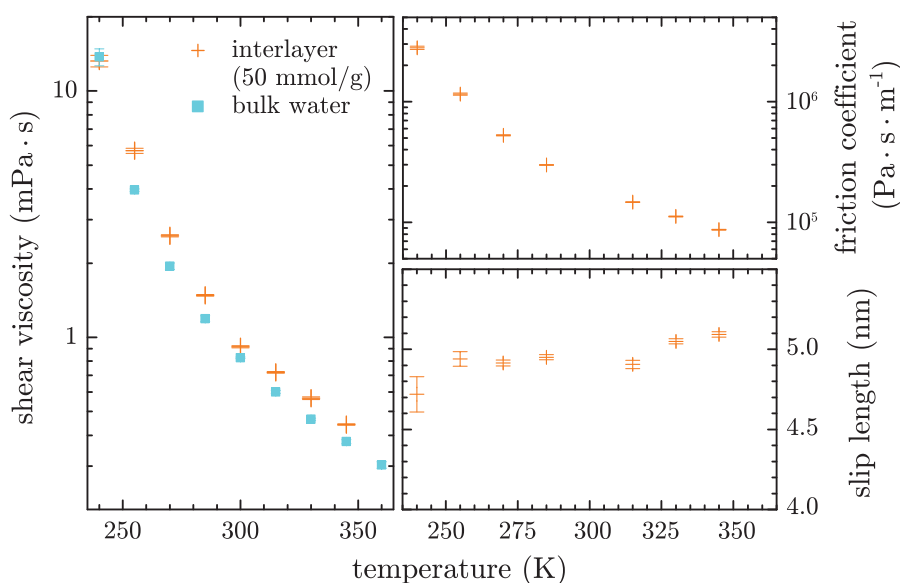


**Figure 6.24** ◀ Evolution of the shear viscosity of interlayer water, and of the clay-water friction coefficient and slip length with respect to the temperature. The shear viscosity values calculated numerically for bulk water in Chap. 3 are also plotted for comparison.

surprising since there are a lot of cations solvated inside interlayer water, and we showed in Chap. 5 that numerical models predicts an increase of the shear viscosity when the salt concentration is increased in the case of small ions. The shear viscosity can be extrapolated at lower temperatures to investigate about a possible glass transition. Consequently, repeating those calculations at low temperatures might help to identify the various phase transitions observed in the previous section.

We also looked at the evolution with the temperature of the properties of the water-clay interface, through its friction coefficient and its slip length using nonequilibrium steady-state shear flow calculations. The corresponding curves are plotted in Fig. 6.24. Contrary to what was observed in the case of the hydrophobic model surface (see Chap. 4), the friction coefficient calculated under shear-flow evolves monotonically over the range of temperatures considered here, with an increase at low temperatures. Interestingly, the slip length remains almost constant with the temperature, meaning the increase of the friction coefficient follow that of the shear viscosity of interlayer water. The value, around 5 nm, is much

higher than the molecular size (about 3 Å). This indicates a hydrophobic behavior, and this is in strong disagreement with calculations by Botan et al. who found about 3 Å for the slip length [Botan et al., 2011]. This might indicate a failure of the model used for clays, and thus, those results must be considered cautiously. Since we do not use the water force field that was used to develop ClayFF, water-clay interactions might be misevaluated. The slip length could be thus used to calibrate interaction parameters, for example comparing experimental and calculated slip length of water over mica surfaces. This is beyond the scope of the present dissertation, but it is of particular interest for future studies since the slip length influences the permeability of the interlayer space. Especially, a fast increase of the slip length at low temperatures, similar to what we observed in Chap. 4 for a model surface, would enable fast transport inside the interlayer space. This would be problematic for applications of clays for the storage of nuclear waste we mentioned in the Introduction.

## 4 Summary and conclusion

---

In this chapter, by investigating the now relatively well understood mechanisms of swelling and shrinkage of clays, we showed that the infrared probe can be used as a standalone probe to monitor water inside clay. The vibrational properties of adsorbed water are well restituted by molecular dynamics simulations, that should be used with benefits in the future to make the best from infrared spectra. We then applied infrared spectrometry to study the low temperature dynamics of water adsorbed in clays. We reported a complex mechanism of exchange of water between the different kind of pores when the temperature is increased, and freezing of water of all pores, including interlayer water, at various temperatures depending on the pore type. Finally, we showed that molecular simulations could be used with interest in the future to analyze the low temperature dynamics of interlayer water, but the present numerical model must be first corrected to have a good restitution of the properties of the water-clay interface.

## 5 Appendix: Temperature dependence of the far-infrared absorption spectrum for various hydration states

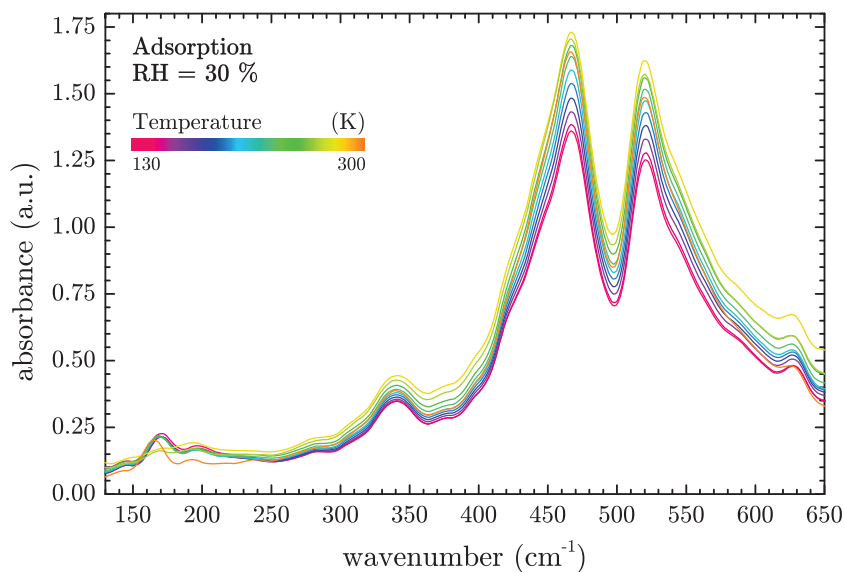


**Figure 6.25** ◀ Evolution of the FIR adsorption spectrum with temperature at RH = 30 % during adsorption.

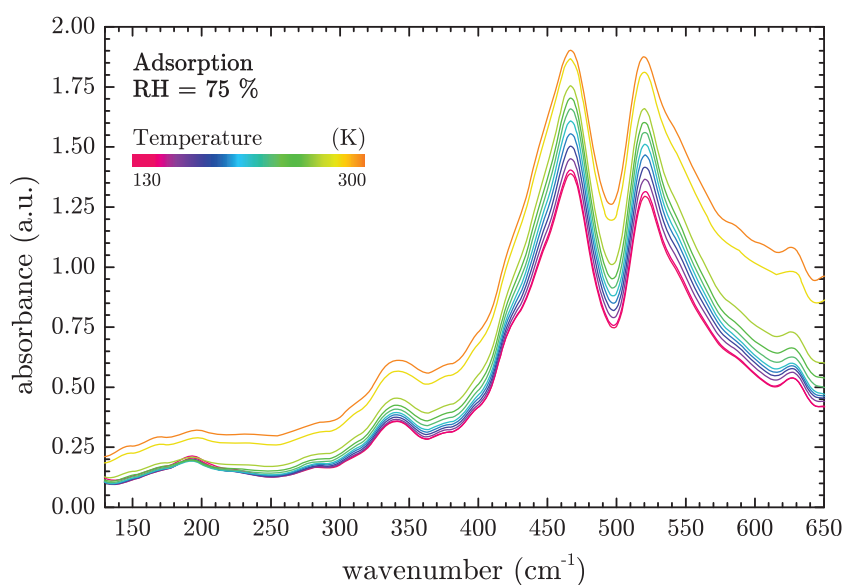


**Figure 6.26** ◀ Evolution of the FIR adsorption spectrum with temperature at RH = 75 % during adsorption.

**Figure 6.27** ▶  
Evolution of the FIR adsorption spectrum with temperature at RH = 90 % during adsorption.

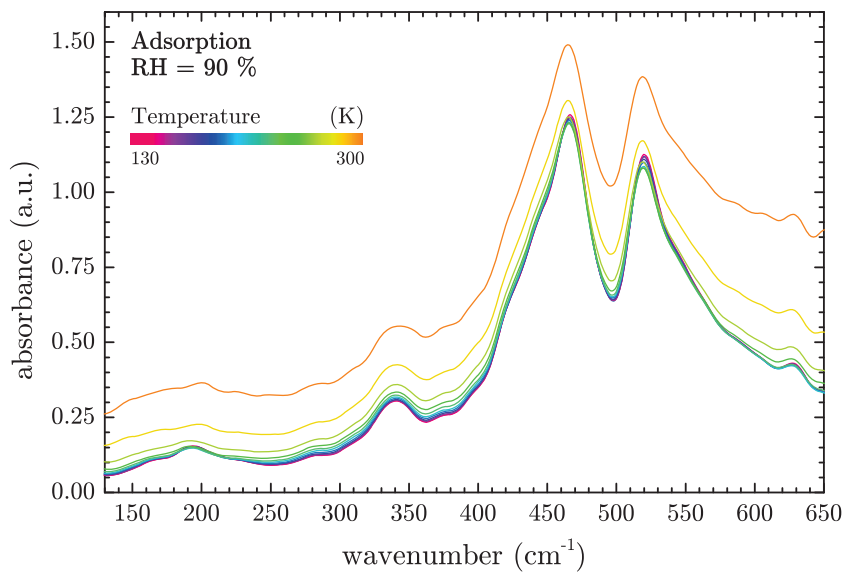


**Figure 6.28** ▶  
Evolution of the FIR adsorption spectrum with temperature at RH = 75 % during desorption.

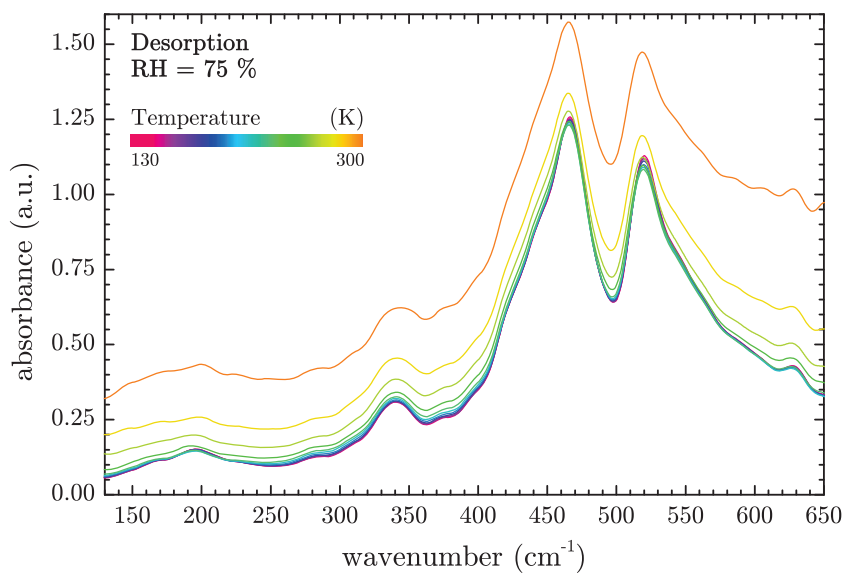
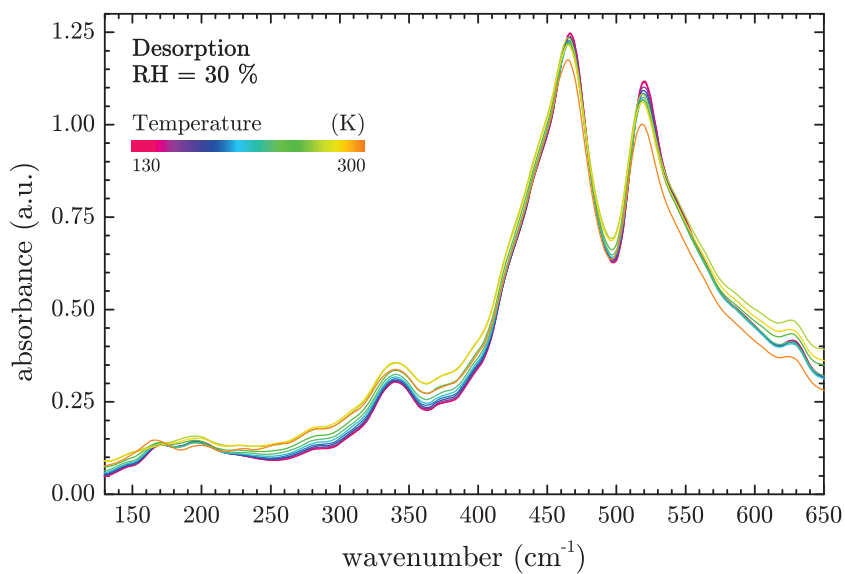


**Figure 6.29** ▶  
Evolution of the FIR adsorption spectrum with temperature at RH = 30 % during desorption.



# Conclusion

Looking at the structural and dynamical properties of water in various environments – in pure bulk, near a hydrophobic wall or mixed with salts – we assessed the accuracy of classical molecular dynamics to describe water over a wide range of temperatures, including the supercooled regime. Especially, we showed in Chap. 3 that the TIP4P/2005f force field reproduces the tabulated shear viscosity of bulk water over both stable and supercooled domains at ambient pressure. Then, we used those viscosity calculations, combined with structural relaxation time calculations, to investigate the debated glass transition of water, and pointed out the influence of the choice of the observable used to predict the glass transition temperature. We also showed that the low temperature long-time dynamics of water (e.g. its viscosity and structural relaxation time) can be well described by the so called “elastic models”. Finally, we provided a method to perform accurate *ab initio* calculations in the isothermal-isobaric ensemble, which, when applied with some dispersion functionals such as VdW-DF2, provided a quantitative agreement with several dynamical observables such as the liquid shear viscosity. In Chap. 4, we focused on the behavior of water near a model hydrophobic surface when decreasing the temperature. We observed a very large increase of the water-wall slip length at low temperatures that might be due to a transition from a liquid-solid to a solid-solid friction regime, and which could, if confirmed, improve considerably the hydrodynamic permeability of nano-channels. In Chap. 5, we developed a new force field to describe accurately water hydrodynamic transport when small ions, like lithium or sodium, are dissolved inside water. However, our model fails for larger ions. Nevertheless, putting everything together, one can expect a good modeling of the interlayer space of sodium-exchanged montmorillonite clays, that can be seen as a layer of interfacial water with sodium cations inside. To this extent, we confronted infrared absorption measurements and classical molecular dynamics calculations in the last chapter to study both room temperature and low temperature dynamics of water confined in clay minerals. We showed that the infrared probe, and, in particular, the far-infrared probe, can be used as a standalone probe to discriminate the water molecules depending on the nature of the pore where they are confined. However, a large part of the infrared absorption spectrum is hard to interpret without additional information. From this point of view, molecular dynamics constitutes an interesting complement, able to isolate molecular configurations corresponding to specific hydration states of clays. Then, decreasing the temperature, we highlighted a complex dynamic of water, with progressive freezing and transfer between the different pores. However, since infrared spectroscopy cannot distinguish fluid water from its glassy counterpart, molecular dynamics simulations are necessary to reach a complete characterization of the dynamics of water at low temperatures. Along the way, this low temperature molecular study pointed out a weakness of our model, with a wrong restitution of interfacial friction, which needs to be adjusted in the future.

This work introduced the key elements to analyze water confined in clays, and more generally various aqueous media, but is, of course, far from being complete. We just mentioned the necessity to adjust the clay model to improve water-clay interactions. There is also a need for a more general ion force field, compatible with the TIP4P/2005f force field. Then, using those elements, one could couple molecular dynamics and infrared spectrometry to reach a complete interpretation of the adsorption spectrum, and thus the structure and connectivity of water adsorbed in clays. One should also look at the influence of the nature of substitutions inside the layers and the nature of the interlayer cation. *Ab initio* calculations might help to understand these effects, for which dielectric properties of water are expected to play an important role. Then, a precise understanding of the structure of confined

water and of the interactions between clay layers and water should help to understand the role of clay as catalyst, and to assess the hydrodynamic permeability of clays in the context of waste management and civil engineering.

# Conclusion

En étudiant les propriétés structurales et dynamiques de l'eau dans divers environnements – eau pure en volume, près d'une surface hydrophobe, ou en présence de sels – nous avons évalué la précision de la dynamique moléculaire classique pour décrire l'eau sur une large gamme de températures, notamment dans le domaine surfondu. En particulier, nous avons montré au Chap. 3 que le champ de force TIP4P/2005f reproduit la viscosité tabulée pour l'eau pure en volume aussi bien dans le domaine stable que dans le domaine surfondu à pression atmosphérique. En combinant ensuite ces valeurs de viscosité à des calculs du temps de relaxation structural, nous nous sommes intéressés à la transition vitreuse controversée de l'eau, et avons mis en avant l'influence du choix de l'observable utilisée pour prédire la température de transition vitreuse. Nous avons également montré que la dynamique aux temps long de l'eau à basse température (sondée à travers sa viscosité et le temps de relaxation structural) est bien décrite par les modèles dits « élastiques ». Enfin, nous avons mis en place une méthode pour réaliser des calculs *ab initio* précis dans l'ensemble isotherme-isobare, qui, lorsqu'elle est mise en œuvre avec des fonctionnelles dispersives telles que VdW-DF2, permettent d'évaluer de manière quantitative différentes observables dynamiques telles que la viscosité du liquide. Dans le Chap. 4, nous nous sommes intéressés au comportement de l'eau près d'une surface hydrophobe modèle lorsque l'on diminue la température. Nous avons observé une forte augmentation de la longueur de glissement de l'eau à l'interface qui pourrait être due à une transition entre un régime de frottement de type solide-liquide et un régime de frottement solide-solide, et qui pourrait, si elle est confirmée, améliorer considérablement la perméabilité hydrodynamique des nano-canaux. Dans le Chap. 5, nous avons développé un nouveau champ de force pour décrire de façon précise les propriétés de transport hydrodynamique de l'eau en présence de petits ions tels que le lithium ou le sodium. Cependant, notre modèle est mis en défaut pour les ions plus gros. Néanmoins, en regroupant tous les résultats, nous pouvons espérer une bonne modélisation de l'espace interfoliaire des montmorillonites sodiques, que l'on peut voir comme un film d'eau interfaciale avec des cations sodium. Pour cette raison, nous avons confronté des mesures d'absorption infrarouge et des calculs de dynamique moléculaire dans le dernier chapitre pour étudier la dynamique de l'eau confinée dans les argiles à la fois à température ambiante et à basse température. Nous avons montré que la spectroscopie infrarouge, et plus particulièrement la spectroscopie dans l'infrarouge lointain, peut être utilisée comme un outil unique pour discriminer les molécules d'eau en fonction de la nature du pore dans lequel elles sont confinées. Cependant, une grande partie de l'information contenue dans le spectre infrarouge est difficile à interpréter sans plus d'indications. À ce titre, la dynamique moléculaire constitue un outil complémentaire intéressant, permettant d'isoler des configurations moléculaires correspondant à des états d'hydratation particuliers de l'argile. Puis, en diminuant la température, nous avons mis en évidence une dynamique complexe de l'eau, qui gèle progressivement et migre entre les différents types de pores. Cependant, comme la spectrométrie infrarouge ne permet pas de distinguer l'eau liquide de sa phase vitreuse, des simulations de dynamique moléculaire sont nécessaires pour caractériser complètement la dynamique de l'eau à basse température. Cette étude moléculaire à basse température a révélé au passage une faiblesse de notre modèle, à travers une mauvaise restitution des propriétés de frottement interfacial, qui devra être corrigée dans le futur.

Ce travail met en place les principaux éléments nécessaires pour analyser l'eau confinée dans les argiles, et plus généralement dans divers milieux aqueux, mais est, bien sûr, loin d'être complète. Nous venons notamment d'évoquer la nécessité d'ajuster le modèle d'ar-

gile pour améliorer la restitution des interactions eau-argile. Il est également nécessaire de développer un champ de force plus général pour les ions, qui soit compatible avec le modèle TIP4P/2005*f*. Une fois cela fait, il sera possible de coupler la dynamique moléculaire et la spectrométrie infrarouge pour essayer d'interpréter complètement le spectre d'absorption, et dans le même temps la structure et la connectivité de l'eau adsorbée dans les argiles. Il serait également intéressant de regarder l'influence de la nature des substitutions à l'intérieur des feuillets et de la nature du cation interfoliaire. Les simulations *ab initio* devraient aider à appréhender ces effets, pour lesquelles les propriétés diélectriques de l'eau jouent certainement un rôle important. Enfin, une compréhension précise de la structure de l'eau confinée et des interactions entre les feuillets d'argile et l'eau devraient aider à comprendre le rôle de l'argile comme catalyseur, et mieux maîtriser la perméabilité hydrodynamique des argiles dans le contexte du stockage des déchets et du génie civil.

# Bibliography

- [Abascal and Vega, 2005] Abascal, J. L. and Vega, C. (2005). A general purpose model for the condensed phases of water: Tip4p/2005. *The Journal of chemical physics*, 123(23):234505.
- [Abdulagatov et al., 2006] Abdulagatov, I. M., Zeinalova, A. B., and Azizov, N. D. (2006). Experimental viscosity b-coefficients of aqueous liCl solutions. *Journal of molecular liquids*, 126(1):75–88.
- [Adam and Gibbs, 1965] Adam, G. and Gibbs, J. (1965). On the temperature dependence of cooperative relaxation properties in glass-forming liquids. *Journal of Chemical Physics*, 43:139–146.
- [Alfè et al., 2014] Alfè, D., Bartók, A., Csanyi, G., and Gillan, M. (2014). Analyzing the errors of dft approximations for compressed water systems. *The Journal of chemical physics*, 141(1):014104.
- [Alfe and Gillan, 1998] Alfe, D. and Gillan, M. J. (1998). First-principles calculation of transport coefficients. *Physical review letters*, 81(23):5161.
- [Allen and Tildesley, 1989] Allen, M. P. and Tildesley, D. J. (1989). *Computer simulation of liquids*. Oxford university press.
- [Alleva et al., 2012] Alleva, K., Chara, O., and Amodeo, G. (2012). Aquaporins: another piece in the osmotic puzzle. *FEBS letters*, 586(19):2991–2999.
- [Amann-Winkel et al., 2016] Amann-Winkel, K., Böhmer, R., Fujara, F., Gainaru, C., Geil, B., and Loerting, T. (2016). Colloquium: Water's controversial glass transitions. *Reviews of Modern Physics*, 88(1):011002.
- [Ambrosetti et al., 2012] Ambrosetti, A., Ancilotto, F., and Silvestrelli, P. L. (2012). van der waals-corrected ab initio study of water ice–graphite interaction. *The Journal of Physical Chemistry C*, 117(1):321–325.
- [Angell, 2002] Angell, C. A. (2002). Liquid fragility and the glass transition in water and aqueous solutions. *Chemical reviews*, 102(8):2627–2650.
- [Asthagiri et al., 2004] Asthagiri, D., Pratt, L. R., Kress, J. D., and Gomez, M. A. (2004). Hydration and mobility of ho-(aq). *Proceedings of the National Academy of Sciences of the United States of America*, 101(19):7229–7233.
- [Atkins and de Paula, 2010] Atkins, P. and de Paula, J. (2010). *Physical Chemistry*. OUP Oxford.
- [Atkins and Friedman, 2011] Atkins, P. and Friedman, R. (2011). *Molecular Quantum Mechanics*. OUP Oxford.
- [Auerbach et al., 2004] Auerbach, S. M., Carrado, K. A., and Dutta, P. K. (2004). *Handbook of layered materials*. CRC Press.
- [Baer et al., 2014] Baer, M. D., Kuo, I.-F. W., Tobias, D. J., and Mundy, C. J. (2014). Toward a unified picture of the water self-ions at the air–water interface: A density functional theory perspective. *The Journal of Physical Chemistry B*, 118(28):8364–8372.
- [Baer and Mundy, 2011] Baer, M. D. and Mundy, C. J. (2011). Toward an understanding of the specific ion effect using density functional theory. *The Journal of Physical Chemistry Letters*, 2(9):1088–1093.
- [Baer and Mundy, 2013] Baer, M. D. and Mundy, C. J. (2013). An ab initio approach to understanding the specific ion effect. *Faraday discussions*, 160:89–101.
- [Baer et al., 2011] Baer, M. D., Mundy, C. J., McGrath, M. J., Kuo, I.-F. W., Siepmann, J. I., and Tobias, D. J. (2011). Re-examining the properties of the aqueous vapor–liquid interface using dispersion corrected density functional theory. *The Journal of chemical physics*, 135(12):124712.
- [Bakli and Chakraborty, 2015] Bakli, C. and Chakraborty, S. (2015). Electrokinetic energy conversion in nanofluidic channels: Addressing the loose ends in nanodevice efficiency. *Electrophoresis*, 36(5):675–681.
- [Bankura et al., 2013] Bankura, A., Carnevale, V., and Klein, M. L. (2013). Hydration structure of salt solutions from ab initio molecular dynamics. *The Journal of chemical physics*, 138(1):014501.
- [Barrat et al., 1999] Barrat, J.-L. et al. (1999). Influence of wetting properties on hydrodynamic boundary conditions at a fluid/solid interface. *Faraday discussions*, 112:119–128.
- [Barrat and Hansen, 2003] Barrat, J.-L. and Hansen, J.-P. (2003). *Basic concepts for simple and complex liquids*. Cambridge University Press.
- [Bässler, 1987] Bässler, H. (1987). Viscous flow in supercooled liquids analyzed in terms of transport theory for random media with energetic disorder. *Physical review letters*, 58(8):767.
- [Becke, 1988] Becke, A. D. (1988). Density-functional exchange-energy approximation with correct asymptotic behavior. *Physical review A*, 38(6):3098.
- [Beran, 2002] Beran, A. (2002). Infrared spectroscopy of micas. *Reviews in Mineralogy and Geochemistry*, 46(1):351–369.

- [Bérend et al., 1995] Bérend, I., Cases, J. M., François, M., Uriot, J. P., Michot, L., Masion, A., and Thomas, F. (1995). Mechanism of Adsorption and Desorption of Water Vapor by Homoionic Montmorillonites: 2. The Li<sup>+</sup>, Na<sup>+</sup>, K<sup>+</sup>, Rb<sup>+</sup>, and Cs<sup>+</sup>-exchanged Forms. *Clays and Clay Minerals*, 43(3):324–336.
- [Berendsen et al., 1987] Berendsen, H., Grigera, J., Straatsma, T., et al. (1987). The missing term in effective pair potentials. *J. phys. Chem*, 91(24):6269–6271.
- [Berendsen et al., 1981] Berendsen, H., Postma, J., Van Gunsteren, W., and Hermans, J. (1981). Intermolecular forces, D. B. Pullman, Reidel, Dordrecht, page 331.
- [Bergonzi et al., 2014] Bergonzi, I., Mercury, L., Brubach, J.-B., and Roy, P. (2014). Gibbs free energy of liquid water derived from infrared measurements. *Physical Chemistry Chemical Physics*, 16(45):24830–24840.
- [Bernasconi et al., 1995] Bernasconi, M., Chiarotti, G., Focher, P., Scandolo, S., Tosatti, E., and Parrinello, M. (1995). First-principle-constant pressure molecular dynamics. *Journal of Physics and Chemistry of Solids*, 56(3):501–505.
- [Berthier, 2011] Berthier, L. (2011). Dynamic heterogeneity in amorphous materials. *Physics*, 4:42.
- [Berthier et al., 2004] Berthier, L., Chandler, D., and Garrahan, J. P. (2004). Length scale for the onset of fickian diffusion in supercooled liquids. *Europhysics Letters*, 69:320.
- [Bertolini et al., 1982] Bertolini, D., Cassettari, M., and Salvetti, G. (1982). The dielectric relaxation time of supercooled water. *The Journal of Chemical Physics*, 76(6):3285–3290.
- [Bocquet and Barrat, 1994] Bocquet, L. and Barrat, J.-L. (1994). Hydrodynamic boundary conditions, correlation functions, and Kubo relations for confined fluids. *Physical review E*, 49(4):3079.
- [Bocquet and Barrat, 2007] Bocquet, L. and Barrat, J.-L. (2007). Flow boundary conditions from nano- to micro-scales. *Soft matter*, 3(6):685–693.
- [Bocquet and Charlaix, 2010] Bocquet, L. and Charlaix, E. (2010). Nanofluidics, from bulk to interfaces. *Chemical Society Reviews*, 39(3):1073–1095.
- [Bocquet and Netz, 2015] Bocquet, L. and Netz, R. R. (2015). Nanofluidics: Phonon modes for faster flow. *Nature nanotechnology*, 10(8):657–658.
- [Bocquet and Tabeling, 2014] Bocquet, L. and Tabeling, P. (2014). Physics and technological aspects of nanofluidics. *Lab on a Chip*, 14(17):3143–3158.
- [Boeck et al., 1995] Boeck, E., Coveney, J., and Skipper, N. (1995). Monte carlo molecular modeling studies of hydrated li-, na-, and k-smectites: understanding the role of k as a clay swelling inhibitor. *J. Am. Chem. Soc*, 117:12608–12617.
- [Boek et al., 1995] Boek, E., Coveney, P., Skipper, N., et al. (1995). Monte-carlo molecular modeling studies of hydrated li-smectites, na-smectites, and k-smectites-understanding the role of potassium as a clay swelling inhibitor. *Journal of the American Chemical Society*, 117(50):12608–12617.
- [Bonthuis et al., 2011] Bonthuis, D. J., Rinne, K. F., Falk, K., Kaplan, C. N., Horinek, D., Berker, A. N., Bocquet, L., and Netz, R. R. (2011). Theory and simulations of water flow through carbon nanotubes: prospects and pitfalls. *Journal of Physics: Condensed Matter*, 23(18):184110.
- [Botan et al., 2013] Botan, A., Marry, V., Rotenberg, B., Turq, P., and Noetinger, B. (2013). How electrostatics influences hydrodynamic boundary conditions: Poiseuille and electro-osmotic flows in clay nanopores. *The Journal of Physical Chemistry C*, 117(2):978–985.
- [Botan et al., 2011] Botan, A., Rotenberg, B., Marry, V., Turq, P., and Noetinger, B. (2011). Hydrodynamics in clay nanopores. *The Journal of Physical Chemistry C*, 115:16109–16115.
- [Bouazizi et al., 2006] Bouazizi, S., Nasr, S., Jaïdane, N., and Bellissent-Funel, M.-C. (2006). Local order in aqueous nacl solutions and pure water: X-ray scattering and molecular dynamics simulations study. *The Journal of Physical Chemistry B*, 110(46):23515–23523.
- [Boukili et al., 2003] Boukili, B., Holtz, F., Bény, J.-M., Abdelouafi, A., and Niazi, S. (2003). Infrared spectra of annite in the interlayer and lattice vibrational range. *Swiss Bulletin of Mineralogy and Petrology*, 83(1):33–46.
- [Brubach et al., 2005] Brubach, J.-B., Mermet, A., Filabozzi, A., Gerschel, A., and Roy, P. (2005). Signatures of the hydrogen bonding in the infrared bands of water. *The Journal of chemical physics*, 122(18):184509.
- [Buch et al., 2007] Buch, V., Milet, A., Vácha, R., Jungwirth, P., and Devlin, J. P. (2007). Water surface is acidic. *Proceedings of the National Academy of Sciences*, 104(18):7342–7347.
- [Buchenau and Zorn, 1992] Buchenau, U. and Zorn, R. (1992). A relation between fast and slow motions in glassy and liquid selenium. *EPL (Europhysics Letters)*, 18(6):523.
- [Car and Parrinello, 1985] Car, R. and Parrinello, M. (1985). Unified approach for molecular dynamics and density-functional theory. *Physical review letters*, 55(22):2471.
- [Carrier et al., 2013] Carrier, B., Wang, L., Vandamme, M., Pellenq, R. J.-M., Bornert, M., Tanguy, A., and Van Damme, H. (2013). Esem study of the humidity-induced swelling of clay film. *Langmuir*, 29(41):12823–12833.
- [Cases et al., 1997] Cases, J., Bérend, I., François, M., Uriot, J., Michot, L., and Thomas, F. (1997). Mechanism of adsorption and desorption of water vapor by homoionic montmorillonite; 3, the mg (super 2+), ca (super 2+), and ba (super 3+) exchanged forms. *Clays and Clay Minerals*, 45(1):8–22.
- [Cases et al., 1992] Cases, J. M., Berend, I., Besson, G., Francois, M., Uriot, J. P., Thomas, E., and Poirier, J. E. (1992). Mechanism of adsorption and desorption of water vapor by homoionic montmorillonite. 1. The sodium-exchanged form. *Langmuir*, 8(11):2730–2739.

- [Ceriotti et al., 2016] Ceriotti, M., Fang, W., Kuslik, P. G., McKenzie, R. H., Michaelides, A., Morales, M. A., and Markland, T. E. (2016). Nuclear quantum effects in water and aqueous systems: Experiment, theory, and current challenges. *Chemical reviews*, 116(13):7529–7550.
- [Chang et al., 1997] Chang, F.-R. C., Skipper, N., and Sposito, G. (1997). Monte carlo and molecular dynamics simulations of interfacial structure in lithium-montmorillonite hydrates. *Langmuir*, 13(7):2074–2082.
- [Chaplin, 2017] Chaplin, M. (2017). Water structure and science.
- [Chaplin, 2010] Chaplin, M. F. (2010). Structuring and behaviour of water in nanochannels and confined spaces. In *Adsorption and phase behaviour in nanochannels and nanotubes*, pages 241–255. Springer.
- [Charlaix and Ciccotti, 2010] Charlaix, E. and Ciccotti, M. (2010). Capillary condensation in confined media. In *Handbook of Nanophysics: Principles and Methods*, pages 1–17. CRC Press.
- [Chen et al., 2002a] Chen, B., Ivanov, I., Park, J. M., Parrinello, M., and Klein, M. L. (2002a). Solvation structure and mobility mechanism of  $\text{OH}^-$ : A car-parrinello molecular dynamics investigation of alkaline solutions. *The Journal of Physical Chemistry B*, 106(46):12006–12016.
- [Chen et al., 2002b] Chen, B., Park, J. M., Ivanov, I., Tabacchi, G., Klein, M. L., and Parrinello, M. (2002b). First-principles study of aqueous hydroxide solutions. *Journal of the American Chemical Society*, 124(29):8534–8535.
- [Chen et al., 2006] Chen, S.-H., Mallamace, E., Mou, C.-Y., Broccio, M., Corsaro, C., Faraone, A., and Liu, L. (2006). The violation of the stokes–einstein relation in supercooled water. *Proceedings of the National Academy of Sciences*, 103(35):12974–12978.
- [Chen et al., 1982] Chen, S.-H., Teixeira, J., and Nicklow, R. (1982). Incoherent quasielastic neutron scattering from water in supercooled regime. *Physical Review A*, 26(6):3477.
- [Choudhuri and Chandra, 2014] Choudhuri, J. R. and Chandra, A. (2014). An ab initio molecular dynamics study of the liquid-vapor interface of an aqueous nacl solution: Inhomogeneous density, polarity, hydrogen bonds, and frequency fluctuations of interfacial molecules. *The Journal of chemical physics*, 141(19):194705.
- [Ciamarra and Sollich, 2015] Ciamarra, M. P. and Sollich, P. (2015). Elastic models of the glass transition applied to a liquid with density anomalies. *Journal of Non-Crystalline Solids*, 407:23–28.
- [Cicero et al., 2008] Cicero, G., Grossman, J. C., Schwegler, E., Gygi, F., and Galli, G. (2008). Water confined in nanotubes and between graphene sheets: A first principle study. *Journal of the American Chemical Society*, 130(6):1871–1878.
- [Cohen-Tanugi and Grossman, 2012] Cohen-Tanugi, D. and Grossman, J. C. (2012). Water desalination across nanoporous graphene. *Nano letters*, 12(7):3602–3608.
- [Corsetti et al., 2013] Corsetti, F., Artacho, E., Soler, J. M., Alexandre, S. S., and Fernández-Serra, M.-V. (2013). Room temperature compressibility and diffusivity of liquid water from first principles. *The Journal of chemical physics*, 139(19):194502.
- [Costanzo and Guggenheim, 2001] Costanzo, P. and Guggenheim, S. (2001). Baseline studies of the clay minerals society source clays: preface. *Clays and Clay Minerals*, 49(5):371–371.
- [Cygan et al., 2004] Cygan, R. T., Liang, J.-J., and Kalinichev, A. G. (2004). Molecular models of hydroxide, oxyhydroxide, and clay phases and the development of a general force field. *The Journal of Physical Chemistry B*, 108(4):1255–1266.
- [Dalla Bernardina, 2015] Dalla Bernardina, S. (2015). *Structure and connectivity of water molecules at the interfaces of nanoconfined systems*. PhD thesis, Université Paris-Saclay.
- [Dalla Bernardina et al., 2014] Dalla Bernardina, S., Alabarse, F., Kalinko, A., Roy, P., Chapuis, M., Vita, N., Hienerwadel, R., Berthomieu, C., Judeinstein, P., Zanotti, J.-M., et al. (2014). New experimental set-ups for studying nanoconfined water on the ailes beamline at soleil. *Vibrational Spectroscopy*, 75:154–161.
- [de Groot and Grubmüller, 2001] de Groot, B. L. and Grubmüller, H. (2001). Water permeation across biological membranes: mechanism and dynamics of aquaporin-1 and glpf. *Science*, 294(5550):2353–2357.
- [de Groot and Grubmüller, 2005] de Groot, B. L. and Grubmüller, H. (2005). The dynamics and energetics of water permeation and proton exclusion in aquaporins. *Current opinion in structural biology*, 15(2):176–183.
- [Debenedetti, 2003] Debenedetti, P. G. (2003). Supercooled and glassy water. *Journal of Physics: Condensed Matter*, 15(45):R1669.
- [Debenedetti and Stillinger, 2001] Debenedetti, P. G. and Stillinger, F. H. (2001). Supercooled liquids and the glass transition. *Nature*, 410(6825):259–267.
- [Dehaoui et al., 2015] Dehaoui, A., Issenmann, B., and Caupin, F. (2015). Viscosity of deeply supercooled water and its coupling to molecular diffusion. *Proceedings of the National Academy of Sciences*, 112(39):12020–12025.
- [Del Ben et al., 2013] Del Ben, M., Schönher, M., Hutter, J., and VandeVondele, J. (2013). Bulk liquid water at ambient temperature and pressure from mp2 theory. *The Journal of Physical Chemistry Letters*, 4(21):3753–3759.
- [Delage et al., 2010] Delage, P., Cui, Y.-J., and Tang, A. M. (2010). Clays in radioactive waste disposal. *Journal of Rock Mechanics and Geotechnical Engineering*, 2(2):111–123.
- [Demontis et al., 2013] Demontis, P., Masia, M., and Suffritti, G. B. (2013). Water nanoconfined in clays: the structure of na vermiculite revisited by ab initio simulations. *The Journal of Physical Chemistry C*, 117(30):15583–15592.
- [Ding et al., 2014] Ding, Y., Hassanali, A. A., and Parrinello, M. (2014). Anomalous water diffusion in salt solutions. *Proceedings of the National Academy of Sciences*, 111(9):3310–3315.

- [DiStasio Jr et al., 2014] DiStasio Jr, R. A., Santra, B., Li, Z., Wu, X., and Car, R. (2014). The individual and collective effects of exact exchange and dispersion interactions on the ab initio structure of liquid water. *The Journal of chemical physics*, 141(8):084502.
- [Diu et al., 2007] Diu, B., Guthmann, C., Lederer, D., and Roulet, B. (2007). *Thermodynamique*. Hermann.
- [Donohue and Aranovich, 1998] Donohue, M. and Aranovich, G. (1998). Classification of gibbs adsorption isotherms. *Advances in colloid and interface science*, 76:137–152.
- [Drda and Wang, 1995] Drda, P. P. and Wang, S.-Q. (1995). Stick-slip transition at polymer melt/solid interfaces. *Physical review letters*, 75(14):2698.
- [Dyre, 2006] Dyre, J. C. (2006). Colloquium: The glass transition and elastic models of glass-forming liquids. *Reviews of modern physics*, 78(3):953.
- [Dyre and Olsen, 2004] Dyre, J. C. and Olsen, N. B. (2004). Landscape equivalent of the shoving model. *Physical Review E*, 69(4):042501.
- [Dyre et al., 1996] Dyre, J. C., Olsen, N. B., and Christensen, T. (1996). Local elastic expansion model for viscous-flow activation energies of glass-forming molecular liquids. *Physical Review B*, 53(5):2171.
- [Dyre and Wang, 2012] Dyre, J. C. and Wang, W. H. (2012). The instantaneous shear modulus in the shoving model. *The Journal of chemical physics*, 136(22):224108.
- [Ediger, 2000] Ediger, M. (2000). Spatially heterogeneous dynamics in supercooled liquids. *Annual Review of Physical Chemistry*, 51:99–128.
- [Falk et al., 2010] Falk, K., Sedlmeier, F., Joly, L., Netz, R. R., and Bocquet, L. (2010). Molecular origin of fast water transport in carbon nanotube membranes: superlubricity versus curvature dependent friction. *Nano letters*, 10(10):4067–4073.
- [Falk et al., 2012] Falk, K., Sedlmeier, F., Joly, L., Netz, R. R., and Bocquet, L. (2012). Ultralow liquid/solid friction in carbon nanotubes: comprehensive theory for alcohols, alkanes, omcts, and water. *Langmuir*, 28(40):14261–14272.
- [Feibelman, 2013] Feibelman, P. J. (2013). Viscosity of ultrathin water films confined between aluminol surfaces of kaolinite: Ab initio simulations. *The Journal of Physical Chemistry C*, 117(12):6088–6095.
- [Ferrage et al., 2005] Ferrage, E., Lanson, B., Sakharov, B. A., and Drits, V. A. (2005). Investigation of smectite hydration properties by modeling experimental x-ray diffraction patterns: Part i. montmorillonite hydration properties. *American Mineralogist*, 90(8-9):1358–1374.
- [Fleury et al., 2013] Fleury, M., Kohler, E., Norrant, F., Gautier, S., M'Hamdi, J., and Barré, L. (2013). Characterization and quantification of water in smectites with low-field nmr. *The Journal of Physical Chemistry C*, 117(9):4551–4560.
- [Forney and Brandl, 1992] Forney, C. F. and Brandl, D. G. (1992). Control of humidity in small controlled-environment chambers using glycerol-water solutions. *HortTechnology*, 2(1):52–54.
- [Frenkel and Smit, 1996] Frenkel, D. and Smit, B. (1996). Understanding molecular simulations: from algorithms to applications. Academic, San Diego.
- [Frenkel and Smit, 2001] Frenkel, D. and Smit, B. (2001). *Understanding molecular simulation: from algorithms to applications*, volume 1. Academic press.
- [Frigo and Johnson, 2005] Frigo, M. and Johnson, S. G. (2005). The design and implementation of fftw3. *Proceedings of the IEEE*, 93(2):216–231.
- [Froyen and Cohen, 1986] Froyen, S. and Cohen, M. L. (1986). Structural properties of nacl and kcl under pressure. *Journal of Physics C: Solid State Physics*, 19(15):2623.
- [Furukawa and Tanaka, 2011] Furukawa, A. and Tanaka, H. (2011). Direct evidence of heterogeneous mechanical relaxation in supercooled liquids. *Physical Review E*, 84:061503.
- [Gaiduk et al., 2015] Gaiduk, A. P., Gygi, F., and Galli, G. (2015). Density and compressibility of liquid water and ice from first-principles simulations with hybrid functionals. *The journal of physical chemistry letters*, 6(15):2902–2908.
- [Gailhanou, 2005] Gailhanou, H. (2005). *Détermination expérimentale des propriétés thermodynamiques et étude des nanostructures de minéraux argileux*. PhD thesis, Université Paul Cézanne Aix-Marseille 3.
- [Gallo et al., 1996] Gallo, P., Sciortino, F., Tartaglia, P., and Chen, S.-H. (1996). Slow dynamics of water molecules in supercooled states. *Physical review letters*, 76(15):2730.
- [Gee et al., 1990] Gee, M. L., McGuiggan, P. M., Israelachvili, J. N., and Homola, A. M. (1990). Liquid to solidlike transitions of molecularly thin films under shear. *The Journal of chemical physics*, 93(3):1895–1906.
- [Gillan et al., 2016] Gillan, M. J., Alfè, D., and Michaelides, A. (2016). Perspective: How good is dft for water? *The Journal of chemical physics*, 144(13):130901.
- [Goedecker et al., 1996] Goedecker, S., Teter, M., and Hutter, J. (1996). Separable dual-space gaussian pseudopotentials. *Physical Review B*, 54(3):1703.
- [Goldsack and Franchetto, 1977] Goldsack, D. E. and Franchetto, R. (1977). The viscosity of concentrated electrolyte solutions. i. concentration dependence at fixed temperature. *Canadian Journal of Chemistry*, 55(6):1062–1072.
- [Goniakowski et al., 2007] Goniakowski, J., Finocchi, F., and Noguera, C. (2007). Polarity of oxide surfaces and nanostructures. *Reports on Progress in Physics*, 71(1):016501.

- [González and Abascal, 2011] González, M. A. and Abascal, J. L. (2011). A flexible model for water based on tip4p/2005. *The Journal of chemical physics*, 135(22):224516.
- [Gonzalez et al., 2016] Gonzalez, M. A., Valeriani, C., Caupin, F., and Abascal, J. L. (2016). A comprehensive scenario of the thermodynamic anomalies of water using the tip4p/2005 model. *arXiv preprint arXiv:1605.05383*.
- [Gotze and Sjogren, 1992] Gotze, W. and Sjogren, L. (1992). Relaxation processes in supercooled liquids. *Reports on progress in Physics*, 55(3):241.
- [Gravelle et al., 2013] Gravelle, S., Joly, L., Detchevery, F., Ybert, C., Cottin-Bizonne, C., and Bocquet, L. (2013). Optimizing water permeability through the hourglass shape of aquaporins. *Proceedings of the National Academy of Sciences*, 110(41):16367–16372.
- [Greathouse et al., 2009] Greathouse, J. A., Durkin, J. S., Larentzos, J. P., and Cygan, R. T. (2009). Implementation of a morse potential to model hydroxyl behavior in phyllosilicates. *The Journal of chemical physics*, 130(13):134713.
- [Griffiths and De Haseth, 2007] Griffiths, P. R. and De Haseth, J. A. (2007). *Fourier transform infrared spectrometry*, volume 171. John Wiley & Sons.
- [Grimme et al., 2010] Grimme, S., Antony, J., Ehrlich, S., and Krieg, H. (2010). A consistent and accurate ab initio parametrization of density functional dispersion correction (dft-d) for the 94 elements h-pu. *The Journal of chemical physics*, 132(15):154104.
- [Grimme et al., 2011] Grimme, S., Ehrlich, S., and Goerigk, L. (2011). Effect of the damping function in dispersion corrected density functional theory. *Journal of computational chemistry*, 32(7):1456–1465.
- [Grossman et al., 2004] Grossman, J. C., Schwegler, E., Draeger, E. W., Gygi, F., and Galli, G. (2004). Towards an assessment of the accuracy of density functional theory for first principles simulations of water. *The Journal of chemical physics*, 120(1):300–311.
- [Guillot, 2002] Guillot, B. (2002). A reappraisal of what we have learnt during three decades of computer simulations on water. *Journal of Molecular Liquids*, 101(1-3):219–260.
- [Gusev, 2017] Gusev, V. (2017). Mcm-41.
- [Hallett, 1963] Hallett, J. (1963). The temperature dependence of the viscosity of supercooled water. *Proceedings of the Physical Society*, 82(6):1046.
- [Hansen and McDonald, 2013] Hansen, J.-P. and McDonald, I. R. (2013). *Theory of Simple Liquids: With Applications to Soft Matter*. Academic Press.
- [Harris and Woolf, 2004] Harris, K. R. and Woolf, L. A. (2004). Temperature and volume dependence of the viscosity of water and heavy water at low temperatures. *Journal of Chemical & Engineering Data*, 49(4):1064–1069.
- [Hartkamp and Coasne, 2014] Hartkamp, R. and Coasne, B. (2014). Structure and transport of aqueous electrolytes: From simple halides to radionuclide ions. *The Journal of chemical physics*, 141(12):124508.
- [Hartwigsen et al., 1998] Hartwigsen, C., Gøedecker, S., and Hutter, J. (1998). Relativistic separable dual-space gaussian pseudopotentials from h to rn. *Physical Review B*, 58(7):3641.
- [Hasegawa and Tanimura, 2011] Hasegawa, T. and Tanimura, Y. (2011). A polarizable water model for intramolecular and intermolecular vibrational spectroscopies. *The Journal of Physical Chemistry B*, 115(18):5545–5553.
- [Hatch et al., 2012] Hatch, C. D., Wiese, J. S., Crane, C. C., Harris, K. J., Kloss, H. G., and Baltrusaitis, J. (2012). Water adsorption on clay minerals as a function of relative humidity: application of bet and freundlich adsorption models. *Langmuir*, 28(3):1790–1803.
- [Hatzikiriakos, 2015] Hatzikiriakos, S. G. (2015). Slip mechanisms in complex fluid flows. *Soft Matter*, 11(40):7851–7856.
- [Hecksher and Dyre, 2015] Hecksher, T. and Dyre, J. C. (2015). A review of experiments testing the shoving model. *Journal of Non-Crystalline Solids*, 407:14–22.
- [Heiranian et al., 2015] Heiranian, M., Farimani, A. B., and Aluru, N. R. (2015). Water desalination with a single-layer mos2 nanopore. *Nature communications*, 6.
- [Heller-Kallai et al., 1996] Heller-Kallai, L., Goldstein, T., and Navrotsky, A. (1996). Active components in clay condensates and extracts as potential geocatalysts. *Clays and clay minerals*, 44(3):393–397.
- [Holmboe et al., 2012] Holmboe, M., Wold, S., and Jonsson, M. (2012). Porosity investigation of compacted bentonite using xrd profile modeling. *Journal of Contaminant Hydrology*, 128(1):19–32.
- [Horinek et al., 2009] Horinek, D., Mamatkulov, S. I., and Netz, R. R. (2009). Rational design of ion force fields based on thermodynamic solvation properties. *The Journal of chemical physics*, 130(12):124507.
- [Horn et al., 2004] Horn, H. W., Swope, W. C., Pitera, J. W., Madura, J. D., Dick, T. J., Hura, G. L., and Head-Gordon, T. (2004). Development of an improved four-site water model for biomolecular simulations: Tip4p-ew. *The Journal of chemical physics*, 120(20):9665–9678.
- [Huang and Bartell, 1995] Huang, J. and Bartell, L. S. (1995). Kinetics of homogeneous nucleation in the freezing of large water clusters. *The Journal of Physical Chemistry*, 99(12):3924–3931.
- [Ishii et al., 1967] Ishii, M., Shimanouchi, T., and Nakahira, M. (1967). Far infra-red absorption spectra of layer silicates. *Inorganica Chimica Acta*, 1:387–392.
- [Isono, 1984] Isono, T. (1984). Density, viscosity, and electrolytic conductivity of concentrated aqueous electrolyte solutions at several temperatures. alkaline-earth chlorides, lanthanum chloride, sodium chloride, sodium nitrate, sodium bromide, potassium nitrate, potassium bromide, and cadmium nitrate. *Journal of chemical and engineering data*, 29(1):45–52.

- [Israelachvili et al., 1990] Israelachvili, J., McGuiggan, P., Gee, M., Homola, A., Robbins, M., and Thompson, P. (1990). Liquid dynamics in molecularly thin films. *Journal of Physics: Condensed Matter*, 2(S):SA89.
- [Israelachvili, 2011] Israelachvili, J. N. (2011). *Intermolecular and surface forces*. Academic press.
- [Iwashita et al., 2013] Iwashita, T., Nicholson, D. M., and Egami, T. (2013). Elementary excitations and crossover phenomenon in liquids. *Physical Review Letters*, 110(20):205504.
- [Jenkins, 1989] Jenkins, D. M. (1989). Empirical study of the infrared lattice vibrations (1100–350 cm<sup>-1</sup>) of phlogopite. *Physics and Chemistry of Minerals*, 16(4):408–414.
- [Joly et al., 2016] Joly, L., Tocci, G., Merabia, S., and Michaelides, A. (2016). Strong coupling between nanofluidic transport and interfacial chemistry: How defect reactivity controls liquid–solid friction through hydrogen bonding. *The journal of physical chemistry letters*, 7(7):1381–1386.
- [Jonchiere et al., 2011] Jonchiere, R., Seitsonen, A. P., Ferlat, G., Saitta, A. M., and Vuilleumier, R. (2011). Van der waals effects in ab initio water at ambient and supercritical conditions. *The Journal of chemical physics*, 135(15):154503.
- [Jorgensen et al., 1983] Jorgensen, W. L., Chandrasekhar, J., Madura, J. D., Impey, R. W., and Klein, M. L. (1983). Comparison of simple potential functions for simulating liquid water. *The Journal of chemical physics*, 79(2):926–935.
- [Jorgensen and Madura, 1985] Jorgensen, W. L. and Madura, J. D. (1985). Temperature and size dependence for monte carlo simulations of tip4p water. *Molecular Physics*, 56(6):1381–1392.
- [Kann and Skinner, 2014] Kann, Z. and Skinner, J. (2014). A scaled-ionic-charge simulation model that reproduces enhanced and suppressed water diffusion in aqueous salt solutions. *The Journal of chemical physics*, 141(10):104507.
- [Kawasaki and Kim, 2017] Kawasaki, T. and Kim, K. (2017). Identification of time-scales that support violation or preservation of stokes-einstein relation in supercooled water. *arXiv preprint arXiv:1701.06028*.
- [Kell, 1975] Kell, G. S. (1975). Density, thermal expansivity, and compressibility of liquid water from 0. deg. to 150. deg.. correlations and tables for atmospheric pressure and saturation reviewed and expressed on 1968 temperature scale. *Journal of Chemical and Engineering Data*, 20(1):97–105.
- [Kestin et al., 1981a] Kestin, J., Khalifa, H. E., and Correia, R. J. (1981a). Tables of the dynamic and kinematic viscosity of aqueous kcl solutions in the temperature range 25–150 c and the pressure range 0.1–35 mpa. *Journal of Physical and Chemical Reference Data*, 10(1):57–70.
- [Kestin et al., 1981b] Kestin, J., Khalifa, H. E., and Correia, R. J. (1981b). Tables of the dynamic and kinematic viscosity of aqueous nacl solutions in the temperature range 20–150 c and the pressure range 0.1–35 mpa. *Journal of physical and chemical reference data*, 10(1):71–88.
- [Kühne et al., 2010] Kühne, T. D., Pascal, T. A., Kaxiras, E., and Jung, Y. (2010). New insights into the structure of the vapor/water interface from large-scale first-principles simulations. *The journal of physical chemistry letters*, 2(2):105–113.
- [Kim et al., 2012] Kim, J. S., Wu, Z., Morrow, A. R., Yethiraj, A., and Yethiraj, A. (2012). Self-diffusion and viscosity in electrolyte solutions. *The Journal of Physical Chemistry B*, 116(39):12007–12013.
- [Kim and Yethiraj, 2008] Kim, J. S. and Yethiraj, A. (2008). The effect of salt on the melting of ice: A molecular dynamics simulation study. *The Journal of chemical physics*, 129(12):124504.
- [Kittrick and Hope, 1963] Kittrick, J. and Hope, E. (1963). A procedure for the particle-size separation of soils for x-ray diffraction analysis. *Soil Science*, 96(5):319–325.
- [Klameth and Vogel, 2015] Klameth, F. and Vogel, M. (2015). Slow water dynamics near a glass transition or a solid interface: a common rationale. *The journal of physical chemistry letters*, 6(21):4385–4389.
- [Klimeš et al., 2009] Klimeš, J., Bowler, D. R., and Michaelides, A. (2009). Chemical accuracy for the van der waals density functional. *Journal of Physics: Condensed Matter*, 22(2):022201.
- [Klimeš and Michaelides, 2012] Klimeš, J. and Michaelides, A. (2012). Perspective: Advances and challenges in treating van der waals dispersion forces in density functional theory. *The Journal of chemical physics*, 137(12):120901.
- [Koch and Holthausen, 2015] Koch, W. and Holthausen, M. C. (2015). *A chemist's guide to density functional theory*. John Wiley & Sons.
- [Kotsalis, 2008] Kotsalis, E. M. (2008). *Multiscale modeling and simulation of fullerenes in liquids*. PhD thesis, Swiss Federal Institute of Technology Zürich.
- [Krack, 2005] Krack, M. (2005). Pseudopotentials for h to kr optimized for gradient-corrected exchange-correlation functionals. *Theoretical Chemistry Accounts*, 114(1-3):145–152.
- [Krynicky et al., 1978] Krynicky, K., Green, C. D., and Sawyer, D. W. (1978). Pressure and temperature dependence of self-diffusion in water. *Faraday Discussions of the Chemical Society*, 66:199–208.
- [Kühne et al., 2009] Kühne, T. D., Krack, M., and Parrinello, M. (2009). Static and dynamical properties of liquid water from first principles by a novel car-parrinello-like approach. *Journal of chemical theory and computation*, 5(2):235–241.
- [Kuligiewicz et al., 2015] Kuligiewicz, A., Derkowski, A., Szczerba, M., Gionis, V., and Chryssikos, G. D. (2015). Revisiting the infrared spectrum of the water–smectite interface. *Clays and Clay Minerals*, 63(1):15–29.

- [Kumar et al., 2007] Kumar, P., Buldyrev, S. V., Becker, S. R., Poole, P. H., Starr, F. W., and Stanley, H. E. (2007). Break-down of the stokes-einstein relation in supercooled water. *Proceedings of the National Academy of Sciences*, 103(35):12955–12956.
- [Kumar and Skinner, 2008] Kumar, R. and Skinner, J. (2008). Water simulation model with explicit three-molecule interactions. *The Journal of Physical Chemistry B*, 112(28):8311–8318.
- [Kuo and Mundy, 2004] Kuo, I.-F. W. and Mundy, C. J. (2004). An ab initio molecular dynamics study of the aqueous liquid-vapor interface. *Science*, 303(5658):658–660.
- [Kuo et al., 2006] Kuo, I. W., Mundy, C. J., Eggimann, B. L., McGrath, M. J., Siepmann, J. I., Chen, B., Vieceli, J., and Tobias, D. J. (2006). Structure and dynamics of the aqueous liquid-vapor interface: A comprehensive particle-based simulation study? *The Journal of Physical Chemistry B*, 110(8):3738–3746.
- [Laasonen et al., 1993] Laasonen, K., Sprik, M., Parrinello, M., and Car, R. (1993). “abinitio” liquid water. *The Journal of chemical physics*, 99(11):9080–9089.
- [Landry et al., 2008] Landry, E., Hussein, M., and McGaughey, A. (2008). Complex superlattice unit cell designs for reduced thermal conductivity. *Physical Review B*, 77(18):184302.
- [Lang et al., 1984] Lang, E., Lüdemann, H.-D., and Piculell, L. (1984). Nuclear magnetic relaxation rate dispersion in supercooled heavy water under high pressure. *The Journal of chemical physics*, 81(9):3820–3827.
- [Laperche and Prost, 1991] Laperche, V. and Prost, R. (1991). Assignment of the far-infrared absorption bands of k in micas. *Clays and Clay Minerals*, 39(3):281–289.
- [Larini et al., 2008] Larini, L., Ottochian, A., De Michele, C., and Leporini, D. (2008). Universal scaling between structural relaxation and vibrational dynamics in glass-forming liquids and polymers. *Nature Physics*, 4(1):42–45.
- [Le Caër et al., 2014] Le Caër, S., Klein, G., Ortiz, D., Lima, M., Devineau, S., Pin, S., Brubach, J.-B., Roy, P., Pomeret, S., Leibl, W., et al. (2014). The effect of myoglobin crowding on the dynamics of water: an infrared study. *Physical Chemistry Chemical Physics*, 16(41):22841–22852.
- [Lee et al., 2014] Lee, D., Schwegler, E., and Kanai, Y. (2014). Dependence of water dynamics on molecular adsorbates near hydrophobic surfaces: First-principles molecular dynamics study. *The Journal of Physical Chemistry C*, 118(16):8508–8513.
- [Lee and Tuckerman, 2006] Lee, H.-S. and Tuckerman, M. E. (2006). Structure of liquid water at ambient temperature from ab initio molecular dynamics performed in the complete basis set limit. *The Journal of chemical physics*, 125(15):154507.
- [Lee and Tuckerman, 2007] Lee, H.-S. and Tuckerman, M. E. (2007). Dynamical properties of liquid water from ab initio molecular dynamics performed in the complete basis set limit. *The Journal of chemical physics*, 126(16):164501.
- [Lee et al., 2010a] Lee, K., Murray, É. D., Kong, L., Lundqvist, B. I., and Langreth, D. C. (2010a). Higher-accuracy van der waals density functional. *Physical Review B*, 82(8):081101.
- [Lee et al., 2010b] Lee, K., Yu, G., Woo, E., Hwang, S., and Shin, K. (2010b). Freezing and melting in nanopores. In *Adsorption and Phase Behaviour in Nanochannels and Nanotubes*, pages 257–272. Springer.
- [Li and Wang, 2015] Li, J. and Wang, F. (2015). Pairwise-additive force fields for selected aqueous monovalent ions from adaptive force matching. *The Journal of chemical physics*, 143(19):194505.
- [Li et al., 2007] Li, T.-D., Gao, J., Szoszkiewicz, R., Landman, U., and Riedo, E. (2007). Structured and viscous water in subnanometer gaps. *Physical Review B*, 75(11):115415.
- [Lide, 1997] Lide, D. (1997). *Handbook of chemistry and physics*, 78th edition. CRC Press.
- [Liu et al., 2006] Liu, L., Chen, S.-H., Faraone, A., Yen, C.-W., Mou, C.-Y., Kolesnikov, A. I., Mamontov, E., and Leao, J. (2006). Quasielastic and inelastic neutron scattering investigation of fragile-to-strong crossover in deeply supercooled water confined in nanoporous silica matrices. *Journal of Physics: Condensed Matter*, 18(36):S2261.
- [Liu et al., 2011] Liu, L.-M., Laio, A., and Michaelides, A. (2011). Initial stages of salt crystal dissolution determined with ab initio molecular dynamics. *Physical Chemistry Chemical Physics*, 13(29):13162–13166.
- [Lock et al., 2002] Lock, A., Bakker, H., et al. (2002). Temperature dependence of vibrational relaxation in liquid h<sub>2</sub>o. *Journal of Chemical Physics*, 117(4):1708–1713.
- [Ma et al., 2015] Ma, M., Grey, F., Shen, L., Urbakh, M., Wu, S., Liu, J. Z., Liu, Y., and Zheng, Q. (2015). Water transport inside carbon nanotubes mediated by phonon-induced oscillating friction. *Nature nanotechnology*, 10(8):692–695.
- [Ma et al., 2017] Ma, X., Cambré, S., Wenseleers, W., Doorn, S. K., and Htoon, H. (2017). Quasiphase transition in a single file of water molecules encapsulated in (6, 5) carbon nanotubes observed by temperature-dependent photoluminescence spectroscopy. *Physical Review Letters*, 118(2):027402.
- [Ma et al., 2012] Ma, Z., Zhang, Y., and Tuckerman, M. E. (2012). Ab initio molecular dynamics study of water at constant pressure using converged basis sets and empirical dispersion corrections. *The Journal of chemical physics*, 137(4):044506.
- [Madejová and Komadel, 2001] Madejová, J. and Komadel, P. (2001). Baseline studies of the clay minerals society source clays: infrared methods. *Clays and clay minerals*, 49(5):410–432.
- [Maduar et al., 2015] Maduar, S., Belyaev, A., Lobaskin, V., and Vinogradova, O. (2015). Electrohydrodynamics near hydrophobic surfaces. *Physical review letters*, 114(11):118301.

- [Maheshwari et al., 2013] Maheshwari, P., Pujari, P. K., Sharma, S. K., Dutta, D., Sudarshan, K., Mithu, V., Madhu, P. K., Deshpande, S., Patil, P. N., and Raje, N. (2013). Phase transition of nanoconfined water in clay: Positron annihilation, nuclear magnetic resonance, and dielectric relaxation studies. *The Journal of Physical Chemistry C*, 117(27):14313–14324.
- [Mahoney and Jorgensen, 2000] Mahoney, M. W. and Jorgensen, W. L. (2000). A five-site model for liquid water and the reproduction of the density anomaly by rigid, nonpolarizable potential functions. *The Journal of Chemical Physics*, 112(20):8910–8922.
- [Majumder et al., 2015] Majumder, S., Dhar, J., and Chakraborty, S. (2015). Resolving anomalies in predicting electrokinetic energy conversion efficiencies of nanofluidic devices. *Scientific reports*, 5.
- [Malikova et al., 2005] Malikova, N., Cadene, A., Marry, V., Dubois, E., Turq, P., Zanotti, J.-M., and Longeville, S. (2005). Diffusion of water in clays—microscopic simulation and neutron scattering. *Chemical Physics*, 317(2):226–235.
- [Mallamace et al., 2007] Mallamace, F., Branca, C., Broccio, M., Corsaro, C., Mou, C.-Y., and Chen, S.-H. (2007). The anomalous behavior of the density of water in the range  $30\text{ K} < T < 373\text{ K}$ . *Proceedings of the National Academy of Sciences*, 104(47):18387–18391.
- [Mallamace et al., 2006] Mallamace, F., Broccio, M., Corsaro, C., Faraone, A., Wanderlingh, U., Liu, L., Mou, C.-Y., and Chen, S. (2006). The fragile-to-strong dynamic crossover transition in confined water: nuclear magnetic resonance results. *The Journal of Chemical Physics*, 124:161102.
- [Mancinelli et al., 2007] Mancinelli, R., Botti, A., Bruni, F., Ricci, M., and Soper, A. (2007). Perturbation of water structure due to monovalent ions in solution. *Physical Chemistry Chemical Physics*, 9(23):2959–2967.
- [Mao and Pappu, 2012] Mao, A. H. and Pappu, R. V. (2012). Crystal lattice properties fully determine short-range interaction parameters for alkali and halide ions. *The Journal of chemical physics*, 137(6):064104.
- [Marcus, 2009] Marcus, Y. (2009). Effect of ions on the structure of water: structure making and breaking. *Chemical reviews*, 109(3):1346–1370.
- [Maréchal, 2006] Maréchal, Y. (2006). *The hydrogen bond and the water molecule: The physics and chemistry of water, aqueous and bio-media*. Elsevier.
- [Markesteyn et al., 2012] Markesteyn, A., Hartkamp, R., Luding, S., and Westerweel, J. (2012). A comparison of the value of viscosity for several water models using poiseuille flow in a nano-channel. *The Journal of chemical physics*, 136(13):134104.
- [Marry et al., 2002] Marry, V., Turq, P., Cartailier, T., and Levesque, D. (2002). Microscopic simulation of structure and dynamics of water and counterions in a monohydrated montmorillonite. *The Journal of chemical physics*, 117(7):3454–3463.
- [Martyna et al., 1994] Martyna, G. J., Tobias, D. J., and Klein, M. L. (1994). Constant pressure molecular dynamics algorithms. *The Journal of Chemical Physics*, 101(5):4177–4189.
- [Marx and Parrinello, 1996] Marx, D. and Parrinello, M. (1996). Ab initio path integral molecular dynamics: Basic ideas. *The Journal of chemical physics*, 104(11):4077–4082.
- [Massat et al., 2016] Massat, L., Cuisinier, O., Bihannic, I., Claret, F., Pelletier, M., Masroui, F., and Gaboreau, S. (2016). Swelling pressure development and inter-aggregate porosity evolution upon hydration of a compacted swelling clay. *Applied Clay Science*, 124:197–210.
- [Mattsson et al., 2009] Mattsson, J., Wyss, H. M., Fernandez-Nieves, A., Miyazaki, K., Hu, Z., Reichman, D. R., and Weitz, D. A. (2009). Soft colloids make strong glasses. *Nature*, 462(7269):83–86.
- [Mauro et al., 2009] Mauro, J. C., Yue, Y., Ellison, A. J., Gupta, P. K., and Allan, D. C. (2009). Viscosity of glass-forming liquids. *Proceedings of the National Academy of Sciences*, 106(47):19780–19784.
- [McGrath et al., 2011] McGrath, M. J., Kuo, I.-F. W., and Siepmann, J. I. (2011). Liquid structures of water, methanol, and hydrogen fluoride at ambient conditions from first principles molecular dynamics simulations with a dispersion corrected density functional. *Physical Chemistry Chemical Physics*, 13(44):19943–19950.
- [McGrath et al., 2006] McGrath, M. J., Siepmann, J. I., Kuo, I.-F. W., Mundy, C. J., VandeVondele, J., Hutter, J., Mohamed, F., and Krack, M. (2006). Simulating fluid-phase equilibria of water from first principles. *The Journal of Physical Chemistry A*, 110(2):640–646.
- [Megyes et al., 2008] Megyes, T., Bálint, S., Grósz, T., Radnai, T., Bakó, I., and Sipos, P. (2008). The structure of aqueous sodium hydroxide solutions: A combined solution x-ray diffraction and simulation study. *The Journal of chemical physics*, 128(4):044501.
- [Meleshyn and Bunnenberg, 2005] Meleshyn, A. and Bunnenberg, C. (2005). The gap between crystalline and osmotic swelling of na-montmorillonite: A monte carlo study. *The Journal of chemical physics*, 122(3):034705.
- [Miceli et al., 2015] Miceli, G., de Gironcoli, S., and Pasquarello, A. (2015). Isobaric first-principles molecular dynamics of liquid water with nonlocal van der waals interactions. *The Journal of chemical physics*, 142(3):034501.
- [Michot et al., 2004] Michot, L. J., Bihannic, I., Porsch, K., Maddi, S., Baravian, C., Mougél, J., and Levitz, P. (2004). Phase diagrams of wyoming na-montmorillonite clay. influence of particle anisotropy. *Langmuir*, 20(25):10829–10837.
- [Michot et al., 2013] Michot, L. J., Bihannic, I., Thomas, F., Lartiges, B. S., Waldvogel, Y., Caillet, C., Thieme, J., Furnari, S. S., and Levitz, P. (2013). Coagulation of na-montmorillonite by inorganic cations at neutral ph. a combined transmission x-ray microscopy, small angle and wide angle x-ray scattering study. *Langmuir*, 29(10):3500–3510.

- [Mignon et al., 2009] Mignon, P., Ugliengo, P., and Sodupe, M. (2009). Theoretical study of the adsorption of rna/dna bases on the external surfaces of na<sup>+</sup>-montmorillonite. *The Journal of Physical Chemistry C*, 113(31):13741–13749.
- [Mignon et al., 2010] Mignon, P., Ugliengo, P., Sodupe, M., and Hernandez, E. R. (2010). Ab initio molecular dynamics study of the hydration of li<sup>+</sup>, na<sup>+</sup> and k<sup>+</sup> in a montmorillonite model. influence of isomorphic substitution. *Physical Chemistry Chemical Physics*, 12(3):688–697.
- [Miomandre et al., 2011] Miomandre, E., Sadki, S., Audebert, P., and Méallet-Renault, R. (2011). *Électrochimie-2e éd.: Des concepts aux applications*. Dunod.
- [Møgelhøj et al., 2011] Møgelhøj, A., Kelkkanen, A. K., Wikfeldt, K. T., Schiøtz, J., Mortensen, J. J., Pettersson, L. G., Lundqvist, B. L., Jacobsen, K. W., Nilsson, A., and Nørskov, J. K. (2011). Ab initio van der waals interactions in simulations of water alter structure from mainly tetrahedral to high-density-like. *The Journal of Physical Chemistry B*, 115(48):14149–14160.
- [Morón et al., 2016] Morón, M. C., Prada-Gracia, D., and Falo, F. (2016). Macro and nano scale modelling of water–water interactions at ambient and low temperature: relaxation and residence times. *Physical Chemistry Chemical Physics*, 18(14):9377–9387.
- [Mott, 1988] Mott, C. (1988). Clay minerals-an introduction. *Catalysis today*, 2(2-3):199–208.
- [Müller et al., 2016] Müller, D., Knoll, C., Seifried, M., and Weinberger, P. (2016). Atr or transmission-a variable temperature study comparing both techniques using [fe (3ditz) 3](bf 4) 2 as model system. *Vibrational Spectroscopy*, 86:198–205.
- [Müller and Hertz, 1996] Müller, K. and Hertz, H. (1996). A parameter as an indicator for water- water association in solutions of strong electrolytes. *The Journal of Physical Chemistry*, 100(4):1256–1265.
- [Mundy and Kuo, 2006] Mundy, C. J. and Kuo, I.-F. W. (2006). First-principles approaches to the structure and reactivity of atmospherically relevant aqueous interfaces. *Chemical reviews*, 106(4):1282–1304.
- [Murata et al., 2000] Murata, K., Mitsuoaka, K., Hirai, T., Walz, T., et al. (2000). Structural determinants of water permeation through aquaporin-1. *Nature*, 407(6804):599.
- [Nakai et al., 1996] Nakai, T., Sawamura, S., Taniguchi, Y., and Yamaura, Y. (1996). Effect of pressure on the viscosity b coefficient of cesium chloride in water. *Journal of the Society of Materials Science, Japan*, 45(9Appendix):143–147.
- [Ngouana W and Kalinichev, 2014] Ngouana W, B. F. and Kalinichev, A. G. (2014). Structural arrangements of isomorphic substitutions in smectites: Molecular simulation of the swelling properties, interlayer structure, and dynamics of hydrated cs–montmorillonite revisited with new clay models. *The Journal of Physical Chemistry C*, 118(24):12758–12773.
- [NIST, 2017] NIST (2017). Nist standard reference data.
- [Nucci and Vanderkooi, 2008] Nucci, N. V. and Vanderkooi, J. M. (2008). Effects of salts of the hofmeister series on the hydrogen bond network of water. *Journal of molecular liquids*, 143(2):160–170.
- [OEIS Foundation Inc., 2017] OEIS Foundation Inc. (2017). *The On-Line Encyclopedia of Integer Sequences*. OEIS Foundation Inc.
- [Osipov et al., 1977] Osipov, Y. A., Zheleznyy, B. V., and Bondarenko, N. F. (1977). The shear viscosity of water supercooled to -35 °C. *Russian Journal of Physical Chemistry*, 51(5):748–749.
- [Oswald, 2009] Oswald, P. (2009). *Rheophysics: the deformation and flow of matter*. Cambridge University Press.
- [Ottochian et al., 2009] Ottochian, A., De Michele, C., and Leporini, D. (2009). Universal divergenceless scaling between structural relaxation and caged dynamics in glass-forming systems. *The Journal of Chemical Physics*, 131(22):224517.
- [Overduin and Patey, 2015] Overduin, S. and Patey, G. (2015). Fluctuations and local ice structure in model supercooled water. *The Journal of chemical physics*, 143(9):094504.
- [Pallares et al., 2016] Pallares, G., Gonzalez, M. A., Abascal, J. L. F., Valeriani, C., and Caupin, F. (2016). Equation of state for water and its line of density maxima down to -120 mpa. *Physical Chemistry Chemical Physics*, 18(8):5896–5900.
- [Pastore et al., 2015] Pastore, R., Coniglio, A., and Ciamarra, M. P. (2015). Dynamic phase coexistence in glass-forming liquids. *Scientific Reports*, 5:11770.
- [Pedroza et al., 2015] Pedroza, L. S., Poissier, A., and Fernández-Serra, M.-V. (2015). Local order of liquid water at metallic electrode surfaces. *The Journal of chemical physics*, 142(3):034706.
- [Pellenq et al., 2001] Pellenq, R. J.-M., Rousseau, B., and Levitz, P. E. (2001). A grand canonical monte carlo study of argon adsorption/condensation in mesoporous silica glasses. *Physical Chemistry Chemical Physics*, 3(7):1207–1212.
- [Petrvac and Harrowell, 2007] Petrvac, J. and Harrowell, P. (2007). On the equilibrium calculation of the friction coefficient for liquid slip against a wall. *The Journal of chemical physics*, 127(17):174706.
- [Plimpton, 1995] Plimpton, S. (1995). Fast parallel algorithms for short-range molecular dynamics. *Journal of computational physics*, 117(1):1–19.
- [Plimpton et al., 2005] Plimpton, S. et al. (2005). *Lammps user's manual*. Sandia National Laboratory.
- [Poole et al., 1992] Poole, P. H., Sciortino, F., Essmann, U., and Stanley, H. E. (1992). Phase behaviour of metastable water. *Nature*, 360(6402):324–328.

- [Potuzak et al., 2013] Potuzak, M., Guo, X., Smedskjaer, M. M., and Mauro, J. C. (2013). Are the dynamics of a glass embedded in its elastic properties? *The Journal of chemical physics*, 138(12):12A501.
- [Price et al., 1999] Price, W. S., Ide, H., and Arata, Y. (1999). Self-diffusion of supercooled water to 238 k using pgse nmr diffusion measurements. *The Journal of Physical Chemistry A*, 103(4):448–450.
- [Prost et al., 1990] Prost, R., Laperche, V., et al. (1990). Far-infrared study of potassium in micas. *Clays and Clay Minerals*, 38(4):351–355.
- [Puosi and Leporini, 2012a] Puosi, F. and Leporini, D. (2012a). Communication: Correlation of the instantaneous and the intermediate-time elasticity with the structural relaxation in glassforming systems. *The Journal of chemical physics*, 136(4):041104.
- [Puosi and Leporini, 2012b] Puosi, F. and Leporini, D. (2012b). Communication: Fast and local predictors of the violation of the stokes-einstein law in polymers and supercooled liquids. *The Journal of chemical physics*, 136(21):211101.
- [Rana and Chandra, 2013] Rana, M. K. and Chandra, A. (2013). Ab initio and classical molecular dynamics studies of the structural and dynamical behavior of water near a hydrophobic graphene sheet. *The Journal of chemical physics*, 138(20):204702.
- [Raviv et al., 2001] Raviv, U., Laurat, P., and Klein, J. (2001). Fluidity of water confined to subnanometre films. *Nature*, 413(6851):51–54.
- [Ren and Stein, 2008] Ren, Y. and Stein, D. (2008). Slip-enhanced electrokinetic energy conversion in nanofluidic channels. *Nanotechnology*, 19(19):195707.
- [Rinnert, 2004] Rinnert, E. (2004). *Etats d'hydratation d'argiles suivis par analyses vibrationnelles de l'eau et des hydroxyles dans le proche infrarouge: Applications aux systèmes saponite et bentonite*. PhD thesis, Université Henri Poincaré-Nancy I.
- [Rønne and Keiding, 2002] Rønne, C. and Keiding, S. R. (2002). Low frequency spectroscopy of liquid water using thz-time domain spectroscopy. *Journal of Molecular Liquids*, 101(1-3):199–218.
- [Rotenberg, 2014] Rotenberg, B. (2014). Water in clay nanopores. *MRS Bulletin*, 39(12):1074–1081.
- [Rotenberg et al., 2010] Rotenberg, B., Marry, V., Malikova, N., and Turq, P. (2010). Molecular simulation of aqueous solutions at clay surfaces. *Journal of Physics: Condensed Matter*, 22(28):284114.
- [Ryckaert et al., 1977] Ryckaert, J.-P., Ciccotti, G., and Berendsen, H. J. (1977). Numerical integration of the cartesian equations of motion of a system with constraints: molecular dynamics of n-alkanes. *Journal of Computational Physics*, 23(3):327–341.
- [Salles et al., 2008] Salles, F., Beurroies, I., Bildstein, O., Jullien, M., Raynal, J., Denoyel, R., and Van Damme, H. (2008). A calorimetric study of mesoscopic swelling and hydration sequence in solid na-montmorillonite. *Applied Clay Science*, 39(3):186–201.
- [Salles et al., 2010] Salles, F., Bildstein, O., Douillard, J., Jullien, M., Raynal, J., and Van Damme, H. (2010). On the cation dependence of interlamellar and interparticular water and swelling in smectite clays. *Langmuir*, 26(7):5028–5037.
- [Salles et al., 2015] Salles, F., Douillard, J.-M., Bildstein, O., El Ghazi, S., Pre'lot, B., Zajac, J., and Van Damme, H. (2015). Diffusion of interlayer cations in swelling clays as a function of water content: Case of montmorillonites saturated with alkali cations. *The Journal of Physical Chemistry C*, 119(19):10370–10378.
- [Schmidt et al., 2009] Schmidt, J., VandeVondele, J., Kuo, I.-F. W., Sebastiani, D., Siepmann, J. I., Hutter, J., and Mundy, C. J. (2009). Isobaric- isothermal molecular dynamics simulations utilizing density functional theory: An assessment of the structure and density of water at near-ambient conditions. *The Journal of Physical Chemistry B*, 113(35):11959–11964.
- [Schneider and Stoll, 1978] Schneider, T. and Stoll, E. (1978). Molecular-dynamics study of a three-dimensional one-component model for distortive phase transitions. *Physical Review B*, 17(3):1302.
- [Scilab Enterprises, 2012] Scilab Enterprises (2012). *Scilab: Le logiciel open source gratuit de calcul numérique*. Scilab Enterprises, Orsay, France.
- [Secchi et al., 2016] Secchi, E., Marbach, S., Niguès, A., Stein, D., Siria, A., and Bocquet, L. (2016). Massive radius-dependent flow slippage in carbon nanotubes. *Nature*, 537(7619):210–213.
- [Sellberg et al., 2014] Sellberg, J. A., Huang, C., McQueen, T., Loh, N., Laksmono, H., Schlesinger, D., Sierra, R., Nordlund, D., Hampton, C., Starodub, D., et al. (2014). Ultrafast x-ray probing of water structure below the homogeneous ice nucleation temperature. *Nature*, 510(7505):381–384.
- [Sendner et al., 2009] Sendner, C., Horinek, D., Bocquet, L., and Netz, R. R. (2009). Interfacial water at hydrophobic and hydrophilic surfaces: Slip, viscosity, and diffusion. *Langmuir*, 25(18):10768–10781.
- [Shannon, 1976] Shannon, R. t. (1976). Revised effective ionic radii and systematic studies of interatomic distances in halides and chalcogenides. *Acta crystallographica section A: crystal physics, diffraction, theoretical and general crystallography*, 32(5):751–767.
- [Shi et al., 2013] Shi, Z., Debenedetti, P. G., and Stillinger, F. H. (2013). Relaxation processes in liquids: Variations on a theme by stokes and einstein. *Journal of Chemical Physics*, 138:12A526.
- [Sholl and Steckel, 2011] Sholl, D. and Steckel, J. A. (2011). *Density functional theory: a practical introduction*. John Wiley & Sons.
- [Singh et al., 2016] Singh, R. S., Biddle, J. W., Debenedetti, P. G., and Anisimov, M. A. (2016). Two-state thermodynamics and the possibility of a liquid-liquid phase transition in supercooled tip4p/2005 water. *The Journal of chemical physics*, 144(14):144504.

- [Siria et al., 2013] Siria, A., Poncharal, P., Bianco, A.-L., Fulcrand, R., Blase, X., Purcell, S. T., and Bocquet, L. (2013). Giant osmotic energy conversion measured in a single transmembrane boron nitride nanotube. *Nature*, 494(7438):455–458.
- [Sit and Marzari, 2005] Sit, P.-L. and Marzari, N. (2005). Static and dynamical properties of heavy water at ambient conditions from first-principles molecular dynamics. *The Journal of chemical physics*, 122(20):204510.
- [Skipper et al., 1995] Skipper, N., Chang, F.-R. C., and Sposito, G. (1995). Monte carlo simulation of interlayer molecular structure in swelling clay minerals. i: Methodology. *Clays and Clay Minerals*, 43(3):285–293.
- [Skipper et al., 1991] Skipper, N., Soper, A., and McConnell, J. (1991). The structure of interlayer water in vermiculite. *The Journal of chemical physics*, 94(8):5751–5760.
- [Skipper et al., 2006] Skipper, N. T., Lock, P. A., Titiloye, J. O., Swenson, J., Mirza, Z. A., Howells, W. S., and Fernandez-Alonso, F. (2006). The structure and dynamics of 2-dimensional fluids in swelling clays. *Chemical geology*, 230(3):182–196.
- [Smith et al., 2005] Smith, J. D., Cappa, C. D., Wilson, K. R., Cohen, R. C., Geissler, P. L., and Saykally, R. J. (2005). Unified description of temperature-dependent hydrogen-bond rearrangements in liquid water. *Proceedings of the National Academy of Sciences of the United States of America*, 102(40):14171–14174.
- [Smith et al., 2000] Smith, R. S., Dohnalek, Z., Kimmel, G. A., Stevenson, K. P., and Kay, B. D. (2000). The self-diffusivity of amorphous solid water near 150 k. *Chemical Physics*, 258(2):291–305.
- [Soper, 2007] Soper, A. (2007). Joint structure refinement of x-ray and neutron diffraction data on disordered materials: application to liquid water. *Journal of Physics: Condensed Matter*, 19(33):335206.
- [Soper and Benmore, 2008] Soper, A. and Benmore, C. (2008). Quantum differences between heavy and light water. *Physical review letters*, 101(6):065502.
- [Sosso et al., 2016] Sosso, G. C., Tribello, G. A., Zen, A., Pedevilla, P., and Michaelides, A. (2016). Ice formation on kaolinite: Insights from molecular dynamics simulations. *The Journal of Chemical Physics*, 145(21):211927.
- [Sparreboom et al., 2009] Sparreboom, W. v., Van Den Berg, A., and Eijkel, J. (2009). Principles and applications of nanofluidic transport. *Nature nanotechnology*, 4(11):713–720.
- [Sposito and Prost, 1982] Sposito, G. and Prost, R. (1982). Structure of water adsorbed on smectites. *Chemical Reviews*, 82:553–573.
- [Sposito et al., 1999] Sposito, G., Skipper, N. T., Sutton, R., Park, S.-h., Soper, A. K., and Greathouse, J. A. (1999). Surface geochemistry of the clay minerals. *Proceedings of the National Academy of Sciences*, 96(7):3358–3364.
- [Sprik et al., 1996] Sprik, M., Hutter, J., and Parrinello, M. (1996). Abinitio molecular dynamics simulation of liquid water: Comparison of three gradient-corrected density functionals. *The Journal of chemical physics*, 105(3):1142–1152.
- [Spura et al., 2015] Spura, T., John, C., Habershon, S., and Kühne, T. D. (2015). Nuclear quantum effects in liquid water from path-integral simulations using an ab initio force-matching approach. *Molecular Physics*, 113(8):808–822.
- [Staib and Hynes, 1993] Staib, A. and Hynes, J. T. (1993). Vibrational predissociation in hydrogen-bonded oh...o complexes via oh stretch-oo stretch energy transfer. *Chemical physics letters*, 204(1-2):197–205.
- [Stanley and Teixeira, 1980] Stanley, H. E. and Teixeira, J. (1980). Interpretation of the unusual behavior of h<sub>2</sub>o and d<sub>2</sub>o at low temperatures: tests of a percolation model. *The Journal of Chemical Physics*, 73(7):3404–3422.
- [Sui et al., 2001] Sui, H., Han, B.-G., Lee, J. K., Walian, P., and Jap, B. K. (2001). Structural basis of water-specific transport through the aqp1 water channel. *Nature*, 414(6866):872–878.
- [Sulpizi et al., 2012] Sulpizi, M., Gaigeot, M.-P., and Sprik, M. (2012). The silica–water interface: how the silanols determine the surface acidity and modulate the water properties. *Journal of chemical theory and computation*, 8(3):1037–1047.
- [Swadling et al., 2013] Swadling, J. B., Suter, J. L., Greenwell, H. C., and Coveney, P. V. (2013). Influence of surface chemistry and charge on mineral–rna interactions. *Langmuir*, 29(5):1573–1583.
- [Synchrotron Soleil, 2017] Synchrotron Soleil (2017). About soleil.
- [Tainter et al., 2015] Tainter, C. J., Shi, L., and Skinner, J. L. (2015). Reparametrized e3b (explicit three-body) water model using the tip4p/2005 model as a reference. *Journal of chemical theory and computation*, 11(5):2268–2277.
- [Tanaka, 1996] Tanaka, H. (1996). A self-consistent phase diagram for supercooled water. *Nature*, 380:328–330.
- [Tardy et al., 1999] Tardy, Y., Mercury, L., Roquin, C., and Vieillard, P. (1999). Le concept d'eau ice-like: hydratation-déshydratation des sels, hydroxydes, zeolites, argiles et matières organiques vivantes ou inertes. *Comptes Rendus de l'Académie des Sciences-Series IIA-Earth and Planetary Science*, 329(6):377–388.
- [Tazi et al., 2012] Tazi, S., Boğan, A., Salanne, M., Marry, V., Turq, P., and Rotenberg, B. (2012). Diffusion coefficient and shear viscosity of rigid water models. *Journal of Physics: Condensed Matter*, 24(28):284117.
- [Teixeira, 1993] Teixeira, J. (1993). The physics of liquid water. *Le Journal de Physique IV*, 3(C1):C1–163.
- [Teixeira et al., 1985] Teixeira, J., Bellissent-Funel, M.-C., Chen, S.-H., and Dianoux, A.-J. (1985). Experimental determination of the nature of diffusive motions of water molecules at low temperatures. *Physical Review A*, 31(3):1913.
- [Teleman et al., 1987] Teleman, O., Jönsson, B., and Engström, S. (1987). A molecular dynamics simulation of a water model with intramolecular degrees of freedom. *Molecular Physics*, 60(1):193–203.

- [Thomas and McGaughey, 2008] Thomas, J. A. and McGaughey, A. J. (2008). Reassessing fast water transport through carbon nanotubes. *Nano letters*, 8(9):2788–2793.
- [Thomas et al., 2013] Thomas, M., Brehm, M., Fligg, R., Vöhringer, P., and Kirchner, B. (2013). Computing vibrational spectra from ab initio molecular dynamics. *Physical Chemistry Chemical Physics*, 15(18):6608–6622.
- [Tobias and Hemminger, 2008] Tobias, D. J. and Hemminger, J. C. (2008). Getting specific about specific ion effects. *Science*, 319(5867):1197–1198.
- [Tocci et al., 2014] Tocci, G., Joly, L., and Michaelides, A. (2014). Friction of water on graphene and hexagonal boron nitride from ab initio methods: very different slippage despite very similar interface structures. *Nano letters*, 14(12):6872–6877.
- [Tocci and Michaelides, 2014] Tocci, G. and Michaelides, A. (2014). Solvent-induced proton hopping at a water-oxide interface. *The journal of physical chemistry letters*, 5(3):474–480.
- [Todorova et al., 2006] Todorova, T., Seitsonen, A. P., Hutter, J., Kuo, I.-F. W., and Mundy, C. J. (2006). Molecular dynamics simulation of liquid water: hybrid density functionals. *The Journal of Physical Chemistry B*, 110(8):3685–3691.
- [Torre et al., 2004] Torre, R., Bartolini, P., and Righini, R. (2004). Structural relaxation in supercooled water by time-resolved spectroscopy. *Nature*, 428(6980):296–299.
- [Tuckerman et al., 1995] Tuckerman, M., Laasonen, K., Sprik, M., and Parrinello, M. (1995). Ab initio molecular dynamics simulation of the solvation and transport of  $\text{h}_3\text{o}^+$  and  $\text{oh}^-$  ions in water. *The Journal of Physical Chemistry*, 99(16):5749–5752.
- [Tuckerman et al., 2006] Tuckerman, M. E., Chandra, A., and Marx, D. (2006). Structure and dynamics of  $\text{oh}^-$ (aq). *Accounts of chemical research*, 39(2):151–158.
- [Tuckerman et al., 2002] Tuckerman, M. E., Marx, D., and Parrinello, M. (2002). The nature and transport mechanism of hydrated hydroxide ions in aqueous solution. *Nature*, 417(6892):925–929.
- [Van Horn, 2001] Van Horn, J. D. (2001). Electronic table of shannon ionic radii.
- [VandeVondele and Hutter, 2007] VandeVondele, J. and Hutter, J. (2007). Gaussian basis sets for accurate calculations on molecular systems in gas and condensed phases. *The Journal of chemical physics*, 127(11):114105.
- [VandeVondele et al., 2005a] VandeVondele, J., Krack, M., Mohamed, E., Parrinello, M., Chassaing, T., and Hutter, J. (2005a). Quickstep: Fast and accurate density functional calculations using a mixed gaussian and plane waves approach. *Computer Physics Communications*, 167(2):103–128.
- [VandeVondele et al., 2005b] VandeVondele, J., Mohamed, E., Krack, M., Hutter, J., Sprik, M., and Parrinello, M. (2005b). The influence of temperature and density functional models in ab initio molecular dynamics simulation of liquid water. *The Journal of chemical physics*, 122(1):014515.
- [Vega, 2015] Vega, C. (2015). Water: one molecule, two surfaces, one mistake. *Molecular Physics*, 113(9-10):1145–1163.
- [Vega et al., 2009] Vega, C., Abascal, J. L., Conde, M., and Aragoñes, J. (2009). What ice can teach us about water interactions: a critical comparison of the performance of different water models. *Faraday discussions*, 141:251–276.
- [Villar et al., 2012] Villar, M., Gómez-Espina, R., and Gutiérrez-Nebot, L. (2012). Basal spacings of smectite in compacted bentonite. *Applied Clay Science*, 65:95–105.
- [Walrafen et al., 1986] Walrafen, G., Hokmabadi, M., and Yang, W.-H. (1986). Raman isosbestic points from liquid water. *The Journal of chemical physics*, 85(12):6964–6969.
- [Wang et al., 2011] Wang, J., Román-Pérez, G., Soler, J. M., Artacho, E., and Fernández-Serra, M.-V. (2011). Density, structure, and dynamics of water: The effect of van der waals interactions. *The Journal of chemical physics*, 134(2):024516.
- [Wang, 2012] Wang, W. H. (2012). The elastic properties, elastic models and elastic perspectives of metallic glasses. *Progress in Materials Science*, 57(3):487–656.
- [Wikipedia, 2017] Wikipedia (2017). Hill climbing.
- [Xu et al., 2000] Xu, W., Johnston, C. T., Parker, P., and Agnew, S. F. (2000). Infrared study of water sorption on na-, li-, ca-, and mg-exchanged (swy-1 and saz-1) montmorillonite. *Clays and Clay Minerals*, 48(1):120–131.
- [Yamamoto and Onuki, 1998] Yamamoto, R. and Onuki, A. (1998). Heterogeneous diffusion in highly supercooled liquids. *Physical Review Letters*, 81:4915.
- [Yan et al., 1996] Yan, L., Roth, C. B., and Low, P. F. (1996). Changes in the si-o vibrations of smectite layers accompanying the sorption of interlayer water. *Langmuir*, 12(18):4421–4429.
- [Yao et al., 2015] Yao, Y., Berkowitz, M. L., and Kanai, Y. (2015). Communication: Modeling of concentration dependent water diffusivity in ionic solutions: Role of intermolecular charge transfer. *The Journal of chemical physics*.
- [Yeh and Hummer, 2004] Yeh, I.-C. and Hummer, G. (2004). System-size dependence of diffusion coefficients and viscosities from molecular dynamics simulations with periodic boundary conditions. *The Journal of Physical Chemistry B*, 108(40):15873–15879.
- [Yoo et al., 2009] Yoo, S., Zeng, X. C., and Xantheas, S. S. (2009). On the phase diagram of water with density functional theory potentials: The melting temperature of ice ih with the perdew–burke–ernzerhof and becke–lee–yang–parr functionals. *The Journal of chemical physics*, 130(22):221102.

- [Yoshizawa and Israelachvili, 1993] Yoshizawa, H. and Israelachvili, J. (1993). Fundamental mechanisms of interfacial friction. 2. stick-slip friction of spherical and chain molecules. The Journal of Physical Chemistry, 97(43):11300–11313.
- [Yu and Schmidt, 2011] Yu, K. and Schmidt, J. (2011). Elucidating the crystal face- and hydration-dependent catalytic activity of hydrotalcites in biodiesel production. The Journal of Physical Chemistry C, 115(5):1887–1898.
- [Zahn et al., 1997] Zahn, K., Méndez-Alcaraz, J. M., and Maret, G. (1997). Hydrodynamic interactions may enhance the self-diffusion of colloidal particles. Physical review letters, 79(1):175.
- [Zaytsev and Aseyev, 1992] Zaytsev, I. D. and Aseyev, G. G. (1992). Properties of aqueous solutions of electrolytes. CRC press.
- [Zhang et al., 2011] Zhang, C., Donadio, D., Gygi, F., and Galli, G. (2011). First principles simulations of the infrared spectrum of liquid water using hybrid density functionals. Journal of chemical theory and computation, 7(5):1443–1449.
- [Zhang et al., 2013] Zhang, C., Gygi, F., and Galli, G. (2013). Strongly anisotropic dielectric relaxation of water at the nanoscale. The Journal of Physical Chemistry Letters, 4(15):2477–2481.
- [Zhu et al., 2012] Zhu, H., Ghoufi, A., Szymczyk, A., Balannec, B., and Morineau, D. (2012). Anomalous dielectric behavior of nanoconfined electrolytic solutions. Physical review letters, 109(10):107801.